

UNDER THE SKIN
MONTE CARLO RADIATION TRANSFER MODELLING OF PHOTODYNAMIC THERAPY

Catherine Louise Campbell

**A Thesis Submitted for the Degree of PhD
at the
University of St Andrews**



2016

**Full metadata for this item is available in
St Andrews Research Repository
at:**

<http://research-repository.st-andrews.ac.uk/>

Please use this identifier to cite or link to this item:

<http://hdl.handle.net/10023/9899>

This item is protected by original copyright

Under the skin

Monte Carlo radiation transfer modelling of photodynamic therapy

by

Catherine Louise Campbell



University of
St Andrews

FOUNDED

1413

Submitted for the degree of Doctor of Philosophy in Physics

March 2016

Declaration

I, Catherine Louise Campbell, hereby certify that this thesis, which is approximately 40,000 words in length, has been written by me, that it is the record of work carried out by me and that it has not been submitted in any previous application for a higher degree.

Date

Signature of candidate

I was admitted as a research student in 2012 and as a candidate for the degree of PhD in September 2012; the higher study for which this is a record was carried out in the University of St Andrews between 2012 and 2016.

Date

Signature of candidate

I hereby certify that the candidate has fulfilled the conditions of the Resolution and Regulations appropriate for the degree of PhD in the University of St Andrews and that the candidate is qualified to submit this thesis in application for that degree.

Date

Signature of supervisor

Date

Signature of supervisor

Date

Signature of supervisor

Copyright Agreement

In submitting this thesis to the University of St Andrews I understand that I am giving permission for it to be made available for use in accordance with the regulations of the University Library for the time being in force, subject to any copyright vested in the work not being affected thereby. I also understand that the title and the abstract will be published, and that a copy of the work may be made and supplied to any bona fide library or research worker, that my thesis will be electronically accessible for personal or research use unless exempt by award of an embargo as requested below, and that the library has the right to migrate my thesis into new electronic forms as required to ensure continued access to the thesis. I have obtained any third-party copyright permissions that may be required in order to allow such access and migration, or have requested the appropriate embargo below.

The following is an agreed request by candidate and supervisors regarding the electronic publication of this thesis: Access to Printed copy and electronic publication of thesis through the University of St Andrews.

Date

Signature of candidate

Date

Signature of supervisor

Date

Signature of supervisor

Date

Signature of supervisor

Collaboration Statement

This thesis is the result of my own work carried out at the University of St Andrews between September 2012 and March 2016. Parts of the work presented in this thesis have been peer reviewed and published. All the text in this chapter has been written entirely by me. All figures have been produced by me or reproduced with permission.

- The material from Chapter 3 formed the basis of publication: "*Monte Carlo modelling of daylight activated photodynamic therapy*", **C L Campbell**, K Wood, R M Valentine, C T A Brown and H Moseley, *Physics in Medicine and Biology*, Volume 60, Number 10. K Wood provided the Monte Carlo radiation transfer code which I subsequently adapted substantially to enable simulation of photodynamic therapy.
- Chapter 5 formed the bases of the peer reviewed conference proceeding: "*3D Monte Carlo radiation transfer modelling of photodynamic therapy*", **C L Campbell**, C Christison, C T A Brown, K Wood, R M Valentine, H Moseley, *Proc. SPIE 9531, Biophotonics South America, 95311H*. I developed the code and established the simulation parameters that were adopted for the work presented in chapter 5. C Christison performed the simulations under my close supervision. The results were plotted and analysed by me prior to inclusion in the publications as well as chapter 5.

All the publications and chapters above have benefitted from collaboration with the listed authors. Except for when stated otherwise, the work within this thesis is my own. At the time of submission of this thesis the work in chapter 6 has been submitted for publication as a research article.

Louise Campbell
March 2016

Publications and Presentations

Publications

- "*Monte Carlo modelling of daylight activated photodynamic therapy*", **C L Campbell**, K Wood, R M Valentine, C T A Brown and H Moseley, *Physics in Medicine and Biology* (2015) , Volume 60, Number 10
- "*3D Monte Carlo radiation transfer modelling of photodynamic therapy*", **C L Campbell**, C Christison, C T A Brown, K Wood, R M Valentine, H Moseley, *Proc. SPIE 9531* (2015), *Biophotonics South America*, 95311H.
- "*New insights into photodynamic therapy treatment through the use of 3D Monte Carlo radiation transfer modelling*", **C L Campbell**, K Wood, C T A Brown, H Moseley, *Proc. SPIE (2016)*, *Photonics West*
- "*Monte Carlo Modelling of Photodynamic Therapy Treatment Including Clustered Three Dimensional Tumour Structures*". **C L Campbell**, K Wood, C T A Brown, H Moseley, *Physics in Medicine and Biology (in press, 2016)*
- "*Theoretical determination of continuous Protoporphyrin IX production during photodynamic therapy*". **C L Campbell**, K Wood, C T A Brown, H Moseley, *Physics in Medicine and Biology (in prep)*
- "*A quantitative study of in vivo protoporphyrin IX fluorescence build up during occlusive treatment phases*". **C L Campbell**, K Wood, C T A Brown, A G Salvio, N M Inada, V S Bagnato, H Moseley, *Photodiagnosis and Photodynamic Therapy (in prep)*

Presentations

- "*Monte Carlo Modelling of Sunlight-Activated PDT*", Laser Europe, Manchester, UK, May 2013
- "*The benefits and limitations of daylight PDT as predicted by Monte Carlo Modelling*", European Society of Photobiology Congress, Liege, Belgium, September 2013

- "Mathematical modelling of daylight activated PDT for continuous accumulation of PpIX", Laser Europe, Amsterdam, Holland, May 2014
- "Mathematical modelling of Photodynamic Therapy", British Medical Laser Association (BMLA), Brighton, UK, April 2015
- "3D Monte Carlo Radiation Transfer modelling of Photodynamic therapy", SPIE Biophotonics South America, Rio de Janeiro, Brazil, May 2015
- "New insights into photodynamic therapy treatment through the use of 3D Monte Carlo radiation transfer modelling", SPIE Photonics West, San Francisco, February 2016
- "Monte Carlo modelling of photodynamic therapy through heterogeneous tumour tissue", BMLA, Darlington, UK, May 2016

Posters

- "A Qualitative Study of In Vivo Protoporphyrin IX Fluorescence build up during occlusive treatment phase", International Photodynamic Association Congress, Rio de Janeiro, Brazil, May 2015

Awards

- The Russell Trust Award, 2014
- Santander Mobility Award, 2014
- Photodiagnosis and Photodynamic Therapy, Elsevier PDT Prize for best conference presentation
- British Medical Laser Association (BMLA) Education Award, 2015

Field work

- I spent nine weeks in Jaù, Brazil (October - December 2014) working on a clinical study (see chapter 7) where I planned, conducted and performed the whole study. All measurements were recorded by myself.

Collaborations

- The work presented in this thesis was done by me in collaboration with the photobiology unit at Ninewells Hospital, Dundee.

Abstract

Photodynamic therapy (PDT) is a non-invasive treatment method used for treating superficial skin lesions such as non-melanoma skin cancer (NMSC). The combination of light, a photosensitive molecule and oxygen results in selective tissue destruction. Even though PDT has resulted in many successful treatment outcomes, the treatment parameters such as required light dose and preferred light source have not yet been optimised. Since monitoring of the treatment progress is limited to surface observations, it is difficult to observe what is happening under the surface of the skin.

In this thesis, the development of complex numerical modelling techniques is considered with the aim of increasing the understanding of how PDT works within the living skin tissue. In particular, the potential of using daylight as an alternative therapeutic light source is explored. Daylight PDT is associated with lower experienced pain and has the potential of reducing pressure on the clinics as well as the number of treatment occasions.

A Monte Carlo radiation transfer (MCRT) model was developed to track photon propagation during treatment. The first theoretical investigation of daylight PDT is presented where the results indicate a potential treatment depth of over 2 mm, which is sufficient for treating superficial skin cancer lesions. Additional models are developed, which consider the drug interaction and the diffusion of the drug. To include different patient characteristics and more detailed skin models, multi-layered tissue as well as complex three dimensional tumour tissues are included within the MCRT model framework.

There is no such thing as a generic patient, making it difficult to generate standardised treatment protocols. The research performed in this thesis provides further insights into light interaction with skin tissue for different patient and treatment characteristics, which is a vital step towards achieving more individualised treatment regimes.

Acknowledgments

As my dear friend Kit said, “This is the longest gap year ever”. I first came to St Andrews in 2008, intending to stay for one year. Eight years later I am still here. Who knew my gap year would turn into a PhD in Physics: the one subject I said I would never study? I would like to thank my physics teacher at school, Henrik Sjödin for the inspiration - you always believed in me and provided me with advice.

This PhD would not have been possible without my supervisors: Kenny Wood, Tom Brown and Harry Moseley. Thank you Kenny for always making time for me and for keeping me at the edge of my comfort zone. Thank you Tom for always being honest and telling me what I need to hear and not what I want to hear. You have helped me keep sane during these past three years. I sincerely believe that I would not be writing these acknowledgements without your support and all those cups of coffee. Thank you also to Harry for encouraging me to give presentations, sending me to Brazil and reassuring me when needed.

My trip to Brazil during autumn of 2014 really changed me as a scientist and as a person. There are so many people I have to thank for making my time in Brazil unforgettable. Gabriela, Ary and Elis-Angela at the hospital in Jaú, thank you for finding me patients and allowing me to perform my clinical study. I will never forget how you introduced me to your families, looked after me, served me my very first Caipirinha and made my stay enjoyable. Thank you also to everyone in São Carlos: especially to Didi and Natalia. Didi, your booming laugh and eagerness to help meant a lot to me. Natalia, thank you for being, all in all, lovely! I hope we will stay friends for many more years.

Thank you also to everyone at Ninewells for always making me feel welcome and always providing help and support. Especially thank you to Nicki and Sukirti for always being up for a nice chat over a cup of tea, and to Gordon for making me coffee. Thank you also to Ronan for not only being an excellent conference buddy but also for all your help during my PhD. I am grateful for you always making time for me and generously sharing all of your knowledge and expertise.

What would a PhD be without one’s fellow students? Thank you to everyone who has

shared an office with me and my messy desk, listened to my long rants, helped me with computer related problems and dragged me to the pub when needed. I hope I have been able to provide the same support in return.

I would like to dedicate this thesis to my family, who have always been there for me and believed in me in a way no one else could ever do. Mum for your constant Skype chatting advice, Dad for always helping out when I needed it, Christina and Fredrik for helping me think rationally and logically and Annie for being the most beautiful niece one could ever ask for. Thank you also to my extended family, especially thank you to Björn for helping me with statistics, to Gitta for never doubting my ability and to mormor and morfar for being an inspiration. I would also like to thank my beloved friends. Gabriella, Lisa, Elin, Kristin and Lena - you guys have provided food, cups of tea, glasses of wine, excellent company and most importantly a huge amount of support. Charlotte, Carrie, Kit, Sarah, Naomi, Jen and Scott - the reasons my gap year got extended. You are all truly awesome!

Finally I would like to thank my boys: Ewan and Jim, my two biggest fans. Ewan, thank you for always believing in me, discussing statistical modelling at midnight in Tesco, for putting up with my food rage and PhD related dramas as well as teaching me a healthy work/life balance. Jim, thank you for dragging me out of the office for walks, always making me smile however bad the day has been and for your unconditional love.



“Tänka fritt är stort men tänka rätt är större”

Thomas Thorild

List of Abbreviations

3D	Three dimensional
ALA	5 - Aminolevulinic acid
AK	Actinic keratosis
BD	Bowen's disease
(n)BCC	(nodular) Basal cell carcinoma
CDF	Cumulative distribution function
FECH	Ferrocetate
GCP	Good clinical practice
GLMM	Generalized mixed effects model
HPD	Hematoporphyrin derivatives
LE	Living epidermis
LED	Light emitting diode
MAL	Methyl aminolevulinate
MCRT	Monte Carlo radiation transfer
NMSC	Non-melanoma skin cancer
OBS	Optical biopsy system
PD	Papillary dermis
PDD	Photodynamic dose
PDF	Probability distribution function
PDT	Photodynamic therapy
PpIX	Protoporphyrin IX
RD	Reticular dermis
RTE	Radiative transfer equation
SC	Stratum corneum
SCC	Squamous cell carcinoma
UV	Ultraviolet

Contents

Declaration	i
Copyright Agreement	iii
Collaboration Statement	v
Publications and Presentations	vii
Abstract	ix
Acknowledgments	xi
List of Abbreviations	xv
1 Introduction	1
1.1 Thesis outline and objective	1
1.2 The skin	2
1.3 Non-melanoma skin cancer	4
1.4 Photodynamic therapy	6
1.5 Photosensitiser	9
1.6 Mechanism of action	13
1.6.1 Photobleaching	15
1.6.2 Fluorescence	16
1.6.3 Oxygen	16
1.7 Light propagation through skin tissue	17
1.8 Light sources	18
1.8.1 Daylight activated PDT	21
1.9 Role of theoretical simulation	23
1.10 Synopsis and thesis objectives	24

2	Monte Carlo radiation transfer modelling, code set-up and validation	27
2.1	Summary	27
2.2	Introduction and background	28
2.2.1	Benefits of theoretical modelling	28
2.2.2	Limitations of theoretical modelling	28
2.3	Light propagation through tissue	29
2.3.1	Beer-Lambert law	33
2.3.2	Diffusion approximation	33
2.3.3	Monte Carlo radiation transfer method	34
2.4	Method	35
2.4.1	Code details	36
2.5	Experimental validation	44
2.5.1	Experimental design	45
2.5.2	Simulation design	47
2.5.3	Results, experimental validation	50
2.6	Theoretical validation	51
2.6.1	Simulation design	54
2.6.2	Results of the theoretical validation	56
2.7	Discussion	59
2.8	Conclusion	60
3	Monte Carlo radiation transfer modelling of daylight activated photodynamic therapy	61
3.1	Summary	61
3.2	Introduction and background	62
3.3	Methods	63
3.3.1	Optical properties	63
3.3.2	Coding implementation	65
3.3.3	Natural and artificial light sources	67
3.4	Results for Monte Carlo modelling of daylight PDT	70
3.5	Discussion	78
3.6	Conclusions	80

4	Theoretical determination of continuous protoporphyrin IX production	81
4.1	Summary	81
4.2	Introduction and background	82
4.3	Methods	84
4.3.1	Prodrug diffusion	85
4.3.2	PpIX production	86
4.3.3	Different treatment modalities	87
4.3.4	Determination of constants	88
4.3.5	Fluorescence code implementation	90
4.4	Results	92
4.4.1	Clinical study	98
4.5	Discussion	102
4.6	Conclusion	105
5	Light distribution modelling of skin ageing and different skin types	107
5.1	Summary	107
5.2	Introduction	108
5.2.1	Optical properties	108
5.2.2	Anisotropy	110
5.2.3	Skin ageing and pigmentation	112
5.3	Method	113
5.3.1	Skin models	114
5.4	Results	117
5.5	Discussion	120
5.6	Conclusion	121
6	Photodynamic therapy through heterogeneous tumour tissue	123
6.1	Summary	123
6.2	Introduction	124
6.3	Method	125
6.3.1	Tumour models	127
6.4	Results	130
6.5	Discussion	145

6.6	Conclusion	146
7	A quantitative study of in vivo protoporphyrin IX fluorescence build-up during occlusive treatment phases	149
7.1	Summary	149
7.2	Introduction	150
7.3	Method	151
7.3.1	Study design	152
7.3.2	Study population	154
7.3.3	Statistical model development	154
7.4	Results	158
7.5	Discussion	167
7.6	Conclusion	169
8	Concluding remarks and future prospects	171
8.1	Summary	171
8.1.1	Theoretical modelling of photodynamic therapy	171
8.1.2	Clinical data collection	174
8.2	Future prospects	175
8.2.1	Further investigation of PDT	175
8.2.2	Areas where MCRT can be adopted for light based treatments	177
8.2.3	Further experimental and clinical explorations	177
8.3	Conclusion	178
A	Appendix: Monte Carlo radiation transfer modelling, code set-up and validation	179
A.1	Path length summation	179
A.1.1	Absorption rate	179
A.1.2	Fluence rate	180
B	Appendix: Theoretical determination of continuous protoporphyrin IX production	183
C	Appendix: Light distribution modelling of skin ageing and different skin types	195
D	Appendix: A quantitative study of in vivo protoporphyrin IX fluorescence build up during occlusive treatment phases: ethical approval	199

E	Appendix: A quantitative study of in vivo protoporphyrin IX fluorescence build up during occlusive treatment phases: individual patient measurements	207
F	Appendix: A quantitative study of in vivo protoporphyrin IX fluorescence build-up during occlusive treatment phases: pain during treatment	213
F1	Method	214
F2	Results	214
F3	Discussion	218
F4	Conclusion	219
	Bibliography	221

List of Figures

List of Figures	xxvii
1.1 Main layers associated with human skin tissue.	4
1.2 Different types of non-melanoma skin cancer (NMSC).	8
1.3 The development of the lesion (BCC) during treatment.	9
1.4 Absorption coefficient of PpIX	11
1.5 Chemical structure of ALA and MAL, PpIX as well as heme.	12
1.6 Heme pathway for ALA (and MAL) induced PpIX	13
1.7 The main photodynamic reactions through a simplified Jablonski diagram of the photosensitive molecule.	15
1.8 Absorbance of the main absorbing chromophores.	19
1.9 Aktelite	20
2.1 Cylindrical volume element demonstrating energy flow.	30
2.2 Energy flow through volume area element.	30
2.3 Description of light travelling through a medium where absorption is dominating.	33
2.4 Representation of the Cartesian grid adapted in the developed MCRT model.	36
2.5 Flowchart demonstrating the movement of the photons through the MCRT grid.	37
2.6 Representation of the step size calculation within the MCRT grid.	39
2.7 Reflection and refraction of light at the interface of two media of different refractive indices.	43
2.8 Repeated boundary conditions.	44
2.9 Experimental set-up.	46
2.10 Schematics of the OBS system.	46
2.11 Scattering coefficient for Intralipid 20%.	49
2.12 Absorption coefficient and fluorescence signal associated with Coproporphyrin III	49

2.13	Power law fitted between three scaling factors associated with various concentrations of Intralipid 20 %.	50
2.14	Fluorescence signal generated both experimentally and theoretically for varied concentrations of Intralipid 20 %.	51
2.15	Fluence rate (normalised) from fitted equations and MCRT simulations.	57
2.16	Proportion of the fluorescence emission that escapes the tissue originating at depth z (x-axis).	57
2.17	Fluorescence observed as it changed with elapsed exposure time where both 420 nm (blue) and 630 nm (red) are used as excitation wavelengths.	58
2.18	Photodynamic dose (PDD) in the presence of photobleaching as a function of depth and time elapsed.	58
3.1	Skin optical properties.	63
3.2	MCRT simulation region.	65
3.3	Direct and diffuse light.	67
3.4	Illuminating spectra.	70
3.5	Photodynamic dose for 405 nm and 630 nm.	73
3.6	Photodynamic dose for conventional PDT and daylight PDT.	73
3.7	Photodynamic dose for high initial concentration of PpIX.	74
3.8	Photodynamic dose for low initial concentration of PpIX.	74
3.9	Photodynamic dose for a long treatment times.	75
3.10	Wavelength distribution of the absorption of a total light dose of 75 Jcm^{-2} .	75
3.11	Proportion of the photons being absorbed in different wavelength ranges at different depths.	76
3.12	Proportion of the photons being absorbed at different wavelengths at different depths.	76
3.13	Effect of different illumination angles during daylight PDT.	77
3.14	The photodynamic dose comparing different values for the photobleaching dose constant.	77
4.1	PpIX cross section as a function of wavelength.	84
4.2	Fluorescence signal generated by the PpIX, normalised by the total fluorescence signal.	91
4.3	Graphical representation of the fluorescence modelling.	91
4.4	Number density of PpIX molecules as a function of time for different sets of parameters.	93

4.5	Distribution of PpIX after 3 hours of occlusive treatment.	93
4.6	Graphical representation of the change in PpIX distribution during the light treatment.	94
4.9	Photodynamic dose for different initial starting points.	95
4.7	Photodynamic dose as a function of wavelength where the initial distribution of PpIX non-uniform and the uniform are compared.	96
4.8	Photodynamic dose as a function of wavelength for different light doses.	96
4.10	Fluorescence signal change with time doe set 1.	99
4.11	Fluorescence signal change with time for set B1.	99
4.12	Fluorescence signal change with time for set B2.	100
4.13	Change in photo-toxicity with death for set B1.	100
4.14	Change in photo-toxicity with death for set B2.	101
4.15	Concentration after 30, 60 and 180 min of incubation time (no light interaction) for set B1 and B2.	101
5.1	Absorption properties for melanin and blood.	112
5.2	Multi-layered skin phantom	114
5.3	Optical properties adopted in the MCRT model to represent different ages and skin types.	116
5.4	Absorption properties of the dermal and hypodermal layers.	117
5.5	Normalised fluence rate as a function of depth for different ages and skin types.	118
5.6	Photodynamic dose at age 30, 55 and 80 years for skin types I, III and VI.	119
6.1	Tumour slice demonstrating the heterogeneous tissue structure of a nodular basal cell carcinoma.	125
6.2	MCRT simulation region.	126
6.3	Demonstration of the clustered fractal model in two dimensions (2D).	128
6.4	Density distribution of different tumour models.	131
6.5	Density distribution of different tumour models.	132
6.6	Histogram of density distribution of different tumour models.	133
6.7	Average fluence rate through different fractal tumour structures.	136
6.8	Cross section of fluence rate through different fractal tumour structures.	137
6.9	Cross section of fluence rate through different fractal tumour structures.	138
6.10	Photodynamic dose for different fractal tumour structures for conventional PDT.	139

6.11	Photodynamic dose for different fractal tumour structures for daylight PDT during clear conditions.	140
6.12	Photodynamic dose for different fractal tumour structures for daylight PDT during overcast conditions.	141
6.13	Cross section of the photodynamic dose through different fractal tumour structures.	142
6.14	Cross section of the photodynamic dose through different fractal tumour structures.	143
6.15	Simulated wide field fluorescence for different tumour fractal structures.	144
7.1	Patient with extensive Aktinic Keratosis (AK) on both arms.	151
7.2	Black out cap.	153
7.3	Patient undergoing PDT using the LINCE developed in Brazil.	153
7.4	Typical lesions included within the study.	159
7.5	Typical fluorescence signal observed from one of the patients included within the study.	159
7.6	Data for the repeated measurements for the first treatment session.	160
7.7	Average of the repeated measurements for the first treatment session.	160
7.8	Data associate with five randomly sampled patients from the total data set of patients.	161
7.9	Data for the repeated measurements for the second treatment session.	162
7.10	Average of the repeated measurements for the second treatment session.	162
7.11	Simple linear regression (first session)	163
7.12	Residuals associated with simple linear regression (first session).	163
7.13	Simple linear regression (second session)	164
7.14	Residuals associated with simple linear regression (second session).	164
7.15	Generalized Linear Mixed Effects Model (first session).	166
7.16	Residuals for the Generalized Linear Mixed Effects Model.	166
7.17	Comparison between first and second session.	167
B.1	Photodynamic dose for set 1.	186
B.2	Fluorescence signal during the occlusive treatment phase for set 1.	186
B.3	Photodynamic dose for set 2.	187
B.4	Fluorescence signal during the occlusive treatment phase for set 2.	187
B.5	Photodynamic dose for set 3.	188

B.6	Fluorescence signal during the occlusive treatment phase for set 3.	188
B.7	Photodynamic dose for set 4.	189
B.8	Fluorescence signal during the occlusive treatment phase for set 4.	189
B.9	Photodynamic dose for set 5.	190
B.10	Fluorescence signal during the occlusive treatment phase for set 5.	190
B.11	Photodynamic dose for set 6.	191
B.12	Fluorescence signal during the occlusive treatment phase for set 6.	191
B.13	Photodynamic dose for set 7.	192
B.14	Fluorescence signal during the occlusive treatment phase for set 7.	192
B.15	Photodynamic dose for set 8.	193
B.16	Fluorescence signal during the occlusive treatment phase for set 8.	193
C.1	Optical properties adopted in the MCRT model to represent different ages and skin types (II, IV and V).	196
C.2	Normalised fluence rate (ψ/ψ_0) as a function of depth for different ages and skin types (I, IV and V).	197
C.3	Photodynamic dose for age 30, 55 and 80 for skin types II, IV and V.	198
F.1	Average recorded pain during first and second treatment.	216
F.2	Average recorded pain for different lesion sizes.	216
F.3	Fluorescence signal and experiences pain.	217
F.4	Experiences pain for males and females.	217
F.5	Experiences pain for different lesion locations.	218

List of Tables

List of Tables	xxix
1.1 Environmental factors increasing the risk of developing NMSC.	6
2.1 Intralipid solutions used for the experimental validation.	47
2.2 Tissue parameters used for model validation.	52
4.1 Description of the different treatment modalities.	88
4.2 Parameter exploration for PpIX production model.	89
4.3 Summary of the results from the toxicity and fluorescence signal when adopting different sets of parameters.	97
4.4 Parameters that best match the fluorescence data collected for chapter 6.	98
5.1 Parameters adopted to compute scattering coefficients for epidermal and dermal layers.	109
5.2 Skin type classification.	113
5.3 Thicknesses of different tissue layers.	115
5.4 Input parameters used for the melanin and hemoglobin levels for the Living Epidermis (LE), the Papillary Dermis (PD) and the Reticular Dermis (RD).	115
5.5 Effective treatment depths generated from the MCRT simulations for different skin types and different ages.	120
6.1 Parameters used to generate different density structures representing different tumour structures.	129
7.1 Estimated parameters from different statistical models.	165



Introduction

1.1 Thesis outline and objective

This thesis is concerned with the development of advanced modelling techniques for understanding how cancer treatment based on photodynamic therapy (PDT) works within living tissue. The modelling techniques are based on the development of three dimensional (3D) Monte Carlo radiation transfer (MCRT) codes, which track the propagation of light through tissue and additional codes to model the light drug interactions and the diffusion of drugs into the skin.

PDT is a non-invasive method mainly used for treating precancerous and superficial malignant skin tumours [1]. Although it was initially introduced for dermatological purposes it can today be found in other areas of medicine such as otorhinolaryngology (ear, nose and throat), ophthalmology (eye), neurology (brain), gastroenterology (digestive system) and urology (urinary tract) [2]. PDT relies upon the activation of localised photosensitive molecules by application of a light source. The photosensitiser can be applied systematically, locally or topically

to the lesion. This is followed by illumination, which in the presence of oxygen molecules, leads to tissue destruction. The advantages of PDT are its non-invasiveness, the excellent cosmetic outcome and the selectivity which avoids damaging surrounding tissue. Even though PDT has been used successfully for many years there are still side-effects associated with the treatment, including pain during the treatment and long-lasting tissue photosensitivity [3].

This chapter provides an overview of PDT and the background on which this thesis is based. Firstly the main components of the skin and non-melanoma skin cancer will be introduced, followed by the basic principle behind PDT including the mechanism of action, the important properties of the photosensitiser, photobleaching and fluorescence. Light penetration through skin tissue will be discussed followed by an overview of different light sources adopted for PDT, including daylight PDT. Finally the role of theoretical modelling will be briefly introduced.

1.2 The skin

With a total weight of approximately 11 kg, covering an area of roughly 1.8 m², the skin is the largest organ of the human body [4]. The skin provides a protective barrier against the external environment including friction and impact wounds, harmful chemicals, bacteria, viruses and ultraviolet (UV) radiation. The skin prevents water loss, regulates body temperatures, produces vitamin D when exposed to sunlight and contains several nerve endings making it an efficient sensory organ [5]. The structure and composition of the skin varies depending on factors such as age, race and gender. This not only results in a variable appearance but also demonstrates functional differences [6]. To effectively study light interaction with skin tissue, understanding of the structure and composition of the skin tissue as well as acknowledging the differences between individuals is important.

The thickness of the skin varies depending on the location on the body and can vary from less than 1 mm (eyelid) to over 5 mm (upper back) [5]. The skin can be divided into two distinct layers, divided by a base membrane. The outermost layer of the skin is the epidermis which is typically 100 - 150 μm thick depending on the location and water content. The main cellular components of the epidermis are different types of keratinocytes which generate a layered structure. The keratinocytes change function and structure as they move from the basal layer, where they are produced, towards the outer non-living epidermal layer, referred

to as the stratum corneum. The keratinocytes are lost from the stratum corneum in the form of keratin flakes (corneocytes) at the same rate as new cells are produced at the basal layer [4,6]. Figure 1.1 provides a drawing of the skin structure where the different distinct layers of the epidermis are marked.

The main absorbing molecule in the epidermis is the melanin, produced in the melanocytes, mostly located within the basal layer [4]. The main function of the melanin is to protect against UV radiation. When skin is exposed to UV radiation, the production of melanocytes increases and the production of melanin is accelerated giving the skin a darker colour. This is the reason for skin appearing tanned after prolonged sun exposure. The colour of the skin also depends on genetics, where the melanosomes (containing the melanin) degrade slower in darker skin compared to lighter skin. For darker skin the melanosomes are located across the epidermis, while for lighter skin the melanosomes tend to be restricted to the basal layer [5,7]. It is common to group the appearance of the skin and its behaviour to sunlight into six skin types where skin type I corresponds to the whitest complexion and skin type VI to the darkest skin type [6,8,9]. This will be discussed further in chapter 5.

The dermis resides below the basal layer (figure 1.1). This layer is much thicker than the epidermal layer, typically between 1 mm to over 4 mm, and contains mostly fibres, vasculature and collagen. The dermis can be divided into two sublayers: the reticular dermis and the papillary dermis [10]. The upper layer of these two sub layers is the papillary dermis which contains small blood vessels and a fine network of collagen fibres. The second sublayer, the reticular dermis, contains larger blood vessels and a thicker network of fibres. The main light-absorbing structure within the dermal layers is the blood which is contained within vessels and capillaries. The reticular dermis forms a continuous boundary with the third layer of the skin, the hypodermis which contains a large amount of fat cells. This layer is typically thick (4 - 9 mm), varying between body location and individuals [6].

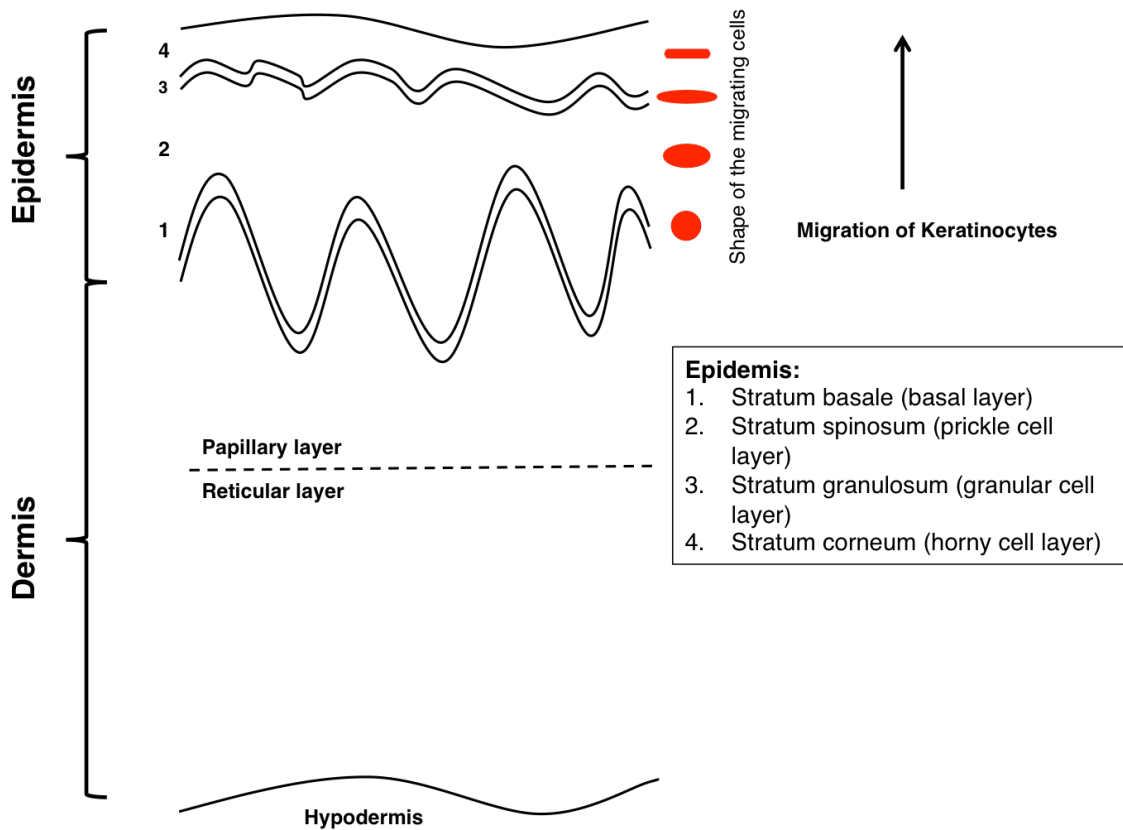


Figure 1.1: Drawing of the main layers associated with human skin. The uppermost layer is the epidermis which can be divided into several sublayers. The main cell type in the epidermis is the keratinocytes that are produced on the basal layer. During the turn-over the keratinocytes gradually travel towards the stratum corneum. During this transition the function and structure of the cells change and the end product is a non-living flat and hard cell which forms the stratum corneum. Below the epidermis, the two dermal layers can be found, the papillary and reticular layer. The hypodermis lies below the dermis [6]. Note that this is not drawn to scale.

1.3 Non-melanoma skin cancer

Nonmelanoma skin cancer (NMSC) is the most common type of cancer affecting humans; however it is rarely included in national cancer statistics. The number of new cases of NMSC per year is estimated to be at least 100 000 in the UK (2005). NMSC is generally thought to be caused by overexposure to sunlight [11–13] and is typically associated with an older age group, where 80 % of cases are in subjects aged 60 years or older [14]. Lighter skin complexions are more commonly affected due to the lower levels of melanin giving reduced protection against sun exposure. It is also thought that the incidence in men is higher than that of women [15–17]. Even though awareness of the negative impact of sun on the skin

has increased, the incidence of NMSC increases annually by 3 - 8 % [16]. This can possibly be explained by a shift in age in the human population as well as in increased skin cancer awareness leading to a higher check up rate. It is also estimated that the risk of developing additional lesions after the primary lesion is 40 - 50 % [17]. The increasing incidence in combination with the high recurrence rate makes NMSC a concern for both the public health as well as medical costs [11, 13, 18, 19]. The two most common types of NMSC are basal cell carcinoma (BCC) and squamous cell carcinoma (SCC), both originating from cells in the epidermis [4,5,20]. Mortality as a result of NMSC is rare and most commonly associated with SCC [11, 17].

Some of the environmental factors which increase the risk of developing NMSC are summarised in table 1.1. Even though factors such as sun exposure have been shown to be important in pathogenesis, there are also complex genetic factors that affect the risk of developing NMSC. Body sites that are affected are typically areas exposed to sun such as the head and neck area. The relationship between sun exposure and occurrence is further supported by the variations of incidence with geographic location, where countries closer to the equator receiving large levels of UV radiation, are associated with an increased incidence of skin cancer among light-skinned Caucasians. For an example, Australia has a considerably higher rate of incidence than Europe. It has been suggested that different lesion types are associated with different exposure patterns. It is thought that SCC is caused by a cumulative lifetime sun exposure, while BCC is more commonly thought to be due to intermittent exposure to the sun as well as sun exposure during childhood [11, 12, 17, 21, 22].

The most dangerous carcinogenic part of the solar spectrum is the ultraviolet (UV) radiation which can be divided into UVA (315 - 400 nm) and UVB (280 - 315 nm). UVB causes direct damage to the DNA and RNA while UVA causes indirect damage through the formation of reactive oxygen species [23]. The damage caused by the UV radiation requires complex and efficient DNA repair. However if the systems responsible for the DNA repair are insufficient, there are possibilities that NMSC or other skin cancers develop [17].

80% of BCCs are located on the head and neck area and even though metastasising is rare, they can spread deeply and cause substantial local damage and disfigurement [19, 24]. There are several subtypes of BCC, such as nodular, superficial and pigmented BCC (figure 1.2 a - c), all with different characteristics, so clinical diagnoses tend to be straightforward.

Table 1.1: Table of environmental factors increasing the risk of developing NMSC. The table has been modified from [17]

Environmental impact	Type of NMSC
Solar radiation [12]	BCC, SCC
UVB radiation [27]	BCC
PUVA (psoralen +UVA) [28]	SCC, (BCC)
Ionising radiation [29]	BCC
Photosensitising drugs [30]	SCC, BCC
Human papillomavirus (HPV) [31]	SCC
HIV/AIDS [32]	SCC, BCC
Arsenic [33]	SCC, BCC

Unlike BCC, SCCs have precursor lesions that are generally considered as precancerous. These include actinic keratoses (AK) (figure 1.2 g - i) and Bowen's disease (BD) (figure 1.2 d - f). SCC (figure 1.2 j - l) is the most aggressive type of NMSC and although the precancerous lesions have a small possibility of developing into the more aggressive type [20], these should be removed to avoid tissue destruction and metastasis.

For cases where the diagnosis is ambiguous, a sample of the lesion tissue can be removed and examined further [17, 25]. It is not always convenient to biopsy all lesions of interest hence non-invasive devices have been developed to try and aid the diagnosis of different skin lesions. These include dermoscopy, optical coherence tomography [25] and fluorescence life time imaging [24, 26].

There are clear medical problems associated with NMSC. There are also cosmetic disadvantages, since most lesions are located in visible areas commonly exposed to the sun such as the highly visible head and neck region. Therefore there is an incentive to develop treatment methods that have a satisfactory cosmetic outcome as well as an efficient lesion eradication. Conventional treatment methods include cryosurgery (freezing), curettage (light scraping), surgical excision and radiotherapy [34]. The treatment method that is chosen depends on lesion properties such as type, size and location as well as the available facilities [17]. The treatment method that will be discussed in this thesis is photodynamic therapy (PDT), which provides a non-invasive treatment method with excellent cosmetic outcome.

1.4 Photodynamic therapy

Examples of the use of light therapy have been found from more than 3500 years ago, where civilisations in China, Egypt and India used light to treat various skin diseases. In the early

twentieth century, Niels Finsen received the Nobel prize (1903) for his achievements in successfully treating cutaneous tuberculosis using light. The concept of PDT was first developed in 1900 when Oscar Raab reported how the combination of light and a specific dye caused cell destruction. In the following decade Hermann von Tappeiner and Albert Jesionek further proved the importance of oxygen and developed the concept of PDT by being first in applying PDT to humans [2, 35–40]. Dougherty et al later carried out extensive work by expanding the clinical use of PDT to treat cutaneous cancers and malignancies which laid the foundations for the current applications of PDT [37]. In recent years many developments have been made both with regards to the photosensitiser that is used, as well as developing user friendly light sources [3]. This thesis will focus on topical PDT, where PDT is used to treat NMSC (BCC) or precancerous NMSC (AK or BD).

The selection of an appropriate photosensitiser has been a challenge throughout the development of PDT. Protoporphyrin IX (PpIX) naturally occurs in the human body and provides a good balance between tumour selectivity and fast clearance from the body. The PpIX can be produced from externally applied prodrug containing either 5-Aminolevulinic acid (ALA) or its methyl-ester, methyl aminolevulinate (MAL) (section 1.5) [42, 43]. Figure 1.3 shows the progression of a typical treatment. Before the treatment, a light curettage removes the upper crust of the lesion, to increase penetration efficiency of the applied cream. After the surface preparation, the prodrug (in the form of a cream) is applied to the lesion, after which the lesion is covered with an occlusive dressing. The occlusive dressing excludes ambient light from interacting with the photosensitive molecule. The dressing is typically applied for 3 hours, during which the cream diffuses through the skin and the prodrug molecules (MAL or ALA) are converted into the photosensitive molecules PpIX (section 1.5). After the three hours the occlusive dressing is removed and any excess cream is removed from the lesion. The lesion is then exposed to the light source of choice (section 1.8). After the appropriate illumination time a dressing is applied and the patient is advised to avoid direct sunlight due to the risk of photosensitivity. After 7 days all of the treatment steps are typically repeated, a typical response after the first treatment can be seen in figure 1.3 b. 30 days after the second treatment, the lesions can be expected to be fully cleared, similar to figure 1.3 c. The slight depigmentation shown in the figure is common, but will in most cases recover with time.



Figure 1.2: Photographs of different types of non-melanoma skin cancer (NMSC). a) superficial basal cell carcinoma (sBCC) b) nodular basal cell carcinoma (nBCC) c) pigmented basal cell carcinoma (pBCC) d) Bowen's disease (BD) e) BD f) BD g) actinic keratoses (AK) h) AK i) AK j) squamous cell carcinoma (SCC) k) SCC l) SCC. All images are taken from [41] with permission.

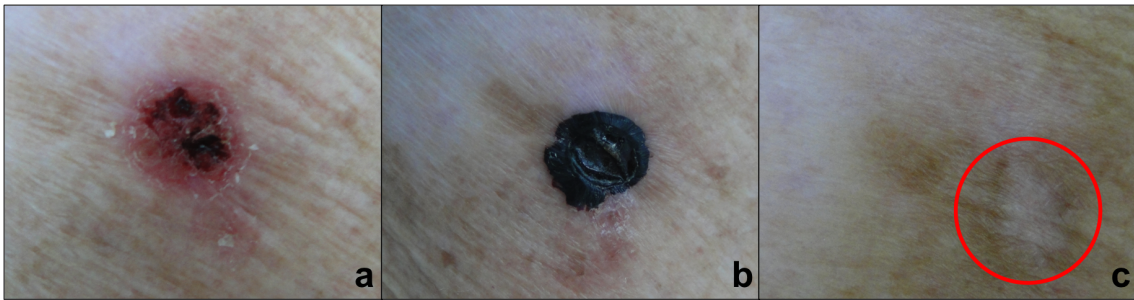


Figure 1.3: Figure showing the development of the lesion (BCC) during treatment. a) picture of the lesion prior to initial treatment. A light curettage removes some of the crusty surface prior to cream application to increase the cream penetration. b) Picture of the lesion one week after the initial PDT session, when the treatment is repeated. c) Picture of the response a month after the treatment. The lesion is cleared and the slight depigmentation will recover with time.

The recommended guidelines suggests that only lesions 2 mm or thinner should be treated with PDT [44, 45]. For topical PDT the response rate for AK is typically reported to be around 89-92 % at the three months follow up. This is on average slightly lower than cryosurgery however the cosmetic outcome is significantly superior for PDT [46, 47]. After one year the typical sustained clearance has been reported to be 63-78 % [48]. BD typically has a response rate of 86-93 % at the three months follow up with a sustained clearance after the 12 months follow up of 68-71 % [49, 50]. For BCC the response rates reported range from 92 - 97 % at the three months follow up, where superficial lesions were more successful than nodular lesions. A typical recurrence rate of 9 % has been reported at the one year follow up [49, 51, 52]. Even though PDT is an established treatment method, there are still aspects of PDT that are not yet fully understood and there is room for further development and optimisation [53]. Treatment parameters such as level of curettage, light source and amount of delivered light differ for different institutes. Differences between individuals contribute to the difficulty in determining optimal treatment parameters and point to the requirement for individualised treatment regimes.

1.5 Photosensitiser

The efficacy of PDT is highly dependent on the properties of the photosensitiser. Engineering of appropriate photosensitisers has been one of the main challenges associated with PDT. There are many features desired of an ideal photosensitiser including high absorption at longer wavelengths, providing deeper penetration and hence improved treatment efficacy.

It is also desirable to develop a photosensitiser that has a strong localising potential where the accumulation within the tissue is sufficient. To achieve time efficient treatment it is advantageous for the concentration of the photosensitiser to reach a peak value shortly after the administration of the substance. To avoid prolonged photosensitivity it is also favourable for the photosensitiser to have a fast clearance rate. If the photosensitiser has a high probability of generating singlet oxygen which is responsible for the tissue destruction, the efficacy of the treatment is improved. See section 1.6 for a more detailed description of the production of singlet oxygen and its role in PDT. The desirable features of the photosensitiser mentioned above have led to major efforts into developing new and improved substances [37,38].

When von Tappeiner and Jesionek first conducted PDT in humans, eosin was topically applied and used in combination with visible light to treat skin tumours, condylomata lata and lupus vulgaris [54]. However eosin did not selectively accumulate in tumour tissue and resulted in undesirable healthy tissue damage. Therefore it was concluded that eosin is not an optimal photosensitiser. The realisation that porphyrin-based photosensitisers on the other hand, have strong tumour localising properties was the origin of the developments of the photosensitisers used for PDT today. It was found that the application of hematoporphyrin derivatives (HPD) selectively accumulated in the tumour [37]. HPD is now available under the commercial name Photofrin (Axcan Pharma, Canada) and was the first photosensitiser to receive approval. Even though Photofrin has resulted in many successful treatments it is associated with several undesirable side effects. The clearance of the drug is long which can leave the patient photosensitive for up to eight weeks. It was also found that the localising properties were not as good as initially thought and in combination with low absorption properties at the desired longer wavelengths, Photofrin has been determined to be a sub-optimal substance for many applications [3, 38, 39].

There are now many different photosensitisers available for different clinical and experimental applications. Most of these are derived from naturally occurring tetrapyrroles, the main building block for porphyrias. Tetrapyrroles typically have a large absorption peak called the Soret band at around 400 nm with several smaller absorption bands at longer wavelengths, referred to as Q bands. For porphyrin the longest wavelength absorption band is around 630 nm, however the absorption peak at this wavelength tends to be small. The absorption spectrum for protoporphyrin IX, which is a naturally occurring porphyrin within the human and the main component of hemoglobin, is plotted in figure 1.4. For topically ap-

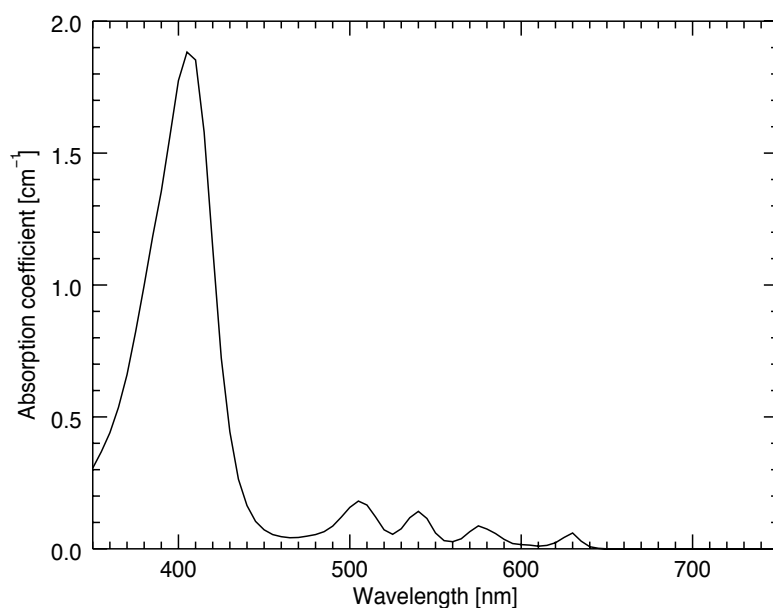


Figure 1.4: Absorption spectrum of Porphyrin IX (PpIX) [55, 56].

plied photosensitisers it is common to use precursors to PpIX such as the naturally occurring amino acid 5-Aminolevulinic acid (ALA) or its methyl ester methyl aminolevulinate (MAL). ALA occurs naturally in the heme biosynthetic pathway. MAL is a methylated version of ALA; it is approved for the use in PDT and is commercially available in Europe. Following the application of MAL, it is converted to ALA *in vivo*. Figure 1.5 shows the molecular structure of ALA, MAL, PpIX and heme (one of the main components of hemoglobin). MAL has been expected to result in deeper penetration within the tumour tissue due to its increased lipophilicity; however little significant difference in the response has been reported between the two substances [42, 44, 57].

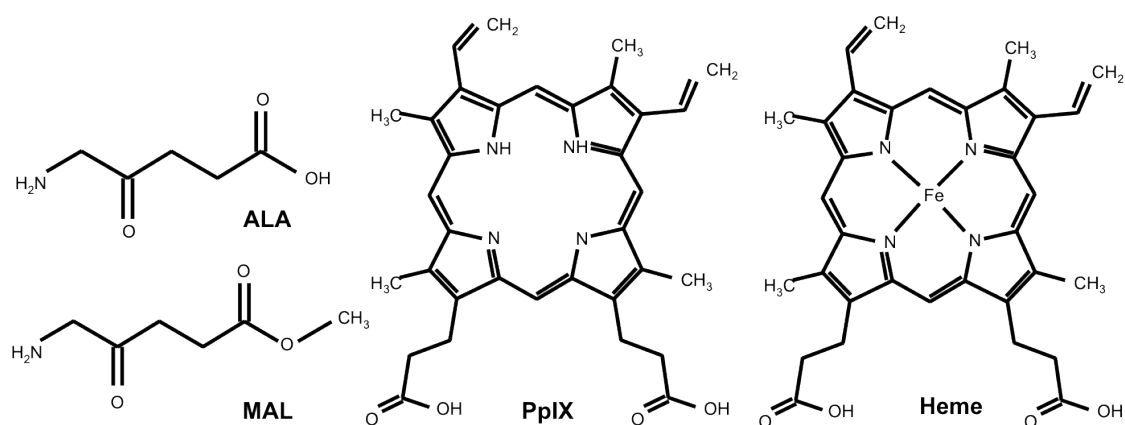


Figure 1.5: Figure showing the chemical structure of ALA and MAL, PpIX as well as heme [38].

When additional ALA is exogenously added to the tumour cells, rate limiting steps within the heme bio-synthetic pathway are bypassed which result in selective accumulation of PpIX within tumour cells. Figure 1.6 shows the most important steps in the heme biosynthesis. ALA is normally produced from glycine and succinyl-CoA. Through conjugation of several ALA molecules PpIX molecules are produced within the mitochondria. The final step of the heme biosynthesis is the addition of iron (Fe^{2+}) into PpIX to produce heme, catalysed by the enzyme ferrochelatase (FECH). The two most important bypassed rate-limiting steps are firstly the negative feedback loop regulating ALA production and secondly the production of heme from PpIX. The amount of naturally occurring ALA will be regulated by the amount of heme in the cell. By exogenously adding ALA this feedback loop will be bypassed which leads to an accumulation of PpIX within the cell. The accumulated PpIX will not automatically be converted into heme due to the rate limiting FECH. The additional selectivity within tumour cells can be explained by the difference between the heme biosynthesis in malignant and non-malignant cells. A decreased activity of FECH as well as a limited amount of available iron within tumour cells is thought to be the reason for the additional accumulation of PpIX within tumour cells. It has also been reported that the levels of enzymes responsible for the conjugation of ALA into PpIX are higher in tumour cells [3, 38, 42, 43, 58].

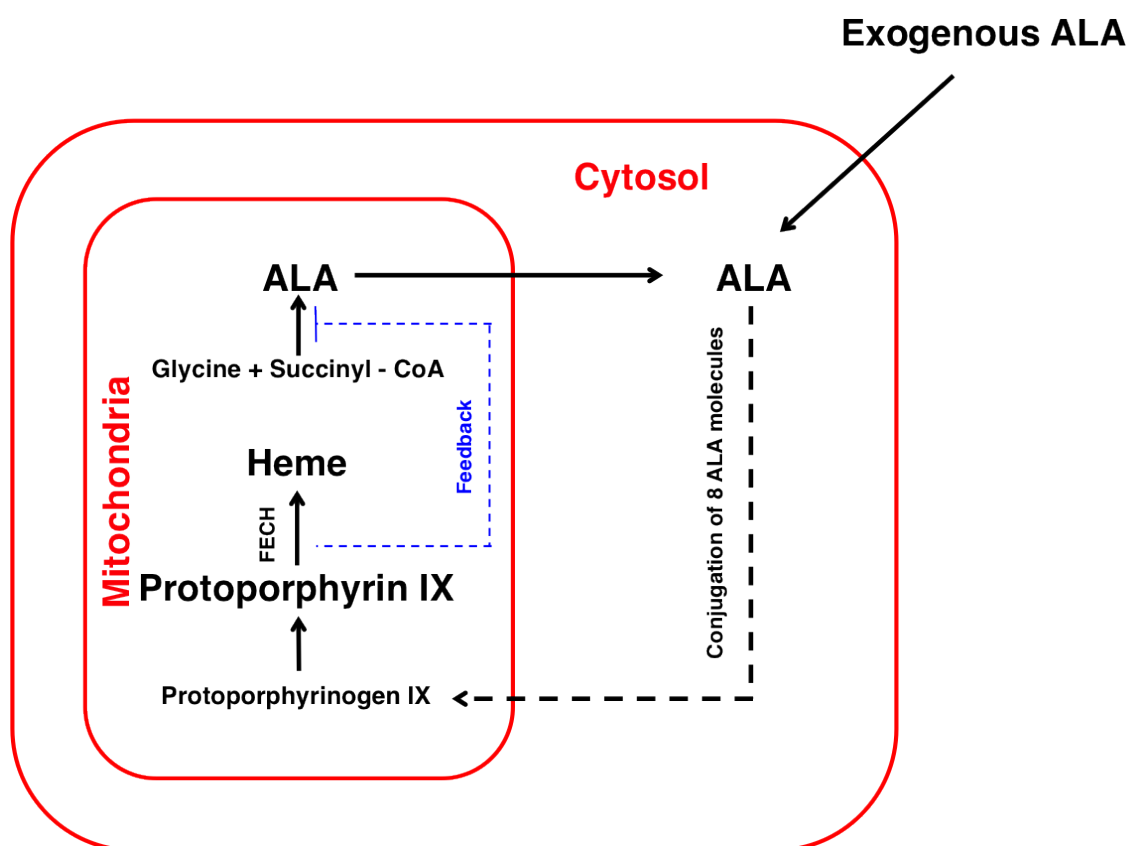


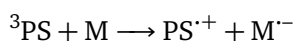
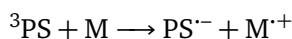
Figure 1.6: Figure showing the heme pathway for ALA (and MAL) induced PpIX. This is naturally occurring in all human cells but the exogenous addition of ALA (or MAL) disrupts the biosynthesis of heme which leads to accumulation of PpIX in the target tissue cells. Eight ALA molecules are conjugated to generate PpIX through various enzyme activated steps. When ALA is exogenously added to the tumour lesion rate limiting steps are bypassed, which results in accumulation of PpIX within the cells. The PpIX is produced within the mitochondria, but quickly diffuses to other part of the cell [3, 58].

1.6 Mechanism of action

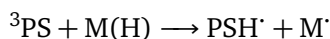
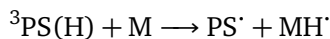
Cell death is caused by light-induced activation of the photosensitiser which generates reactive oxygen species. As previously mentioned, the prodrug used for topical PDT contains ALA or MAL molecules which are converted to PpIX molecules (section 1.5). Figure 1.7 shows the Jablonski diagram for the PpIX molecule containing only a subset of the discrete energy levels. The photosensitising mechanism is initialised by the absorption of a photon. This causes an excitation of the PpIX molecule from its singlet ground state (S_0) to an excited single state (S_1), associated with a short life time (10^{-8} to 10^{-9} seconds) [59]. The excited molecule can decay back to its ground state through dissipation of energy through heat or emission of a fluorescence photon. An alternative route is by intersystem crossing and conversion to a

triplet excited state (T_1) through a spin flip. This state is a more stable state and has a longer life time (10^{-3} seconds) due to the forbidden transition between T_1 and S_0 . The triplet state is responsible for the generation of the cytotoxic species. The long life time makes the PpIX molecule in the triplet excited state more likely to react with the surrounding environment. The probability of the different pathways is determined by the composition of the molecule and engineering of the molecule can increase the likelihood of intersystem crossing.

The photodynamic reaction can be split into two processes known as Type I and Type II. Type I reactions involve direct interaction with a surrounding substrate. Through electron or proton (hydrogen) transfer, free radical or superoxide ions can be produced. This can be expressed as a reaction between the photosensitiser in its triplet state, 3PS and a molecule M . For electron transfer:

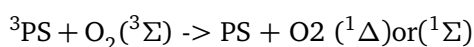


And for hydrogen atom transfer:



Here the dot indicates that the species are radicals, hence that they have an uneven number of electrons. The signs (+/-) indicates the net charge of the molecule. $PS(H)$ indicates that it is only one (of many) of the hydrogen atoms (H) in the PS molecule that is involved in the transfer reaction. The same applies to $M(H)$. In the final two reactions PS^{\cdot} and M^{\cdot} are the original molecules minus one of its hydrogen atoms. These radicals (with one unpaired electrons) tends to be very reactive (in comparison to molecules with even paired electrons) and can react with oxygen to produce reactive oxygen species.

Type II involves an interaction with molecular oxygen in its first step, where the outcome is singlet oxygen, 1O_2 . This process can be expressed as:



where ($^3\Sigma$) corresponds to the triplet state of O_2 , ($^1\Delta$) corresponds to the first excited singlet state and ($^1\Sigma$) corresponds to the second excited singlet state. In the case when $O_2(^1\Sigma)$ is produced, a fast decay will result in a rapid conversion to $O_2(^1\Delta)$ (responsible for the type II reaction).

The ratio between Type I and Type II depends on the photosensitiser and the available concentration of oxygen; however Type II is thought to be the main cytotoxic agent involved in PDT [37, 59–61].

The different oxygen species induced by the light absorption can lead to destruction of multiple cellular structures. Both proteins and lipids are targeted which leads to functional and structural changes to the cells which finally leads to apoptosis and/or necrosis [62]. It is believed that the different oxygen species only diffuse small distances ($\sim 10 \mu\text{m}$) which emphasises the importance of the localisation of the photosensitiser. If the photosensitiser is efficiently and selectively accumulated within the tumour region, only tumour tissue will be affected by the photodynamic reactions [63, 64].

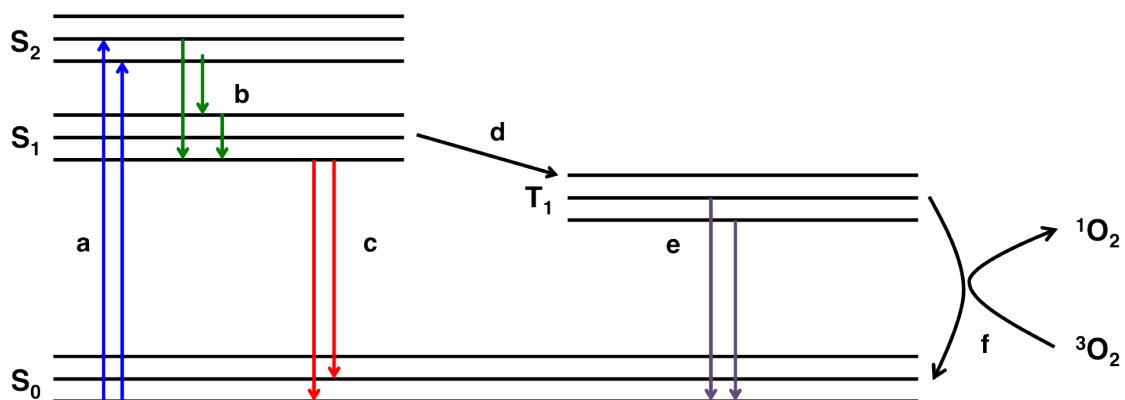


Figure 1.7: Figure demonstrating the main photodynamic reactions through a simplified Jablonski diagram of the photosensitive molecule. S_0 represents the ground state level and S_1 and S_2 represents two singlet excited states. T_1 corresponds to an excited triplet state of the photosensitive molecule. The different arrows demonstrate different energy transitions during photon absorption. a) Excitation, b) Internal Conversion / vibrational relaxation, c) Fluorescence, d) Intersystem Crossing, e) Phosphorescence f) Excitation of oxygen by energy transfer.

1.6.1 Photobleaching

Ideally the photosensitive molecule (here PpIX) would act as a catalyst for tissue destruction without actually being destroyed itself. By generating singlet oxygen molecules, the energy in

the photosensitiser is transferred to the oxygen which results in a ground state photosensitiser. This way the photosensitiser is fully recycled (figure 1.7). However, during the photodynamic process the sensitiser is used up, which results in photobleaching. During the process of developing the reactive oxygen species, the photosensitiser can be destroyed or chemically modified. This results in a dysfunctional photosensitive molecule. It is also possible that the produced singlet oxygen can react with the photosensitiser itself. Again this would change the properties associated with the molecule and result in reduction of available photosensitiser [59, 65]. The photobleaching results in decay of the photosensitiser, which is typically expressed by an exponential decay and will be further discussed in chapter 2 (section 2.6) and chapter 3 (section 3.3.2).

1.6.2 Fluorescence

One of the options for a molecule in its singlet excited state S_1 is to emit a fluorescence photon (figure 1.7). The fluorescence spectrum of a photosensitiser is always shifted towards longer wavelengths and the PpIX has a characteristic fluorescence peak at 635 nm. This can be experimentally useful since it provides an indirect indication of the quantity of PpIX within the measured tissue. The fluorescence properties allow for the edges of the tumour to be determined using e.g. a Woods lamp. The drug delivery efficiency can also be investigated by measuring the fluorescence signal at different time points [59]. In addition, the fluorescence signal produced by accumulated PpIX can be used to aid the diagnosis of some skin diseases that are more difficult to diagnose by eye [3]. Indirectly it is thought that the fluorescence signal indicates the singlet oxygen production, this is typically referred to as implicit dosimetry [66]. Since the fluorescence signals can reveal important information, developing a photosensitiser with strong fluorescence characteristics appears to be of interest [67]. The fluorescence spectrum of PpIX and techniques of measuring the spectrum will be further discussed and illustrated in chapter 7.

1.6.3 Oxygen

Oxygen plays a key role in PDT, mostly due to the production of singlet oxygen which is thought to be the main contributor to the photodynamic effect. The level of oxygenated blood will also affect the penetration of light since oxygenated and deoxygenated blood have different optical properties which effect the light propagation at certain wavelengths. The

level of available oxygen within the tumour will deplete due to singlet oxygen production (as well as other reactive oxygen species) and vessel damage as a result of long exposure times [68]. For this reason, it has been suggested that fractionated treatment would allow the oxygen levels to recover in-between light bursts. Delivering the light in smaller fractions with a pause in between bursts, allows the oxygen concentrations to recover. The frequency of the pulses vary from multiple illumination periods where the light source is turned off/on every 60 seconds [69] to fractionation with only two periods of light illumination with a pause of 2 hours in between [70]. Both in vitro and in vivo studies suggest that using a fractionated treatment results in an improved PDT outcome [71]. Optimised treatment regimes and illumination patterns have not been established and fractionated PDT is not yet a commonly adopted technique.

1.7 Light propagation through skin tissue

The photodynamic effects are dependent on the light interaction with skin tissue. As the light travels through the skin it is either scattered or absorbed as the photons interact with the skin tissue. This will be discussed in more detail in chapter 2. The optical properties of the skin tissue determine the propagation of the light through skin. The values and implications of these properties will be discussed further in chapter 5.

It is common to refer to light dose when comparing different light based therapies. The light dose describes the amount of light delivered to the tissue and is expressed in units of J cm^{-2} . The light dose is defined as,

$$\text{Light dose} = I \cdot t \tag{1.1}$$

where I is the irradiance of the source light at the surface of the skin (W cm^{-2}) and t is the total irradiation time (seconds). This allows for different light sources of varying intensities to be compared for the same delivered light dose, corresponding to different treatment times. Light doses between 37 and 540 J cm^{-2} have been shown to result in effective PDT treatment. The total light dose delivered does not consider the differing spectral contributions during PDT. Different wavelengths contribute to different levels of absorption of the photosensitive molecule. An alternative way to consider the light dose is therefore by weighting it by the absorption properties of the photosensitive molecule [72]. A typical light dose (non-weighted)

delivered during conventional PDT treatment at Ninewells Hospital in Dundee is 75 J cm^{-2} [56], and is therefore the light dose considered and compared for many of the simulations in this thesis.

The different light sources that have been proven to result in effective PDT differ not only in wavelength but also in intensity and uniformity. The irradiance of the applied light sources is recommended to not be higher than 150 mW cm^{-2} since a high irradiance can lead to unwanted hyperthermic damage [72].

1.8 Light sources

When choosing an appropriate light source for PDT there are several aspects to consider. Firstly, the wavelengths have to match the absorption bands of the photosensitiser so that a sufficient amount of singlet oxygen is produced. The illumination area has to be sufficient to treat the selected region and the irradiance has to be high enough to provide a good treatment response without causing too much pain. There are also aspects of the equipment that have to be considered such as cost and user friendliness. The type of light source chosen is often dictated by the location of the lesion, the light dose that is required as well as the photosensitiser that is used.

To enable deep penetration within the skin tissue, the absorption properties of tissue have to be considered. Figure 1.8 shows the absorbance of the main chromophores in skin tissue. Melanin and hemoglobin are strongly absorbing in the shorter blue wavelength range while water is strongly absorbing at longer wavelengths. Wavelengths between these two regions ensures deeper penetration within biological tissue. This wavelength range is typically referred to as the therapeutic window. The targeted wavelength range for PDT is however between 600 nm and 800 nm. Longer wavelengths do not provide enough energy for triplet state conversion to subsequently excite oxygen molecules. When using the photosensitiser PpIX, it is common to target the absorption peak at 630 nm to ensure the deepest possible penetration [1, 3].

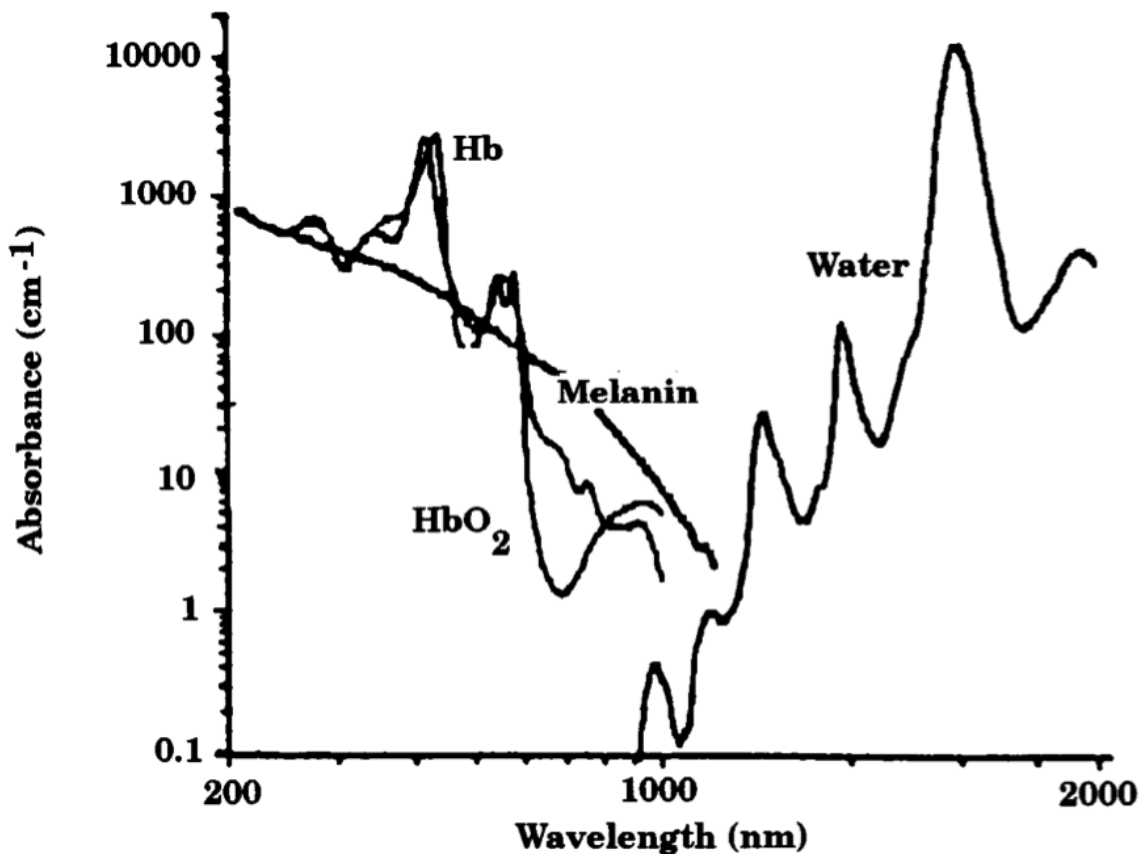


Figure 1.8: Figure showing the absorbance of the main absorbing chromophores in tissue which demonstrates the therapeutic window in which deeper tissue penetration is achieved. The main absorbers are melanin, hemoglobin and water. Reproduced with [73]

Three main classes of light sources have been adopted for PDT: lasers, filtered lamps and light emitting diodes (LED). Even though lasers provide a monochromatic high powered light source, they are not optimal light sources for topical applications when treating larger lesions due to the requirement of expanding the beam, which requires the addition of optical instruments. In addition the lasers tend to be expensive and associated with additional safety requirements. In addition, the requirement for technical support makes these less attractive for topical PDT applications; however, successful results have been reported for internal PDT application where the laser has been coupled to an optical fibre. Different lamps have the advantage of being cheap and easy to maintain as well as providing a portable device. However due to the wide spectrum, more care is required to calculate the desired light dose. Coupling lamps into optical fibres tends to limit the output power which limits lamps to topical applications such as to treat skin lesions. Currently, LED-based light sources are commonly adopted in PDT with the main advantage of being cheap and versatile with a reliable power output.

They provide a portable device with the flexibility of arranging the LEDs in different geometries for different body locations [1, 74]. Valentine et al (2011) performed a theoretical study comparing different non-laser light sources, demonstrating the importance of an appropriate choice of light source [75].

The light source adopted for clinical treatment at Ninewells Hospital in Dundee is the Aktilite, which is an array-based red LED light source. The arrangement of LEDs can be adjusted so that the illuminating region is appropriate relative to the size of the lesion. An image of the device is shown in figure 1.9.



Figure 1.9: Image of Aktilite, which is the light source adopted at Ninewells Hospital [72].

By delivering the light during a longer period of time at a lower irradiance, it is thought that the oxygen consumption is also slower. This is therefore considered to be as effective, if not more so, compared to the conventional high-dose PDT using e.g. Aktilite [69]. The lower levels of pain reported for the low-dose PDT has shown a clinical advantage. Successful results have been reported using a portable LED low irradiance light source (Ambulight; Ambicare

Health Ltd, Scotland). The Ambulight provides a convenient wearable source associated with a lower experienced pain [76, 77]. Unfortunately, these devices are still limited in size and therefore not appropriate for treating larger affected areas, typically associated with AK. The same theory of delivering light during a longer period at a lower irradiance supports the investigation of daylight activated PDT, where daylight is used as the excitation light source [76, 78, 79].

1.8.1 Daylight activated PDT

One of the limitations with many light sources used in PDT is the restriction in the size of the possible treated area. By using daylight, the only restriction is in the ability to expose the affected region to daylight. With conventional treatment modalities, only a few lesions can be treated during the same hospital visit. Utilising daylight as the therapeutic light source would lead to a reduction in the number of treatment sessions for patients with extensive coverage of lesions. Efficient daylight PDT would lead to a more convenient treatment modality for both patient as well as the treating clinic, leading to a higher throughput of patients.

The first clinical study of daylight PDT took place during the summer of 2006 in Denmark (Copenhagen). 29 patients with AK of the face and scalp were included in the study. Each patient received both daylight PDT and conventional PDT (using a red LED) on separate lesions. This allowed the patients to compare the two treatment methods. During the conventional PDT the area was occluded for three hours after the application of the cream (containing MAL) after which a total light dose of 37 J cm^{-2} was delivered. For daylight PDT the area was occluded for only 30 minutes after which the area was treated with daylight for 2.5 hours. The weather conditions varied although most patients were treated on days with no or few clouds. The study showed no significant difference in the treatment response between the two treatment protocols (79 % vs. 71 %). Treatments using daylight PDT resulted in a significantly lower pain score compared to conventional treatment modalities. The study also successfully demonstrated that daylight PDT was the preferred choice of treatment for 62% of the patients [80].

Since this first study, several supporting studies on AK have been published in Europe [81–88], Australia [89], North America [90] and Latin America [91] with response rates between 70 - 89%. All studies show no inferior response rates to conventional PDT with lower recorded pain scores and better skin reactions such as reduced erythema. Daylight PDT has

also been shown to be the preferred choice of treatment by patients. The European consensus recommends 2 hours of daylight exposure, 30 minutes after application of MAL cream. The treatment is suggested to be possible in all weather conditions however a minimum temperature of 10 °C is recommended for the comfort of the patient (it is also recommended that the temperature should not be too high to cause discomfort or danger to the patient). A shorter exposure is thought to result in an insufficient amount of PpIX produced within the lesion and for a longer exposure the probability of extensive erythema (without improved treatment results) is increased [78]. The recommended effective light dose is typically suggested to be 8 J cm^{-2} (weighted by the normalised absorption properties of the photosensitiser) [92]. To protect patients from damaging UV radiation, a sunscreen should be applied to all exposed areas. Typically sunscreens only overlap the absorption spectrum of PpIX by a small amount and are not thought to reduce the penetration of the light, and thereby not affect the efficacy of the treatment [93].

The reason for the reduced pain is not only due to the lower irradiance, but also due to the continuous build-up of PpIX. During conventional PDT the PpIX builds up during 3 hours after which the region of interest is exposed to a light source of high irradiance during a short period of time [94]. This results in a high concentration of reactive oxygen species (including singlet oxygen) shortly after the start of the illumination, thought to be one of the reasons for the high levels of experienced pain. During daylight PDT the PpIX is produced continuously during the illumination resulting in a continuous production of reactive oxygen species and considerably lower levels of pain [78].

So far it is only common to treat AK of grade I and II [95] using daylight PDT; however a study in Denmark reports successful results using daylight PDT to treat BCCs. The response rate at the 3 months follow up was 90 % [34], again comparable to results achieved using conventional PDT [51, 96]. The response was reduced to 74% after 12 months and the high recurrence rate has been speculated to be due to the thickness of the lesion making this treatment less suitable for thicker lesions such as BCC [78].

Unpredictable weather conditions altering the treatment conditions as well as the lack of supervision during the treatment are the main limitations with daylight PDT. In northern Europe daylight treatments can only be scheduled for the summer months of the year and in warmer climates the heat of direct sunlight is an additional restriction. If the treatment is per-

formed during unsupervised conditions, the full exposure time is not guaranteed. Discomfort can be achieved if the region of interest is exposed to varied degrees of daylight. For example, prolonged time in dark shadowy areas can increase the production of PpIX, leading to increased pain when subsequently exposed to daylight [78]. Daylight PDT has recently become very popular with both patients and clinics. Even though there are treatment guidelines, there is little evidence for the justification of treatment time and treatment conditions. To fully explore the potential and limitations of using daylight PDT further studies on treatment depths and treatment times should be explored.

1.9 Role of theoretical simulation

Theoretical approaches are useful when establishing links between measurements and the properties of skin tissue. They also aid further development of new treatment techniques since theoretical simulations can reveal important information about the interaction between light and tissue. For example PDT requires knowledge of the photodynamic dose and penetration depth [97], which are difficult to measure. Through theoretical simulations, these properties can be easily determined and subsequently aid the development and comparison of new treatment modalities [98]. This thesis focuses on the implementation of Monte Carlo radiation transfer (MCRT) modelling of PDT, where photons are followed through their random walk through skin tissue. Due to the flexibility and accuracy associated with MCRT modelling, this technique is thought to be the gold standard in radiation transport modelling.

MCRT has been used for over two decades to simulate light propagation through skin tissue [99] and has since then been used multiple times to simulate PDT [97, 100–102]. In the work presented here we use MCRT as a tool to compare different treatment modalities and different treatment conditions. Many previously published studies simulate reflectance and fluorescence measurements [103–105] however here we focus on simulating daylight PDT and how different treatment parameters such as PpIX concentration and different optical properties affect the treatment outcome. These are properties that cannot be directly measured and therefore theoretical modelling provides a tool to work towards a more personalised treatment. Chapter 2 will discuss the theory behind MCRT modelling and also discuss the benefits and limitations of theoretical models further.

1.10 Synopsis and thesis objectives

This thesis focuses mainly on topical PDT during different treatment conditions. Treatment conditions vary between different institutes where, for example, the total delivered light doses vary significantly. By investigating light interacting with skin tissue during different treatment conditions the aim of this thesis is to increase the understanding of PDT and work towards finding optimised treatment parameters. Due to the non-invasive nature of the treatment the monitoring of the treatment progress is limited to surface measurements and observations. The challenges associated with these limitations can be assisted by implementing theoretical techniques. By developing appropriate simulations information about the light distribution and photo-toxicity within the skin tissue during the treatment can be established. A major focus of this thesis is to investigate appropriate properties and skin models to achieve accurate results. Patients with different tissue properties respond differently to treatment. Therefore there is incentive to develop a more personalised treatment plan. To develop current treatment plans the effects of different types of skin (with regards to for example age and skin colour) and different tumour shapes during PDT are investigated for the first time. A further aim of this thesis is to investigate new treatment modalities such as theoretically exploring the potential and limitations of using daylight as a potential light source.

Chapter 2 discusses the importance of theoretical modelling of PDT as well as the development of the Monte Carlo radiation transfer (MCRT) model adopted in the majority of the subsequent chapters. A thorough validation is presented where both experimental and previously published theoretical results are reproduced successfully. Chapter 3 demonstrates a theoretical model for daylight PDT during different weather conditions in comparison to conventional treatment modalities where an artificial light source is adopted. The toxicity during daylight PDT is determined as a function of depth for different weather conditions indicating sufficient treatment depths for superficial lesions after only 30 min of daylight illumination.

Chapter 4 considers the production of the photosensitiser within the tumour as it changes with depth from the surface as well as time since application of the prodrug. The properties of the production of the photosensitiser are investigated and explored and compared to clinical data. Chapter 5 discusses the importance of the allocation of appropriate optical properties, where the effect of different optical properties is demonstrated through the investigation of different ages and skin types. It will be shown that light propagates deeper through lighter

skin complexions and older skin. Chapter 6 explores the importance of including three dimensional (3D) structures in the MCRT model. By redistributing the mass of the tumour in a clustered way, keeping the total mass constant, it is found that the light penetrates deeper through heterogeneous tissue. This supports further development of 3D heterogeneous skin phantoms.

Chapter 7 presents a clinical study performed in Brazil, where the PpIX fluorescence signal was recorded during the occlusive treatment phase prior to light illumination. The fluorescence signal can be used as an indication of the amount of PpIX present within the skin tissue. The results from the study suggest a linear build-up of PpIX during the three hour long occlusive treatment. This indicates that the light treatment could be initialised later to ensure that the PpIX penetrates deeper into the skin. Chapter 8 presents overall conclusions and suggestions of future work based on the results obtained in this thesis.

2

Monte Carlo radiation transfer modelling, code set-up and validation

2.1 Summary

Monte Carlo Radiation Transfer (MCRT) is a flexible and robust technique for studying light propagation through turbid media. Due to its ability to accurately simulate light interactions with different tissue types, it is a useful tool for assisting photodynamic therapy (PDT) dosimetry and treatment planning [106, 107]. This chapter describes the fundamentals of MCRT modelling and the development of the code that will be used in subsequent chapters to simulate different treatment conditions. For any established code, validation is essential. The code that was developed here was rigorously validated by successfully reproducing both experimental observations and theoretical predictions from independently produced codes. The experimental validation reproduced the fluorescence signal generated by Coproporphyrin III in various aqueous concentrations of the fat emulsion Intralipid 20 %. The theoretical valida-

tion successfully reproduced MCRT results generated by Jacques et al in 1993 [97].

2.2 Introduction and background

By simulating the light propagation through the skin tissue during the light treatment, further information about the potential and limitations for different PDT treatment conditions can be explored. This chapter discusses different alternative methods of studying light propagation through a turbid medium, with a focus on MCRT modelling. The majority of the work presented in this thesis uses MCRT modelling to investigate different aspects of PDT. This chapter provides a detail description of the development and validation of the code used for subsequent chapters.

2.2.1 Benefits of theoretical modelling

The number of light applications in medicine is growing, which increases the need of theoretical models that link the measurable properties with tissue characteristics. From surface measurements alone (e.g. reflected light and fluorescence) it is impossible to study light interaction under the surface of the skin and thereby the treatment progress during illumination. For PDT the simulated light distribution helps to determine optimal light sources and wavelengths. By considering the properties and dynamics of the skin, additional information and knowledge can be acquired from surface observations such as the generated fluorescence signal [98, 108]. In addition to allowing more information to be gained from surface observations, theoretical simulations also allow investigation and exploration of features of the treatment impossible to observe from the surface [107, 109]. Simulations of PDT allow for different treatment modalities to be investigated and compared and provide a useful tool when developing new techniques [110]. By adopting a sufficient and appropriately validated model, scattering, absorption, treatment depths, energy deposition and fluorescence signal can be thoroughly studied during a simulated light treatment.

2.2.2 Limitations of theoretical modelling

Theoretical models rely on appropriate and reasonable input parameters to generate accurate results. Only when realistic input parameters are adopted is it possible to generate useful information. When simulating PDT it is not only crucial to include all the important features and processes involved, but also to represent accurately the optical properties of the simulated

tissue region. Unfortunately the available *in vivo* data necessary for accurate representation is relatively limited [111, 112]. The optical properties are very different between and within individuals which makes the allocation of appropriate optical properties challenging as discussed in chapter 5. With more assumptions and approximations the result tends to be a less accurate model. However, a model with fewer assumptions typically results in a too simple model. The balance between these factors is important to as accurately as possible, represent the desired situation. Therefore it is imperative, when adopting a theoretical model to consider the associated assumptions and approximations where the limitations only allows the results to be used as a guide under the circumstances stated by the simulations.

2.3 Light propagation through tissue

The radiative transfer equation (RTE) describes the distribution and propagation of light through any medium. The RTE can be derived from the energy conservation principles of the energy flow, dP , through a cylindrical volume element, within the solid angle $d\Omega$, in the direction \hat{s} , per unit time (figure 2.1) [106, 113]. The energy conservation equation is described as:

$$dP = -dP_{\text{div}} - dP_{\text{ext}} + dP_{\text{sca}} + dP_{\text{src}} \quad (2.1)$$

Where dP_{div} is the energy lost due to divergence of the photon beam, per unit time. dP_{ext} is the energy lost per unit time due to absorption and scattering. dP_{sca} is energy gained (per unit time) due to scattering from any other direction \hat{s}' into \hat{s} and dP_{src} is the energy contribution from the sources per unit time. These different contributions will be separately discussed and finally combined to derive the RTE (Boltzmann equation).

The overall change in energy per unit time in the volume element (figure 2.1) can be expressed as

$$dP = \frac{1}{c} \frac{\partial L(\vec{r}, \hat{s}, t)}{\partial t} dV d\Omega \quad (2.2)$$

where $L(\vec{r}, \hat{s}, t)$ is defined as the radiance of the light at position \vec{r} , travelling in the direction, \hat{s} , at time t . L has the units $\text{W m}^{-2} \text{sr}^{-1}$ and in equation 2.2, c represents the speed of

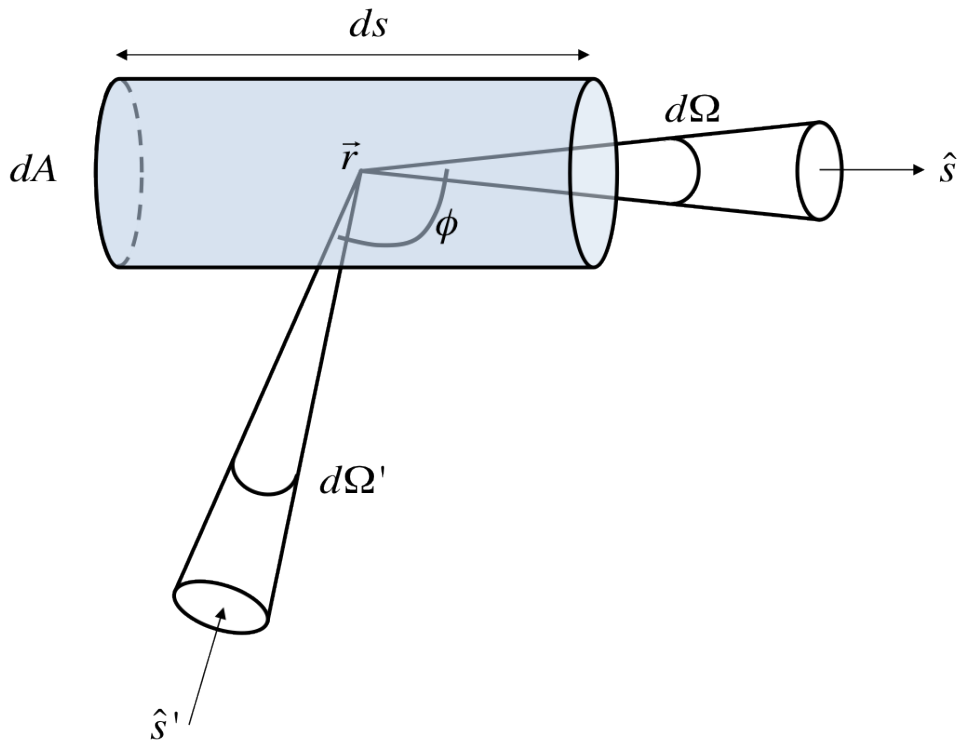


Figure 2.1: Figure showing the cylindrical volume element. The energy flow through the volume element is used to derive the radiative transfer equation [113].

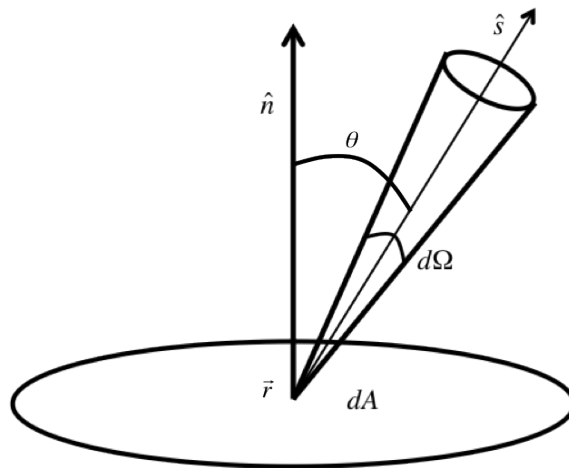


Figure 2.2: Figure demonstrating the energy flow through area dA in direction \hat{s} . θ in equation 2.3 is the angle between the unit outwards direction \hat{s} and the normal unit vector \hat{n} [113].

light. The radiance is defined as the specific intensity over a narrow frequency range. The radiance is what describes the light distribution through the medium and the end goal with the RTE is to determine $L(\vec{r}, \hat{s}, t)$ since this contains all the important and relevant information to describe additional physical properties.

The radiance, $L(\vec{r}, \hat{s}, t)$ can be used to determine the energy flow through the small area dA , within solid angle $d\Omega$ during dt by:

$$dE = L(\vec{r}, \hat{s}, t) \cos\theta dA d\Omega dt \quad (2.3)$$

Where θ is the angle between the unit outwards direction \hat{s} and the unit normal vector of dA (figure 2.2). The radiance can also be used to determine the fluence rate, which is defined as the energy flow per unit area and time independent of flow direction and has the units $W\text{cm}^{-2}$. The fluence rate is therefore generated by integrating the radiance over the 4π solid angle:

$$\psi(\vec{r}, t) = \int_{4\pi} L(\vec{r}, \hat{s}, t) d\Omega \quad (2.4)$$

To determine the radiance, the losses and contributions in equation 2.1 have to be considered. The two losses of energy (per unit time) in the equation are due to divergence and extinction. First of all, the energy diverging out of the photon beam (per unit time), can be expressed as,

$$dP_{\text{div}} = \frac{\partial L(\vec{r}, \hat{s}, t)}{\partial s} ds dA d\Omega = \frac{\partial L(\vec{r}, \hat{s}, t)}{\partial s} dV d\Omega \quad (2.5)$$

and describes the energy flow out of the volume element dV and the solid angle $d\Omega$ (per unit time). The second loss, the extinction, is expressed by,

$$dP_{\text{ext}} = (\mu_t ds) L(\vec{r}, \hat{s}, t) dA d\Omega = \mu_t L(\vec{r}, \hat{s}, t) dV d\Omega \quad (2.6)$$

where $\mu_t = \mu_s + \mu_a$, is the total attenuation coefficient (length^{-1}), defined as the probability of being either scattered or absorbed per unit distance. Light that is scattered into the

volume element and into the solid angle $d\Omega$ from any other direction, \hat{s}' (figure 2.1) contributes to the total dP by,

$$dP_{\text{sca}} = (N_s dV) \left[\int_{4\pi} L(\vec{r}, \hat{s}', t) \text{Ph}(\hat{s}', \hat{s}) \sigma_s d\Omega' \right] d\Omega = (\mu_s dV) \left[\int_{4\pi} L(\vec{r}, \hat{s}', t) \text{Ph}(\hat{s}', \hat{s}) d\Omega' \right] d\Omega \quad (2.7)$$

where N_s represented the density of the number of scatterers, hence $N_s dV$ represents the number of scatterers within the volume element. σ_s is the cross section of the scatterer, where $N_s \sigma_s = \mu_s$. Since $L(\vec{r}, \hat{s}', t) \sigma_s d\Omega'$ describes the energy flow (per unit time) through area σ_s and solid angle $d\Omega'$, this denotes the energy interacting with a single scatterer per unit time. The phase function, $\text{Ph}(\hat{s}', \hat{s})$, describes the distribution of scattering angles, which depends on the angle ϕ , between \hat{s} and \hat{s}' . The phase function is a probability distribution which equals to one when integrated over all angles. The phase function can therefore equally be written as, $\text{Ph}(\phi)$, since the new scattering angle is related to the original direction of propagation.

The second contribution to the energy (per unit time) in the volume element in equation 2.1, is the energy produced by the source (per unit time),

$$dP_{\text{src}} = S(\vec{r}, \hat{s}, t) dV d\Omega \quad (2.8)$$

Here S , is the volume emissivity generated by the source, with units $\text{W m}^{-3} \text{sr}^{-1}$. Hence dP_{src} describes the energy in the volume element within $d\Omega$, per unit time due to the source. Putting all of these contributions and losses together, the RTE becomes,

$$\begin{aligned} \frac{1}{c} \frac{\partial L(\vec{r}, \hat{s}, t)}{\partial t} = & -\frac{\partial L(\vec{r}, \hat{s}, t)}{\partial s} - \mu_t L(\vec{r}, \hat{s}, t) \\ & + \mu_s \int_{4\pi} L(\vec{r}, \hat{s}', t) \text{Ph}(\phi) d\Omega' + S(\vec{r}, \hat{s}, t) \end{aligned} \quad (2.9)$$

This is the equation that analytically describes the light propagation through biological material and any turbid media. The RTE is however difficult to solve analytically, therefore approximations are typically applied to more easily describe the light propagation [106, 113, 114]. The two most obvious approximations are either the assumption that scattering or

absorption is dominating the light interaction.

2.3.1 Beer-Lambert law

For a medium where the absorption is much larger than the scattering, the intensity of the light is attenuated exponentially with distance z (figure 2.3). The irradiance, $I(z)$ can therefore be expressed only as a function of distance travelled:

$$I(z) = I_0 e^{-\mu_a z} \quad (2.10)$$

where μ_a is the absorption coefficient within the media, and $\mu_a z$ is the optical depth of the slab of depth z . The optical depth refers to the level of absorption over a certain depth. This is known as the Beer-Lambert law, which is appropriate to use in a highly absorbing medium where it can be assumed that there is no scattering. However, tissue is highly scattering, therefore this approximation is not appropriate when considering light propagation through tissue [106].

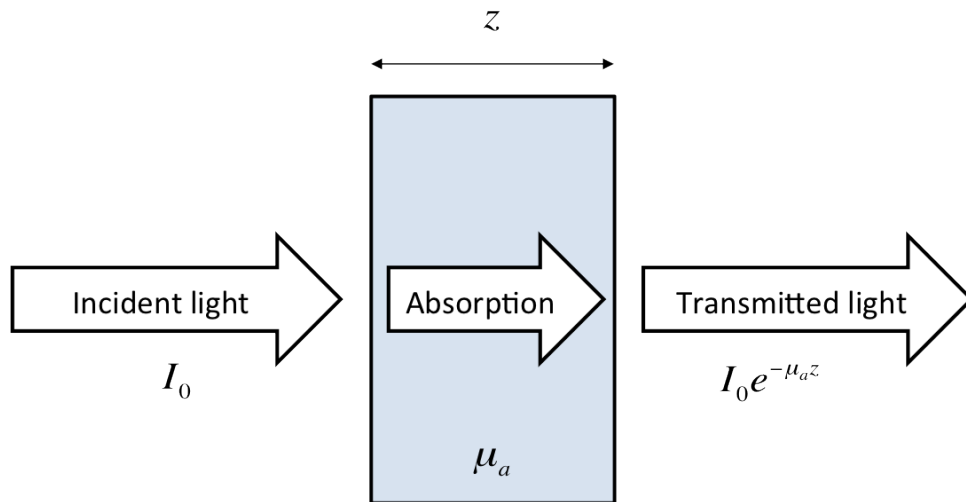


Figure 2.3: Description of light travelling through a medium where absorption is dominating. The transmitted light depends on the thickness of the medium and the absorption coefficient within the medium. The strength of the intensity of the light exponentially attenuates as it travels through the slab [106].

2.3.2 Diffusion approximation

For a medium where the scattering is dominant, i.e. a medium with a high albedo, and where the scattering is nearly isotropic, the radiance can be expanded in terms of spherical

harmonics. This approximation is less valid for an anisotropic media, such as skin tissue, which is highly forward scattering. In particular it is not valid close to the surface when simulating illumination of the skin surface [115]. Another issue with diffusion theory is the required uniformity of the tissue type [101]. The tissue has to have uniform optical properties throughout the simulated region. It is therefore a challenge in diffusion theory to include different tissue types such as tumour tissue in a three dimensional fashion [101].

Studies by for example Flock et al (1989) [98] and Wang and Jacques (2000) [116] have compared diffusion theory to more exact solutions to the RTE. These studies show that diffusion theory produces accurate results deeper into the surface for isotropic scattering. However, determining the light distribution close to the surface boundary is associated with large errors. This is not a desirable effect, since it is close to the surface where a lot of the intense light-tissue interactions, important for light treatment in medicine, occur [116]. The Diffusion approximation is an attractive method due to its simplicity and the fact that it is not computationally expensive.

2.3.3 Monte Carlo radiation transfer method

Monte Carlo Radiation Transfer (MCRT) is a numerical simulation to the RTE, where no assumptions of the levels of absorption or scattering are required. MCRT is a stable, yet flexible technique which allows accurate information about the light distribution within tissue phantoms to be generated. MCRT is a computer based solution to the light transport problem which utilises the probabilistic nature of the photon interactions. The random walk of the photons is simulated, and by following each photon's trajectory the description of the distribution of the light is built up. Scattering and absorption events are tracked until the photons are either absorbed or exit the simulation region. By repeating this process for many several photons, or energy packets, the light distribution and energy depositions start to approach their true values. Due to the sophistication of the technique, MCRT is an appropriate method of describing light based therapies, such as PDT. The more accurately the tissue is described in terms of optical properties, the more accurate the computed MCRT results will be [101, 107, 117].

The term 'the Monte Carlo method' was first introduced as a way of investigating neutron propagation through different media in 1949 [118] and since then it has been used for a variety of applications. Modelling light interaction with skin tissue using MCRT was first

introduced by Wilson and Adam in 1983 [99]. Wilson and Adam determined the light attenuation through a homogenous tissue considering only isotropic scattering. Keijzer later (1989) introduced anisotropic scattering and propagation of photons through a system using cylindrical coordinates [119]. This was further extended to Cartesian coordinates by Prahll (1989) making the results easier to interpret [117]. Wang and Jacques developed a multi-layered Monte Carlo (MCML) model, which has subsequently been made publicly available and been utilised frequently to simulate light distribution through skin tissue [107, 120–122]. Several additional MCRT models adopt a layered approach to represent different tissue types in skin [123] in liver [101] and heart [124]. There have also been several simulations where tumours have been included to represent diseased tissue. These tumours have typically taken the form of different geometrical shapes such as squares [125], spheres [126] and cylinders [100, 101, 127]. MCRT modelling has also been used to simulate light propagation through brain tissue [128–132] where complex three dimensional (3D) brain tissue has been used as the propagating medium [128]. MCRT has frequently been used to calculate optical properties by comparing simulations and experimental measurements [104, 105, 123], to simulate fluorescence spectroscopy [103, 124] as well as comparing different illumination geometries and wavelengths [121, 126]. Extensive work studying treatment of port wine stains have used MCRT modelling to investigate the effects of the position, diameter and number density of blood vessel in tissue [123, 133, 134].

The drawback with MCRT modelling is that it tends to be computationally expensive compared to using for example the diffusion approximation [116]. However, approaches have been made to speed up the computation time [107] such as mesh based grid systems [131], combining MCRT with diffusion theory [125, 135] and computer parallelising [132].

2.4 Method

The MCRT model presented here was originally developed for astronomy research, but has been adapted for this project where the light propagation through skin tissue is simulated [136, 137]. In general terms, the MCRT model tracks photons as they enter a grid containing multiple voxels. The photons travel through the simulated region undergoing scattering events. These interactions are tracked until the photons are absorbed (or escape the simulated region), and the locations of the absorption events are recorded. The scattering and absorption events are determined by the optical properties of the medium in which the photons are

propagating, which can be varied on a voxel by voxel basis. The step size as well as angular distribution are sampled from probability distribution functions (PDFs) using random number generators. The developed code described here simulates a three dimensional (3D) Cartesian grid with the voxel dimensions 100 x 100 x 100 voxels (note that chapter 5 adopts different voxel dimensions) with a variable grid size (figure 2.4).

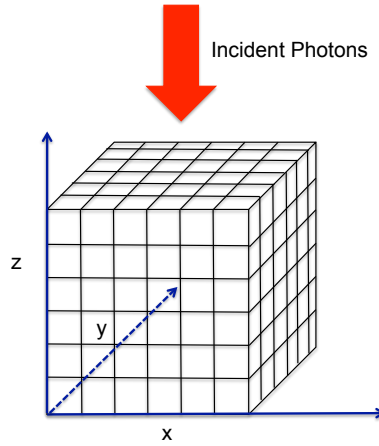


Figure 2.4: Representation of the Cartesian grid adapted in the developed MCRT model. The voxel based system allows for optical properties within each individual grid cell to be defined independently. This allows for structures and layers of different tissue types to be included in a three dimensional fashion.

2.4.1 Code details

A photon simulated within the MCRT model, is described as an energy packet and is related to the number of 'real' photons, N_γ , by,

$$N_\gamma = \frac{E_i}{h\nu_i} \quad (2.11)$$

where E_i is energy per MCRT photon, h is Plank's constant and ν is the frequency of the photon. The energy per MCRT photon, E_i depends on the total amount to energy delivered to the simulation as well as the total number of MCRT photons (here after referred to as photons) simulated, N :

$$E_i = \frac{IA\Delta t}{N} \quad (2.12)$$

here I is the irradiance (W cm^{-2}) of the incident light sources and A is the area of the

illuminating region (cm^2) and Δt is the time of illumination (s). The amount of energy per unit time that is simulated is divided into small energy packets. It would not be convenient to simulate individual photons due to the large number of photons emitted per second from the simulated light source (of the order or 10^{17} photons per second). Instead the energy packets are traced on their random walk through the simulation grid. By ensuring that the results from the simulations are not affected by an increase number of simulated packets an appropriate number of packets can be established. Typically $10^6 - 10^7$ photons were simulated. A flowchart and overview describing photons movement from launch to termination is shown in figure 2.5. The different steps in the flowchart and the build-up of the photon propagation through the medium is described below.

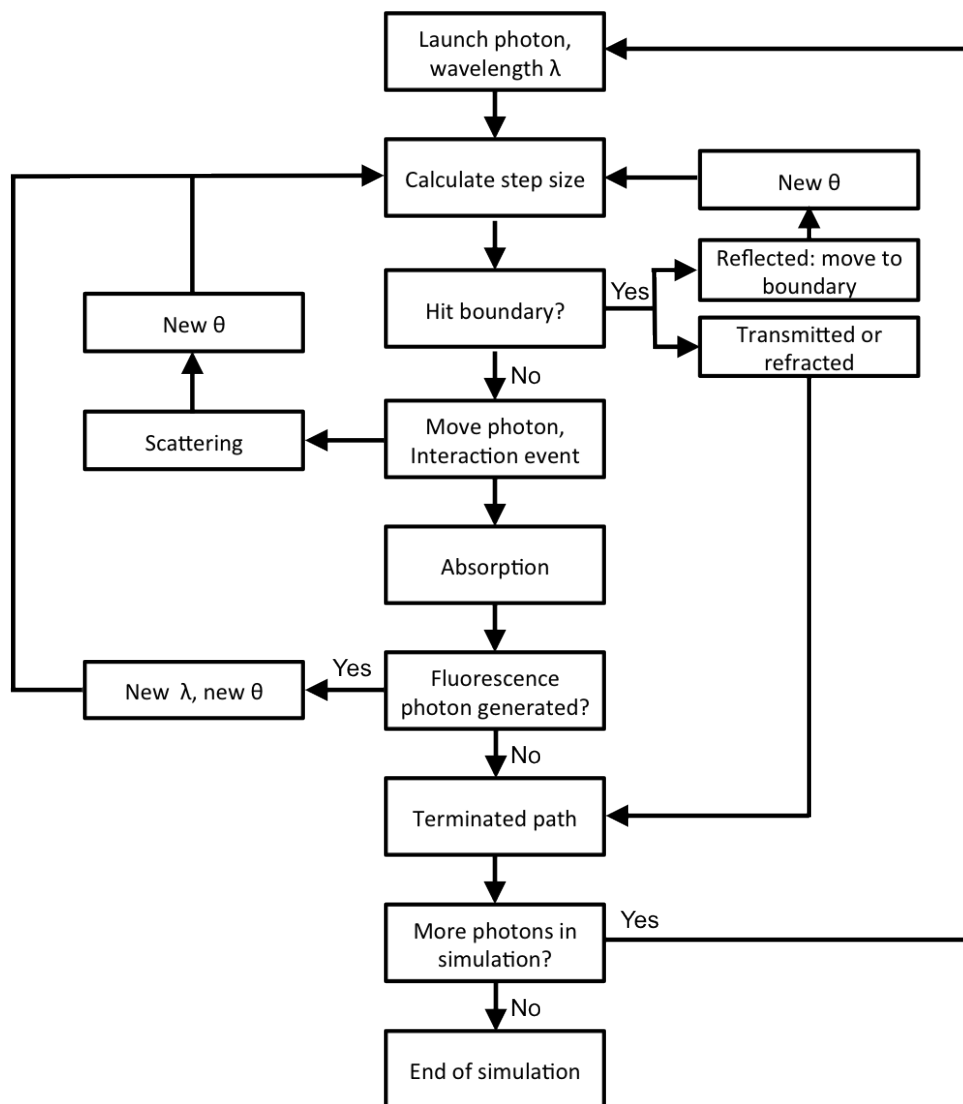


Figure 2.5: Flowchart demonstrating the movement of the photons through the MCRT grid.

Step size

The propagation of the photons through the medium is, as previously mentioned, determined by the optical properties of the medium.

The probability of the light beam interacting (scattering or absorption) over distance ds is $\mu_t ds$ (equation 2.6). The probability of a photon travelling distance ds without an interaction is therefore given by, $1 - \mu_t ds$. The length S can be divided into A segments, such that $ds = S/A$. Hence the probability of the photon travelling the whole distance S without interaction can be expressed as,

$$P(S) = \lim_{A \rightarrow \infty} (1 - \mu_t S/A)^A = e^{-\mu_t S} = e^{-\tau} = P(\tau) \quad (2.13)$$

Here τ is the optical depth, defined as the number of mean free paths over a given distance. The mean free path, is the average distance a photon travels between interactions and is given by $1/\mu_t$. As the optical properties (μ_t) may change over the distance the photon travel, the optical depth can be translated to a physical distance S by,

$$\tau = \int_0^S \mu_t ds \quad (2.14)$$

Within MCRT many parameters are generated through random sampling from PDFs. Since the repetition of the sampling reproduces the PDF, this is an appropriate way of randomly sampling parameters to accurately represent reality. To randomly sample the optical depth, the PDF, $P(\tau)$, (equation 2.13) has to be normalised over all τ to generate the cumulative distribution function (CDF). This is the probability of the variable taking a value less than or equal to a specific τ ,

$$\text{CDF} = \int_0^\tau P(\tau) d\tau = \int_0^\tau e^{-\tau} d\tau \quad (2.15)$$

From this we can then sample an optical depth by generating a random number between 0 and 1, ξ , which is sampled from a uniform distribution.

$$\xi = \int_0^{\tau_{\text{sample}}} e^{-\tau} d\tau \quad (2.16)$$

Where it is assumed that 0 is the lower limit of the range at which τ is defined and τ_{sample} is the sampled optical depth. The solution for this equation is,

$$\tau_{\text{sample}} = -\ln(1 - \xi) \quad (2.17)$$

This sampled optical depth τ_{sample} , is thereafter converted to a physical distance S , using equation 2.14.

Equation 2.14 determines the physical distance travelled before an interaction within a continuous medium. For the situation considered here, the photons travel through an spatial grid containing small voxels where the optical properties can be different in each individual voxel. Therefore the optical properties within the medium are not continuous and step size is determined by,

$$\tau = \sum_i \mu_t \Delta s_i \quad (2.18)$$

where, Δs_i , is the step size within voxel i , with total attenuation coefficient μ_t . Figure 2.6 shows a simplified example where the calculation of the physical distance is demonstrated.

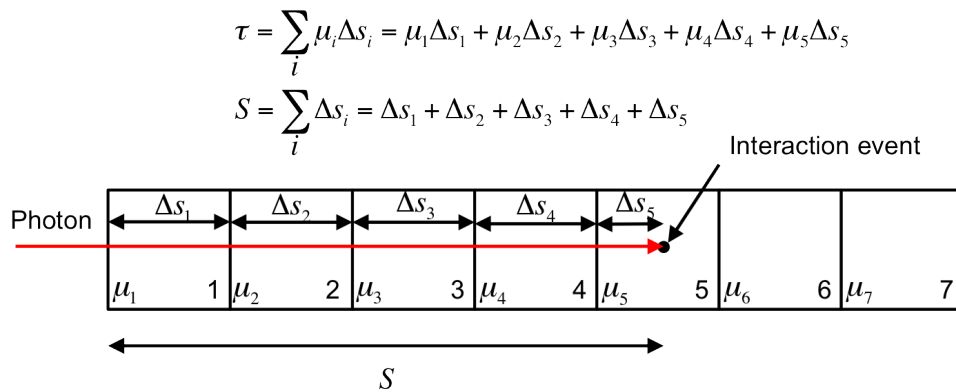


Figure 2.6: Representation of the step size calculation within the MCRT grid. This shows a one dimensional case, however the same technique is used for three dimensional grids.

Interaction event

After travelling a physical distance S , the photon is either scattered or absorbed. The probability of the photon being scattered is determined by the albedo,

$$a = \frac{\mu_s}{\mu_a + \mu_s} = \frac{\mu_s}{\mu_t} \quad (2.19)$$

where the scattering coefficient, μ_s and absorption coefficient μ_a , are the local optical properties at the interaction site (in the units of length^{-1}). The interaction event is determined again by random number generating. If the randomly generated number ξ is less than or equal to the albedo, the photon is scattered and given a new direction and a new optical depth. When determining the scattering angle, both the polar angle, θ ($0 \leq \theta \leq \pi$), and the azimuthal angle ϕ ($0 \leq \phi \leq 2\pi$) have to be determined. The azimuthal angle is assumed to have a isotropic distribution and hence is sampled by,

$$\phi = 2\pi\xi \quad (2.20)$$

The most common way of describing the polar scattering in tissue is through the Henyey-Greenstein phase function. The phase function was originally introduced to describe scattering of light from distant galaxies by dust in our galaxy. The phase function, $\text{Ph}(\theta)$ [138], describes the probability of a photon travelling in direction \hat{s} scattering into the direction \hat{s}' and is expressed as follows,

$$\text{Ph}(\theta) = \frac{1 - g^2}{4\pi(1 + g^2 - 2g\cos\theta)^{3/2}} \quad (2.21)$$

Here θ is the angle between the direction of travel (\hat{s}) to the direction after scattering (\hat{s}'). g is the anisotropy factor, which is defined as the average of $\cos\theta$,

$$g = \langle \cos\theta \rangle = \int_0^\pi \text{Ph}(\theta)\cos\theta 2\pi\sin\theta d\theta \quad (2.22)$$

The phase function allows for scattering that is not symmetric relative to the direction of travel. g takes a value between -1 and 1, where $g=0$ for photons that are isotropically

scattered. Skin tissue is however very forward scattering and therefore a typical value for g is in the range 0.7 - 0.9 [139]. To sample the scattering angle from the probability distribution (equation 2.21), the CDF has to be generated in a similar way as the optical depth. The CDF equals to one when the the phase function (equation 2.21) is integrated over all solid angles such that

$$\int_0^{2\pi} d\phi \int_0^\pi \text{Ph}(\theta)\sin\theta d\theta = 2\pi \int_0^\pi \text{Ph}(\theta)\sin\theta d\theta = 1 \quad (2.23)$$

The angle θ can therefore be sampled such that,

$$2 \int_0^{\theta_{\text{sample}}} \text{Ph}(\theta)\sin\theta d\theta = \xi \quad (2.24)$$

Hence,

$$\cos\theta_{\text{sample}} = \begin{cases} \frac{1}{2g} \left\{ 1 + g^2 - \left(\frac{1-g^2}{1-g+2g\xi} \right)^2 \right\}, & g \neq 0. \\ 2\xi - 1, & g = 0. \end{cases} \quad (2.25)$$

The sampled angle will be in relation to original direction of the photon. Hence to translate the new angle to the global Cartesian coordinate system, the following transformations are applied [113],

$$\begin{aligned} n'_x &= \frac{\sin\theta(n_x n_z \cos\phi - n_y \sin\phi)}{\sqrt{1 - n_z^2}} + n_x \cos\theta \\ n'_y &= \frac{\sin\theta(n_y n_z \cos\phi + n_x \sin\phi)}{\sqrt{1 - n_z^2}} + n_y \cos\theta \\ n'_z &= -\sqrt{1 - n_z^2} \sin\theta \cos\phi + n_z \cos\theta \end{aligned} \quad (2.26)$$

Where n'_x , n'_y and n'_z corresponds to the new directions and n_x , n_y and n_z are the original directions. To avoid division by small numbers, trajectories close to alignment along the z-axis (i.e. $|n_z|$ close to 1), the following components of a unit vector are adopted,

$$\begin{aligned}
 n'_x &= \sin\theta \cos\phi \\
 n'_y &= \sin\theta \sin\phi \\
 n'_z &= \text{sgn}(n_z) \cos\theta
 \end{aligned} \tag{2.27}$$

This approximation is adopted when $|n_z|$ is larger or equal to 0.999. The reason for adopting these approximations is to avoid division by small numbers and thereby round-off errors.

Reflection and refraction

To take into account for the reflection and refraction at the surface boundary (both from above and below) Fresnel's equations and Snell's law were implemented. The probability that a photon is reflected at the boundary (figure 2.7) between two different media $R(\theta_i, \theta_t)$ can be expressed using the following equation [140],

$$R(\theta_i, \theta_t) = \frac{1}{2} \left[\left| \frac{n_i \cos\theta_i - n_t \cos\theta_t}{n_i \cos\theta_i + n_t \cos\theta_t} \right|^2 + \left| \frac{n_i \cos\theta_t - n_t \cos\theta_i}{n_i \cos\theta_t + n_t \cos\theta_i} \right|^2 \right] \tag{2.28}$$

where n_i is the refractive index of the incident medium and n_t is the refractive index of the second medium. θ_i is the incident angle that the photon hits the boundary and θ_t is the refractive angle determined by Snell's law,

$$n_i \sin\theta_i = n_t \sin\theta_t \tag{2.29}$$

Again, a random number, ξ , is generated to determine if the photon is reflected or refracted between the boundary. If $\xi > R(\theta_i, \theta_t)$, the photon is reflected and does not cross the boundary.

Other important parameters

When a photon is absorbed, an amount of energy is deposited in the tissue. Instead of counting each individual absorption event, the energy absorption per cubic centimetre per second is computed by,

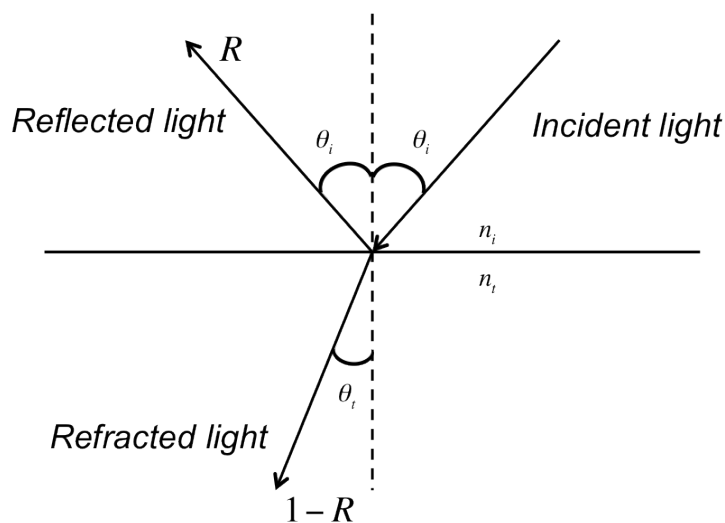


Figure 2.7: Representation of the reflection and refraction of light at the interface of two media of different refractive indices. The angle of refraction, θ_r , is determined by Snell's law (equation 2.29) and the probability of refraction ($1-R$) and reflection (R) is determined by Fresnel's equation (equation 2.28).

$$Q = \frac{IA}{N\Delta V} \sum_i \mu_a s_i \quad (2.30)$$

Here $\mu_a s_i$ is the probability of absorption over the photon path s_i in voxel i . I is the irradiance (W cm^{-2}) of the light, A is the area of the top of the grid (cm^2), N is the number of simulated MCRT photons and ΔV is the volume of each grid cell. The fluence rate ψ (W cm^{-2}), which describes the light distribution (equation 2.4) within the tissue, is computed through similar techniques,

$$\psi = \frac{IA}{N\Delta V} \sum_i s_i \quad (2.31)$$

Here $\sum_i s_i$ is the sum of photon path length within a cell i . This technique of computing the light distribution and energy deposition within the simulated region drastically improves the signal to noise ratio due to the scattering dominating the interaction events. If each absorption event was counted this would result in poor statistics [141]. A further discussion on the path length summation can be found in appendix A.

As previously mentioned the photon paths are tracked until they are either absorbed or exit the simulation region. If the photons exit the grid through the top or the bottom (i.e. z -faces) of the grid their paths are terminated. For photons exiting the sides of the simulation

grid (i.e. x- and y-faces), their paths are not terminated if repeated boundary conditions are adopted (adopted in all chapters except for simulations performed in section 2.5.2). When repeated boundary conditions are adopted, the photons that exit one side of the grid are re-launched on the opposite side of the simulation region. Figure 2.8 demonstrates how the repeated boundary conditions are adopted. The photons that exit the grid through the x- or y-face will continue its projection on the opposite side of the grid. If the photon for example left the simulation grid through its y-face at (x, y_{\max}, z) , it will continue in the same direction from location $(x, 0, z)$. This results in the representation of a semi-infinite tissue slab where the light source is assumed to be larger than the simulation grid and thereby considering light contributions from a larger area. The code that was used for the simulations in this thesis was written in FORTRAN on a contemporary computer (MacBook Pro, 2.9 GHz processor). A typical simulation in this thesis where 10^6 photons is simulated at 405 nm takes less than 20 seconds to run (serial, single processor (not parallelised)). This might to some present-day readers appear to be fast. However, I hope that those reading this thesis in several years time will consider this slow.

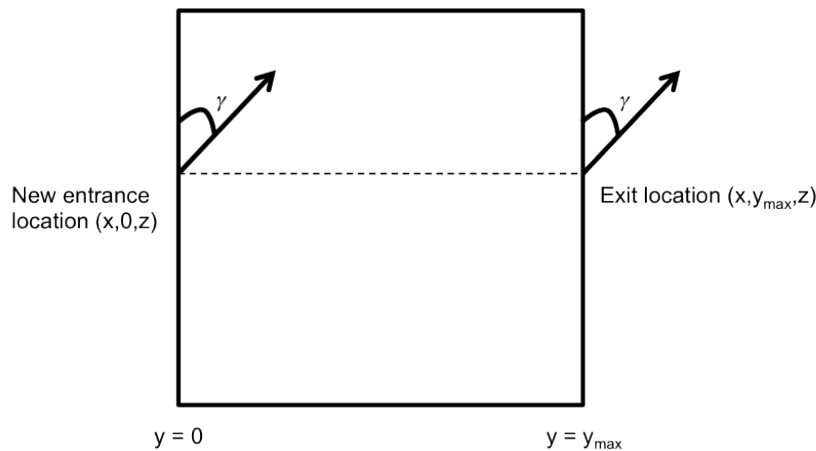


Figure 2.8: Figure demonstrating the principles behind repeated boundary conditions. Photons exiting the simulation region from the sides (x- or y-face) will continue their trajectories in the same direction on the opposite side of the grid as demonstrated here. This results in the representation of a semi-infinite tissue slab.

2.5 Experimental validation

The MCRT model describes the photon propagation through a turbid medium and can be used to determine optical properties of the medium by comparing the experimental results to theoretical results. The aim with the experimental validation was to both determine the

concentration dependent optical properties of Intralipid as well as successfully reproduce the experimental measurements.

2.5.1 Experimental design

The solutions that were prepared contained Coproporphyrin III with varied concentrations of Intralipid 20% (Fresenius Kabi, Germany) and distilled water. Intralipid is highly scattering and is frequently used for studying light propagation through turbid media [142]. Coproporphyrin III is a stable fluorescing standard (stable compared to for example protoporphyrin IX). Due to the stability of Coproporphyrin, it is ideal for comparing the fluorescence signal in different solutions. The different solutions were added to a 10 mm x 10 mm cuvette which was placed in a cuvette holder (figure 2.9). The fluorescence signal was measured using an optical biopsy system (OBS). The OBS operates on the principles of fluorescence spectroscopy [143]. It houses a low powered 405 nm laser diode (approximate 1mW output) and can be used for *in vivo*, non-invasive monitoring of tissue fluorescence. The blue light is coupled to a fibre probe (inner diameter of 600 μm), which is both used for excitation light as well as collecting the resulting fluorescence light. The probe has to be in contact with the subject of measurements, which in this case was one of the cuvette sides. This is however equally valid for measurements in contact with skin tissue (chapter 7) [103]. A bifurcated fibre (Avantes FCB-UV400-2) 455 nm long-pass filter is introduced to allow the excitation light and collected signal to be separated and the backscattered light from the excitation to be eliminated from the recorded spectra. The collected light was recorded using a compact grating spectrometer interfaced with a PC (figure 2.10) [144].

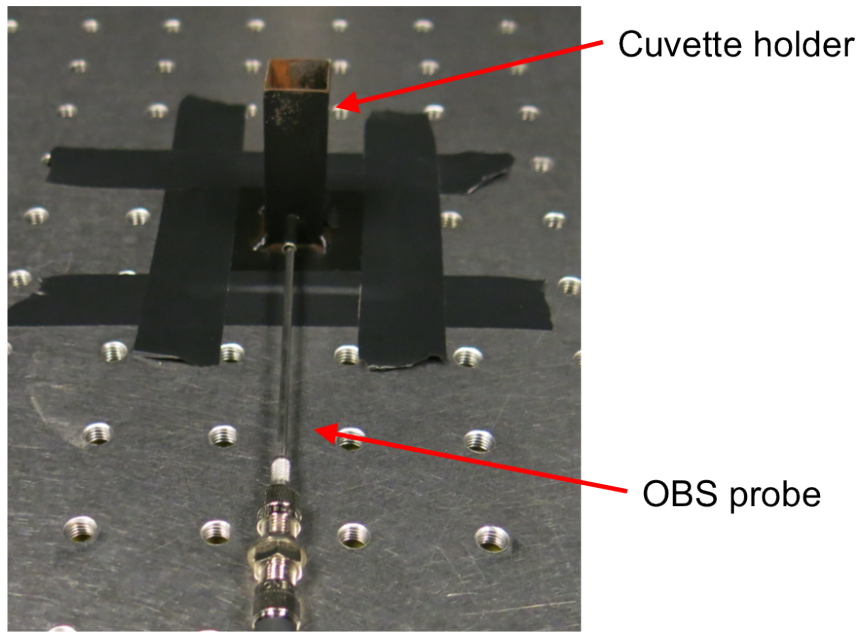


Figure 2.9: Experimental set of where the cuvette was placed in the cuvette holder. The fluorescence signal was acquired through the probe which was assured to be in contact with the cuvette surface. In the laboratory experiment, the cuvette replaced the skin in figure 2.10.

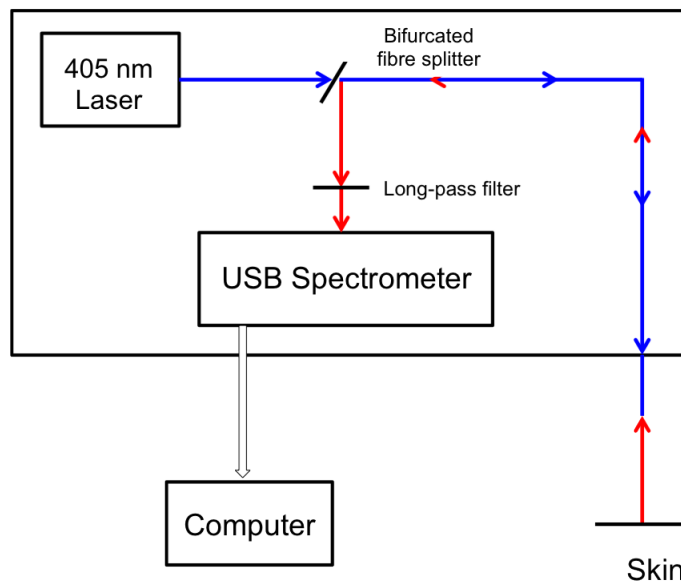


Figure 2.10: Schematics of the optical biopsy system (OBS) where all components, except for the laptop computer are eclipsed within a box to prevent any stray light effecting the measurements. The multimode fibres has a core diameter of $600\ \mu\text{m}$ and a outer (cladding) diameter of approximately $2\ \text{mm}$.

5 ml of each concentration of Intralipid 20 % was made up to generate concentrations of 0.2, 0.5 and 0.8 % of Intralipid 20 %. To each 5 ml solution, 1 ml of Corpoporphyrin III was added, the volume concentration of Intralipid 20 % was therefore adjusted according to table

2.1.

Table 2.1: *Intralipid solutions used for the experimental validation .*

Intralipid 20%	H ₂ O	Volume measurements (ml)	
		Coproporphyrin III	Intralipid 20 % concentration
0.04	4.96	1	0.67%
0.03	4.98	1	0.42%
0.01	4.99	1	0.17%

2 ml of each solution in table 2.1 was added to a cuvette and the fluorescence signal was recorded (by the OBS). In addition the fluorescence signal from a cuvette containing only Coproporphyrin III as well as from an empty cuvette. The reason for the fluorescence signal being recorded for the Coproporphyrin only was to determine the fluorescence signal when there were no scatterers present. This generated the fluorescence emission spectrum for PpIX which was subsequently used for the simulations (see below). The background effect from the cuvette was determined through the empty cuvette. The fluorescence signal acquired from the cuvette containing distilled water was subtracted from the other solutions to remove the background signal generated by the cuvette. The same cuvette was used for all measurements to ensure consistency. The absorption properties of the Coproporphyrin III (100 %) were measured using a spectrophotometer and the total attenuation coefficient can thereafter be determined through Beer-Lambert's law (equation 2.10) [113].

2.5.2 Simulation design

The aim with the theoretical simulations was to generate a computer model which successfully reproduced the experimental measurements. Two species were included in the model and were assumed to be uniformly distributed throughout the simulated region. The first species was the solution containing Intralipid 20 % and the second species represented the Coproporphyrin III. The optical properties for these two different species had to be determined and included within the simulation. Intralipid is highly scattering and therefore the albedo was assumed to be 0.999 [144]. The anisotropy factor was assumed to be 0.7 following work from Flock et al [145]. Coproporphyrin is highly absorbing and therefore it was assumed that the scattering associated with Coproporphyrin was negligible (i.e. the albedo is assumed to be zero). The refractive index was set to be 1.33 (water). The scattering coefficient for

Intralipid 20 % is previously known [142] (figure 2.11), however the scattering properties do not scale linearly with Intralipid concentration in aqueous suspensions [146]. Previous work at Ninewells hospital, Dundee [144] determined the total attenuation coefficient for the concentrations 0.2, 0.5 and 0.8 % of Intralipid 20 % at only three wavelengths (632, 532 and 405 nm). For the work presented here a larger wavelength range was required since the Coproporphyrin fluorescence signal covers a wavelength range between approximately 550 and 700 nm. In an attempt to scale the optical properties associated with the investigated concentrations, a power law was fitted to the concentration dependent attenuation coefficient previously determined. The power law function was used to scale the scattering coefficient for Intralipid 20% (figure 2.11). To ensure that these coefficients are correct, the relationship between the change in fluorescence signal due to change in concentration of scatterers have to be the same for the experimental measurements as well as the MCRT simulations. The absorption properties adopted for the Coproporphyrin is displayed in figure 2.12 a.

The Cartesian grid was given the dimension $10\text{ mm} \times 10\text{ mm} \times 10\text{ mm}$, to represent the same dimensions as the cuvette. It was assumed that the light from the OBS was emitted at 405 nm, through a circular region with a diameter of $600\ \mu\text{m}$. 10^9 photons were simulated to ensure good signal to noise. The fluorescence quantum yield was assumed to be 1 and the fluorescence photons were assumed to be isotropically emitted from the absorption location. A new wavelength sampled from the Coproporphyrin fluorescence spectrum (figure 2.12 b) was given to the fluorescence photon. The fluorescence photons were samples from the fluorescence spectrum such that the probability distribution function of the spectrum was reproduced. In reality the fluorescence yield is considerably lower than 1, however the results are linearly scalable with the fluorescence yield. Only fluorescence photons exiting the surface of the grid at an angle corresponding to a numerical aperture of 0.22 were collected and binned according to wavelength.

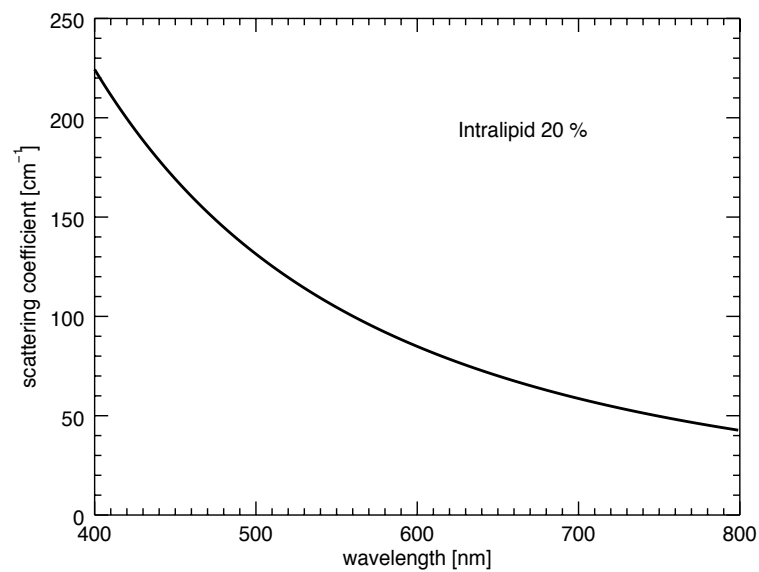


Figure 2.11: Scattering coefficient for Intralipid 20% [142].

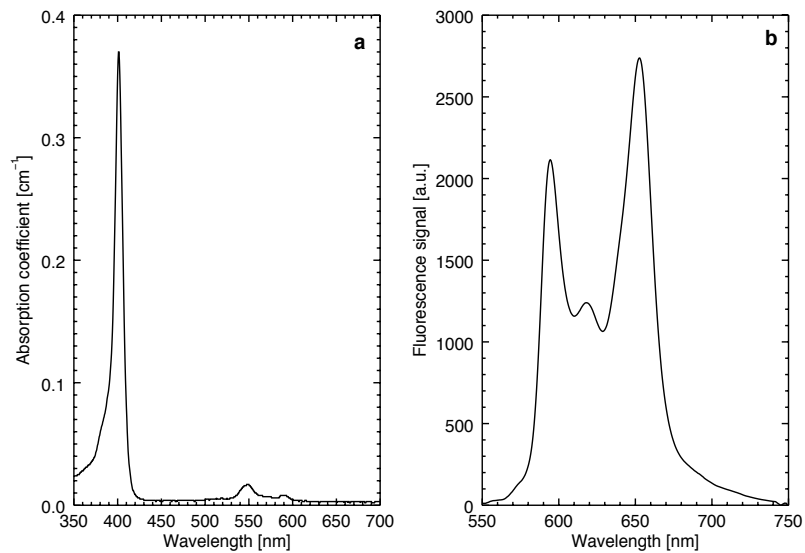


Figure 2.12: a) Absorption coefficient for Coproporphyrin III b) Fluorescence signal generated by sample of pure Coproporphyrin III

2.5.3 Results, experimental validation

The scaling power law function determined from the properties already known from previous work, is displayed in figure 2.13. The fitted function B scales the optical properties $\mu_s(\lambda, 20\%)$ in figure 2.11 such that $\mu_s(\lambda, 20\%) = B\mu_t(\lambda, \text{Concentration})$. B is determined to be $6.98 \times x^{-0.96}$ where x is the concentration in % of Intralipid 20 %. μ_t was determined instead of μ_s since μ_a is small (the albedo is set to be 0.999). By scaling the optical properties in figure 2.11 by B, the optical properties for the different concentrations were determined.

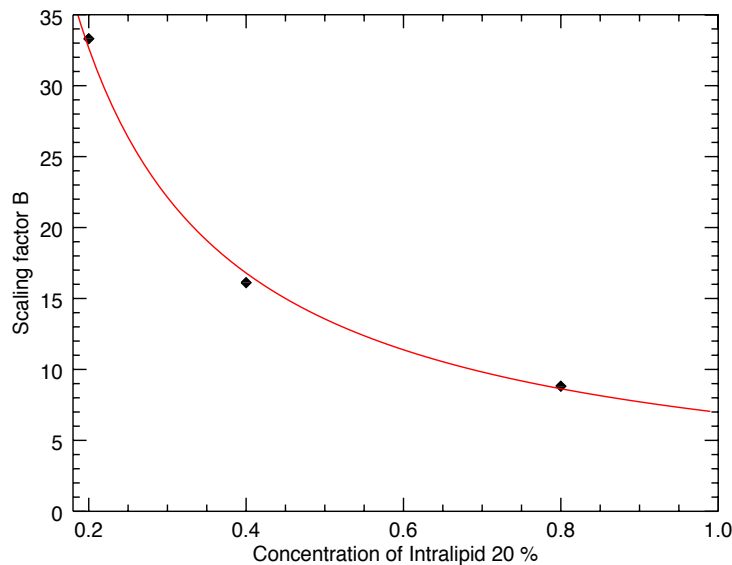


Figure 2.13: Power law fitted between three scaling factors between Intralipid 20 % and lower concentrations of Intralipid 20 %. The fitted function has the form $B = 6.98x^{-0.96}$ where x is the concentration of Intralipid 20 % [144].

The fluorescence signal recorded through the described experimental set-up, and the theoretically generated fluorescence signal from the MCRT code, are both shown in figure 2.14. The experimental measurements (solid line) showed that the fluorescence signal reduced with increasing Intralipid concentration. This was also demonstrated successfully with the MCRT model using the scaling of the optical properties described above. The change in signal strength can be explained by the increasing concentration of scatterers resulting in a more dispersed fluorescence signal. This results in a reduction of the collected light through the

small probe region. It was important to include the restricted collection region for the probe to accurately represent the smaller amount of collected light.

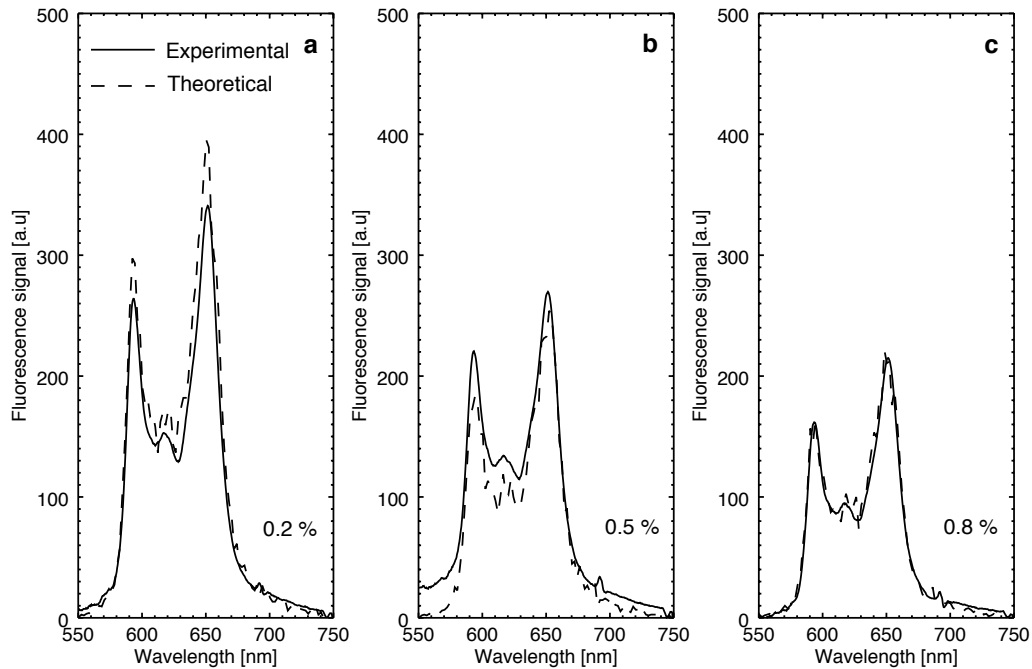


Figure 2.14: Figure showing the fluorescence signal generated both experimentally and theoretically for varied concentrations of Intralipid 20 %. The solid lines corresponds to the experimentally measured fluorescence signal using the OBS. The dashed lines corresponds to the theoretically determined fluorescence signal through the MCRT modelling. The varied concentrations for Intralipid 20 % was a) 0.2 %, b) 0.5 % and c) 0.8 % (concentration before Coproporphyrin III was added).

2.6 Theoretical validation

To ensure the accuracy of the code it is important to be able to reproduce previously generated results at any point during the code development. Jacques et al [97] presented results from a MCRT code where several of the important parameters that are used in subsequent chapters were discussed [97]. Jacques fitted functions to data generated from MCRT simulations, to describe several properties associated with light propagation through skin tissue during PDT treatment. The MCRT model adopted uniform illumination of the surface of the simulated

region. The absorption and scattering events were determined using the optical properties presented in table 2.2. The reflection and refraction from the upper boundary was considered (equation 2.28). The fluence rate (equation 2.4), $\psi(z)$, through skin tissue of known optical properties (table 2.2) as a function of depth was described through the following equation,

$$\psi(z) = \psi_0(C_1 e^{-k_1 z/\delta} - C_2 e^{-k_2 z/\delta}) \quad (2.32)$$

where C_1 , k_1 , C_2 , and k_2 are the fitting parameters specific for different wavelengths (table 2.2). ψ_0 corresponds to the incident irradiance of the light source. Jacques also modelled PDT where the light sensitive molecule protoporphyrin IX (PpIX) was introduced within the simulated region. The simulated region was assumed to have an initial homogeneous distribution of the PpIX. The escaping fluorescence emission, $E(z)$, was suggested to follow the function,

$$E(z) = C_3 e^{-k_3 z/\delta} \quad (2.33)$$

The escaping fluorescence emission is the proportion of the fluorescence photons that escape the simulated region originating from a specific depth (z). The simulated region was assumed to have optical properties as suggested by table 2.2. The escaping fluorescence signal (equation 2.33) describes the fluorescence signal generated at 705 nm after being excited by 630 nm light. The MCRT model assumed that each absorbed photon (by the PpIX) resulted in a fluorescence photon, isotropically re-emitted at 705 nm. Equation 2.33 was fitted to the MCRT result generated by Jacques with C_3 , k_3 and δ corresponding to the established fitting parameters (table 2.2) [97].

Table 2.2: Tissue optics parameters for equation 2.32 and 2.33 as well as the MCRT model [97].

λ [nm]	μ_a [cm ⁻¹]	μ_s [cm ⁻¹]	C_1	k_1	C_2	k_2	C_3	k_3	δ [cm]
420	1.8	82	5.76	1.00	1.31	10.2			0.290
630	0.23	21	6.27	1.00	1.18	14.4			0.290
705	0.23	17					0.771	0.994	0.290

During the light illumination the distribution of PpIX is reduced due to the photobleaching (section 1.6.1, chapter 1). Therefore, when simulating the PDT treatment, photobleaching is a very important property to include. It is typically assumed that the photobleaching follows

first order kinetics where the local distribution of PpIX, $C(z, t)$ reduces with time as follows [147],

$$C(z, t) = C_0 e^{-\psi(z)t/\beta} \quad (2.34)$$

Here C_0 is the local initial concentration prior to illumination. β is the photobleaching constant (J cm^{-2}) which is defined as the light dose required for the fluorescence signal generated by the PpIX to be reduced to $1/e$ (37 %) of its original value [56]. β is unique for the excitation wavelength (section 3.3.2) and will be discussed further in chapter 3. t is the total treatment time, hence a time dependent simulation is required. When the concentration of PpIX is reduced, the optical properties associated with the PpIX are also affected, since $\mu_t = n\sigma = C\varepsilon$. Here ε is the extinction coefficient ($\text{cm}^{-1}(\mu\text{g/ml})^{-1}$), σ is the cross section (cm^2), C is the local concentration ($\mu\text{g/ml}$) and n is the number density of scatterers (cm^{-3}). As the amount of the photosensitiser reduces the resulting fluorescence signal will also reduce. The function explaining the reduction of the observed fluorescence with time that was fitted to the MCRT results generated by Jacques et al was expressed by the equation,

$$F(t) = \int_0^\infty \psi_{\text{ex}}(z)\varepsilon C(z, t)\Phi E(z)f dz \quad (2.35)$$

where Φ is the fluorescence yield which was assumed to be 1, in order to improve signal to noise (section 2.5.2). f is the collection efficiency which was also assumed to be 1, $\psi_{\text{ex}}(z)$ refers to the excitation fluence rate (equation 2.32).

Jaques also introduced photodynamic dose (PDD), which is defined as the number of absorbed photons (by the sensitiser) per cubic centimetre. The accumulation of the PDD was expressed as,

$$\frac{\partial PDD(z, t)}{\partial t} = b\psi(z)\varepsilon C(z, t) \quad (2.36)$$

Hence,

$$PDD(z, t) = b\varepsilon C_0\beta(1 - e^{-\psi(z)t/\beta}) \quad (2.37)$$

where b is the conversion from energy to number of photons,

$$b = \frac{1}{h\nu} = \frac{\lambda}{hc} \quad (2.38)$$

where h is Planck's constant, ν is the photon frequency, c is the speed of light and λ is the wavelength of light.

The initial concentration of PpIX was assumed to be $0.2 \mu\text{g ml}^{-1}$. The photobleaching constant β was assumed by Jacques to be 105 J cm^{-2} and the extinction coefficient was assumed to be $0.0265 \text{ cm}^{-1}(\mu\text{g/ml})^{-1}$ at 630 nm and $0.105 \text{ cm}^{-1}(\mu\text{g/ml})^{-1}$ at 420 nm. These are the properties used in both the equations above as well as the MCRT model described below. The irradiance was set to be 0.1 W cm^{-2} .

2.6.1 Simulation design

The equations outlined here (equation 2.32 - 2.37) are the ones presented by Jacques et al describing the light propagation through tissue of known optical properties. The equations were developed from fitting equations to results generated by a MCRT model. As a validation of the developed model presented in this thesis, the equivalent results were generated using the MCRT model developed and described previously in this chapter.

The code that was used for this validation was given the dimensions $2 \text{ mm} \times 2 \text{ mm} \times 2 \text{ mm}$ ($100 \times 100 \times 100$ grid cells). The grid was assumed to be uniformly illuminated over the top surface of the grid (figure 3.2). By adopting the optical properties in table 2.2 the fluence rate was generated in the developed MCRT code using the techniques described above (equation 2.31). To determine the escaping fluorescence, similar techniques described above were adopted. The excitation light was assumed to be 630 nm, and all absorption events were assumed to result in a isotropic reemission of a photon at 705 nm. The fluorescence emission was recorded for those photons that escaped the simulated grid through the top surface.

To incorporate the photobleaching, a time parameter had to be included in the developed code. This was done by adding an iterative time loop where the time was increased stepwise. For each time iteration the same number of photons were simulated and a new concentration of the sensitizer was determined (equation 2.34). The length of each time step was adjusted appropriately. At the start of the treatment, the photobleaching results in large reductions

of PpIX, hence the time steps have to be small (seconds). After the first couple of simulated minutes the majority of the PpIX at superficial layers have been bleached and the reduction of PpIX concentration at deeper layers is slower and therefore larger time steps can be adopted (minutes).

As with the escaping fluorescence, when determining the fluorescence evolution with time, the number of escaping fluorescence photons during each time step was recorded. This simulation was performed for both excitation wavelengths 420 nm and 630 nm.

The PDD, which is an important parameter when determining the photo-toxicity within the skin tissue as it changes with time, also required the time iterations described above. This quantity will be utilised in subsequent chapters and therefore it is especially important to validate this.

During each time step the amount of absorbed energy per second ΔQ was determined (equation 2.30). This quantity was thereafter converted into the number of real photons (equation 2.38) and multiplied by the time step Δt . This way the number of photons absorbed, per cubic centimetre during Δt was calculated,

$$\Delta PDD = \Delta Q b \Delta t \quad (2.39)$$

The accumulated PDD over the full illumination period t , was calculated by summing all the individual contributions over the total illuminated time

$$PDD(t) = \sum_t \Delta PDD \quad (2.40)$$

For the simulations of PDD a toxic threshold is included. The toxic threshold is an approximation of the number of photons required to be absorbed for an effective PDT outcome. The value of 8.6×10^{17} photons cm^{-3} is based on Photofrin in liver tissue, where Photofrin is an alternative photosensitiser [148]. The same threshold will be adopted throughout the following chapters since it allows for comparison between the different conditions investigated as well as providing quantitative results. Typical values stated for a toxic threshold are in the regions of $10^{17} - 10^{19}$ photons cm^{-3} [1, 148, 149], therefore the toxic threshold applied is an approximation of the required dose.

2.6.2 Results of the theoretical validation

The four different quantities: fluence rate $\psi(z)$, escaping fluorescence $E(z)$, observed fluorescence $F(z)$ and PDD, were computed from the fitted functions introduced by Jacques et al [97] as well as through the MCRT model developed here. As displayed in figures 2.15-2.18, all four quantities showed good agreement between the predictive equations and MCRT results. Figure 2.15 shows the normalised fluence rate for 630 nm and 420 nm, where the optical properties in table 2.2 were adopted within the MCRT model. The normalised fluence rate, ψ/ψ_0 is defined as the fluence rate divided by the incident irradiance of the light source. The escaping fluorescence at 705 nm when excited with 630 nm light is shown in figure 2.16. The results from the model of the observed fluorescence is displayed in figure 2.17 where both 420 nm and 630 nm were used as excitation wavelengths. When simulating the PDD, figure 2.18 was produced where the MCRT modelling and predicted equations are compared showing excellent agreement. Here the same time points during illumination were displayed for the theoretical predictive model as well as from the MCRT model.

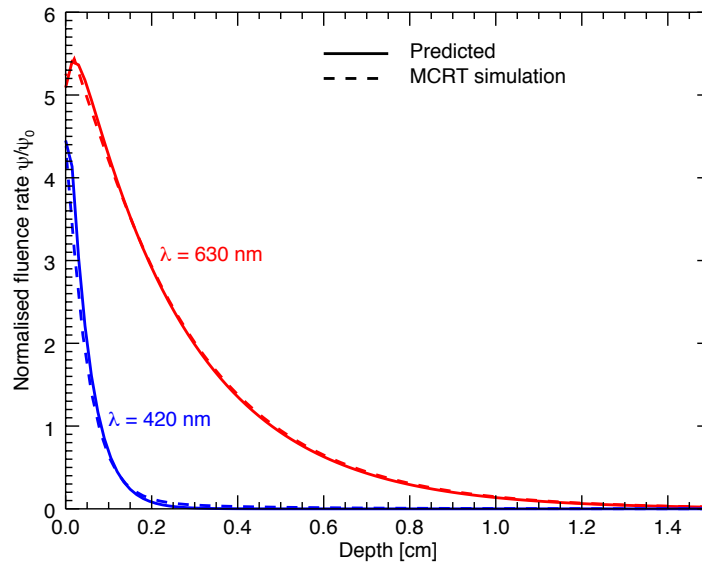


Figure 2.15: Figure showing the fluence rate (normalised) generated using equation 2.32 (solid) as well as the fluence rate generated by the MCRT simulation (dashed). The optical properties adopted in the simulations are reported in table 2.2. The fluence rate for 420 nm (blue) and 630 nm (red) are represented in the figure.

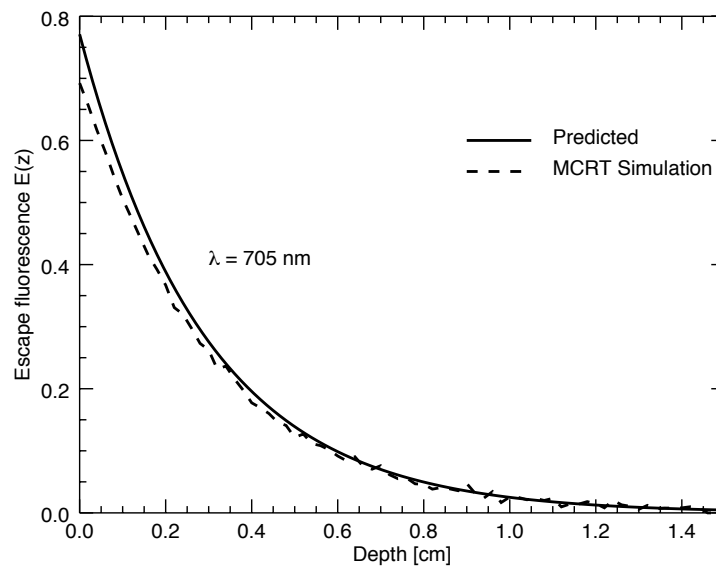


Figure 2.16: Figure showing the proportion of the fluorescence emission that escapes the tissue originating at depth z (x -axis). Both the predicted escape fluorescence (equation 2.33; solid) and MCRT simulations (dashed) are displayed. The figure was generated from emission of 630 nm where the fluorescence signal isotropically re-emitted at 705 nm.

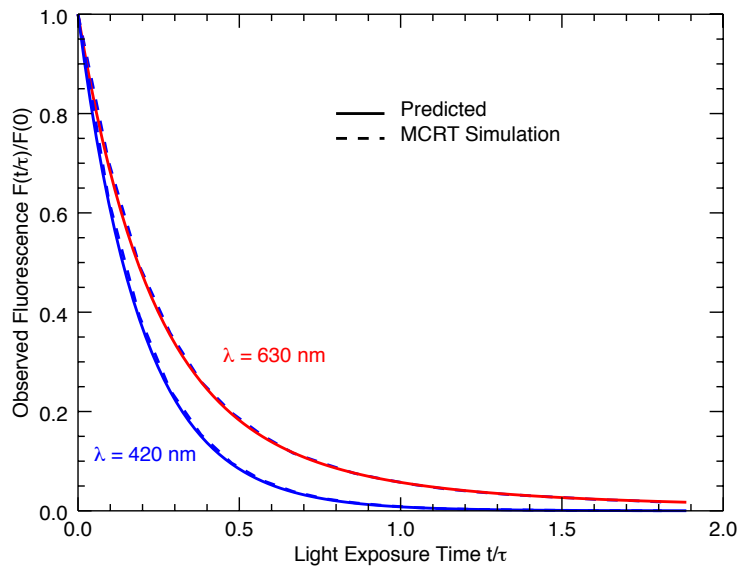


Figure 2.17: Figure representing the fluorescence observed as it changes with elapsed exposure time where both 420 nm (blue) and 630 nm (red) are used as excitation wavelengths for isotropic re-emission of 705 nm. The observed fluorescence is defined as the proportion of fluorescence photons escaping the top of the simulated grid relative to the initial fluorescence (fluorescence observed at time zero). The observed fluorescence is plotted as a function of t/τ where $\tau = \beta/\psi_0$ where ψ_0 is defined as the irradiance of the light source and β is the photobleaching dose constant. The observed fluorescence predicted by equation 2.35 (solid) is plotted together with the results generated by MCRT simulations using the appropriate parameters (table 2.2 ; dashed)

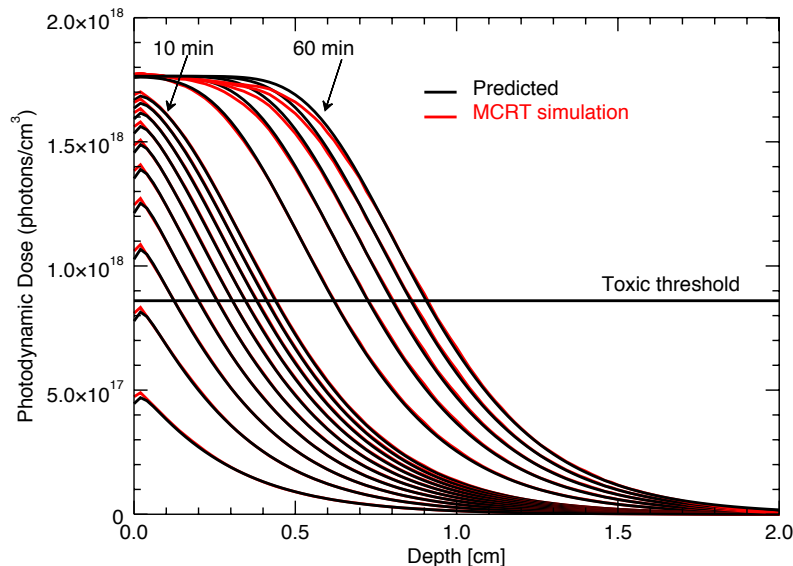


Figure 2.18: Figure showing the photodynamic dose (PDD) in the presence of photobleaching as a function of depth and time elapsed. The initial concentration of the photosensitiser is assumed to be uniformly $0.2 \mu\text{g ml}^{-2}$ and the irradiance is assumed to uniformly illuminate the top surface of the simulating grid at 0.1 W cm^{-2} . Both the prediction based on equation 2.37 (black) as well as MCRT simulations (red) are displayed at time 1-10 min in steps of 1 min as well as 10 - 60 min in steps of 10 min. The horizontal line corresponds to the toxic threshold which is assumed to be $8.6 \times 10^{17} \text{ photons cm}^{-3}$.

2.7 Discussion

MCRT is a recognised technique for studying light distribution through a turbid medium. This chapter describes the technique and the developed code that will be used in chapters 3 - 6. The aim with the developed code is to study light interaction with skin tissue during PDT. By rigorous validation of the code, the accuracy of subsequent simulations is supported. It is important to revisit the same simulations during further code developments to ensure that the same results are generated. By adopting a voxel based approach, errors due to the boundaries between voxels as well as issues arising at the edge of the simulating envelope can arise, which are important to consider when analysing simulation output [109].

The experimental validation demonstrates the potential of using MCRT to determine optical properties of a turbid medium. Similar surface measurements can be used to determine optical properties of skin tissue by using a diffuse reflectance measurements technique and relating the observations to specific optical properties using a MCRT model [105, 150, 151]. By successfully simulating the observed fluorescence, other simulations of the fluorescence signal are supported (chapter 4). It was clear during the development of the fluorescence code that it was important to represent accurately the collection region of light. Only by implementing the small collection region and the correct angle corresponding to a numerical aperture of 0.22, could the observed fluorescence be reproduced accurately. The importance of including the reflectance from upper boundary was also introduced as a feature to include within the model to enable both the experimental and theoretical validation.

The theoretical validations demonstrate the successful reproduction of predictive equations of many parameters important to light distribution through skin tissue. The PDD will be used extensively in the remaining chapters in this thesis to determine the toxicity caused by different light sources and different treatment conditions. The same toxic threshold will be adopted since this allows for comparison between different treatment conditions.

The code utilises a three dimensional grid system, which allows for complex geometrics of different species within the simulation region. This is an advantage compared to many other developed MCRT models where a 1D layered representations is most commonly adopted [107]. The grid system allows for 3D representation of different skin features such as blood vessels, tumours and melanin content. The possibility of adding 3D structures with different optical properties will be explored further in chapter 5 6.

2.8 Conclusion

The MCRT technique utilises the probabilistic nature of photon interactions, and due to this statistical nature a large number of photons are required to achieve accurate information about the photon propagation. This results in a fast and accurate technique (on contemporary computers) which accurately yields information about reality. This chapter discusses the key features of the MCRT technique and the development of the code that is utilised in the remaining chapters of this thesis. To ensure that the developed code generates accurate results and is appropriate for applying to PDT, rigorous validations were performed. Due to the capability of accurately representing scattering, absorption, reflection, transmission, fluorescence and PDD within skin tissue and other turbid media this technique is shown to be suitable for simulating PDT and other light based therapies.

3

Monte Carlo radiation transfer modelling of daylight activated photodynamic therapy

3.1 Summary

The treatment of superficial skin lesions via daylight activated photodynamic therapy (PDT) has been explored theoretically using three dimensional (3D) Monte Carlo radiation transfer (MCRT) simulations. For similar parameters and conditions, daylight activated PDT was compared to conventional PDT. Under reasonable assumptions for the optical properties of the tissue, protoporphyrin IX (PpIX) concentration, and a treatment dose of 75 J cm^{-2} , it was found that during a clear summer day an effective treatment depth of over 2 mm can be achieved after 30 min of daylight illumination at a latitude of 56 degrees North. The same light dose would require 2.5 h of daylight illumination during an overcast summer day where a treatment depth of just under 2 mm can be achieved. For conventional PDT the developed model suggests that 15 min of illumination is required to deliver a light dose of 75 J cm^{-2} ,

which would result in an effective treatment depth of about 3 mm. The model developed here allows for the determination of photo-toxicity in skin tissue as a function of depth for different weather conditions as well as for conventional light sources. Our theoretical investigation supports clinical studies and shows that daylight activated PDT has the potential for treating superficial skin lesions during different weather conditions.

The work presented in this chapter contributed to the publication "Monte Carlo modelling of daylight activated photodynamic therapy" in "Physics in medicine and biology" (2015) [127].

3.2 Introduction and background

PpIX absorbs light over a wide range of the visible spectrum and therefore a range of different light sources are suitable for treatment. Daylight-PDT removes the need for artificial light sources, results in less pain during treatment [152], and in clinical studies was the preferred choice of treatment for many patients [80]. In addition to the reduced pain, patients have been found to have equally efficient treatment outcomes compared to conventional PDT [34, 81–83, 92, 93]. Due to these recent clinical studies indicating the successful application of daylight-PDT, it is of interest to further investigate the potential and limitations of this treatment modality. To my knowledge, there have not been any theoretical investigations of daylight PDT and in this chapter results from a 3D Monte Carlo radiation transfer (MCRT) model which simulates daylight PDT are presented. The methods used in this work allow the determination of the photo-toxicity at different depths in the simulated skin and tumour tissue for different light sources and, in the case of daylight-PDT, for different weather conditions. The model adopts the same conditions for daylight PDT as for conventional PDT, where the PpIX is already accumulated before the tissue is exposed to the light source. The parameters investigated include initial distribution of PpIX and delivered light dose. In chapter 4, time and depth dependent distribution of PpIX is discussed and compared with the uniform initial distribution. The main aim with this chapter lies in the code development and methodology to allow for further development of the code where more parameters can be considered in subsequent chapters.

3.3 Methods

A MCRT model was developed to simulate the transport, scattering and absorption of light through the skin tissue during illumination. The MCRT, using the probabilistic nature of the photons, generates accurate information about the light distribution and energy deposition during light illumination [108, 117, 153]. The different light sources were simulated by sampling wavelengths from the corresponding light spectra. Different ratios of the diffuse and direct daylight contributions allowed for different weather conditions to be represented.

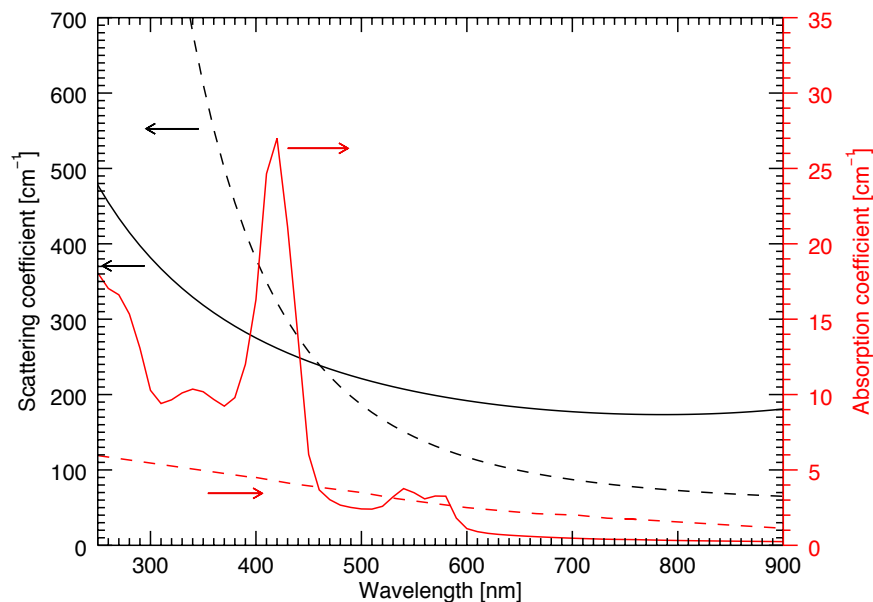


Figure 3.1: Wavelength dependent optical properties of tumour and skin tissue. The black curves correspond to the scattering coefficients (solid line corresponds to healthy skin tissue and dashed line corresponds to nodular BCC tissue). The red curves, plotted on the right axis, indicate the absorption coefficients for both healthy (solid) and nodular BCC tissue (dashed). The optical properties for healthy skin tissue are based on a modelling approach developed by Yudovsky et al [154, 155] which takes into account different contributions of different chromophores. The scattering coefficients for tumour tissue are based on the interpolation of data extracted from Salomatina et al [156] using the approach developed by Jacques [112].

3.3.1 Optical properties

The MCRT code developed here can incorporate optical properties representing different types of tissue, determined from theory or experiment. For the simulations presented in this chapter,

the wavelength dependent scattering (μ_s) and absorption coefficients (μ_a) for skin tissue and tumour tissue shown in figure 3.1 were adopted [154–156] . Many studies report a wide range of values for the optical properties of human skin and are summarised in recent review papers by Lister et al [111] and Jacques [112].

In this work, the model developed by Yudovsky et al [154, 155] was employed. This model is based on *in vivo* measurements, and determines the optical properties for healthy skin tissue over the wavelength range required for daylight PDT modelling. The scattering coefficients for the tumour tissue (nodular basal cell carcinoma, nBCC) were taken from the model developed by Jacques which is based on the data from Salomatina et al [112, 156]. The absorption coefficients for the tumour tissue are based on data determined by *in vitro* measurements of nBCC [156]. For further discussion on optical properties, see chapter 5.

The angular scattering phase function was modelled using the Heyney-Greenstein phase function (chapter 2, section 2.4.1) where the wavelength dependent anisotropy factor $g = 0.62 + 0.29 \times 10^{-3} \lambda (nm)$ was adopted. Polarisation is not considered and the reflectance at the air/tissue interface was determined using Fresnel reflectance assuming a uniform refractive index of 1.38 for the skin surface (equation 2.28).

An initial uniform distribution of PpIX was assumed where the absorption properties of the PpIX affect the photodynamic dose (PDD) and thus the efficacy of different PDT treatments. The wavelength dependent absorption of the photosensitive chemical PpIX is shown in figure 1.4 (chapter 1). The absorption spectrum is measured using a spectrophotometer and was established from previous work in the group [55, 56, 100]. The absorption properties of the PpIX are important to the outcome of the treatment since it affects the amount of energy absorbed by the photosensitiser and thus the efficacy of the PDT treatment. To explore this feature further different initial concentrations of the PpIX were explored in this chapter. By increasing or alternatively reducing the initial concentration of PpIX, a wider range of potential absorption coefficients for the PpIX were investigated.

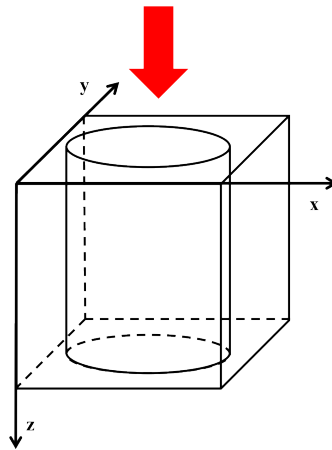


Figure 3.2: The MCRT simulation employs a 3D Cartesian grid (101 grid cells on a side) which is illuminated from above. The optical properties are determined in each individual grid cell. A cylindrical tumour is added in the centre of the grid, where the PpIX is accumulated and assumed to be of uniform density. The dimensions of the grid are 10 mm on a side and the tumour diameter is 6 mm.

3.3.2 Coding implementation

For the model presented here the dimensions of the simulated region was set to be 10 mm x 10 mm x 10 mm where a cylindrical tumour was positioned in the centre of the grid with a diameter of 6 mm (figure 3.2). The tissue outside the tumour was assumed to be of a single tissue type (dermis) with a smooth uniform structure with different optical properties compared to the tumour. The PpIX was restricted to the tumour tissue and was assumed to have a uniform initial distribution within the cylindrical tumour corresponding to a number density of $7.84 \times 10^{13} \text{ cm}^{-3}$. Repeated boundary conditions were adopted to simulate a semi-infinite tissue slab. Source photons were launched from the top of the grid and assigned an initial direction and wavelength depending on the source being simulated (e.g. daylight or an artificial light source). They were followed until they were either absorbed or scattered out of the simulation grid (top or bottom of the grid) as described in chapter 2.

A time dynamic was added to the code to take into account the photobleaching that changes the spatial distribution of PpIX throughout the treatment. At each time step 5×10^6 photons were launched and the photobleaching was determined before the simulated time was increased and the process was repeated. The time dependent photobleaching of the PpIX was considered as described in chapter 2 (section 2.6)). However to take into account for a wide wavelength range (as in the case for Daylight-PDT) a wavelength dependent pho-

photobleaching constant can be adopted [97, 143]. Therefore the previous photobleaching equations discussed in chapter 2 (equation 2.34), can be modified in the following way,

$$C(x, y, z, t) = C_0(x, y, z)e^{-\Psi(x, y, z)t/\beta(\lambda)} \quad (3.1)$$

where again $C(x, y, z, t)$ is the time dependent PpIX concentration at location (x, y, z) at time t , $C_0(x, y, z)$ is the initial concentration, and $\Psi(x, y, z)$ is the local fluence rate in Wcm^{-2} . In the model described in chapter 2 (section 2.6) the fluence rate was kept constant for all simulated time steps. For the work presented here the fluence rate was updated for each time step to take into account the change in PpIX concentration due to photobleaching.

As mentioned in chapter 2, the photobleaching constant, β , is defined as the light dose (Jcm^{-2}) required to reduce the fluorescence signal from the photosensitiser by 37% ($1/e$). The value for β has previously been established to be 14 Jcm^{-2} for 630 nm irradiation [100]. To my knowledge there is no information about how the photobleaching constant changes with wavelength. The assumption that has been made here to make β wavelength dependent is an inverse proportionality between β and the absorption of the photosensitiser. This allows the photobleaching equation to include the difference in absorption for different wavelengths and to account for the different energies carried by photons of different wavelengths. Since clinical data verifying the photobleaching constant is only available at 630 nm, for the simulations presented here the following wavelength dependence was applied to the photobleaching constant

$$\beta(\lambda) = \frac{\beta_{630} \mu_{a630} \lambda_{630}}{\lambda \mu_{a\lambda}} \quad (3.2)$$

where $\beta_{630} = 14 \text{ Jcm}^{-2}$ (clinically determined [100]), μ_{a630} is the absorption coefficient of PpIX at 630 nm, λ_{630} equals 630 nm, λ is the wavelength of the simulated photon in nm and $\mu_{a\lambda}$ is the absorption coefficient for PpIX at that wavelength. The photobleaching equation (equation 3.1) [97, 100] assumes an exponential decay, an unlimited oxygen supply and is assumed to be applied over the wavelength range 350 - 750 nm.

The reason why the proportionality in equation 3.2 was assumed is motivated by the maximum achievable photobleaching. When the PpIX is fully photobleached the PDD is saturated and therefore there is a maximum number of photons that can be absorbed by the photosensitiser before it is fully photobleached and this level is assumed to be the same for all

wavelengths. By adopting the wavelength dependency discussed above, the saturated PDD level is equal for all light sources and treatment conditions and is therefore believed to be plausible.

The value for β_{630} has, as previously mentioned, been clinically determined to be 14 Jcm^{-2} . A range of values have been reported [147, 157–159] which encourages a further exploration of this parameter. For this reason the photobleaching dose constant $\beta(\lambda)$ was multiplied and divided by three in equation 3.2 to further explore the range of possible values.

The PDD was computed in the same way as described in chapter 2 (section 2.6.1) and the same toxic threshold was applied ($8.6 \times 10^{17} \text{ photons cm}^{-3}$). Although this threshold is based on measurements of Photofrin in liver tissue it was adopted for illustrative purposes, allowing for comparison with previously published models [97, 100]. For most of the simulations presented here the maximum light dose delivered was 75 Jcm^{-2} since this is a typical light dose delivered during conventional PDT treatment. This allows for comparison between light sources under the same conditions. To simulate longer treatment times for daylight PDT, a larger light dose was computed.

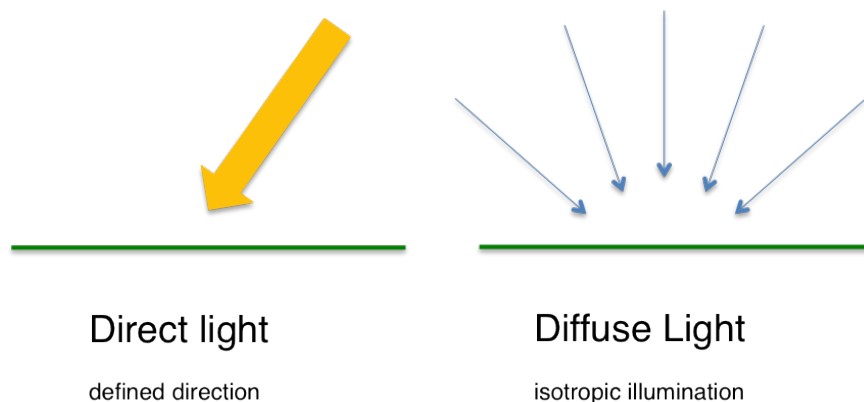


Figure 3.3: Daylight consists of both direct and diffuse light. Direct photons in the MCRT simulation are assigned a single angle of incidence. Diffuse light isotropically illuminates the surface of the skin phantom and consists of photons that have been scattered from particles and aerosols in the atmosphere. On sunny days the proportion of direct light will be larger and on an overcast day 100% of the daylight is assumed to be diffuse light.

3.3.3 Natural and artificial light sources

The light distribution under the surface of the skin depends on the incident light field which in the case of daylight PDT consists of both direct and diffuse sunlight (figure 3.3). Due to

the differences of the spectral and angular illumination between the diffuse and the direct light, it is important to decompose their relative contributions [160]. The light distribution during daylight illumination also depends on weather conditions, time of the day and month of the year [161]. In the simulations it was assumed that the direct sunlight enters the skin at a constant angle depending on the latitude on Earth (and time of day). The diffuse radiation, which was assumed to illuminate the skin isotropically, comprises sunlight that has been scattered by molecules and particles in the atmosphere but still reaches the surface of the Earth. The intensity of daylight is often measured in lux and is referred to as illuminance which is a measure of the irradiance weighted by the luminosity function, which takes into account the sensitivity of the human eye. The illuminance for daylight (at midday) varies from about 120 000 lux for a very clear sunny day to around 20 000 lux for an overcast day during summer, to considerably lower (<7500 lux) in the middle of winter (overcast) [93]. In this study weather conditions in the middle of summer were considered, where the solar zenith angle was assumed to be 30° at 56 degrees North [162], appropriate for the latitudes of Copenhagen in Denmark and Dundee in Scotland. It is possible to extend the spectrum to different latitudes, different time of years and also different time of day. However this is beyond the scope of this chapter.

The direct and diffuse spectra used in the simulations were generated from a model of the solar spectrum reaching Earth [161]. The total spectral irradiance $I_{T\lambda}$ at wavelength λ , incident on a horizontal surface is given by,

$$I_{T\lambda} = I_{d\lambda} \cos\theta + I_{s\lambda} \quad (3.3)$$

where $I_{d\lambda}$ and $I_{s\lambda}$ are the direct and diffuse (scattered) contributions, and θ is the angle from the normal to the surface to the incident light. The direct component is dependent on the solar zenith angle and is expressed by,

$$I_{d\lambda} = H_{o\lambda} D T_{r\lambda} T_{a\lambda} T_{w\lambda} T_{o\lambda} T_{u\lambda} \quad (3.4)$$

where $H_{o\lambda}$ is the extraterrestrial irradiance at the mean sun-earth distance. D is the correction parameter that takes into account the distance between the sun and the earth which depends on the day of the year. The remaining components correspond to transmittance function of the atmosphere at different wavelengths. $T_{r\lambda}$ takes into account the molecular or Rayleigh

scattering, $T_{a\lambda}$ the aerosol attenuation, $T_{w\lambda}$ the water vapour absorption, $T_{o\lambda}$ the ozone absorption and $T_{u\lambda}$ takes into account the uniform mixed gas absorption.

The contribution from diffuse sunlight is

$$I_{s\lambda} = I_{r\lambda} + I_{a\lambda} + I_{g\lambda} \quad (3.5)$$

where $I_{r\lambda}$ is the Rayleigh scattering component, $I_{a\lambda}$ is the contribution from aerosol scattering, and the third component, $I_{g\lambda}$, takes into account the reflection of sunlight between the ground and the air. A more detailed description of the algorithm and model can be found in Bird et al (1986) [161]. The exposure will vary between different people and different body sites depending on orientation [163, 164]. To take this into account different surface orientations were investigated which will alter the intensity of the irradiance according to equation 3.3.

The direct and diffuse spectra that were input to the Monte Carlo simulations (figure 3.4) represent conditions for midday on a clear summer day. In this model the direct light represents 80% of the total illuminance of about 100 000 lux. For daylight PDT simulations of an overcast day, the spectrum was assumed to be 100% diffuse light, corresponding to about 15 000 lux. Daylight PDT was compared to conventional PDT by simulating illumination by an Aktelite lamp (Photocure ASA, Hoffsveien 48, Norway) [72] which is a red LED light source, typically used for conventional PDT treatment (chapter 1, section 1.8). The spectral irradiance for the Aktelite is plotted in figure 3.4. Also shown in figure 3.4 is the spectral shape of the PpIX absorption spectrum, showing the strong absorption around 405 nm and the smaller absorption peak coincident with the Aktelite spectrum.

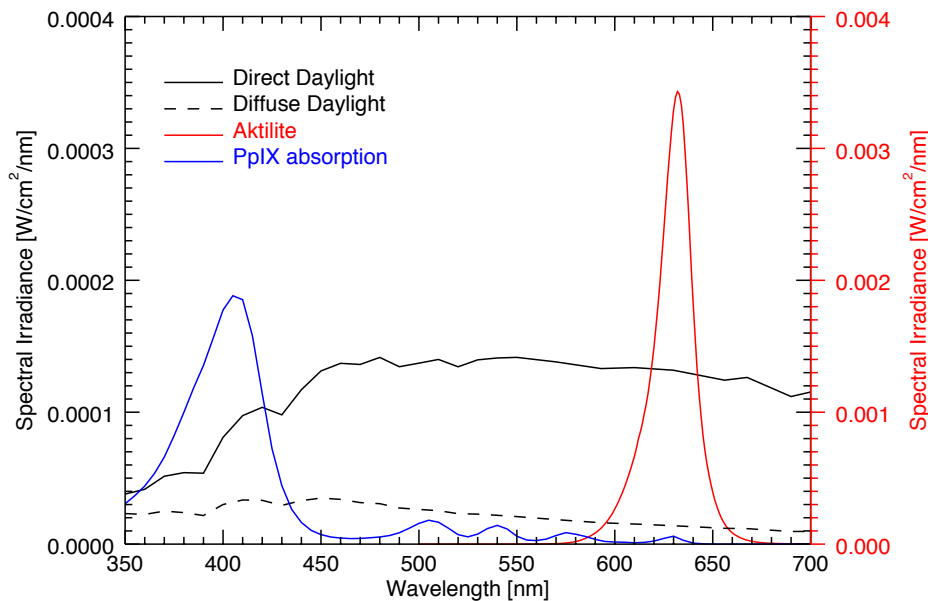


Figure 3.4: Illuminating spectra adopted for the MCRT simulations for daylight [161] and the Aktelite [72]. The indicative absorption curve for PpIX is shown in blue and is provided as a guide to the eye only to highlight the dominant absorbing features. The Aktelite spectrum targets a small absorption peak around 630nm while the daylight utilises the whole absorption spectrum of PpIX which results in more energy being absorbed from the daylight even though the spectral irradiance is lower.

3.4 Results for Monte Carlo modelling of daylight PDT

Daylight may be absorbed by PpIX over a wide wavelength range, while the Aktelite targets the smaller PpIX absorption peak around 630 nm (figure 3.4) to ensure a deeper light penetration [73]. This means that the total absorbed energy (by PpIX) is roughly 5 times greater for daylight compared to the Aktelite. This is determined by calculating the overlap between the light spectra and the PpIX absorption spectra. By multiplying the light spectrum by the absorption spectrum and integrating, the total absorbed energy can be compared for the different light sources. The dominating absorbing wavelengths for daylight and conventional PDT are 405 nm and 630 nm respectively. In figure 3.5 results from two separate Monte Carlo simulations for the PDD, assuming normal illumination by monochromatic light, at 405 nm and 630 nm of an irradiance 82 mW cm^{-2} are shown. Results are displayed for four different light doses of 10, 20, 40 and 75 J cm^{-2} . As one would expect, due to the deeper penetration, the 630 nm light achieves higher PDD at greater depths compared to the 405 nm light.

Although not penetrating as deeply, the 405 nm light achieves the same PDD at superficial layers.

The results of Monte Carlo simulations of the depth dependent PDD using the daylight spectrum (on clear and overcast days) and the Aktelite are shown in figure 3.6 for light doses of 10 and 75 J cm⁻², with a PpIX absorption coefficient at 630 nm obtained from figure 1.4 of 0.06 cm⁻¹. To investigate the full range of published values [159], a higher and lower PpIX concentration were also investigated. Figures 3.7 and 3.8 show the resulting PDD for daylight PDT when the PpIX absorption coefficients at 630 nm are 0.18 cm⁻¹ and 0.02 cm⁻¹, representing higher and lower concentrations of PpIX compared to the results in figure 3.6.

So far, equal light doses have been compared with a maximum light dose corresponding to 75 J cm⁻². During Daylight-PDT a standard illumination time (1.5-2.5 h) is typically applied instead of a specific light dose. To investigate the effect of an extended illumination time, a light dose corresponding to 2.5 hours was simulated for Daylight-PDT (during clear weather conditions). This is equivalent to a total light dose of approximately 370 J cm⁻² (assuming an irradiance of 41 mW cm⁻²). To display the effect of this increased illumination both 75 J cm⁻² (30 min) and 370 J cm⁻² (2.5 hours) are plotted in figure 3.9.

The absorbed photons (by PpIX during daylight PDT) were binned according to both wavelength and absorption location to investigate the contribution from different wavelengths. First of all absorption wavelengths were grouped into two blocks, the first (300-500 nm) representing the shorter wavelength range and the second (500-700 nm) representing the longer wavelengths. In figure 3.10 the total absorption was calculated for four different time blocks during the initial 75 J cm⁻². In figure 3.11 the absorption was compared for the initial 75 J cm⁻² to the prolonged treatment section (75-370 J cm⁻²). For both figure 3.10 and 3.11 the absorption was normalised by the number of bf absorbed photons during the treatment time represented in each figure.

To more specifically investigate different wavelength contributions to the absorption, the absorption distribution for the different wavelengths were plotted at different depths. Here the contribution at different depths were grouped to display how the absorption distribution changes with depth at different points in the treatment during daylight PDT (figure 3.12).

Figure 3.6 - 3.9 show simulations for the case where direct daylight is incident at $\theta = 30^\circ$ from the normal to the skin surface. The results of different surface orientations are shown

in figure 3.13. For the clear daylight situation the PDD has been simulated for additional θ in equation 3.3, of 0° , 60° and 80° . All of the scenarios investigated assumed that the patient would orient the lesion being treated, towards the sun. For this reason only one angle of rotation was considered.

When the photobleaching dose constant was scaled to explore the range of possible values the maximum light dose of 75 J cm^{-2} was compared for the three different light conditions. The PDD for both the higher and lower value for $\beta(\lambda)$ was compared to the case previously explored (figure 3.6) and plotted in figure 3.14. A lower value for $\beta(\lambda)$ results in a fast photobleaching and a fewer number of absorption events before the PpIX is photobleached. This results in a lower PDD at the surface and also a lower effective treatment depth. The opposite is true for a higher value for $\beta(\lambda)$, when the slower photobleaching allows for more absorption events to occur. This results in a higher PDD which stretches deeper into the skin tissue.

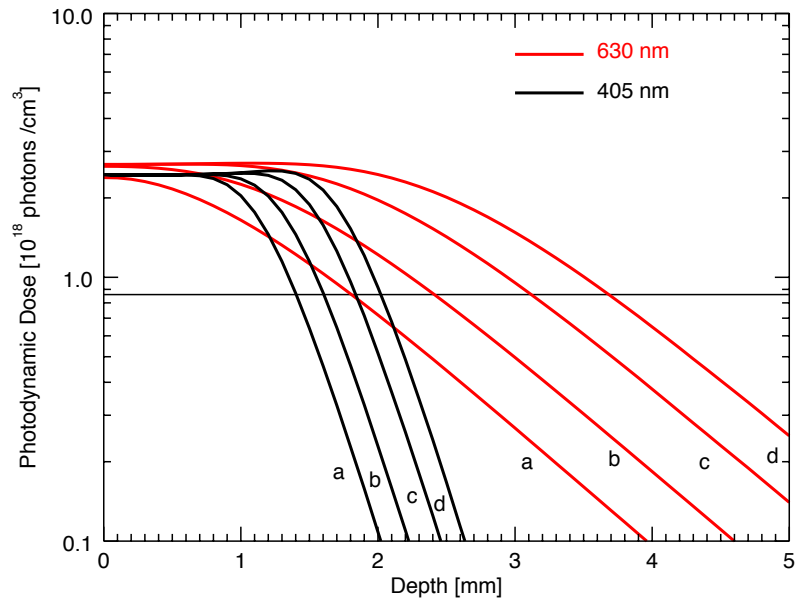


Figure 3.5: Photodynamic dose for two separate wavelengths at normal incidence on the tumour. Four different light doses are plotted: 10 (a), 20 (b), 40 (c) and 75 (d) J cm^{-2} , where both light sources are assumed to have a total irradiance of 82 mW cm^{-2} . The horizontal line corresponds to the toxic threshold which determines the number of photons that have to be absorbed for necrosis to occur.

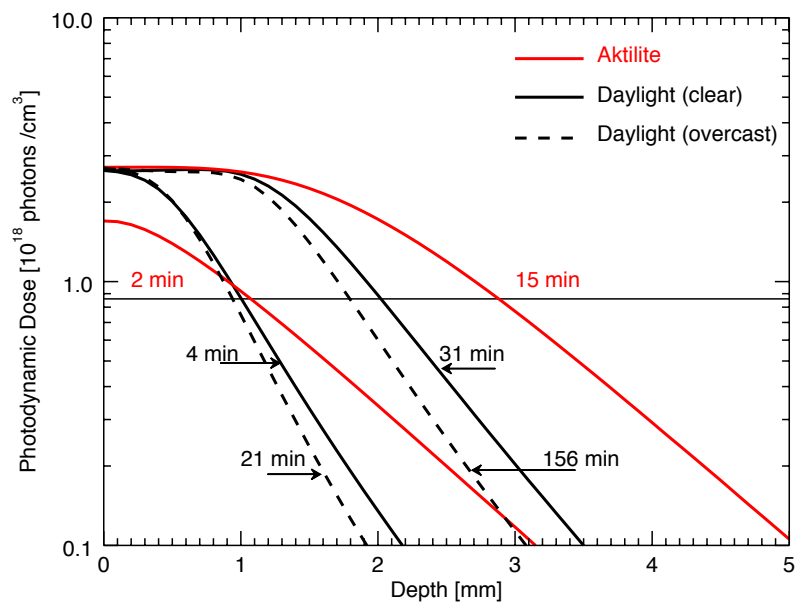


Figure 3.6: Photodynamic dose for conventional PDT treatment (red), and for daylight PDT for both a clear summer day (solid black) as well as an overcast summer day (dashed black). The photodynamic dose is plotted for two light doses, 10 and 75 J cm^{-2} . The irradiance for the Aktelite is assumed to be 82 mW cm^{-2} , while the irradiance for a clear summer day is determined to be 41 mW cm^{-2} and for an overcast summer day the irradiance is determined to be 8 mW cm^{-2} . Corresponding treatment times are displayed in the plot.

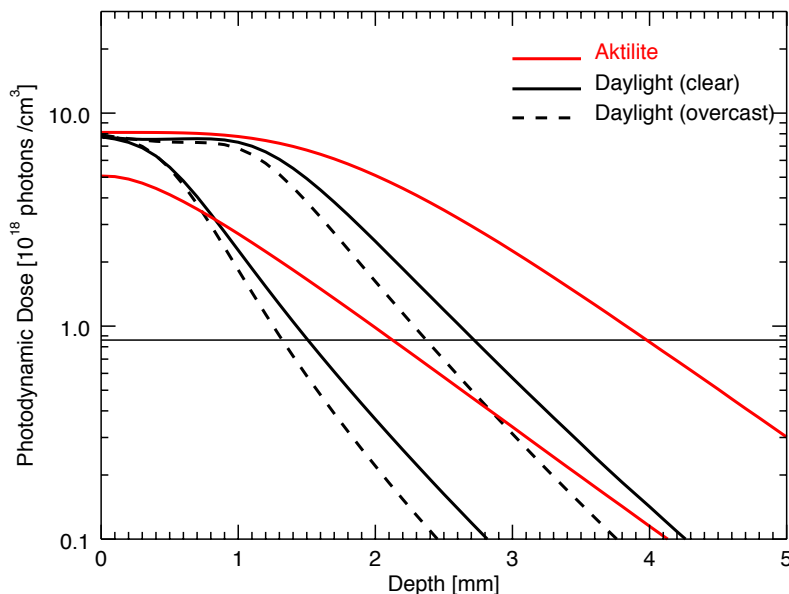


Figure 3.7: Photodynamic dose for the situation where the concentration of PpIX has been increased by a factor of three. This corresponds to an absorption coefficient at 630 nm for PpIX of 0.18 cm^{-1} . Light doses of 10 and 75 Jcm^{-2} are plotted and correspond to the same treatment times as indicated in figure 3.6.

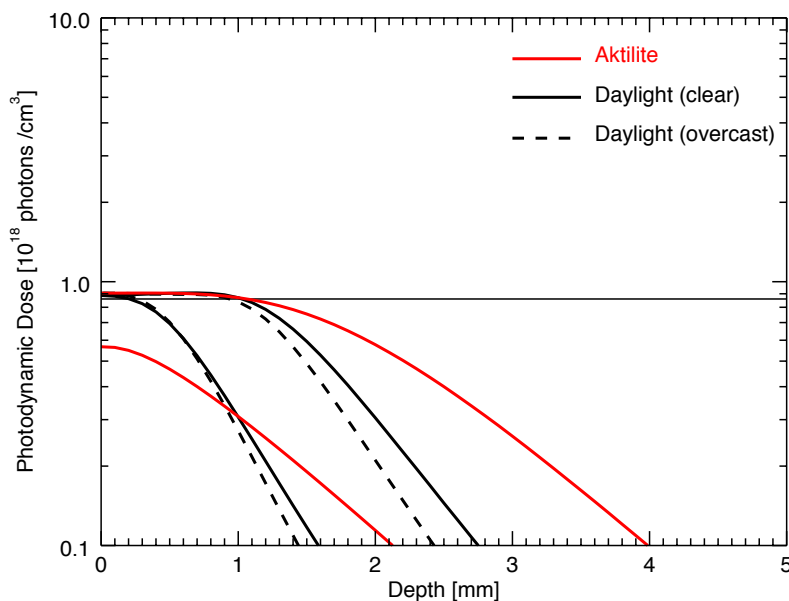


Figure 3.8: Photodynamic dose for the situation where the concentration of PpIX has been reduced by a factor of three. This corresponds to an absorption coefficient at 630nm for PpIX of 0.02 cm^{-1} . The light doses and treatment times are equivalent to those plotted in figure 3.6 and 3.7.

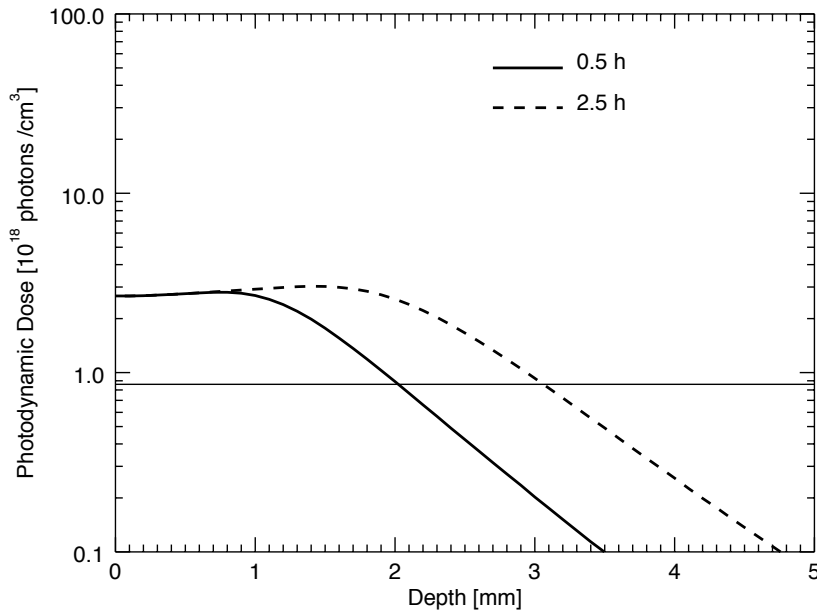


Figure 3.9: Photodynamic dose for a longer treatment time. Here the difference between 30 min (75 J cm^{-2}) and 2.5 hours (370 J cm^{-2}) of simulated treatment time during daylight activated PDT during clear treatment conditions is demonstrated.

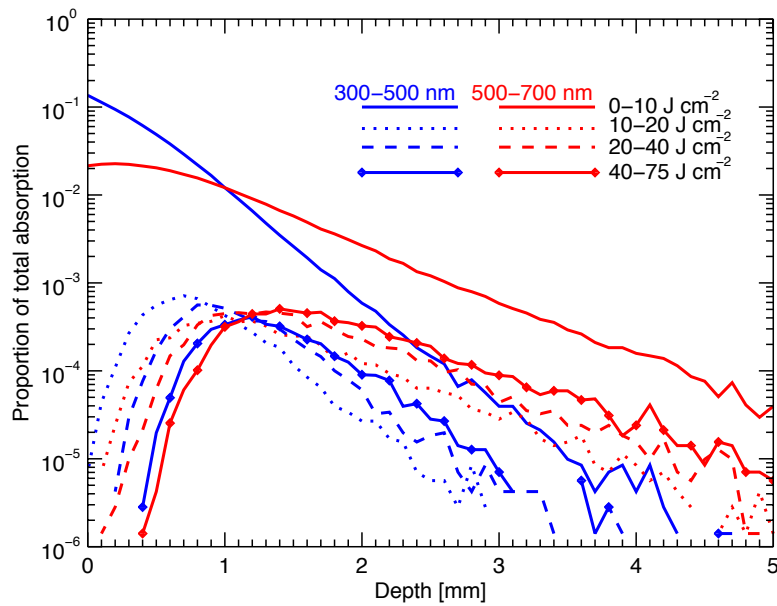


Figure 3.10: Wavelength distribution of the absorption of a total light dose of 75 J cm^{-2} divided into four time sections. As the treatment progresses the longer wavelength range contributes more and more. The photon absorption events are recorded and represented for daylight PDT (during clear weather conditions). Each curve is normalised by the total number of photons absorbed during the first 75 J cm^{-2} .

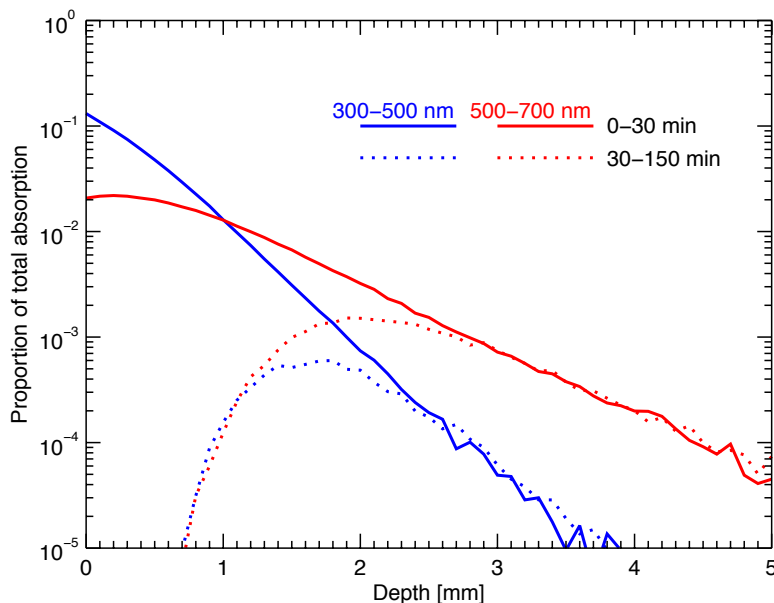


Figure 3.11: Proportion of the photons being absorbed in different wavelength ranges at different depths through the tumour during daylight PDT. Normalised by total number of absorbed photons (by PpIX) during the 150 minutes that was simulated.

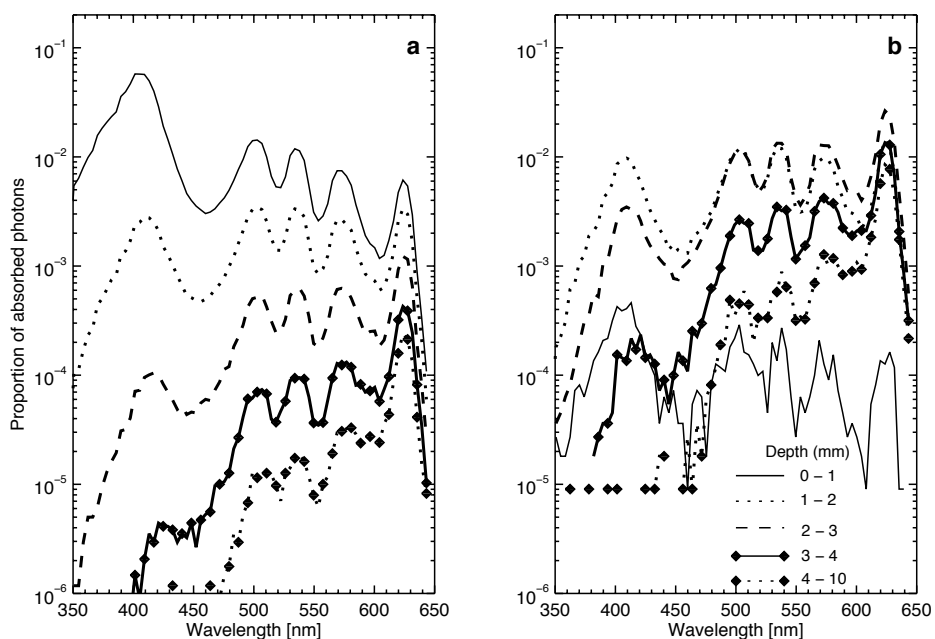


Figure 3.12: Proportion of the photons being absorbed at different wavelengths at different depths during daylight PDT. Normalised by total number of absorbed photons (by PpIX) in each treatment block: a) 0-30 min which corresponds to 0-75 J cm⁻² and b) 30-150 min which corresponds to 75-370 J cm⁻².

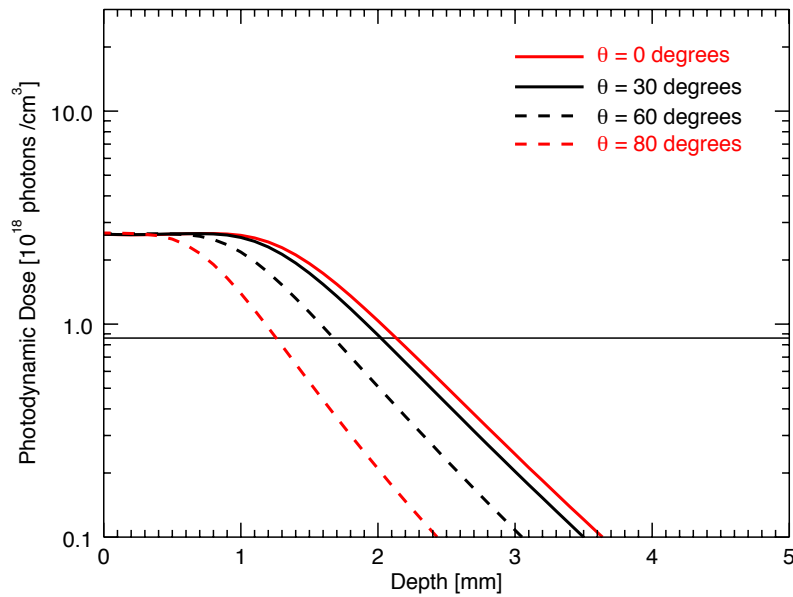


Figure 3.13: Effect of different illumination angles during daylight PDT. The four different angles that have been investigated are $\theta = 0^\circ$, 30° , 60° , and 80° , where θ is the angle between the incident light and the normal to the surface. In each case it is assumed that the person being exposed to daylight faces the sun.

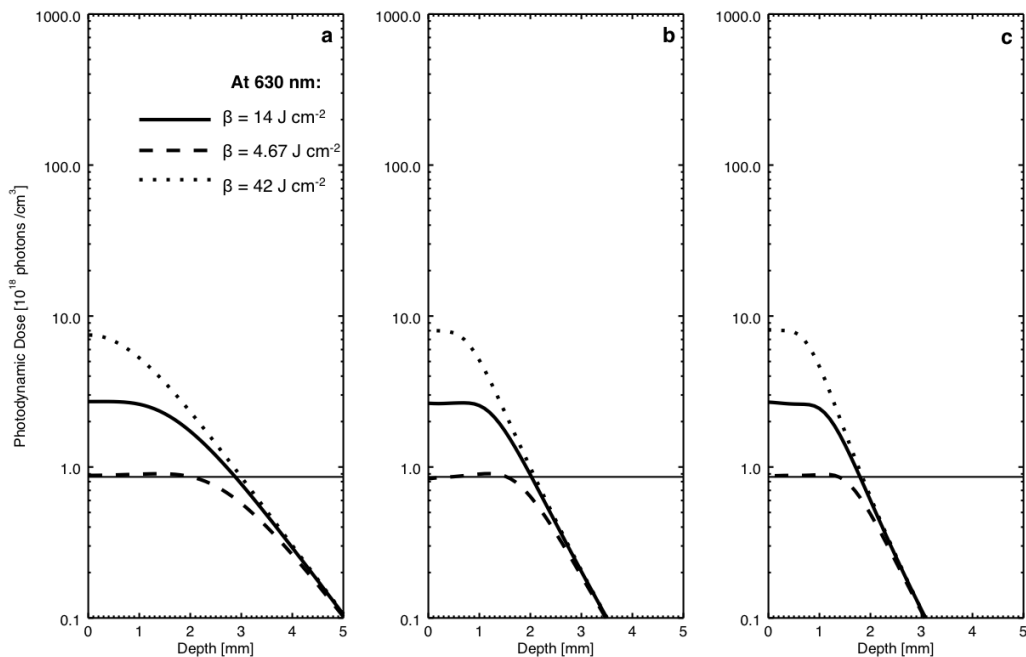


Figure 3.14: The photodynamic dose comparing different values for the photobleaching dose constant $\beta(\lambda)$ which was multiplied and divided by three to explore the range of possible values. The PDD at the light dose 75 J cm^{-2} is compared for the different light conditions: a) conventional PDT where the Aktelite is used as the illuminating light source b) Daylight PDT during clear conditions and c) Daylight PDT during overcast conditions. A higher $\beta(\lambda)$ (dotted) results in a slower photobleaching and therefore a higher PDD. A lower $\beta(\lambda)$ (dashed) results in a faster photobleaching and therefore a lower PDD.

3.5 Discussion

Due to the Soret band of PpIX (the broad absorption peak around 405 nm in figure 3.4) and limited penetration depth at these wavelengths, the PDD caused by daylight will be closer to the surface. This results in rapid photobleaching at the beginning of the treatment that then slows as treatment progresses since the concentration of PpIX is reduced. Figure 3.6 indicates that on a clear sunny day it would take about 30 minutes to deliver a light dose of 75 J cm^{-2} with an effective treatment depth of over 2 mm. The same light dose would take about 2.5 h to deliver on an overcast day with approximately the same effective treatment depth. The Aktelite delivers the same light dose after about 15 min of irradiation, yielding an effective treatment depth of about 3 mm. The wavelength distribution of the absorption for daylight PDT (clear) (figure 3.10) show how the absorption changes with time. During the initial 10 J cm^{-2} the shorter wavelengths dominate the absorption. Gradually as more light is delivered to the skin tissue the ratio between the shorter wavelength contribution and the longer wavelength contribution change. For the last 30 J cm^{-2} ($40 - 75 \text{ J cm}^{-2}$) the longer wavelength range dominates the absorption. Throughout, the longer wavelength range contributes to deeper absorption.

Figure 3.6 suggests that the treatment depth is limited by the light penetration. To investigate this, figure 3.9 was produced. This result shows that prolonging the daylight treatment time, deeper efficient treatment can be achieved. Figures 3.11 and 3.12 show how the wavelength distribution of the absorption changes with time. As shown in figure 3.11, during the initial 75 J cm^{-2} of the treatment the absorption is dominated by shorter wavelengths. However during an extended treatment after the first 75 J cm^{-2} , the absorption is dominated by longer wavelengths. Due to the longer wavelengths penetrating deeper they have the potential of activating the PpIX deeper in the tissue while the shorter wavelengths are restricted to the superficial layers which will be photobleached before the deeper layers. Figure 3.12 shows how the absorption is shifted towards the red part of the spectrum for different parts of the treatment, where the initial 75 J cm^{-2} shows a larger proportion of the absorption in the blue compared to the second treatment block (30-150 min). This figure also shows how at the start of the treatment more photons are absorbed at the top of the tumour while at later times the absorption is dominating in deeper layers of the tumour.

Exploring the range of values for the photobleaching dose constant $\beta(\lambda)$ shows that the

rate of photobleaching effects the penetration and thereby the treatment depth that is achievable. This indicates that an extended investigation of this rate is necessary for further improvements of theoretical models. This would require a clinical study where the PpIX photobleaching properties are explored *in vivo*. This can be achieved by measuring how the PpIX fluorescence signal changes during illumination [100].

The adopted skin phantom is a simplified model, where the well defined layered structure has not been taken into account. The shape of the tumour is not an exact replica of those found in patients but shows the discrepancy between healthy tissue and diseased tissue. The optical properties are assumed to be uniform within the tissue and future developments could include different structures such as blood vessels that may affect the spatial distribution of absorbers and scatterers [165, 166]. In chapter 6 more complex tumour structures will be considered with the aim to explore the importance of including three dimensional affects in theoretical simulations of PDT.

A further complication in clinical treatment is the time dependent build-up of PpIX prior to the commencement of irradiation. In this work a uniform distribution of PpIX was assumed, although treatment depth may also be limited by the distribution of PpIX [167, 168]. This will be discussed in chapter 4 where the difference between treatment protocols for daylight and conventional PDT are considered. However from the initial models presented in this chapter it is clear from figure 3.7 and 3.8 that the concentration, and therefore the uptake and accumulation of PpIX in the tumour, will have a large effect on the treatment outcome.

Even though studies have shown that oxygen is depleted during treatment, the model presented here assumes an unlimited oxygen supply. To accurately take into account the oxygen supply [169–171] both oxygen consumption as well as perfusion would have to be considered. This phenomenon is not well understood and further investigation is required [169].

It is well known that optical properties vary for patients with different skin types and may be a reason for the different treatment outcomes. Other optical properties will be discussed and investigated further in chapter 5. In our simulations, apart from the time dependent effects of photobleaching on the concentration of PpIX, all other optical properties remain constant during treatment.

A patient undergoing daylight PDT will not constantly orient the area of interest perpen-

dicular to the direct sunlight since this will sometimes be inconvenient. Figure 3.13 shows that a steeper angle to the sun results in a lower irradiance and therefore a slightly lower effective penetration depth of the treatment light. Here we only investigate one angle of rotation, however this study validates the principle that a steeper angle results in a more shallow treatment depth.

3.6 Conclusions

A MCRT model has been developed for the simulation of conventional and daylight activated PDT. It was used to investigate the potential and limitations of treating superficial skin lesions with artificial and natural light. The model determines the toxicity (PDD) within the tumour as a function of depth during different weather conditions. Adopting optical properties appropriate for healthy and diseased tissue, simulations show that for a clear summer day it would take around 30 minutes to deliver a light dose of 75 J cm^{-2} , which is comparable to the light dose used in conventional PDT treatments. The simulations predict an effective treatment depth for daylight PDT of over 2 mm, making it ideal for treating superficial skin lesions, though limiting its efficacy for deeper lying tumours. The effect of PpIX concentration was also investigated, finding that a higher concentration yields a greater effective penetration depth. The results of our MCRT simulations support the clinical findings that daylight PDT can be an effective alternative to conventional PDT for appropriate tumour types. Different parameters were investigated in this chapter such as different lesion orientations and initial PpIX concentrations.

4

Theoretical determination of continuous protoporphyrin IX production

4.1 Summary

Most existing models of photodynamic therapy (PDT) assume a uniform initial distribution of the photosensitive molecule, protoporphyrin IX (PpIX). This is an adequate assumption when the prodrug is systemically administered; however for the situation which is considered in this thesis, this is no longer valid. Topical application and subsequent diffusion of the prodrug results in an inhomogeneous distribution of PpIX at the start of the light treatment. In this chapter, a model that takes into account a PpIX distribution that depends on the incubation time and the treatment modality is described. Three steps of the PpIX production are considered. The first is the distribution of the topically applied prodrug, second is the conversion from the prodrug to PpIX. Thirdly the light distribution which affects the PpIX distribution through photobleaching is considered. The results show that prodrug diffusion and PpIX con-

version properties are vital for accurate determination of the spatial and temporal distribution of PpIX. The work presented here suggests that treatment depths are not only limited by the light penetration but also by the PpIX distribution.

4.2 Introduction and background

Traditionally PDT dosimetry is based on a systemic injection of the drug where it is appropriate to assume that the photosensitiser is uniformly distributed throughout the region of interest. When this situation is considered the treatment depth is only limited by the penetration of (the treatment) light. Topically administered sensitisers are commonly used for PDT to treat non-melanoma skin cancer (NMSC) and dysplasia. In this situation it is not appropriate to assume that the drug is uniformly distributed through the tumour tissue when the light treatment is started. The distribution of the drug will depend on the distance from the surface and the total time since application. For topical PDT it is therefore important to include this inhomogeneous distribution (in the vertical plane) of the photosensitiser for a more accurate dosimetry model [167, 172].

During conventional PDT, the prodrug is topically administered to the lesion 3 hours before the light illumination. During this occlusive treatment phase, the prodrug diffuses through the skin and is subsequently converted within the mitochondria of the tumour cells to the photosensitive chemical PpIX [53, 58, 65, 173]. These two processes are discussed further in section 4.3.1 and 4.3.2. For daylight PDT however this occlusive treatment phase is typically (only) 30 minutes. When introducing the model developed in this chapter, it is possible to consider the differences in treatment protocol.

It is of interest to develop topically applied prodrugs which give deep penetration and a high PpIX accumulation, since this results in maximally efficient treatment depth. Due to the variation in tumour tissue and between individuals there is some dispute about the penetration of the prodrug. Studies in mouse tumours show diffusion of the prodrug to a depth of several mm however most prodrug molecules are confined to the top 2 mm of the tumour [53, 69, 174–176]. The most common prodrugs used for topical PDT contain either ALA (aminolevulinic acid) or its methyl ester MAL (methyl-aminolevulinate) [53] where 5-ALA is licensed in the US and MAL is the only commercially available prodrug in Europe. Both molecules are converted within tumour tissue to PpIX, however MAL is required to first

be converted to ALA before finally producing PpIX. See section 1.5 in chapter 1 for a more detailed description of the production of PpIX. It is thought that prodrugs containing MAL result in a deeper penetration of the photosensitiser since it is more lipophilic, however few studies support this theory [42, 43, 177–179]. Previous studies also indicate that the surface fluorescence using ALA-based creams is higher [180], indicating that there might be both a difference in diffusivity as well as conversion rate between ALA and MAL.

Previous studies have considered topical application of the prodrug to theoretically determine the distribution of the PpIX after the occlusive treatment phase. These different studies have used slightly different approaches [167, 168, 181, 182]. The study by Star et al included the most complicated conversion model between the prodrug and the PpIX, however a maximum penetration depth of 0.5 mm was assumed [168]. This contradicts other studies where a deeper penetration is indicated [53, 69, 174–176]. The model developed for this chapter combines ideas demonstrated in several of these earlier studies. Previous work has explored different exponential distributions of PpIX in a light distribution model [183–185]. However this does not combine a molecular diffusion model with Monte Carlo radiation transfer (MCRT) modelling (chapter 2) using an appropriate model of the PpIX distribution. The work presented here attempts to extend current theoretical models by including a more appropriate representation of the PpIX distribution.

The aim of the work presented here is to combine the light distribution model (chapters 2 and 3) with a modelled distribution of PpIX where both temporal and spatial dependence is considered. This allows for not only light penetration limitations to be investigated but also drug penetration limitations, resulting in a more accurate representation of PDT for different treatment conditions. The developed model invites discussion regarding the appropriateness of the length of the occlusive treatment phases and the effect of prolonged daylight exposure. The model developed in this study is primarily based on basic molecular diffusion theory in combination with a simple rate equation. Properties and characteristics of diffusion through skin and the conversion of PpIX are not well understood. Therefore in an attempt to improve knowledge of PpIX production characteristics, the aim was also to generate a theoretical simulation of fluorescence during the incubation time to better understand and explain the clinical data collected in chapter 6.

4.3 Methods

The production of PpIX from topical administration of a prodrug is a complex procedure with multiple steps. The model presented here contains only the most relevant parameters, thus the number of required assumptions and approximations is reduced. A one dimensional case was considered where the concentration of PpIX was assumed to only vary in the vertical direction (from the surface of the tissue).

The addition of the PpIX distribution model will affect the light distribution model through the concentration dependency of the optical properties associated with the PpIX. Hence the absorption coefficient for PpIX ($\mu_a(\lambda)$) will depend on the local number density of PpIX molecules as follows,

$$\mu_a(\lambda) = n_{PpIX}\sigma(\lambda) \quad (4.1)$$

where n_{PpIX} is the number density of PpIX molecules (cm^{-3}) and $\sigma(\lambda)$ is the PpIX cross section (cm^2) (figure 4.1).

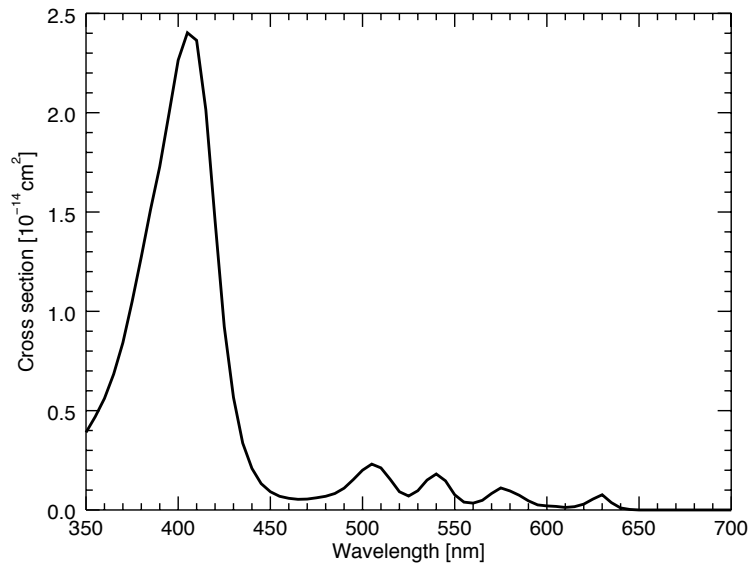


Figure 4.1: Figure showing the PpIX cross section as a function of wavelength. The absorption coefficient is generated by multiplying the cross section (displayed in the figure) with the PpIX number density of PpIX molecules present [181].

The set-up of the code is similar to that described in chapter 3 where a simulated region of $10\text{ mm} \times 10\text{ mm} \times 10\text{ mm}$ was considered. Repeated boundaries were applied with a centrally located cylindrical tumour with a diameter of 6 mm. The PpIX molecules were restricted to the areas occupied by the tumour tissue. The optical properties of the tumour as well as surrounding tissue were the same as adopted in chapter 3.

4.3.1 Prodrug diffusion

Since the distribution of the MAL (or ALA) molecules dictates the distribution of PpIX molecules, the first step of the procedure that is considered is the diffusion of the prodrug. Molecular diffusion, where molecules diffuse from a region of high concentration to a region of lower concentration is described by Fick's (first) law,

$$J = -D \frac{\partial M(z, t)}{\partial z} \quad (4.2)$$

In this equation, J corresponds to the flux which describes the flow of substance (molecules) through a unit area per unit time ($\text{m}^{-2}\text{s}^{-1}$). The magnitude of J is proportional to the gradient of the concentration $M(z,t)$ (m^{-3}). In this case, $M(z,t)$ corresponds to the number density hereafter referred to as concentration of MAL (or ALA) molecules. D (m^2s^{-1}) is the diffusivity, or diffusion coefficient, which describes the speed at which a substance diffuses through another substance.

By applying the continuity equation for mass conservation [167],

$$\frac{\partial J}{\partial z} + \frac{\partial M(z, t)}{\partial t} = 0 \quad (4.3)$$

and combining with equation 4.2, the equation that describes how $M(z,t)$ changes with time is,

$$\frac{\partial M(z, t)}{\partial t} = D \frac{\partial^2 M(z, t)}{\partial z^2} \quad (4.4)$$

Equation 4.4 is a partial differential equation that requires boundary conditions to be solved.

By assuming that the initial concentration, C_0 is introduced at $t=0$ and $z=0$ and thereafter kept constant at C_0 (at the surface) the following solution satisfies equation 4.4 [186]:

$$M(z, t) = C_0 \left(1 - \operatorname{erf} \left(\frac{z}{\sqrt{4Dt}} \right) \right) \quad (4.5)$$

where the Gaussian error function (erf) is defined as

$$\operatorname{erf}(u) = \frac{2}{\sqrt{\pi}} \int_0^u e^{-t^2} dt \quad (4.6)$$

These boundary conditions were assumed due to the excess cream still present on the lesion after 3 hours of occlusive treatment, acting like a reservoir and the concentration of MAL (or ALA) molecules was therefore kept constant at the surface. Since the diffusion problem described here can be compared to a plane source with an extended initial distribution, the standard solution (equation 4.5) was believed to be an appropriate description of the prodrug diffusion. Similar assumptions have previously been argued for and applied in other studies where similar models were developed [167, 168, 181, 182, 186].

4.3.2 PpIX production

The PpIX is produced from ALA molecules (section 1.5, chapter 1). In the work presented in this thesis, a prodrug containing MAL molecules was considered, however the conversion from MAL to ALA was not separately included. Hence only the conversion from MAL to PpIX was considered in the equation describing the production of PpIX. The rate equation that was considered here is expressed as follows [167, 168],

$$\frac{\partial \text{PpIX}(z, t)}{\partial t} = -\frac{\text{PpIX}(z, t)}{\tau_p} + \varepsilon_p \frac{M(z, t)}{\tau_{ap}} \quad (4.7)$$

This rate equation includes the two main features that contribute to the resulting concentration of PpIX, $\text{PpIX}(z, t)$. The source term in the equation (term furthest to the right) corresponds to the conversion from MAL molecules to PpIX molecules. This depends on the distribution of MAL molecules, $M(z, t)$, the yield, ε_p , which determines the proportion of MAL molecules being converted to PpIX, as well as the relaxation time, τ_{ap} . The relaxation time, τ_{ap} determines how fast this conversion happens and is defined as the time it takes for the

concentration ($M(z,t)$) to reduce to $1/e$ (37 %) of its original concentration due to PpIX production. The sink in equation 4.7 is the first term to the right of the equal sign. This term corresponds to the clearance of the PpIX (mostly due to heme production). The rate at which the clearance mechanism happens is dictated by the relaxation time, τ_p .

The rate equation described here does not include any light interaction and only considers the production of PpIX. When PpIX interacts with light, the concentration of PpIX molecules reduces with time due to photobleaching. This type of reduction of concentration was considered within the MCRT model however, it was not included in the rate equation (equation 4.7). Therefore it was assumed that the concentration reduction due to photobleaching did not affect the diffusion of the prodrug molecules or the production of PpIX.

The solution to equation 4.7 has previously been established [167] to be ,

$$PPIX(z, t) = \frac{\epsilon_p}{\tau_{ap}} \int_0^t e^{-\frac{t-t'}{\tau_p}} M(z, t') dt' = \frac{C_0 \epsilon_p}{\tau_{ap}} \int_0^t e^{-\frac{t-t'}{\tau_p}} \left(1 - \operatorname{erf}\left(\frac{z}{\sqrt{4Dt'}}\right)\right) dt' \quad (4.8)$$

This is the equation that was used in the work presented here to calculate the distribution of the PpIX as it changes with time and depth.

4.3.3 Different treatment modalities

During the occlusive treatment phase of conventional (using an artificial light source) PDT the region of interest is covered with an occlusive dressing. Before the light irradiation, the dressing and any excess cream is removed from the lesion. When daylight is used as the alternative light source there is no occlusive dressing applied and any excess cream is left on the lesion for the duration of the treatment. Since the amount of exposure will be different for different patients during daylight PDT, for the work presented here it was assumed that the occlusive treatment phase during daylight PDT was similar to conventional PDT. The light interaction during the occlusive treatment phase was therefore assumed to not occur.

Different treatment modalities had to be considered when modelling the different scenarios and are shown in table 4.1. The most important difference is the continued accumulation and production of PpIX during the light treatment for daylight PDT. This is due to the cream being kept on the lesion during the light application.

Table 4.1: Description of the different treatment modalities where the PpIX is assumed to continue to build-up during the light interaction phase of the treatment during daylight PDT but not during conventional PDT. These values are based on established clinical practice [78].

Concept	Conventional PDT	Daylight PDT
Occlusive treatment, no light	3 hours	30 minutes
PpIX build-up during illumination	NO	YES
Photobleaching during illumination	YES	YES

4.3.4 Determination of constants

For the method described above, the parameters: D , C_0 , ϵ_p , τ_{ap} and τ_p , determine the distribution and production rate of PpIX. There is limited knowledge about the exact values of these parameters, however using educated assumptions based on previously published data an initial set of parameters was adopted (set 1, table 4.2). This set of values were believed to be the most relevant and appropriate; however, it is important to acknowledge that there is a large variability in the published literature.

Star et al [168] developed a similar model to the one discussed here where the relaxation times, τ_{ap} and τ_p were assumed to be: $\tau_p = 1.3$ h and $\tau_{ap} = 2.4$ h. The magnitude of these relaxation times agree with those suggested by Aalders et al (2001) [173]. Another related model, developed by Salas Garcia et al [181, 182], suggested that $\tau_p = 84$ ms and $\tau_{ap} = 24$ h. However, it can be argued that these values are less reasonable, especially since 84 ms is the non radiative relaxation time of the PpIX molecule [187], which is irrelevant to the clearance rate of the molecule. Additionally, considerably longer clearance rates of the photosensitisers from the human body have been identified [53, 188]. It can also be argued that the value for τ_{ap} should be shorter, otherwise a longer incubation time would be introduced. Although they seem unreasonable, the parameters suggested by Salas Garcia et al [181, 182] were also included in this investigation (set 2, table 4.2).

There are no experimentally determined values published for the diffusion coefficient, D , for ALA/MAL diffusion through skin tissue. Svaasand et al [167] suggested that the magnitude of the diffusion coefficient of 5-ALA can be determined by comparison to molecules with similar molecular weight through human tissue. Assuming that the diffusion properties for MAL is not widely different to ALA, this suggest that values of the diffusivity should be in the region of 10^{-10} to 10^{-9} $\text{m}^2 \text{s}^{-1}$ [167] where a value of 0.69×10^{-10} $\text{m}^2 \text{s}^{-1}$ has been

applied by others for MAL diffusion [181].

Table 4.2: Parameter exploration for PpIX production model.

Set	C_0 cm^{-3}	ε_p	τ_{ap} s	A $\text{cm}^{-3} \text{s}^{-1}$	τ_p s	D $\text{m}^2 \text{s}^{-1}$
Initial guess, Set 1	6×10^{16}	0.5	8640	3.82×10^{12}	4680	0.69×10^{-10}
Set 2 [181]	6×10^{20}	0.5	86400	3.82×10^{15}	84×10^{-3}	0.69×10^{-10}
Set 3				3.47×10^{10}	4680	0.69×10^{-10}
Set 4				3.47×10^{14}	4680	0.69×10^{-10}
Set 5				3.47×10^{12}	46.80	0.69×10^{-10}
Set 6				3.47×10^{12}	468000	0.69×10^{-10}
Set 7				3.47×10^{12}	4680	10^{-12}
Set 8				3.47×10^{12}	4680	10^{-8}

The initial concentration of the MAL molecules is also an important parameter to consider. A typical molecular density of MAL molecules in the cream is typically considered to be around 10^{20} cm^{-3} [181]. Previous simulations presented in this thesis (chapter 3) assumed a uniform number density of around 10^{14} cm^{-3} (figure 1.4). By assuming that the concentration at the most superficial layers will be considerably lower than the cream concentration itself, a value of C_0 was assumed in this work to initially be somewhere between the two extremes discussed above. As an initial guess, C_0 was therefore suggested to be $6 \times 10^{16} \text{ cm}^{-3}$. The conversion from MAL molecules to PpIX molecules is also affected by the yield, ε_p , where values between 0.03-0.5 have been suggested. Following the work by Salas Garcia et al, this was initially set to be 0.5 (50 %) [168, 181].

The limited knowledge about these important parameters invites for parameter exploration, where the contribution of different parameters can be determined. The parameters of interest can be grouped together to reduce the unknown constants from five to three such that,

$$\text{PPIX}(z, t) = A \int_0^t e^{-\frac{t-t'}{\tau_p}} \left(1 - \text{erf}\left(\frac{z}{\sqrt{4Dt'}}\right)\right) dt' \quad (4.9)$$

The first three constants in equation 4.8, $\frac{\varepsilon_p C_0}{\tau_{ap}}$ were grouped into one constant A (equation 4.9). It is clear from A that reducing the initial concentration C_0 has the same effect to the

distribution model as an increased relaxation time, τ_{ap} , or indeed a reduced yield, ϵ_p . These three parameters (A, τ_p and D) were first adjusted independently to determine the individual contribution to the PpIX distribution. Table 4.2 displays the different values for the parameters that were explored. Subsequently the parameters were logically adjusted to match the linear fluorescence model describing the clinical data in chapter 6. See section 4.3.5 for further detail of this implementation.

The concentration and treatment depth was explored for different sets of parameters applied to equation 4.9 (table 4.2). Longer treatment times up to 2.5 hours (370 J cm^{-2}) were also explored as well as the effect of different incubation times during daylight PDT.

4.3.5 Fluorescence code implementation

In an attempt to further gain knowledge about the parameters that are under consideration a MCRT model was generated to represent the situation described in chapter 6. By simulating the fluorescence signals that were measured during the occlusive treatment and by adjusting the parameters discussed above, the simulation was matched to the clinical results. This results in determination of a set of parameters that reproduce the experimental results.

The fluorescence spectrum generated in the model was sampled from an experimentally measured fluorescence spectrum (figure 4.2). Similarly to the experimental validation (section 2.5.2) the excitation photons were launched through a small area (diameter of $600 \mu\text{m}$) representing the optical biopsy (OBS) fibre probe (section 2.5.1) and the resulting fluorescence signal was collected through the same region with a numerical aperture of 0.22. It was assumed that each absorption event (by the PpIX) resulted in an isotropic fluorescent photon, i.e. the fluorescence yield was assumed to be one. Due to the narrow spectrum of the OBS it was also assumed that the illuminating light was of a single wavelength (405 nm).

The strength of the recorded signal by the OBS is arbitrary since it depends on the irradiance of the light source and the sensitivity of the measuring equipment. The fluorescence MCRT model is also arbitrary since the strength of the resulting fluorescence signal depends on the number of simulated photons as well as the fluorescence yield (assumed to be 1). As a consequence it is only appropriate to explore the normalised fluorescence signal (generated by the MCRT model) with a linear trend where the signal increases from 0 to 1 over 180 minutes.

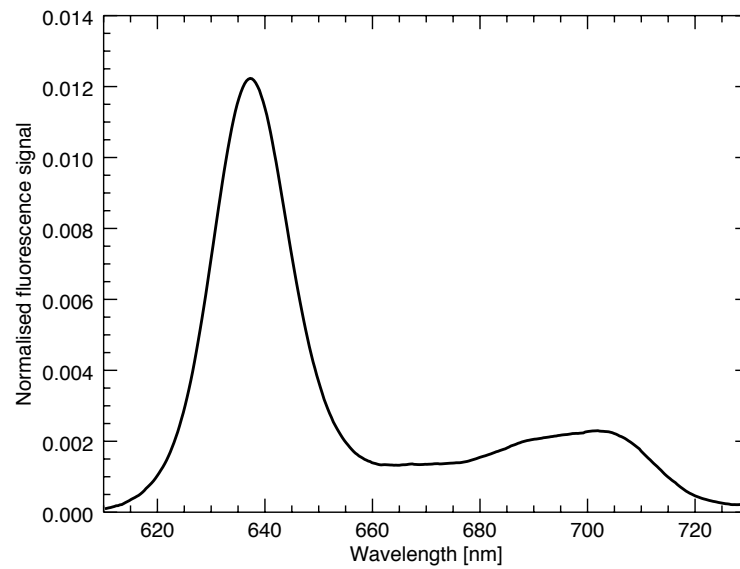


Figure 4.2: Fluorescence signal generated by the PpIX, normalised by the total fluorescence signal.

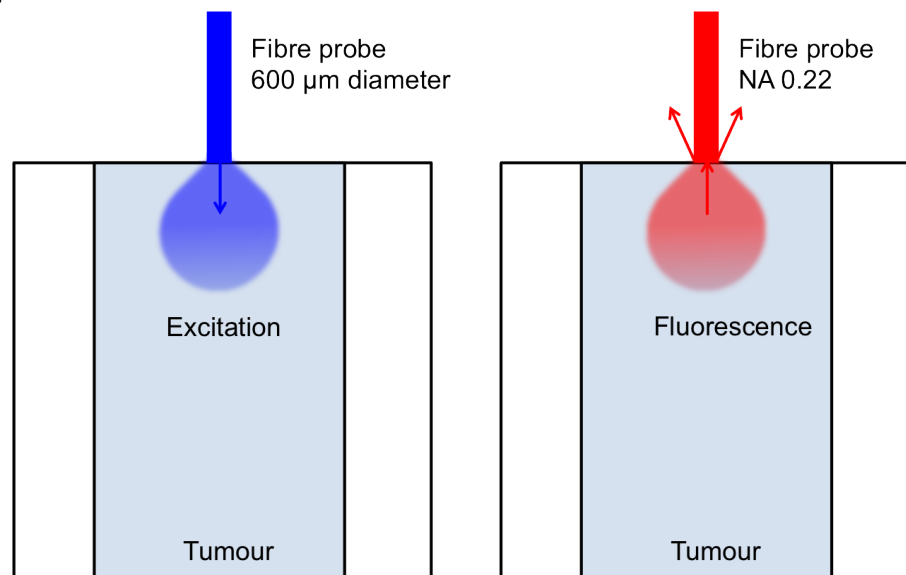


Figure 4.3: Graphical representation of the fluorescence modelling. The PpIX is excited with blue light (405 nm) (left) and re-emits red fluorescence light (figure 4.2) (right)

The parameters (table 4.2) that were used to generate different spatial and temporal distributions of PpIX, were also used to generate the fluorescence signal. The peak of the fluorescence signal was plotted as a function of time and compared to the linear model. By determining the effect that the different sets of parameters (table 4.2, equation 4.9) had on the evolution of the fluorescence signal, values of the parameter that fit the linear model better could be determined. To establish if this results in reasonable effective treatment depths, the photo-toxicity during the light treatment phase was subsequently generated.

4.4 Results

By applying the different sets of parameters, shown in table 4.2, to the PpIX distribution model derived from equation 4.9, a range of different distributions were achieved. The results after 30 min, 1 hour and 3 hours of incubation are illustrate in figure 4.4. The 30 minute time point is, as previously discussed, a typical incubation time for daylight PDT following application of the cream, while 3 hours is the incubation time adopted for conventional PDT. The same distribution of PpIX is assumed in the horizontal plane throughout the tumour area, illustrated in figure 4.5. All sets of parameters are compared to the reference set (set 1, table 4.2) since they have been adjusted accordingly. When A is increased simultaneously as τ_p was reduced (set 2), the resulting concentration profile is comparable to the reference set. However the rate at which the PpIX builds up within the tissue is slightly faster and the differences between the two concentrations profiles increases with time. When A , in equation 4.9 is reduced (set 3) or increased (set 4), the concentration profile is scaled accordingly. For increased and reduced τ_p , the concentration profile is not scaled linearly due to the nature of the model. A reduced τ_p (set 5) results in a lower overall concentration of PpIX compared to set 1. The reduction of τ_p results in a small increase in overall PpIX distribution over three hours of occlusive treatment. An increase (set 6) in the parameter results in a concentration of PpIX comparable to set 1. A reduced diffusion coefficient (set 7) resulted in shallow drug diffusion, with low concentrations of PpIX only present within superficial skin layers. Conversely, an increased diffusion coefficient (set 8) resulted in a more uniform distribution of PpIX. Overall, with time the PpIX distribution reached deeper layers within the tumour tissue which is shown in figure 4.4.

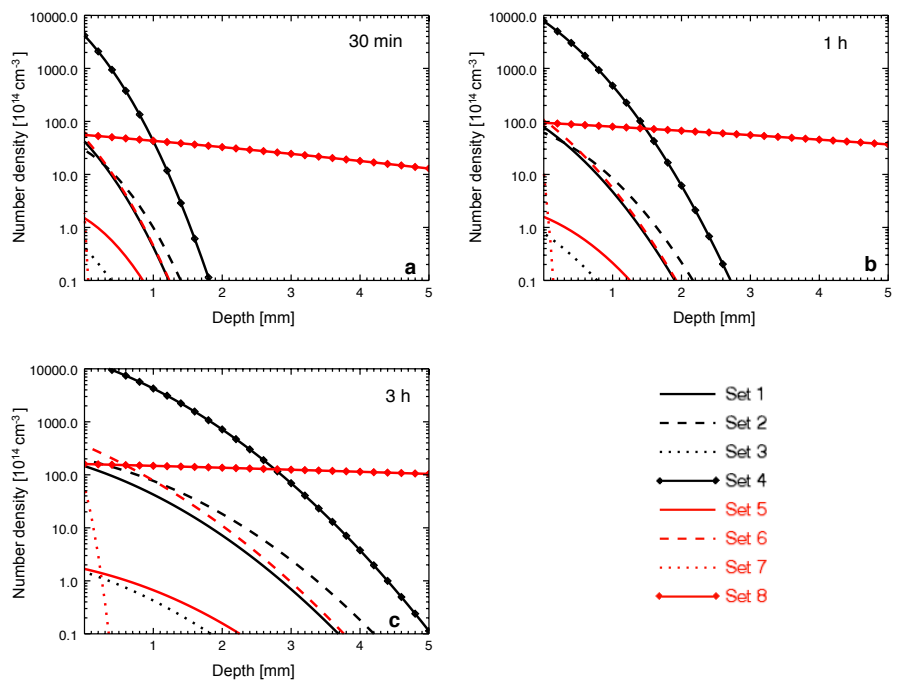


Figure 4.4: Figure showing the number density of PpIX molecules as a function of time for different sets of parameters (table 4.2). Results for three different incubation times are plotted, a) 30 min, b) 1 hour and c) 3 hours. This assumed no light interaction during the production of PpIX and these times are a measure from the time of drug application.

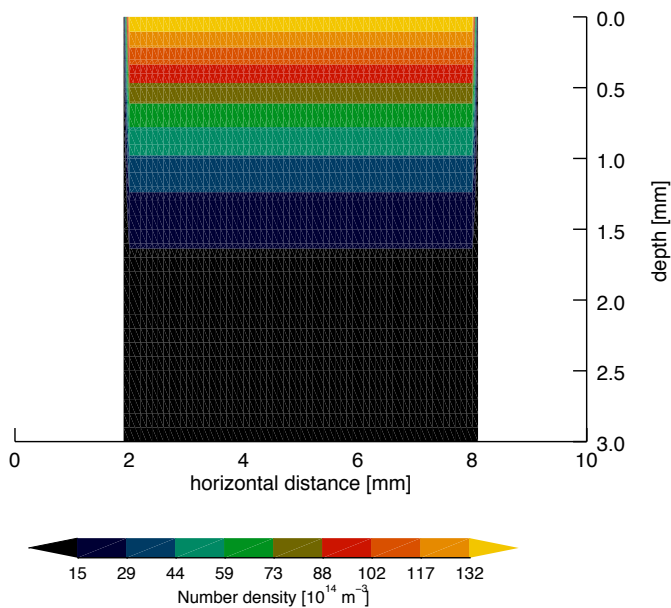


Figure 4.5: Contour plot of the cross section of the distribution of PpIX after 3 hours of occlusive treatment where the parameters in table 4.2 (set 1) were adopted.

The concentration of PpIX is reduced during treatment due to photobleaching. However during daylight PDT (for both clear and overcast conditions) the concentration simultaneously increases as a significant reservoir of the prodrug remains on the surface of the skin. For the uniform case described in chapter 3, the initial concentration of PpIX molecules was assumed to be $7.84 \times 10^{13} \text{ cm}^{-3}$, where the concentration only reduces due to photobleaching, for all different light sources. The change in concentration during the treatment from 0 - 75 J cm^{-2} for both the uniform (where the initial concentration of PpIX was assumed to be uniform) and the non-uniform case (where the initial concentration of PpIX was assumed to follow equation 4.8) were compared for the three different light conditions and the results are displayed in figure 4.6. For the uniform case, the concentration reduction with increased light dose is similar in all light conditions. For the non-uniform case there is a larger difference between the light conditions. Where for example daylight PDT during overcast conditions resulted in overall larger concentrations of PpIX within the tumour tissue compared to treatment during clear conditions. For daylight PDT, PpIX is produced during the light treatment which generates a different reduction in PpIX distribution compared to the conventional PDT situation.

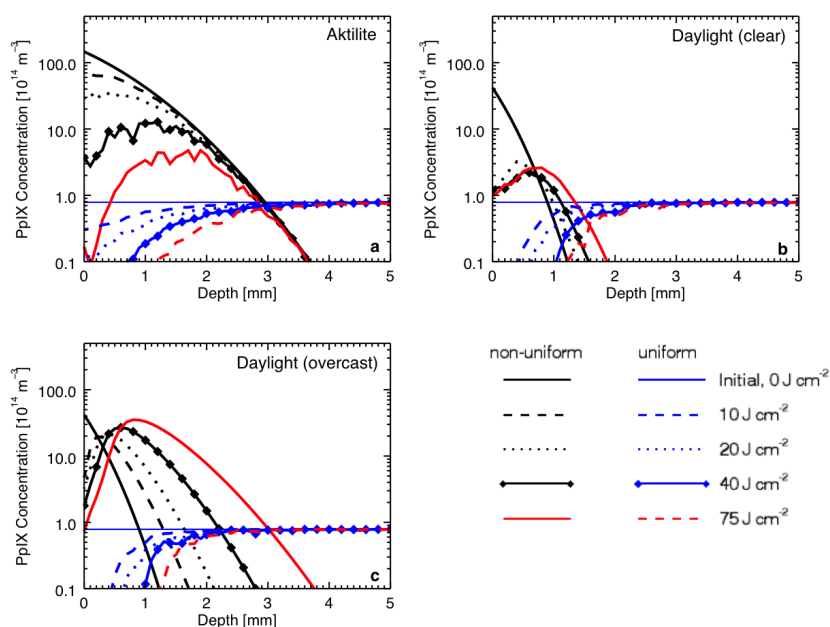


Figure 4.6: Graphical representation of the change in PpIX distribution during the light treatment (set 1 in table 4.2 is adopted). Daylight PDT for overcast (c) and clear (b) conditions as well as conventional PDT (a) is compared for the uniform and non-uniform case. The uniform case is discussed in chapter 3, while the non-uniform case represents the model developed here using basic diffusion theory.

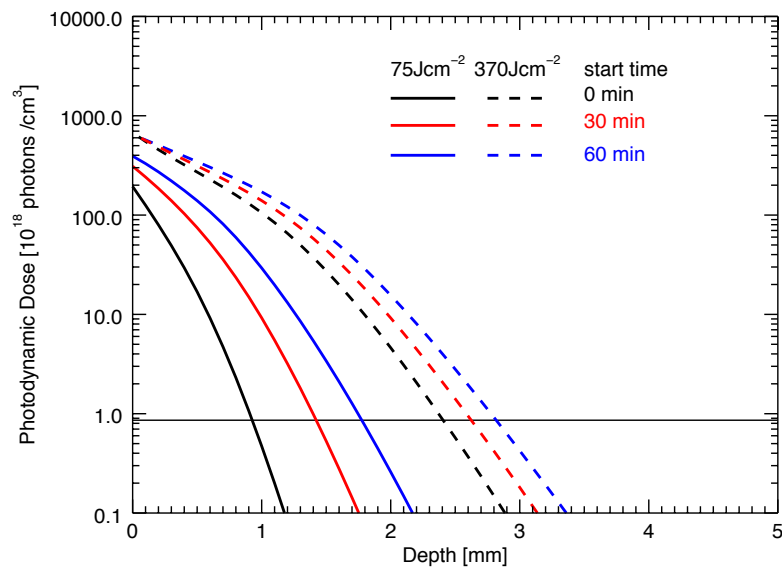


Figure 4.9: Photodynamic dose for different initial starting points (for daylight PDT during clear conditions). The black curves correspond to the situation where the lesion was exposed to the daylight simultaneously to the cream application while the blue curve corresponds to 60 min of incubation time before the lesion was exposed to the light source. The red curves corresponds to an incubation time of 30 min, which corresponds to the typical incubation time applied in the clinic and also the incubation time adopted for all other results (daylight) in this chapter.

When the initial set, set 1 in table 4.2, was compared to the uniform case, similar treatment depths were achieved as shown in figure 4.7. After a delivered light dose of 75 Jcm^{-2} treatment depths of approximately 3 mm were reached during conventional PDT conditions. After the same delivered light dose for daylight PDT during clear conditions, treatment depths of just under 1.5 mm were reached. Daylight PDT, during overcast conditions however reached treatment depth of approximately 2 mm. When the lesion of interest was simulated to be exposed to daylight for 2.5 hours (equivalent to 370 Jcm^{-2} during clear conditions) treatment depths of over 2.5 mm were reached. The results for this are illustrated in figure 4.8. The light doses 75 and 370 Jcm^{-2} were compared for different total incubation times for daylight PDT (clear conditions) and the results are displayed in figure 4.9. A difference in treatment depth of just under 1 mm was achieved after a delivered light dose of 75 Jcm^{-2} between occlusive treatment times of 0 minutes (cream applied simultaneously to light source) and 1 hour. After 370 Jcm^{-2} the difference reduced to approximately 0.5 mm.

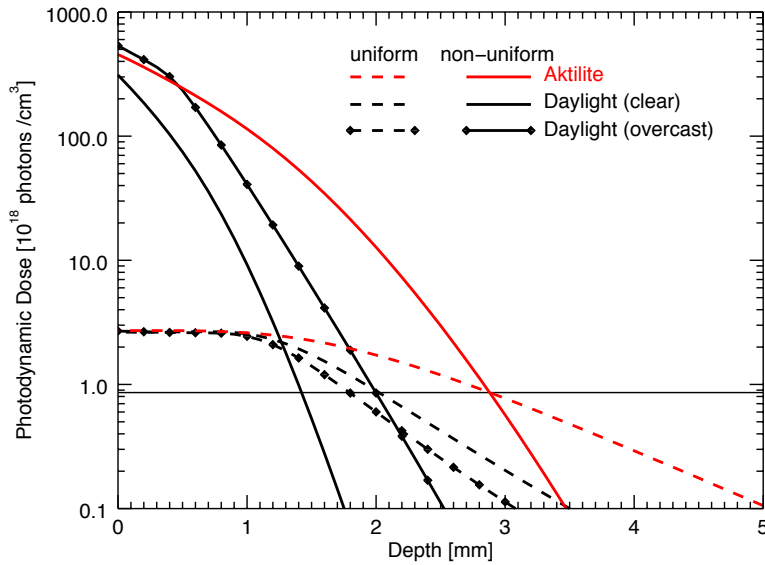


Figure 4.7: Photodynamic dose as a function of depth where the initial distribution of PpIX non-uniform (solid) and the uniform (dashed) are compared. The toxicity corresponding to a light dose of 75 J cm^{-2} is displayed for three light conditions: conventional PDT (Aktilite), daylight PDT (clear) and daylight PDT (overcast).

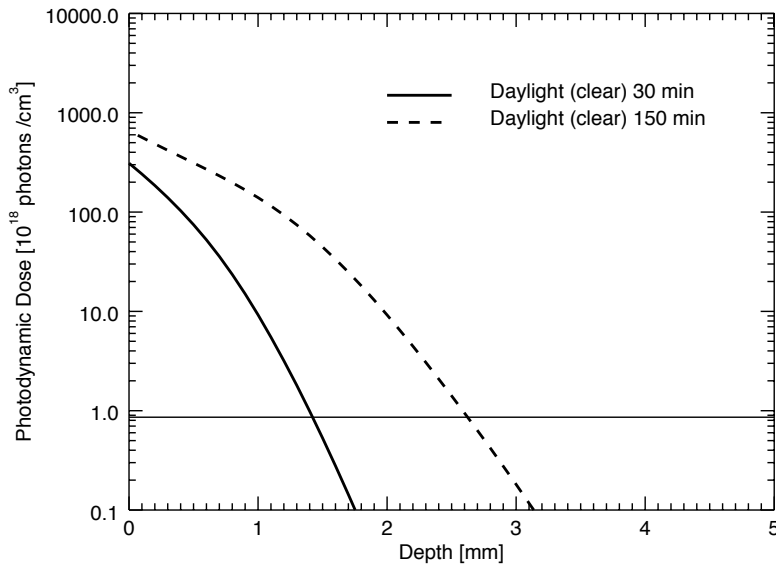


Figure 4.8: Photodynamic dose as a function of depth for daylight PDT (clear) for 75 J cm^{-2} (30 min) and 370 J cm^{-2} (150 min).

The photodynamic dose (PDD) was generated for the different sets of parameters in table 4.2 where both daylight PDT (clear and overcast) as well as conventional PDT was investigated. The results from the simulations show that the deepest penetration is achieved from set 4 and 8. The more shallow penetration depths were achieved by adopting parameters in set 3 and 7. The results are summarised in table 4.3. For further discussion and graphical representation see Appendix B.

Table 4.3: Summary of the results from the toxicity and fluorescence signal when adopting different sets of parameters from table 4.2. Parameter exploration allowed for the sets B1 and B2 to be determined. It is clear from the summary that the shape of the fluorescence signal as it changed with time is not directly correlated with the effective treatment depth. The treatment depths are summarised when the toxic threshold is adopted for the different light conditions, Daylight (clear) (DC), Daylight (overcast) (DO) and Aktelite (A).

Set	Adjustment	Treatment depth (mm)			Fluorescence
		DC	DO	A	
1	-	1.5	2	3	step initial increase
2	reduced τ_p increased A	1.5	2.5	3.2	similar to 1
3	reduced A	0.5	1	1.3	reduced initial steepness
4	Increased A	1.8	2.5	3.8	increased initial steepness
5	reduced τ_p	0.9	1.3	1.7	similar to 1
6	increased τ_p	1.4	2	3	similar to 1
7	reduced D	0.2	0.4	0.4	reduced initial steepness
8	increased D	3.3	3.8	N/A	similar to 1
B1	reduced A reduced D	0.1	0.4	0.4	best fit
B2	reduced τ_p	0	0	0	best fit

For the initial set of parameters (set 1, table 4.2) the change in the peak of the fluorescence signal with time was compared with the linear model established in chapter 7 (shown in figure 4.10). The fluorescence signal increased rapidly before plateauing after approximately 50 min. The fluorescence signal for the other sets of parameters (sets 2-8, table 4.2) were compared to the fluorescence signal generated by this reference set. The results from the fluorescence modelling are summarised in table 4.3. The most noticeable change in the

fluorescence signal was noticed for sets 3 and 7, where the initial increase in the signal was reduced. For further discussion and graphical representation see Appendix B.

Table 4.4: Parameters that best match the fluorescence data collected for chapter 6.

Set	A	τ_p	D
	$\text{cm}^{-3} \text{s}^{-1}$	s	$\text{m}^2 \text{s}^{-1}$
Set B1	3.47×10^{10}	4680	5×10^{-12}
Set B2	3.47×10^{12}	0.47	0.69×10^{-10}

4.4.1 Clinical study

The fluorescence signal was measured during the occlusive treatment in chapter 7. The characteristic red light produced as a result of blue excitation light was collected every 20 minutes for a total of three hours. Statistical modelling showed a linear trend between the fluorescence signal and the occlusive time. A more detailed description of the study can be found in chapter 7. To be able to gain more understanding of the production of PpIX within the tumour lesions the parameters in equation 4.9 were adjusted to generate the set of parameters that best fit the linear model (table 4.4). The peak of the fluorescence signal (from the theoretical results) as it changed with time for these sets (set B1 and B2, table 4.4) and the statistical model compared successfully as shown in figures 4.11 and 4.12. To determine if these sets of parameters are plausible further investigations were carried out. Using parameters B1 and B2 in table 4.4, the light treatment was simulated and the PDD was determined. For set B1 treatment depths of less than 0.5 mm were achieved, which can be seen in figure 4.13. For set B2 the treatment PDD is displayed in figure 4.14, where the applied threshold is higher than the achieved PDD. The concentration profiles generated by sets B1 and B2 (table 4.4) at 30, 60 and 180 min after cream application are displayed in figure 4.15. The results indicate that the distribution of PpIX reached only superficial layers where the overall concentration is low compared to sets 1-8 in table 4.2.

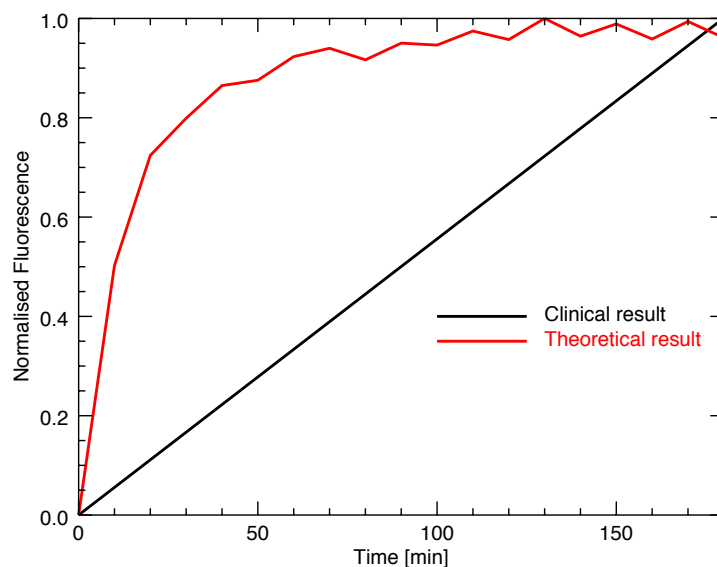


Figure 4.10: Figure showing how the fluorescence signal (red) changes with time for the first set of parameters (set 1) in table 4.2. The linear model (black) corresponds to the clinical results.

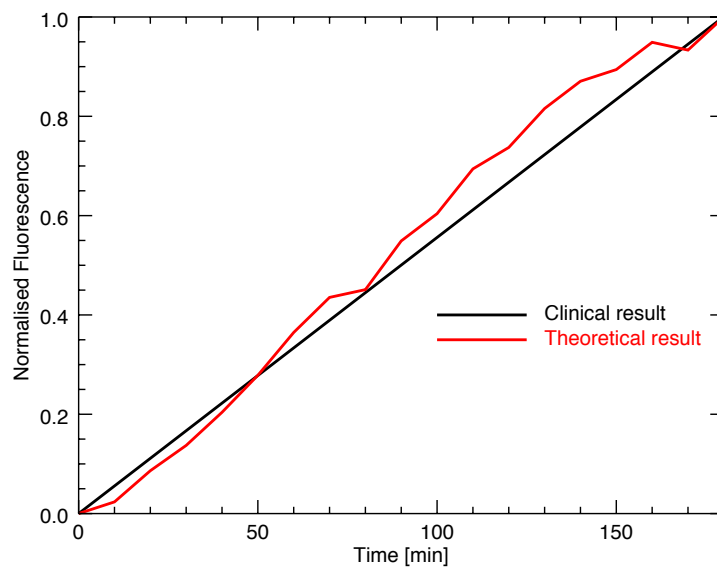


Figure 4.11: Figure showing how the fluorescence signal (red) changes with time for the first set of parameters (set B1) in table 4.4. The linear model (black) corresponds to the clinical results. This shows one of the best combination of parameters that were found to match the clinical results.

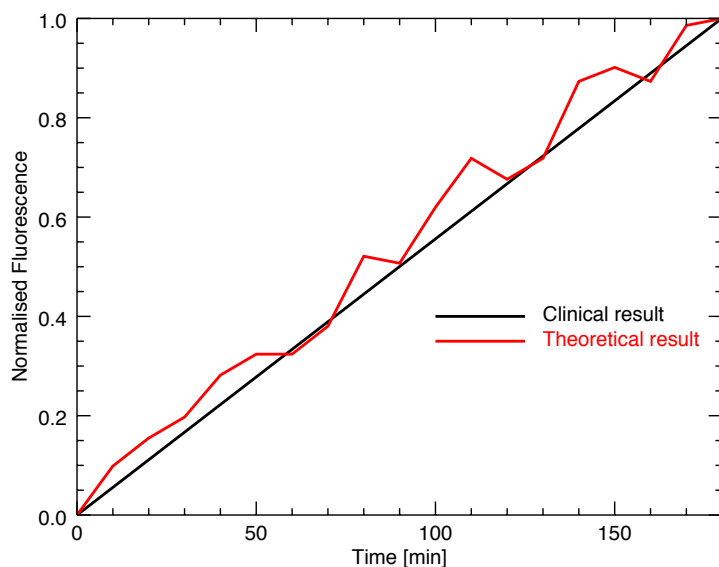


Figure 4.12: Figure showing how the fluorescence signal (red) changes with time for the second set of parameters (set B2) in table 4.4. The linear model (black) corresponds to the clinical results. This shows one of the best combination of parameters that were found to match the clinical results.

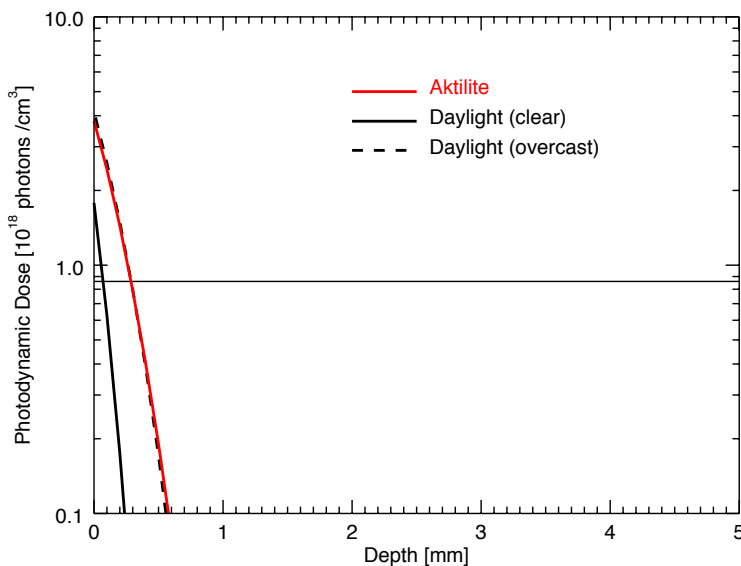


Figure 4.13: Figure showing the photo-toxicity as it changes with depth after 75 J cm^{-2} of delivered light dose where the parameters in set B1 (table 4.4) were adopted. The figure shows the same light conditions as previously been investigated. The figure shows a relatively low penetration compared to the uniform case investigated in previous chapter (chapter 3).

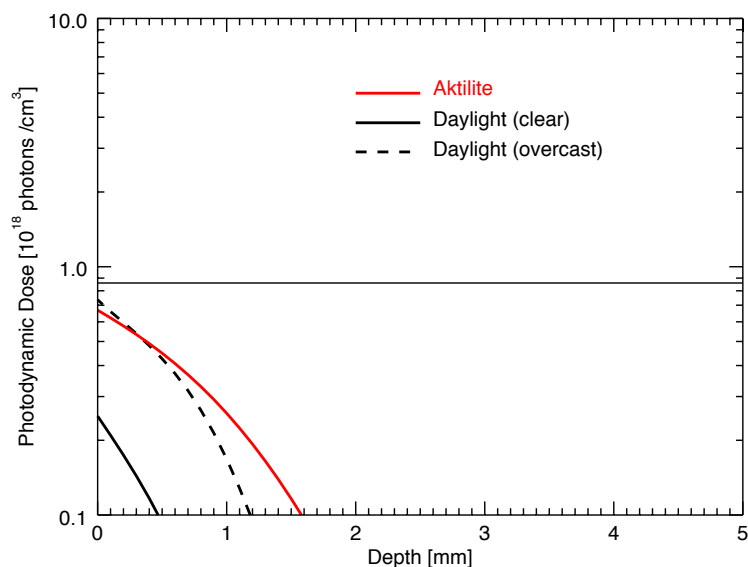


Figure 4.14: Figure showing the photo-toxicity as it changes with depth after 75 J cm^{-2} of delivered light dose where the parameters in set B2 (table 4.4) were adopted. The model presented indicates that this set of parameters results in a reasonable treatment depth, however the validity of the relaxation time τ_p could be argued.

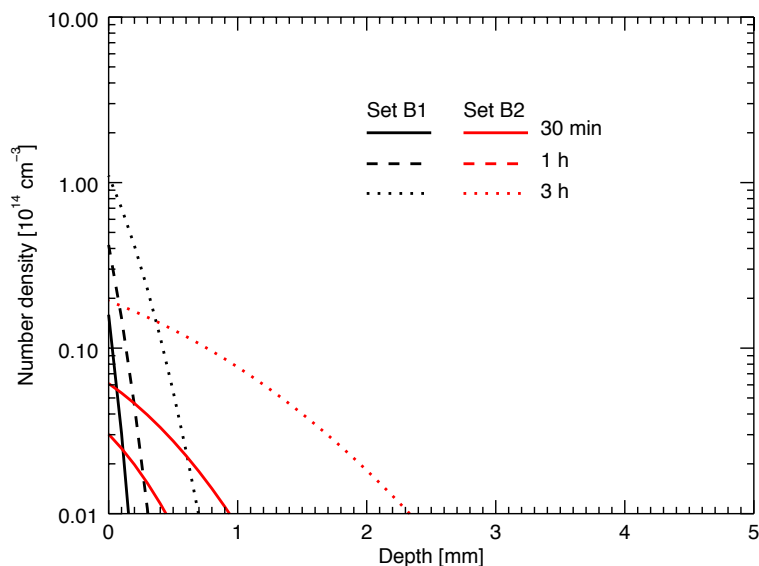


Figure 4.15: Figure showing the concentration after 30, 60 and 180 min of incubation time (no light interaction) for set B1 and B2 from table 4.4. These parameters produced the fluorescent signal from the MCRT model that matched the clinical set most favourably.

4.5 Discussion

It is clear from the investigation performed here, that without accurate knowledge of the different parameters: A , τ_p and D in equation 4.9, it is difficult to generate an appropriate distribution. Therefore the parameter exploration is important in terms of determining the contribution from the different parameters. During the light exposure the concentration reduces due to photobleaching, as demonstrated in figure 4.6. For the two daylight cases (clear and overcast) there is additional PpIX production during the light illumination. For clear conditions during daylight PDT figure 4.6 b demonstrates a large drop in concentration during the initial 10 J cm^{-2} for the non-uniform situation. This drop is larger than the drop for the same light dose for overcast conditions during daylight PDT (non-uniform case), shown in figure 4.6 c. Due to the difference in irradiance between these two weather conditions, the time it takes to deliver the same light dose of 10 J cm^{-2} corresponds to 2 min (clear) and 21 min (overcast). During this time, there is a larger amount of additional PpIX being produced, for the overcast situation compared to the clear situation. This explains the overall larger PpIX concentrations during overcast conditions.

The first set of parameters (set 1 in table 4.2) is what is believed to be a reasonable assumption of the parameters. For this reason this set is the most discussed and explored in this chapter. The results shown in figure 4.7 indicates treatment depths similar to the uniform case described in chapter 3, after a delivered light dose of 75 J cm^{-2} during conventional PDT. This indicates that these parameters result in realistic treatment depths. For daylight PDT the overcast treatment depth is larger than for the clear conditions when considering a total light dose of 75 J cm^{-2} . This feature is consistent for all parameters investigated and is explored in more detail in Appendix B. However when comparing the same treatment time (2.5 hours), the clear conditions results in deeper penetration. This is explained by the increased light dose delivered during 2.5 hours of illumination during clear (370 J cm^{-2}) conditions compared to overcast (75 J cm^{-2}) conditions. This is graphically demonstrated in figure 4.8.

Even though the treatment depths are varied, the fluorescence signal does not in general vary as much (table 4.3). When the relaxation time τ_p , in sets 5 and 6 in table 4.2, is changed the evolution of the fluorescence signal does not change from the initial set of parameters (set 1) however there is a change in effective treatment depth. For the situations where the fluorescence signal carries a closer resemblance to the linear trend, this resulted overall, in

more superficial treatment depths. The two sets of parameters that were found where the fluorescence signal favourably correlated to the linear trend (figure 4.11 and 4.12), resulted in superficial treatment depths as shown in figures 4.13 and 4.14. Even though the applied toxic threshold is an approximation, the light penetration for these two sets of parameters is confined to superficial layers. Hence there is reason to believe that these sets of parameters are not appropriate. In addition the relaxation time τ_p for set B2 in table 4.4 is approximately 0.5 s. This can be argued to be unreasonable since this would correspond to a faster clearance of PpIX than has previously been suggested in the literature [188]. Even though there might be other sets of parameters that match the linear trend as well as results in deeper light penetration these have not yet been found in the work presented here.

There are several potential explanations to why the set of parameter that matched the linear trend best, resulted in unreasonably low penetration depths. First of all the model developed in this chapter might not be sophisticated enough to be able to match the clinical results with the theoretical models. By simplifying the process of accumulating PpIX in the tumour, important information might be lost. It has been suggested in the literature that dose dependent rate equations should be used instead of first order kinetics when considering the production of PpIX since the conversion is controlled by an enzyme reaction. Due to the rate limitation of the process of producing PpIX, it is potentially important to include such aspects within the model [173]. However limited knowledge of these processes *in vivo*, discourages the application of such methods within the model presented here. As will be discussed in chapter 6, there is a possibility that the clinical data was affected by the degree of the surface preparation. By applying a deep curettage some of the measurements would be affected by the amount of blood produced as well as by the thin lesions remaining. Surface preparations are necessary to enable the cream to penetrate however the degree of curettage is varied between different institutes. Other aspects of the clinical study, might also have affected the measurements, such as exposure to light every 20 min. Further discussion of these issues may be found in chapter 6. For this reason alternative trends should not be discarded for future extended studies.

It is believed that the initial set, set 1 in table 4.2, is the most reasonable set of data strengthened by reasonable treatment depths. However these are approximations and the fluorescence signal generated from the models shows in figure 4.10 a steep increase at early times before plateauing. A possible explanation to the reason why the clinical results and the

theoretical results do not coincide is the tumour depth. The curettage associated with the clinical study could result in a shallow tumour depth. If the tumour is very superficial, a set of parameters resulting in a linear fluorescence trend (set B1 and B2) could be motivated. See chapter 6 for a further discussion of the level of curettage. Future developments have to include extension of the theoretical model as well as additional clinical studies where the level of curettage is considered.

By including a distribution of PpIX which changes both temporally and spatially, a more accurate theoretical representation of PDT may be obtained. By increasing the appropriateness of the model more accurate information can be gained from the resulting simulations. However, in the model developed here, several aspects of the PpIX production have not been considered for the sake of simplicity. It was assumed that the PpIX did not diffuse from the location where it is produced. It was also assumed that the concentration gradient of MAL molecules was not affected by the production of PpIX or photobleaching. To include these processes, a more complex model would be required where more parameters would have to be assumed and approximated. Additionally it was also assumed that the light penetration was not affected by the presence of cream on the surface of the lesion. If the optical properties of the cream were known, a thin layer of cream could be added to the simulation. However, due to lack of this information, it was not included in the model. Future developments of the model should consider the steps discussed above as well as the permeability of the cream through the skin. Here the permeability is ignored since it was assumed that the stratum corneum was broken up with a reduced functionality in the region of the tumour [53, 65, 174, 175]. It was additionally approximated that there was no difference between MAL or ALA based creams. Other aspects of the model that have not been included are the non-uniformity in the lateral direction (along the surface) as well as between different types of tumour positioned on different locations of the body [69].

The diffusion model presented here is a step towards a more accurate representation of the different treatment modalities. By adopting reasonable parameters for A , τ_p , and D in equation 4.9 such as the ones suggested in set 1 in table 4.2, the model indicates that the treatment depth is not only limited by the light penetration but also by the drug diffusion and PpIX production rate. These are important factors to consider when calculating and optimising PDT dosimetry. The work presented here is a step towards further exploring the limitations and potential of daylight PDT which can be a useful technique for situations when limited

resources are in place.

4.6 Conclusion

The incubation time associated with different treatment modalities results in different initial distributions of the photosensitive molecule PpIX. A non-uniform distribution of PpIX was investigated where a model was developed which depends on both the distance from the surface as well as the time passed since prodrug application. The main challenges are the limited knowledge about the cream diffusion and PpIX production which forces several assumptions and approximations. The work presented here explores the effect that these parameters have on the distribution of PpIX and the associated treatment depths. By including a non-uniform distribution of PpIX a more accurate representation of PDT was achieved. The results suggest that the treatment depths associated with PDT are not only limited by the penetration of the light but also by the penetration of the prodrug as well as the production of PpIX. Even though further investigation is required to establish the distribution parameters, the work presented here is a stepping stone towards more accurate theoretical simulations of PDT during different treatment conditions. Including a time dependent PpIX production model is key in driving the theoretical simulations of light based therapies forward.

5

Light distribution modelling of skin ageing and different skin types

5.1 Summary

It is important to adopt appropriate optical properties when modelling light distribution through skin tissue. This chapter discusses the techniques of generating the optical properties adopted throughout this thesis. By appropriately adjusting the optical properties and composition of a multi-layered skin phantom, different ages and skin types were represented. The results demonstrate the effect that different optical properties have on the distribution and penetration of light. The developed model shows that the light penetration increases with age and reduces with increasing skin type classification number. The results also indicate that daylight photodynamic therapy (PDT) is more affected by ageing and level of pigmentation compared to conventional PDT methods.

The work presented in this chapter contributed to the conference proceeding (Proc. SPIE,

volume 9531) "3D Monte Carlo radiation transfer modelling of photodynamic therapy" (2015) [189].

5.2 Introduction

The optical properties in skin tissue are inhomogeneous due to its complex structure and vary both within individuals as well as between individuals. The structure of the skin has previously been described in more detail in chapter 1 (section 1.2). In this chapter the optical properties and the method of how to represent different skin types and conditions will be discussed. The aim of this chapter is to demonstrate the effects that differences in skin optical properties and skin composition have on light penetration and PDT treatment outcome. This shows the importance of correct and appropriate allocation of the optical properties of the developed skin phantom.

5.2.1 Optical properties

Skin exhibits a wide range of optical properties due in part to the complex structure of skin and the variability that exists between individuals. Therefore the optical properties are not homogenous as previously assumed and will change for different people with different skin types. There are several publications of optical properties for different tissue types, both human and animal, both *in vivo* and *in vitro* [111, 112, 156, 190]. However to achieve appropriate optical properties for a large wavelength range and allow the optical properties to be flexible for representation of different skin compositions, appropriate estimating equations can be used.

Scattering

Scattering occurs when light interacts with the tissue which results in a change in direction of propagation. The change in direction is described by the Henyey-Greenstein phase function (equation 2.21) and the anisotropy factor (chapter 2). When light is scattered from the direction of a light beam, it reduces the intensity of light within the beam. The scattering is characterised by the scattering coefficient or the reduced scattering coefficient, both in the units of cm^{-1} . The reduced scattering coefficient μ'_s , corresponds to the scattering corrected by the anisotropy factor, g (equation 2.22), hence $\mu'_s = \mu_s(1 - g)$. Filamentous proteins, such as collagen and keratin within the skin tissue dominate the scattering in human skin.

A common way to compute the reduced scattering properties of skin tissue of a desired wavelength is by adopting power law functions that have been fitted to experimental data. Different power-law functions have been suggested in the published literature [112, 154, 155, 191, 192] and in this thesis two different equations have been used to compute the scattering properties.

In chapters 3 and 4 there was no need to distinguish between the epidermal and dermal layers. Hence the following equation was applied,

$$\mu'_s(\lambda) = C \left(\frac{\lambda}{\lambda_0} \right)^{-b} \quad (5.1)$$

where $\lambda_0 = 1$ nm and C and b have been experimentally determined [154, 155] to be, $b = 1.50$ and $C = 5.81 \times 10^5 \text{ cm}^{-1}$. However for the chapter presented here a multi-layered model was developed with distinct epidermal and dermal layers. An extension of the equation 5.1 was applied where both the contributions from Rayleigh and Mie scattering are considered [112, 191],

$$\mu'_s(\lambda) = C' \left(f_{\text{ray}} \left(\frac{\lambda}{\lambda'_0} \right)^{-4} + (1 - f_{\text{ray}}) \left(\frac{\lambda}{\lambda'_0} \right)^{-b'} \right) \quad (5.2)$$

Here f_{ray} corresponds to the fraction of Rayleigh scattering, hence $(1 - f_{\text{ray}})$ corresponds to the fraction of Mie scattering and the reference wavelength $\lambda'_0 = 500$ nm. Following the work by Iglesias-Guitian et al (2015) the values for the parameters in equation 5.2 stated in table 5.1 were adopted [191, 192]. The reduced scattering coefficient for the hypodermis can be determined using the following equation [190],

$$\mu'_s(\lambda) = 1050.60 \lambda^{-0.68} \quad (5.3)$$

In all the above equations the wavelength of light is expressed in the units of nm.

Table 5.1: Table with parameters adopted to compute scattering coefficients for epidermal and dermal layers (equation 5.2).

Layer	C' (cm ⁻¹)	f _{ray}	b'
Epidermis	66.70	0.29	0.69
Dermis	43.60	0.41	0.35

5.2.2 Anisotropy

All the scattering coefficients presented above are the reduced scattering coefficients. The anisotropy factor in skin tissue typically ranges between 0.7-0.9 and a recent publication by Jacques et al summarises current published values for g [112]. The g factor that was used in the majority of work presented in this thesis was published by Van Gemert et al (1989), where a wavelength dependent g was suggested such that

$$g = 0.62 + 0.29\lambda \times 10^{-3} \quad (5.4)$$

where λ has the units of nm [193].

Absorption

The absorption coefficient in a specific tissue can be expressed as the sum of all the contributions of the absorbing chromophores. It is common to include the main absorbers (blood and melanin) in combination with a background absorption to compute the total absorption [154, 155]. This results in a flexible, yet robust expression of the absorption. Chromophores other than blood and melanin tend to have minor contribution and variation and therefore it is convenient to combine them into this background absorption. By allowing the manipulation of the volume fraction of the main absorbers, different tissue types and conditions can be efficiently represented.

The two main absorbers within skin tissue that are considered here are as mentioned above, blood and melanin. However due to the lack of blood in the epidermal layers the sole main absorber in the epidermis is the melanin. The absorption coefficient for the epidermal layers can therefore be expressed as,

$$\mu_{a,epidermis}(\lambda) = f_{mel}\mu_{a,mel}(\lambda) + (1 - f_{mel})\mu_{a,back}(\lambda) \quad (5.5)$$

Where f_{mel} is the volume fraction of melanin within the epidermis [112], $\mu_{a,mel}$ is the absorption coefficient for melanin (cm^{-1}) and $\mu_{a,back}$ is the background absorption of human tissue (cm^{-1}), and is given by [154, 155],

$$\mu_{a,back}(\lambda) = 7.84 \times 10^8 \lambda^{-3.255} \quad (5.6)$$

The dominating absorbing chromophore in the dermal layers is the hemoglobin, since there is no melanin present in the normal dermis or hypodermis. The absorption coefficient for the dermal and hypodermis layers is therefore expressed by,

$$\mu_{a,dermis}(\lambda) = f_{blood}\mu_{a,blood}(\lambda) + (1 - f_{blood})\mu_{a,back}(\lambda) \quad (5.7)$$

where f_{blood} is the volume fraction of blood within the modelled tissue and $\mu_{a,blood}$ is the absorption coefficient for blood (cm^{-1}) [154, 155].

Blood

The main absorber of the dermal layer is as mentioned above the blood. The blood volume fraction within the dermis typically ranges between 0.2 % and 7 % [154]. The absorption for hemoglobin consist of both deoxygenated and oxygenated blood where the oxygen saturation level of the blood, S_{ox} determines the ratio between the two contributions such that

$$\mu_{a,blood}(\lambda) = S_{ox}\mu_{a,ox}(\lambda) + (1 - S_{ox})\mu_{a,deox}(\lambda) \quad (5.8)$$

Following the work by Iglesias-Guitian et al [191], S_{ox} is assumed to be 0.75 for the work presented in this chapter. The blood volume fraction was varied to appropriately represent different age groups. For the other chapters in this thesis the oxygen saturation was assumed to be 0.64 and the blood volume fraction 1.01% [154]. The $\mu_{a,ox}$ and $\mu_{a,deox}$ in equation 5.8 are the absorption coefficients, in units of cm^{-1} , for the oxygenated and deoxygenate hemoglobin respectively. The two contributions are graphically shown in figure 5.1 a.

Melanin

Melanin is the main absorber in the epidermal layers and the absorption coefficient for melanin is shown in figure 5.1 b. As demonstrated in the figure, the melanin has a strong absorption for shorter wavelengths and therefore provides protection against damaging ultraviolet (UV) light.

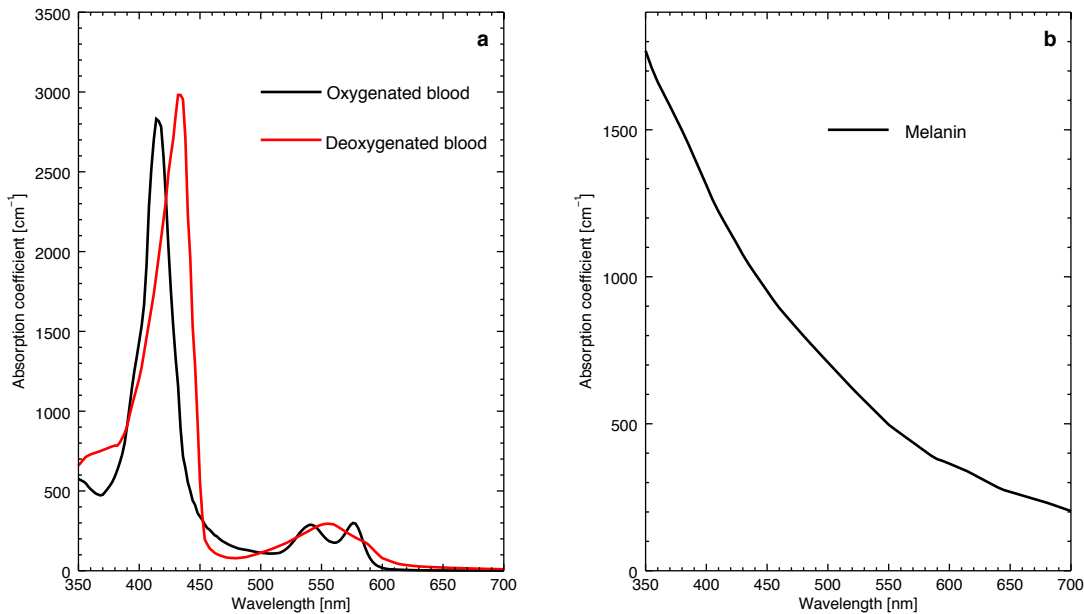


Figure 5.1: Absorption properties for melanin and blood. a) Absorption properties for blood within dermal layer: Both oxygenated and deoxygenated blood are displayed where the oxygen saturation determines the proportion of the two contributions to the total absorption coefficient b) Absorption coefficient for melanin within the epidermal layers [112, 154, 194, 195]







5.2.3 Skin ageing and pigmentation

The composition and structure of the skin changes with age and appropriate care of elderly skin has great medical importance [196]. The ageing of skin is a complex procedure that is due to both endogenous and exogenous factors. The endogenous factors include physiological and chronological changes that affect the skin, as it ages. The exogenous factors that contribute to ageing include UV radiation, toxins and infectious agents that can lead to structural skin damage and DNA changes [197]. Due to the medical implications it is important to understand how ageing changes the response to light based treatment such as PDT. The work presented here follows on from recently published work by Iglesias-Guitian et al [191] where the main changes in composition and structure due to ageing are included. The changes that were considered were thinning of the different skin layers (approximately 6-16 % reduction per decade [198]) and reduction of the main absorbing components in the skin: melanin (epidermis, approximately 8 % per decade [199]) and blood (dermis, approximately 6-10 %

per decade [200]). As well as ageing, different skin types [194] were investigated where the melanin content was adjusted appropriately.

The level of pigmentation, and thereby the appearance of the skin, varies between individuals. A higher level of melanin pigmentation results in a higher level of absorption and therefore higher protection against UV radiation (figure 5.1 b). Different levels of pigmentation are typically divided into different skin types [9]. Table 5.2 presents the different skin types in relation to the appearance of the skin.

Table 5.2: Skin type classification [9] displaying the appearance of the skin and the reaction to sun exposure. A lower skin type classification is associated with a stronger reaction to sun exposure, in the form of burning, due to the lack of melanin.

Skin type	Response to sun exposure	Appearance
I	Always burns, never tans	 white skin colour
II	Burns often, minimal tanning	 white skin colour
III	Burns sometimes, average tanning	 white skin colour
IV	Slightly burns, more than average tanning	 light brown skin colour
V	Rarely burns, tanned strongly	 brown skin colour
VI	Almost never burns	 dark brown skin colour

5.3 Method

In this chapter radiation transport was utilised (chapter 2) to investigate the light distribution for different optical properties. A multi-layered model was developed in an attempt to generate a more realistic and appropriate skin model. The effect of PDT was compared for different skin types and different ages by computing the toxicity and applying the same toxic threshold as in chapters 3 and 4. In the work presented here, the initial distribution of PpIX was assumed to be uniform since the focus on the work is the effect of different optical properties. The same light sources as in chapter 3 and 4 were simulated and compared. Both the fluence

rate as well as the photodynamic dose (PDD) was generated for conventional PDT (Aktilite) as well as daylight PDT. The different skin models generated for different ages and skin types are discussed below.

5.3.1 Skin models

As previously discussed in chapter 1 (section 1.2) the human skin can be divided into several different layers with differing structure and optical properties. The model presented here includes five separate layers of different tissue types. The different layers are presented in figure 5.2. The outermost layer is the epidermis which was divided into two sub-layers; the stratum corneum (SC) and the living epidermis (LE). The second main layer is the dermis, which was divided into two layers: the papillary dermis (PD) and the reticular dermis (RD). The final layer that was included in the model was the hypodermis, situated below the dermal layers. [6,196].

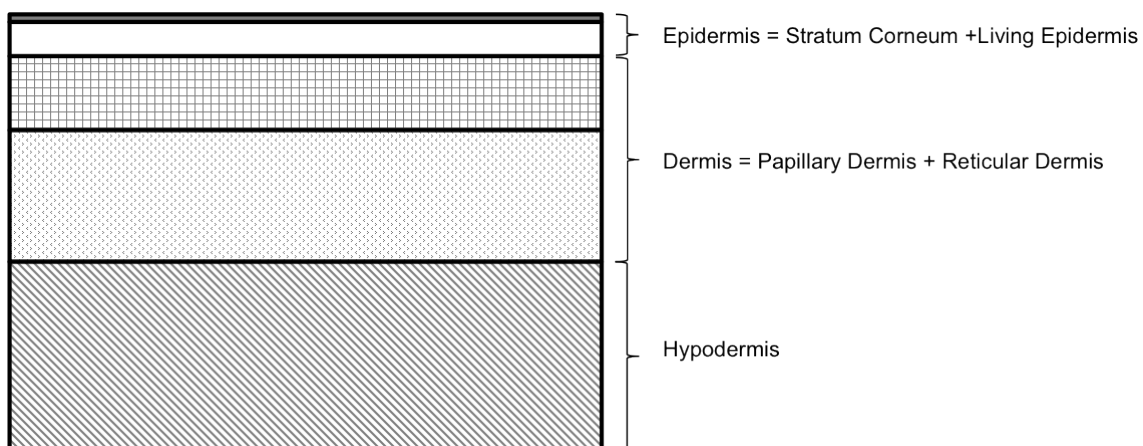


Figure 5.2: Figure representing the multi-layered skin phantom included in the theoretical model. The thickness and the blood/melanin content within the layers was adjusted accordingly to represent ageing and different skin types.

Table 5.3: Thicknesses of the investigated layers that were included in the skin model to represent ageing [191].

Skin layer	Thickness (mm)		
	Age (years)		
	30	55	80
Stratum Corneum	0.02	0.02	0.02
Living Epidermis	0.08	0.07	0.06
Papillary Dermis	0.18	0.15	0.13
Reticular Dermis	1.82	1.55	1.27
Hypodermis	2.90	3.21	3.52

Table 5.4: Input parameters that were used for the melanin and hemoglobin levels for the Living Epidermis (LE), the Papillary Dermis (PD) and the Reticular Dermis (RD). These parameters were used to compute the optical properties of the different skin layers to represent different ages and skin types. The hypodermal layer is assumed to contain 5 % of hemoglobin. The blood oxygen saturation was assumed to be 75 %. [191]. 30, 55 and 80 corresponds to the age of the patient (in years).

Skin type	Melanin and hemoglobin volume fraction (%)								
	Melanin (LE)			Hemoglobin (PD)			Hemoglobin (RD)		
	Age (years)			Age (years)			Age (years)		
	30	55	80	30	55	80	30	55	80
I	1	0.8	0.6	6	3.6	1.2	4.5	2.73	0.9
II	3	2.4	1.8	6	3.6	1.2	4.5	2.73	0.9
III	5	4	3	6	3.6	1.2	4.5	2.73	0.9
IV	10	8	6	6	3.6	1.2	4.5	2.73	0.9
V	20	16	12	6	3.6	1.2	4.5	2.73	0.9
VI	30	24	18	6	3.6	1.2	4.5	2.73	0.9

The dimensions of the code were set to be $5\text{ mm} \times 5\text{ mm} \times 5\text{ mm}$. The voxel based grid was not symmetric since higher resolution was required in the z direction (depth from the surface). Therefore $100 \times 100 \times 500$ grid cells were adopted for the work presented here. To represent a semi-infinite tissue slab, repeated boundaries were adopted (chapter 3). The refractive index between each layer does not vary significantly between the different tissue layers [191] and due to modelling resolution limitations the refractive index ($n = 1.38$) was

assumed to be uniform throughout the skin tissue. The boundary between the different layers were therefore only affected by the different optical properties. The thickness of each layer for the different skin models are presented in table 5.3. Table 5.4 shows the different input parameters used to determine the absorption properties (equation 5.5 and 5.7). The scattering properties for the different layers are shown in figure 5.3 a, where the scattering is assumed to not be affected by skin type or ageing (equation 5.2). The absorption properties for the epidermal layers are shown in figure 5.3 b-d, where only skin type I, III and VI are displayed for three different ages (see appendix C for remaining skin types). The absorption properties for the dermal and hypodermal layers are shown in figure 5.4 for three different ages (30, 55 and 80 years). It was assumed that these properties did not change with skin type.

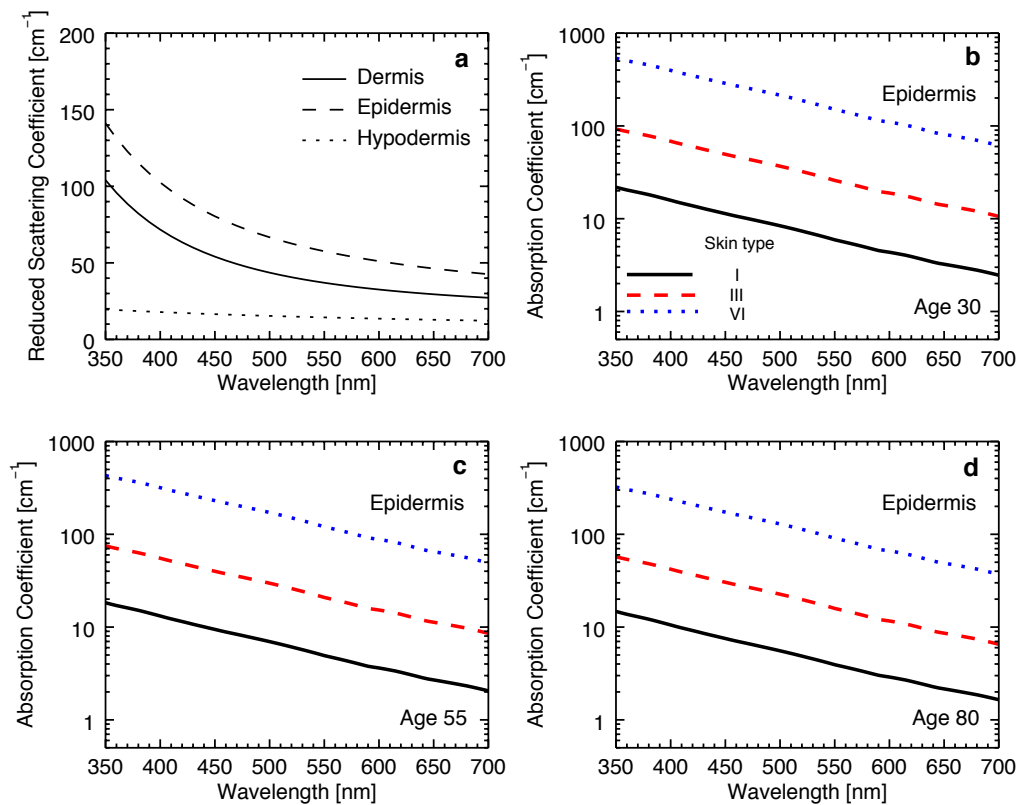


Figure 5.3: Figure showing the optical properties adopted in the MCRT model to represent different ages and skin types. a) Reduced scattering coefficients for the three main layers. These are assumed to be the same both for different skin types and different ages. The absorption properties for the epidermal layers are shown in the figure for three different skin types: I(black), III (red) and VI (blue) for three different ages b) 30 years, c) 55 years and d) 80 years.

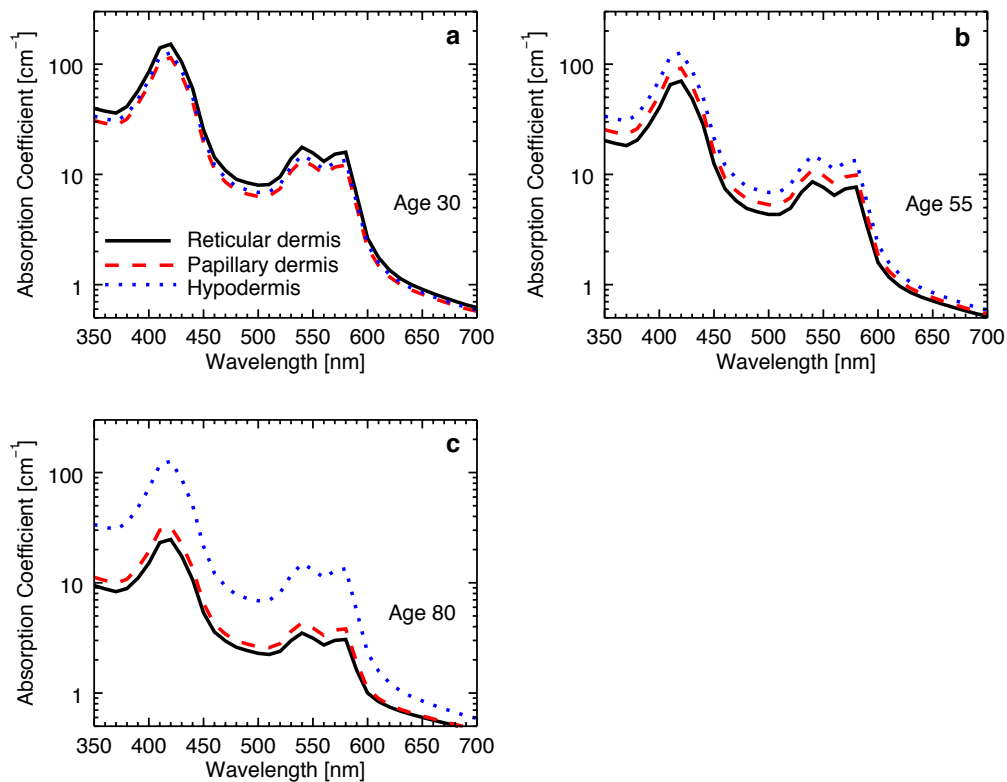


Figure 5.4: Figure showing the absorption properties of the dermal and hypodermal layers adopted in the MCRT model presented. The absorption properties of the dermal and hypodermal layers are assumed to not change with skin type however the effects of ageing are shown in the figure. The different ages that are compared are: a) 30 years, b) 55 years and c) 80 years.

5.4 Results

The penetration of light depends strongly upon the illuminating wavelength due to the wavelength dependency of the optical properties (figures 5.3 and 5.4). To demonstrate this, the fluence rate was generated for three different wavelengths (405, 540 and 630 nm). The effect of the light penetration for the different wavelengths for three different skin types and two different ages are shown in figure 5.5. The remaining skin types can be found in appendix C. The fluence rate describes the distribution of light within the skin tissue and indicates the effect of the investigated changes on the penetration depth. The fluence rate reduces with increasing skin type number and increases with age. The different 'kinks' in the fluence rate is due to the light propagation through the different tissue layers. The change in optical properties

between the different layers result in different propagation properties in the different layers.

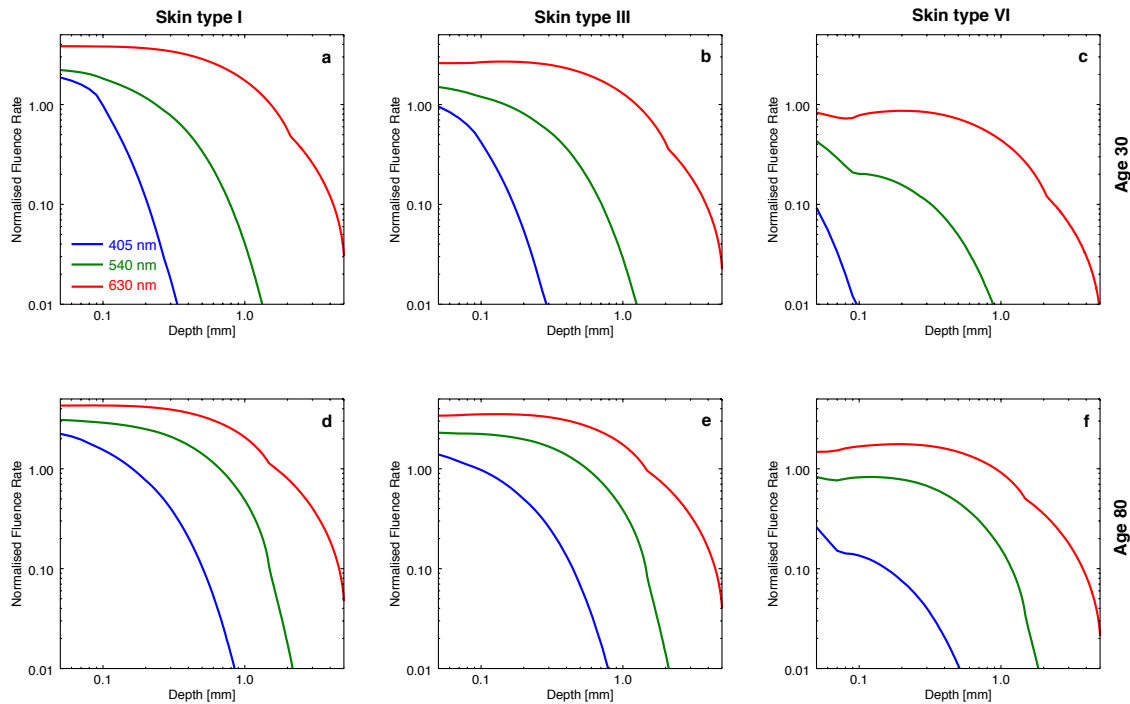


Figure 5.5: Figure showing normalised fluence rate (ψ/ψ_0) as a function of depth for different ages and skin types. The normalised fluence rate is defined as the fluence rate divided by the incident irradiance. Each figure demonstrates fluence rate for a certain age and skin type where three different wavelengths were investigated: 405 nm (blue), 540 nm (green) and 630 nm (red). The figures each correspond to the fluence rate for a) skin type I, age 30, b) skin type III, age 30 c) skin type VI age 30 d) skin type I, age 80, e) skin type III, age 30 and d) skin type VI age 80.

The effects of ageing and different skin types on PDT are displayed in figure 5.6. Here the PDD for (only) 75 J cm^{-2} is shown, since this is believed to be a common light dose delivered during conventional PDT. The three different light conditions that are compared is the Aktelite (conventional PDT) and daylight during two weather conditions, clear and overcast. For conventional PDT the light dose of 75 J cm^{-2} corresponds to 15 min of light exposure while the same light dose for daylight corresponds to 30 min (clear) and 150 min (overcast). Similarly to the fluence rate the light penetration and therefore treatment depth increases with age and reduces with skin type classification number. A higher skin type classification corresponds to a larger amount of melanin and therefore, the resulting treatment depth reduces with skin type. Both blood and melanin content are reduced with age, which results in an increase of light penetration. The difference between age 30 and 80 (figures 5.6 a and c) is approximately 0.5 mm for skin type I for daylight PDT (clear), while the same difference in ageing for skin

type VI corresponds to a difference in treatment depth of over 1 mm (figure 5.6 g and i). The graphical representation of the excluded skin types can be found in appendix C

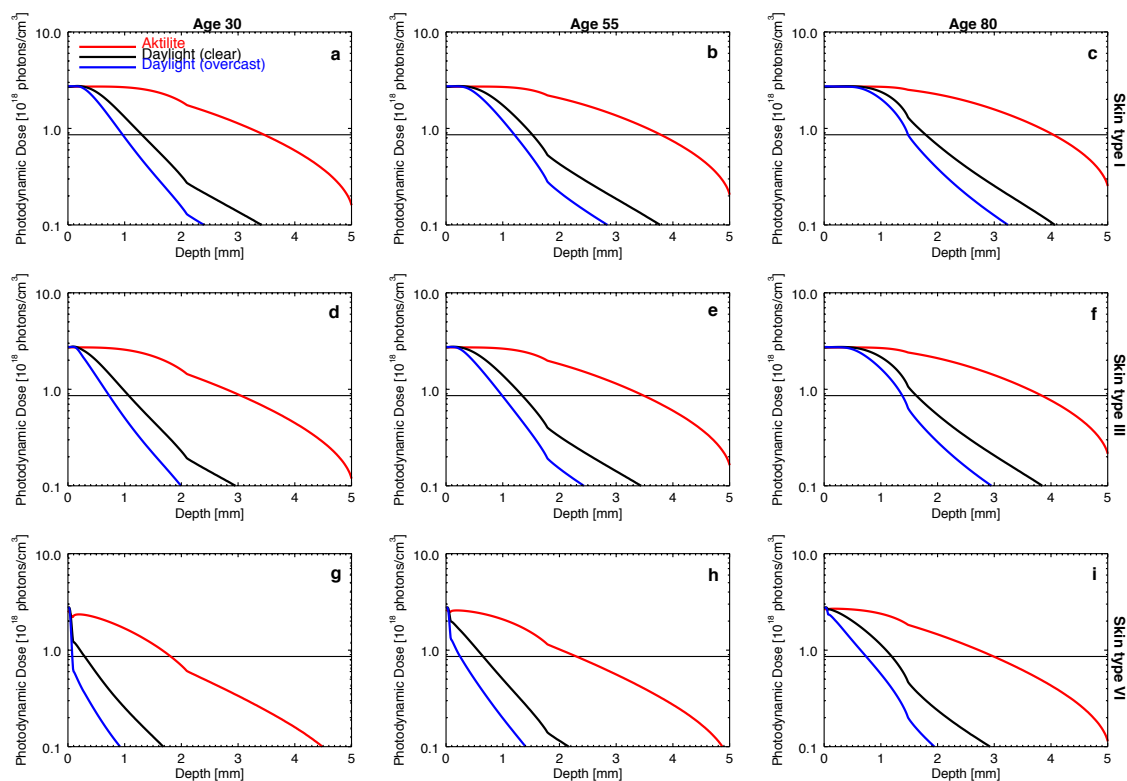


Figure 5.6: Photodynamic dose corresponding to 75 Jcm^{-2} for the different light sources at age 30, 55 and 80 and for skin types I, III and VI. Three light sources were compared: daylight for clear conditions (black), daylight during overcast conditions (blue) and the artificial light source, Aktelite (red). The results show the change in effective penetration depth with age and skin type. The horizontal line corresponds to the adopted toxic threshold, which is the same threshold adopted in previous chapters. The different figures correspond to: a) skin type I, age 30, b) skin type I, age 55, c) skin type I, age 80, d) skin type III, age 30, e) skin type III, age 55, f) skin type III, age 80, g) skin type VI, age 30, h) skin type VI, age 55 and i) skin type VI, age 80.

The different light conditions were compared and the results are summarised in table 5.5. When comparing the different light sources, the results from the simulation suggest that the largest effects in terms of treatment depth are associated with the overcast daylight conditions while the smallest effects are associated with the conventional artificial light source (Aktelite). This is explained by the different spectral distribution of the different light sources (figure 3.4). Since the daylight covers the blue wavelength range, the reduction due to melanin and blood affects the penetration of the daylight more strongly compared to the red conventional light source.

Table 5.5: Table showing the effective treatment depths generated from the MCRT simulations for different skin types and different ages. The different light conditions that are compared are: Daylight, during clear conditions (DC), daylight during overcast conditions (DO) and the Aktelite (A). It is clear from the table that the increase due to age is more significant for daylight PDT (DC and DO). The effects due to skin type is also more significant due to daylight.

Skin type	Effective treatment depth (mm)					
	30 years			80 years		
	DC	DO	A	DC	DO	A
I	1.3	1.0	3.5	1.8	1.5	4.1
VI	0.3	0.1	1.8	1.3	0.7	3.0

5.5 Discussion

The results presented in this chapter, demonstrate the effect on light distribution and toxicity for different skin tissue types for skin corresponding to different ages. The effective treatment depth associated with the toxic threshold is shown to increase with age and decrease with increasing skin type classification number. The deeper treatment depths are associated with older patients of lighter complexion, which is the most common patient group undergoing PDT [17]. A lighter complexion contains lower levels of melanin which results in a deeper light penetration. A higher age corresponds to skin tissue with lower levels of both blood and melanin, which both contributes to a deeper penetration. The reduction of thickness of epidermis and dermis also contributes to the deeper penetration associated with this skin model. The reduction of melanin and blood will have a larger effect on the blue part of the spectrum and this is the reason why the daylight which covers a large wavelength range is more strongly affected by ageing and skin pigmentation.

The model presented here only investigates healthy tissue where no tumour structure has been included. The motivation for this is to show the effect of light penetration through different tissue types. There is limited knowledge of how the optical properties of tumour change with skin type and skin age. However future developments of this work should include confinement of PpIX into restricted areas for application of PDT as well as different surface conditions associated with ageing. Effects such as dryness, surface roughness and uneven pigmentations, which are typically associated with skin ageing has not been included in this work. The work presented here is also applicable to other light based therapies where the

range of ages and skin types is larger. One such area would be laser hair removal, where it would be of both interest and relevance to study a larger range of patient groups.

Different lesion locations will be associated with different thicknesses of the different layers included in the developed model [154,201]. So far no distinction has been made regarding location, however this is something that would be of interest to study further in future work. To enable this, accurate information of the thickness at different locations is required. Recent publications suggests that the rate at which the PpIX is produced in an older age group (65-85 years) is lower compared to a younger age group (18-54 years) [202]. This has not been considered in the work here, where the initial distribution of PpIX was assumed to be equal for all groups of patients.

It is clear from the results presented here that accurate information about the skin composition is important in combination with accurate allocation of optical properties. Even though differences will still exist between skin tissue of the same skin type and age, the presented work attempts to initialise a distinction between different groups of skin tissue with respect to both age and skin type. This categorisation can be further extended by including other features such as location, gender, race [201], appearance and tumour type. There will always be differences between human skin tissue, however this allows for some of the reduction of the errors associated with assuming a generic tissue structure.

5.6 Conclusion

This chapter discusses the relevance of different optical properties and how these can be efficiently determined. The optical properties were generated for the skin models in this way throughout this chapter unless otherwise stated. The importance of different optical properties have been demonstrated in this chapter by investigating the effects that different skin ages and skin types have on light penetration. It was found that the deepest effective treatment depth was associated with older skin groups of lighter complexion. Further studies should attempt to include more classification parameters to extend the range of investigated optical properties.

6

Photodynamic therapy through heterogeneous tumour tissue

6.1 Summary

The effects of three dimensional (3D) tumour structures on depth dependent fluence rates, photodynamic doses (PDD) and fluorescence images through Monte Carlo radiation transfer modelling (MCRT) of photodynamic therapy (PDT) are explored. The aim of this work was to compare the commonly used uniform tumour densities with non-uniform densities to determine the importance of including 3D models in theoretical investigations. It was found that fractal 3D models resulted in deeper penetration on average of therapeutic radiation and deeper treatment. For the fractal structures under investigation, an increase in effective treatment depth of 1 mm for conventional PDT and closer to 1.5 mm for daylight PDT was observed, when comparing to the equivalent smooth model. Wide field fluorescence images were simulated, revealing information about the relationship between tumour structure and

the appearance of the fluorescence intensity. The different models explored indicate that the 3D tumour structure strongly affects the spatial distribution of therapeutic light, the PDD and the wide field appearance of surface fluorescence images.

The work presented in this chapter contributed to the publication "Monte Carlo modelling of photodynamic therapy treatments comparing clustered three dimensional tumour structures with homogeneous tissue structures" in "Physics in medicine and biology" (2016) [203].

6.2 Introduction

The majority of previously published MCRT models of human tissue assume a uniform homogeneous density of tissue. Some models assume that the whole simulation region is of a single homogeneous tissue type [98, 99] while some introduce parallel layers representing different tissue types. However within these layers the tissue is assumed to have a uniform density distribution [119, 124, 204, 205]. Theoretical models that consider different tumours tend to include these in the form of geometrical shapes, such as squares, spheres and cylinders [101, 125, 126]. Geometrical cylindrical shapes have also been included in MCRT models to represent blood vessels, which has been adopted frequently when studying port wine stains [123, 133, 134]. Within these shapes, the density has still been assumed to be uniform. So far in this thesis, the simulation grids have been represented by different tissue types of uniform densities. Cylindrical tumours were explored in chapter 3 and 4 and a layered model was introduced in chapter 5. However within these parallel layers or cylindrical shapes, the tissue has been assumed to have a uniform density.

There are few studies that include 3D geometries that are not symmetric. Brain tissue has been explored, where complex 3D brain structures have been included as the propagating medium [128, 131]. Davis et al introduced a complex vessel network containing different shapes and sizes of blood vessels with the aim to simulate the depth dependence of vascular fluorescence in brain tissue. The study showed differences when compared to an equivalent homogeneous model. It was also shown that to accurately represent the depth dependent fluorescence, the individual vascularisation should be included [206]. To my knowledge there has been no investigation of the importance of including 3D structures within skin tissue when simulating PDT.

In this chapter, 3D effects are included in the form of fractal tumour structures with the

aim to investigate the effects that these have on the treatment outcome. Histological work by for example Scheibe et al [207] demonstrating the principle of reconstructing 3D tumour shapes from individual tumour slices indicates heterogeneous tissue. A typical slice of a nodular basal cell carcinoma (nBCC) is shown in figure 6.1. Additional histological samples have also demonstrated heterogeneous tumour tissue [208]. Therefore it can be argued that simulations of tumour tissue should incorporate these heterogeneities to provide more realistic representations. The aim of this work is to investigate the importance of including such heterogeneities. The work presented in this chapter does not adopt real tumour shapes since the aim is to investigate the effect that heterogeneous tissue has on the light penetration by investigating different degrees of density redistributions. By generating artificial tumour structures it is possible to compare heterogeneous models to an equivalent smooth model as well as to adjust the degree of structure within the heterogeneous simulation in an easy way. The work presented here is an initial step towards more detailed theoretical simulations of light interaction with skin tissue.

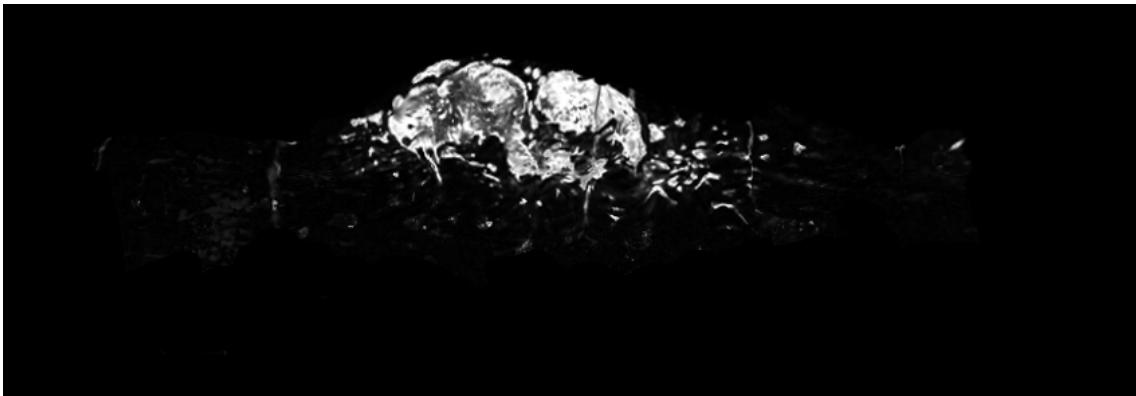


Figure 6.1: Image of a tumour slice demonstrating the heterogeneous tissue structure of a nodular basal cell carcinoma (nBCC). The dimension of this slice is 4.4×12.7 mm. The slice of tumour shown in this image comes from a paraffin embedded specimen (of a nBCC). The $6 \mu\text{m}$ thick slice underwent hematoxylin and eosin (H&E) staining and subsequently digital image processing. For more detailed information see [207]. Image was received from Patrick Scheibe as a result of research at TRM Leipzig [207].

6.3 Method

The MCRT code previously described (chapter 2) was adopted in this chapter to simulate light distribution through skin tissue. The same dimensions of the simulation region as demonstrated in chapter 3 were adopted, where each side of the simulation volume had the dimensions of 10 mm. In accordance with chapter 3 a cylindrical tumour was added, representing

the tumour tissue. The diameter of the tumour was assumed to be 6 mm and the depth from the surface was assumed to be 5 mm (figure 6.2). The tissue surrounding the cylindrical tumour volume was assumed to be uniform and of single (dermis) tissue type. The mass of the tumour was conserved but for the heterogeneous models the mass was regrouped within the cylinder to represent different tumour structures (section 6.3.1). The optical properties for the healthy tissue were assumed to be the same as those adopted in chapter 3. The average optical properties for the tumour tissue were also assumed to be the same as those previously adopted (figure 3.1). For the heterogeneous medium the tumour optical properties were assumed to scale linearly with the density such that the total attenuation coefficient was higher for regions of higher density. The concentration and distribution of the photosensitive molecule protoporphyrin IX (PpIX) was assumed to be proportional to that of the tumour tissue and was assumed to be restricted to the cylindrical region. The average number density of the PpIX was assumed to be $7.84 \times 10^{13} \text{ cm}^{-3}$ (identical to the uniform case investigated in chapter 3).

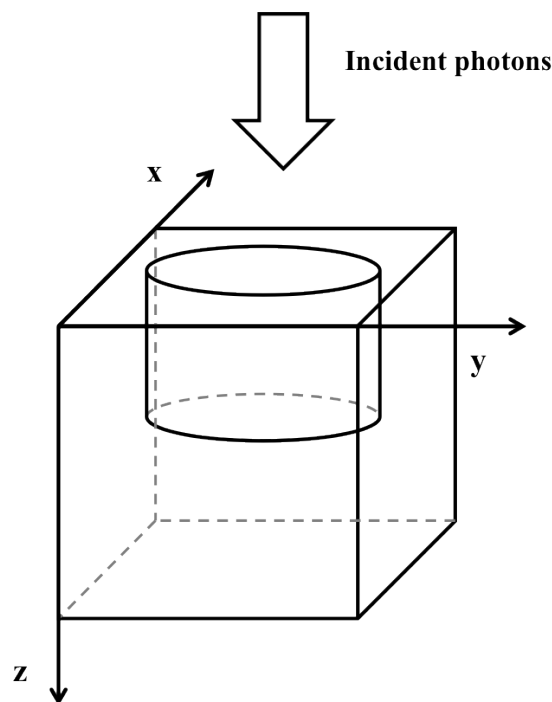


Figure 6.2: Drawing of the MCRT simulation region containing $100 \times 100 \times 100$ grid cells with the dimensions 10 mm on a side. The tumour was assumed to be centrally placed with a diameter of 6 mm and a depth of 5 mm from the surface. Photons were assumed to normally illuminate the surface of the grid.

6.3.1 Tumour models

Representations of non-uniformities within the tumour were introduced by adopting 3D fractal clustered structures. By regrouping the mass of the tumour into clusters in a fractal manner, a 3D structure was formed. The average density over the tumour region was consistent with a smooth equivalent model with a uniform density. The structures were generated following algorithms presented by Elmegreen [209] and is illustrated for a 2D case in figure 6.3. To determine the density of the new tumour models, separate hierarchical levels are set-up. For the first level, N_1 points are cast randomly within a 3D Cartesian grid with the x , y and z coordinates all taking values in the range $(0,1)$. At each subsequent level H , N_H points are cast around each point generated at level $(H-1)$, resulting in a clustered fractal model. The distance between the points at level H and $(H-1)$ decreases with increasing hierarchical level. The maximum distance from the previous level is expressed by,

$$\pm 0.5\Delta^{1-H} \quad (6.1)$$

where H is the hierarchal level and Δ is the dimensionless casting length which is determined through the fractal dimension such that,

$$f_{dim} = \log_{10}N_H / \log_{10}\Delta \quad (6.2)$$

where N_H is the number of points cast at level H . Figure 6.3 demonstrates the basics of the fractal structure that is built up through this routine in 2D. The points that are cast outside of the grid of unit dimensions are instead cast on the other side of the grid. If, for example a point is cast at $x = 1 + \varepsilon$, that point is instead given the x co-ordinate ε , since the x -boundary is set to be 1. The resulting density is proportional to the total number of points at the final hierarchical level cast in each voxel. In figure 6.3 the number of levels is three, hence the resulting density is proportional to the number of plus signs in each pixel (here a 5×5 grid system). The 3D grid of unit dimensions is thereafter mapped to the desired density grid such that the dimensions correspond to the simulated grid. In the case described here the clustered grid system is mapped onto a grid system containing $100 \times 100 \times 100$ voxels. The clustered structure is further restricted to the cylindrical tumour region (figure 3.2 a) by eliminating points located outside of this volume. The density within the cylinder is scaled to ensure that the total mass of the tumour is conserved.

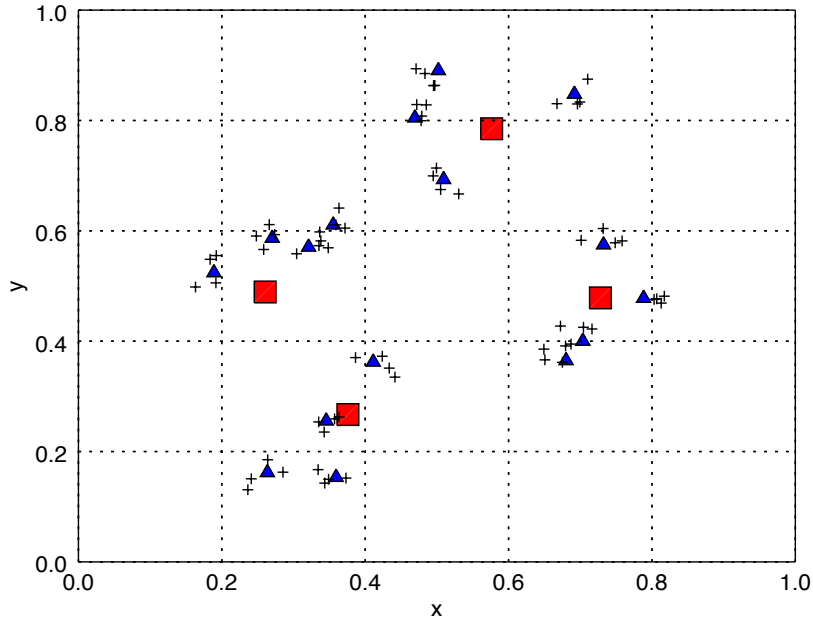


Figure 6.3: Demonstration of the clustered fractal model in two dimensions (2D). Three levels are generate for illustrative purposes. The first level (red squares) cast four random points within the 2D plane. The subsequent level (blue triangles) randomly cast four points around each point generated at the previous level, hence generating 16 new points. The third level (black pluses) cast four points around each point generated at the second level, hence generating 64 new points. Only the points cast at the final level contribute to the resulting density grid, hence only the number of pluses within each pixel (dashed lines) are considered [210].

A fraction, f_{smooth} determines the minimum density within each voxel and represented the density that cannot be resolved within the grid. The remaining fraction is distributed within the clustered fractal model. Hence f_{smooth} determines the minimum relative density present within the tumour region. This ensures that no voxels within the tumour region contains no mass (zero density) and thereby creating a void in the simulation region. For this reason the average density for a 100% smooth/uniform model (i.e. no mass redistribution) and for a model with a proportion of its mass redistributed is equal.

Six different tumour models were compared with the aim to investigate the importance of 3D effects as it changes for different degrees of clustering. For the work presented here both f_{smooth} and f_{dim} are varied to represent different degrees of heterogeneous behaviour. A larger f_{dim} results in a wider spread of the points cast at the final level of the fractal model. A smaller f_{dim} results in a tighter fractal structure containing smaller regions of higher densities. For this

reason, values for f_{dim} were chosen to be between 2 and 3. A large f_{smooth} results in a smaller variation in density between the clusters and the surrounding smooth component while a smaller f_{smooth} results in a larger difference. If f_{smooth} is high, the density distribution would be close to uniform. Conversely, if f_{smooth} is low then regions closer to zero density would appear. For this reason f_{smooth} values between 0.25 and 0.50 were chosen. The different parameters associated with the fractal models are summarised in table 6.1. The motivation for choosing these specific values is to allow for different degrees of heterogeneity to be investigated.

Table 6.1: Parameters used to generate different density structures representing different tumour structures. These values were only chosen to represent different degrees of heterogeneity.

Fractal model	tumour depth (mm)	f_{smooth}	H	f_{dim}	N_i
1	5	25 %	5	3	(16,32,32,32,32)
2	5	25 %	5	2.5	(16,32,32,32,32)
3	5	25 %	5	2	(16,32,32,32,32)
4	5	50%	5	3	(16,32,32,32,32)
5	5	50 %	5	2.5	(16,32,32,32,32)
6	5	50 %	5	2	(16,32,32,32,32)

To localise the tumour structure into the cylindrical region the first level of the fractal model was forced to only cast points within this restricted region. The first locations (x_1, y_1, z_1) were therefore determined as follows

$$x_1 = 0.3 + 0.4\xi_1 \quad (6.3)$$

$$y_1 = 0.3 + 0.4\xi_2 \quad (6.4)$$

$$z_1 = 0.5 + 0.5\xi_3 \quad (6.5)$$

Where ξ_1 , ξ_2 and ξ_3 are different random numbers drawn from a uniform distribution, in the range (0,1). This concentrated the redistribution of the density to a cuboid within the cylinder which can be argued to be a more realistic representation than a model where the points at the first level are randomly cast within the entire Cartesian grid.

For the different fractal density structures that are generated to represent different degrees of heterogeneities both the fluence rate for different wavelengths as well as the PDD was generated. To enable comparison with previous chapters in this thesis, both conventional PDT

(Aktelite) and daylight PDT (for clear and cloudy conditions) have been explored.

The fluorescence generated by the PpIX as a result of light illumination was simulated as previously described in chapters 2 and 4. In this chapter the wide field fluorescence was simulated, where a uniform illumination of 405 nm was assumed. The fluorescence photons were isotropically emitted from the absorption locations and allocated a wavelength from the PpIX fluorescence spectrum (figure 4.2). Fluorescence photons exiting the surface of the grid were recorded and binned according to location of exit. A numerical aperture of 0.22 was implemented allowing only photons exiting the simulation grid within a certain cone to be included within the resulting fluorescence grid. In chapters 2 and 4 only photons within a certain area corresponding to the fibre probe were collected. In the work presented here the wide field fluorescence is simulated, hence photons from the whole simulation region are included. By simulating the wide field fluorescence the intensity variation over the tumour structure can be investigated.

6.4 Results

Figure 6.4 shows cross-sections in both the vertical plane and the top slice of density structures 1 - 3 in the horizontal plane. Figure 6.5 show the same cross-sections for density structures 4 - 6. Figure 6.6 shows the density histograms for the different density structures. The histograms demonstrate the distribution of different densities over the whole tumour region. The bin size for each histogram is set to be 1 to ensure easy comparison. The minimum density within the allocated area is equal to f_{smooth} (table 6.1). The proportion of the voxels with a relative tumour density equal to this smooth component vary for the different structures. The density distributions demonstrated by the histograms are more affected by a changing fractal dimension (f_{dim}) compared to a varying smooth component (f_{smooth}). However a higher smooth component leaves a smaller amount of remaining mass to be distributed within the clustered features. A lower value for the fractal dimension (f_{dim}) results in tighter clusters and hence a large number of voxels are occupied by the smooth component. However a larger proportion of voxels contain higher densities compared to the more open structure associated with higher values for f_{dim} .

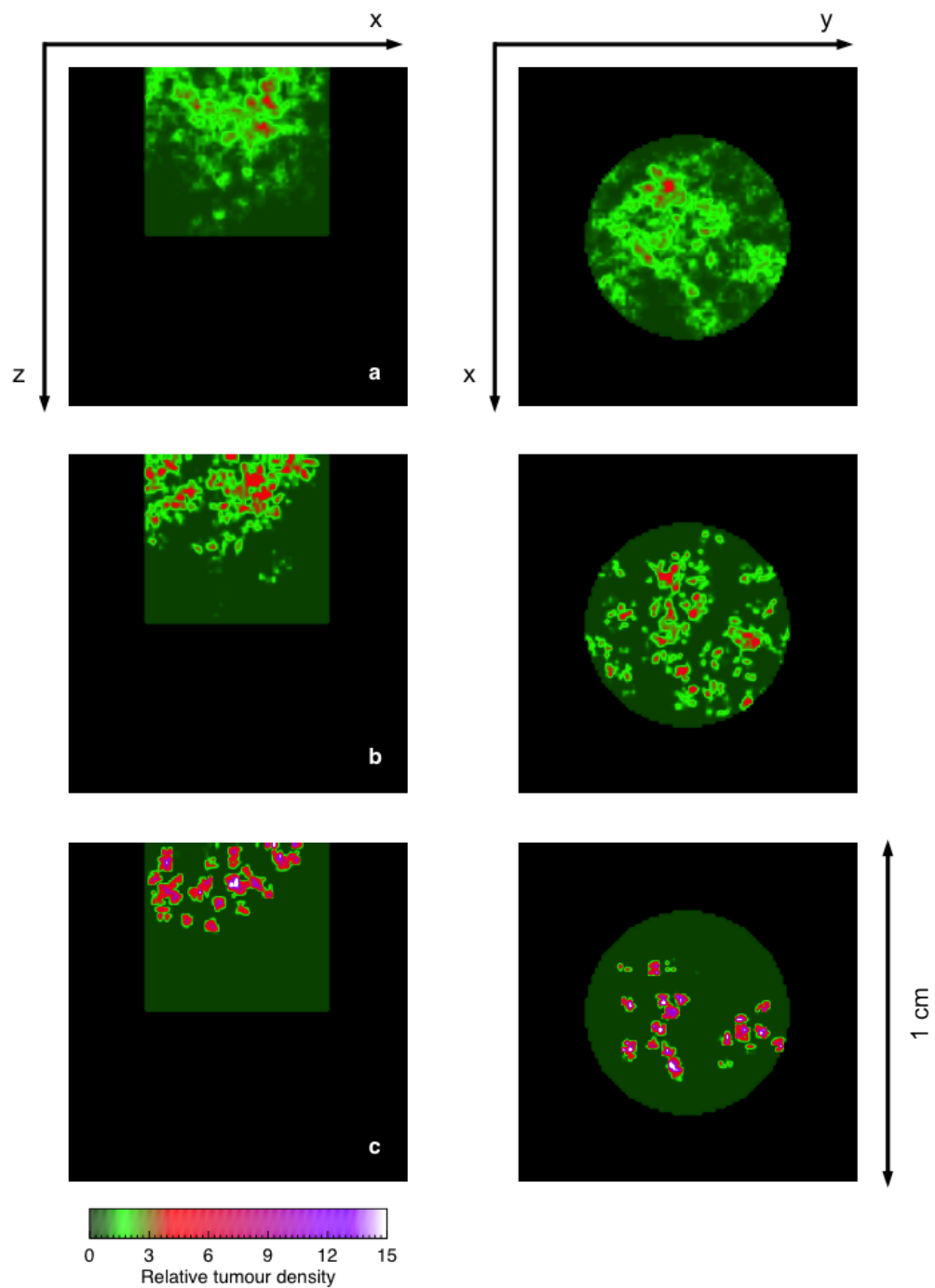


Figure 6.4: Figure demonstrating the density distribution of the different tumour models that are explored. The left column represents a slice in the x - z plane in the middle of the density grid. The right column represents a slice in the x - y plane at the top of the grid. The difference in the tightness of the clusters is caused by the variation of the fractal dimension such that a) $f_{dim} = 3$, b) $f_{dim} = 2.5$ and c) $f_{dim} = 2$. For all the structures in this figure $f_{smooth} = 0.25$ which corresponds to the minimum density in the tumour model and the amount of mass that is uniformly distributed through the tumour region. As the fractal dimension, f_{dim} , reduces the clustered structure becomes tighter with smaller areas of higher densities.

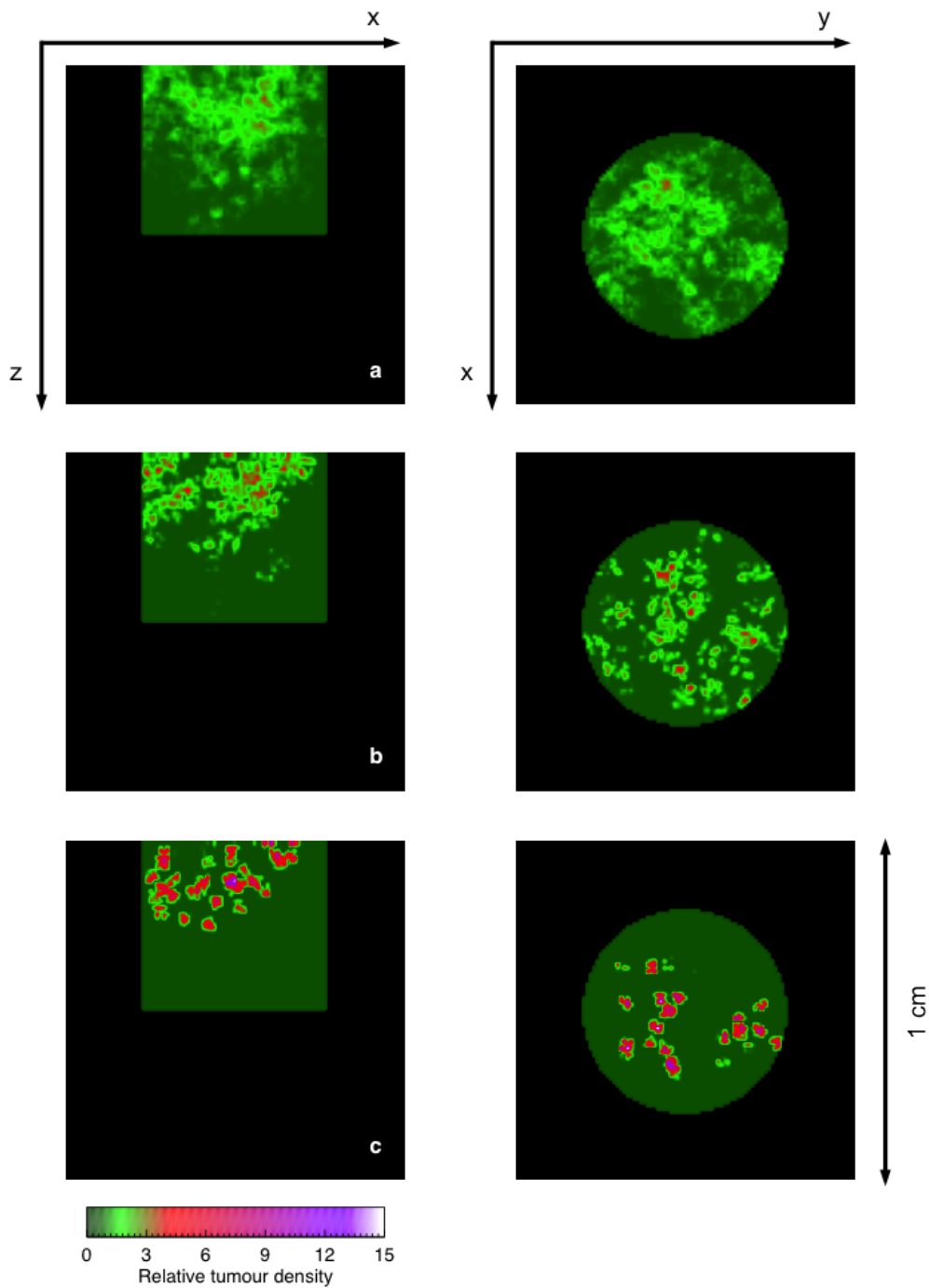


Figure 6.5: Figure demonstrating the density distribution of the different tumour models that are explored. The left column represents a slice in the x-z plane in the middle of the density grid. The right column represents a slice in the x-y plane at the top of the grid. The difference in the tightness of the clusters is caused by the variation of the fractal dimension such that a) $f_{dim} = 3$, b) $f_{dim} = 2.5$ and c) $f_{dim} = 2$. For all the structures in this figure $f_{smooth} = 0.5$. Compared to the density structures in figure 6.4 the minimum density in these structures is higher and therefore a smaller amount of the total mass is redistributed within the clustered features.

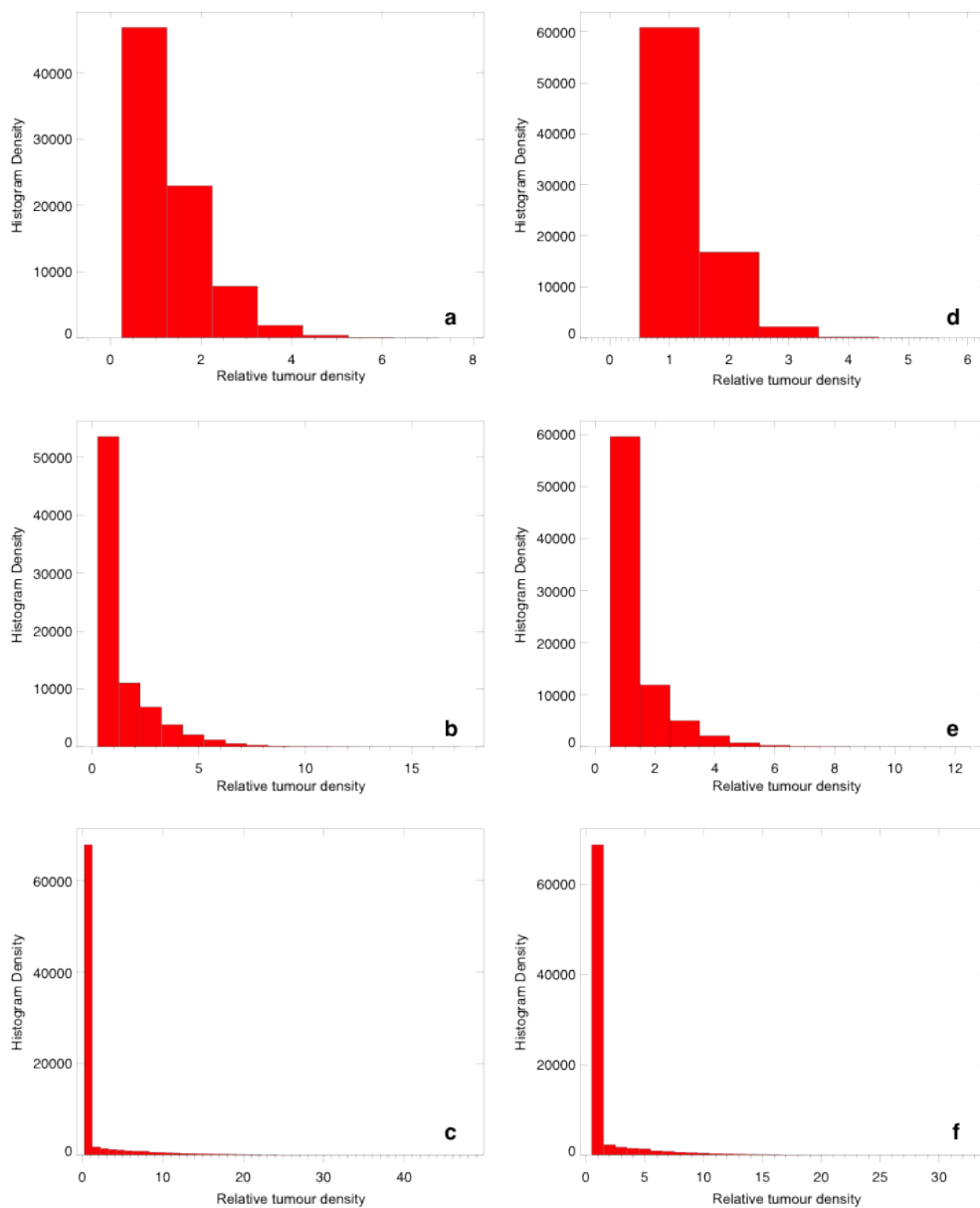


Figure 6.6: Figure demonstrating the density distribution of the different tumour models that are explored. The density was binned to demonstrate the distribution of different densities within the different tumour structures. Figure a - c corresponds to fractal structures 1 - 3 and d - f corresponds to fractal structures 4 - 6 such that a) $f_{dim} = 3$ and $f_{smooth} = 0.25$, b) $f_{dim} = 2.5$ and $f_{smooth} = 0.25$, c) $f_{dim} = 2$ and $f_{smooth} = 0.25$, d) $f_{dim} = 3$ and $f_{smooth} = 0.5$, e) $f_{dim} = 2.5$, and $f_{smooth} = 0.5$ and f) $f_{dim} = 2$ and $f_{smooth} = 0.5$.

The fluence rate was generated in the 3D grid for three different wavelengths: 405 nm, 540 nm and 630 nm. The average fluence rate through the tumour tissue is displayed in

figure 6.7. All six tumour structures are included and compared to the equivalent smooth model (where the tumour tissue is assumed to have a uniform distribution). All fractal models demonstrate an increase in the average fluence rate compared to the smooth model. The difference reduces with increasing wavelength and with increased fractal dimension (f_{dim}). This is explained by the difference in density distribution, which is demonstrated by the histograms in figure 6.6. At shorter wavelengths the optical properties of tumour tissue are more highly affected by change in density compared to longer wavelengths (figure 3.1). A cross sectional representation of the fluence rate, demonstrating the variation across the tumour tissue is displayed in figures 6.8 and 6.9. The images only demonstrate a single pixel wide slice of the tumour to illustrate the variation of fluence rate across the tumour. There will be a 3D variation of the fluence rate across the tumour region due to the density variation.

The PDD for the different fractal models (table 6.1) as well as the corresponding smooth model using the Aktelite as the illuminating light source is shown in figure 6.10. The smooth model assumed an initial uniform distribution of the tumour/PpIX corresponding to the average density of the fractal models. The figures both show the average for the fractal models (solid lines) as well as individual vertical sample sections demonstrating the range of treatment depth through different parts of the tumour (grey dotted lines). From the results it is clear that fractal structure 3 (figure 6.10 c) demonstrates the largest difference in treatment depth. For this structure an additional average treatment depth of approximately 1 mm was gained compared to the corresponding smooth model. However, this fractal model is also associated with the largest spread when considering vertical sample sections. Here the smoothing factor f_{smooth} starts to dominate since the redistributed mass is concentrated to smaller volumes, resulting in deeper light penetration through the lower density regions. Figure 6.10 a, on the other hand corresponds to a fractal model where the smooth part does not make-up as large a part of the mass distribution. This results in an average PDD as a function of depth that does not differ as much from the corresponding smooth model. The vertical sample sections for this fractal model demonstrate the range of treatment depths achieved across the tumour region. Hence even though the average PDD is not significantly different from the smooth model, a large fraction of the individual sample sections penetrate deeper into the skin. Conversely a large fraction also penetrates to a shallower depth (figure 6.10 a). For fractal structures with a higher smooth fraction (fractal models 4 - 6) the difference between the smooth and the fractal PDD is not as significant. This is due to the differences

between higher and lower density regions is not as significant compared to fractal structures 1 - 3.

The PDD for the different fractal models for daylight PDT during clear conditions is shown in figure 6.11 and for overcast conditions in figure 6.12. There is a larger difference between the smooth and the fractal models for daylight PDT compared to conventional PDT (figure 6.10). This is explained by the wavelength dependence of the optical properties of the tumour tissue (figure 3.1). Tumour tissue absorbs more light in the shorter wavelength range, hence the change in experienced absorption due to the redistribution of mass for shorter wavelengths is more significant compared to longer wavelengths. The daylight spectrum (figure 3.4) contains a large fraction of shorter wavelengths which therefore results in higher sensitivity to changes in tumour densities. The difference between the fractal model (solid) and the smooth model (dashed) for fractal structure 3 (table 6.1) is close to 1.5 mm for daylight PDT for both clear and overcast conditions (figures 6.11 c and 6.12 c). The grey lines in figures 6.11 - 6.12 corresponds to vertical sample sections through the tumour volume similar to figure 6.10. This is also due to the increased sensitivity to density variation at shorter wavelengths. To additionally demonstrate the variation of PDD over the tumour region, pixel wide cross sections of the PDD are displayed in figure 6.13 and 6.14. The PDD for a total delivered light dose of 75 J cm^{-2} is displayed for the three different light conditions.

The simulated wide field fluorescence for the different fractal structures under investigation is shown in figure 6.15. The relative fluorescence intensity is displayed and the image comprises fluorescence photons generated throughout the tumour that have escaped the simulated region via scattering. The fluorescence signal appears more uniform than the cross section of the tumour density shown in figures 6.4 and 6.5. The wide field fluorescence also demonstrates the variation that might occur when using a small probe to measure the fluorescence signal. The intensity of the fluorescence signal varies significantly over sub-mm size scales. The higher smooth component in figure 6.15 d - f results in a smoother fluorescence signal across the surface, although variations still occur.

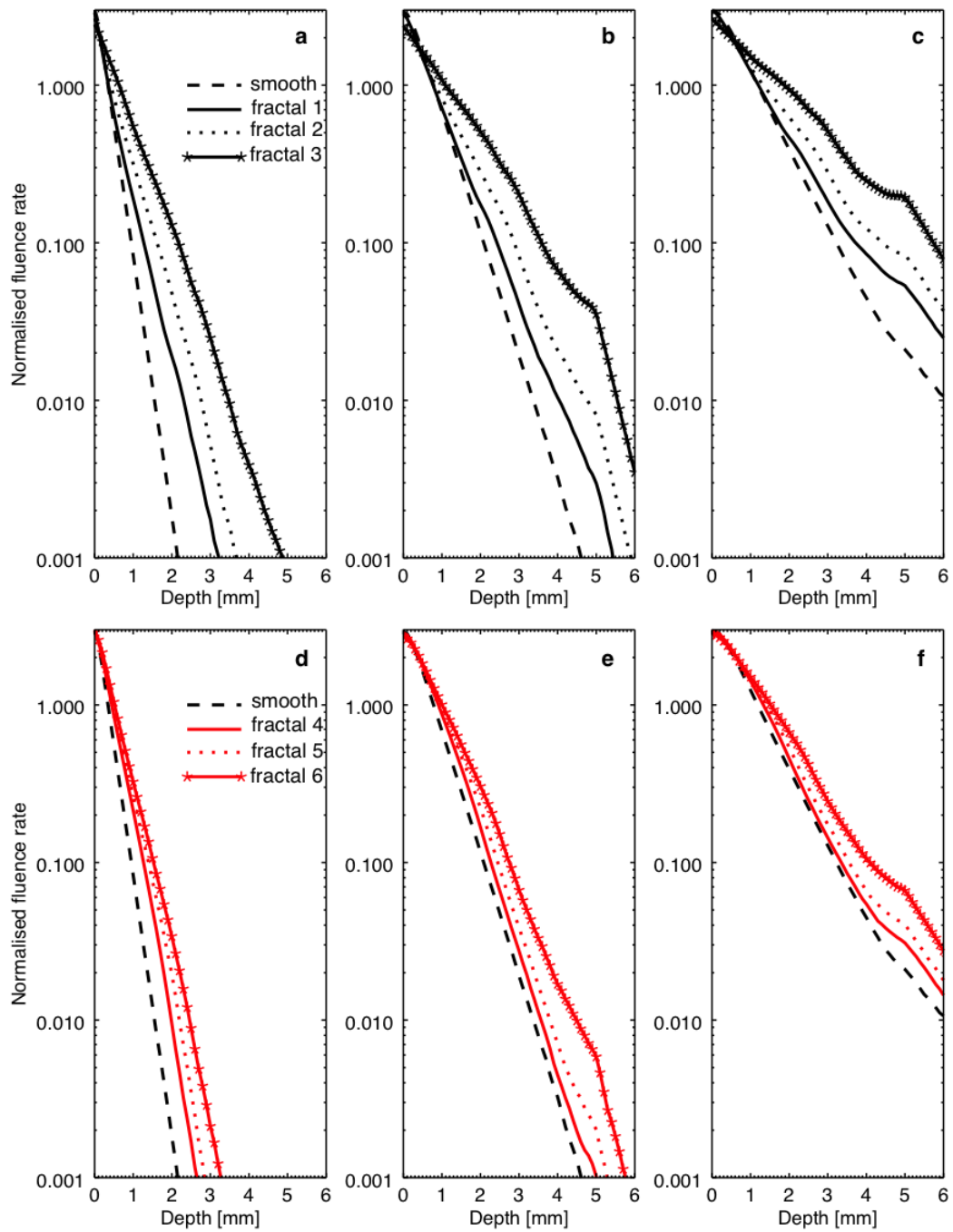


Figure 6.7: Average fluence rate for the different fractal structures under investigation compared with the equivalent smooth model (dashed). Three different wavelengths are compared: 405 nm (a & d), 540 nm (b & e) and 630 nm (c & f). The kink in the fluence rate at 5 mm in figures b, c, e and f corresponds to the boundary between the tumour and the surrounding skin tissue.

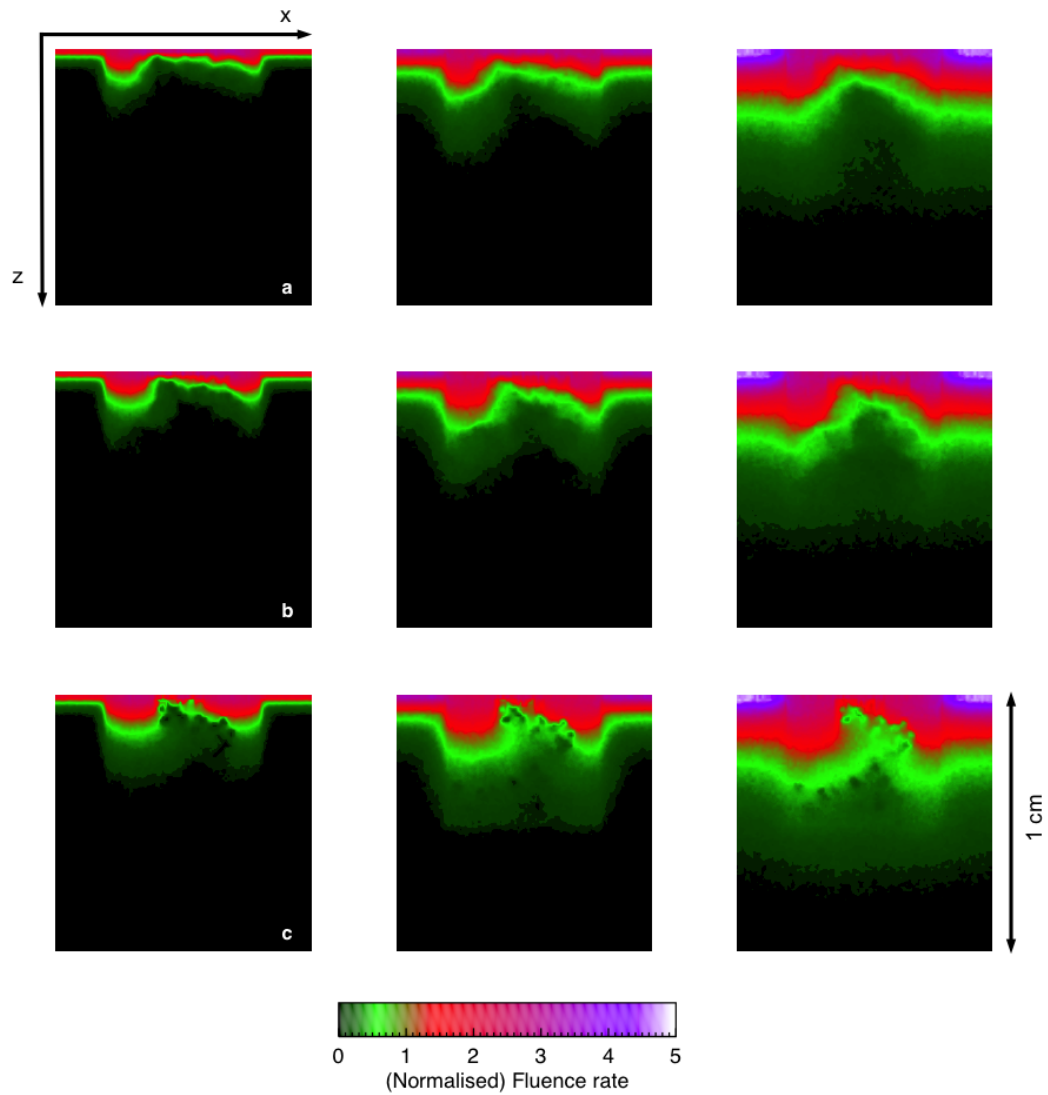


Figure 6.8: Pixel wide cross sectional slices through the tumour tissue representing the fluence rate for tumour density structures a) 1 b) 2 and c) 3 (table 6.1). The left column represents 405 nm light, the middle column 540 nm light and the column to the right represents 630 nm light.

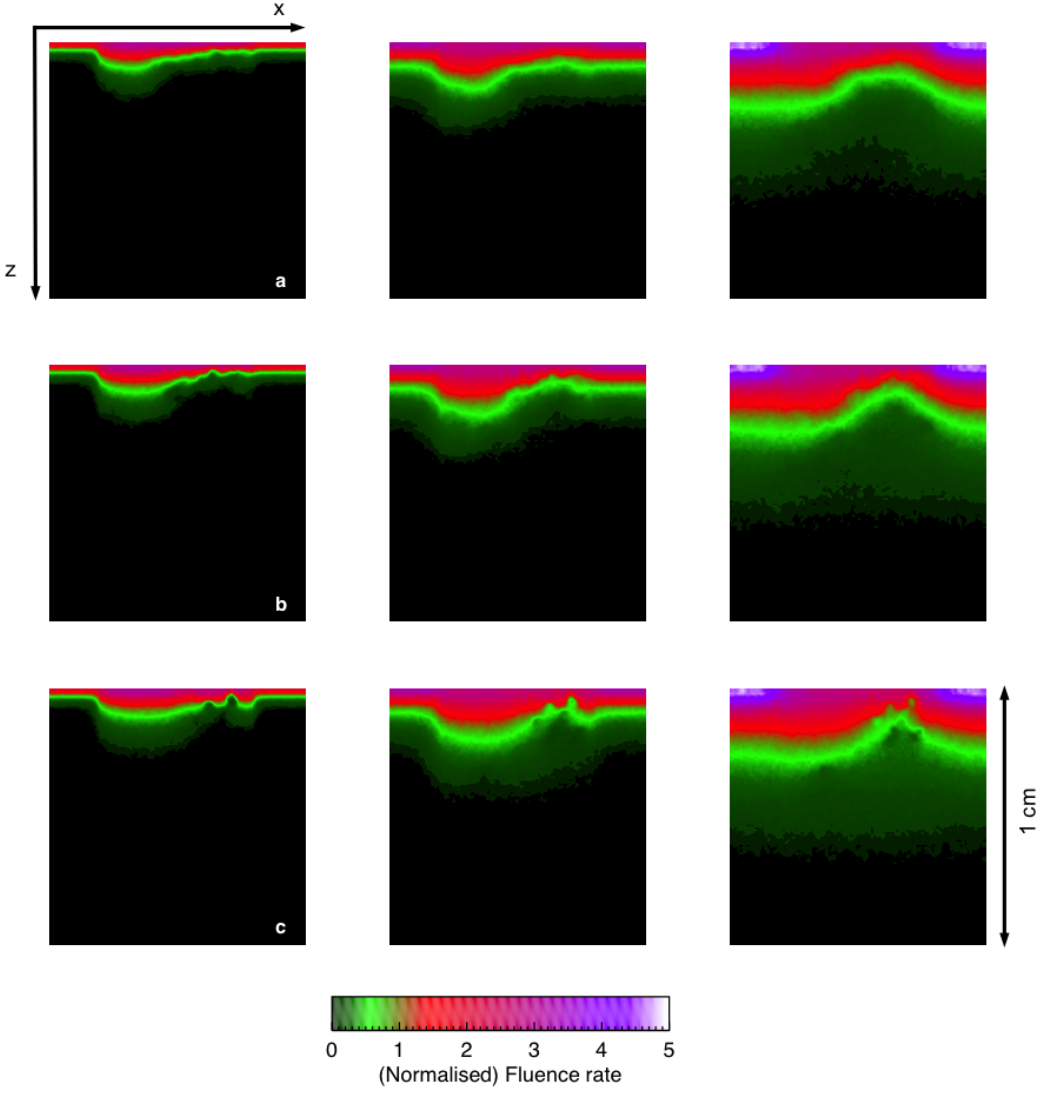


Figure 6.9: Pixel wide cross sectional slices through the tumour tissue representing the fluence rate for tumour density structures a) 4 b) 5 and c) 6 (table 6.1). The left column represents 405 nm light, the middle column 540 nm light and the column to the right represents 630 nm light.

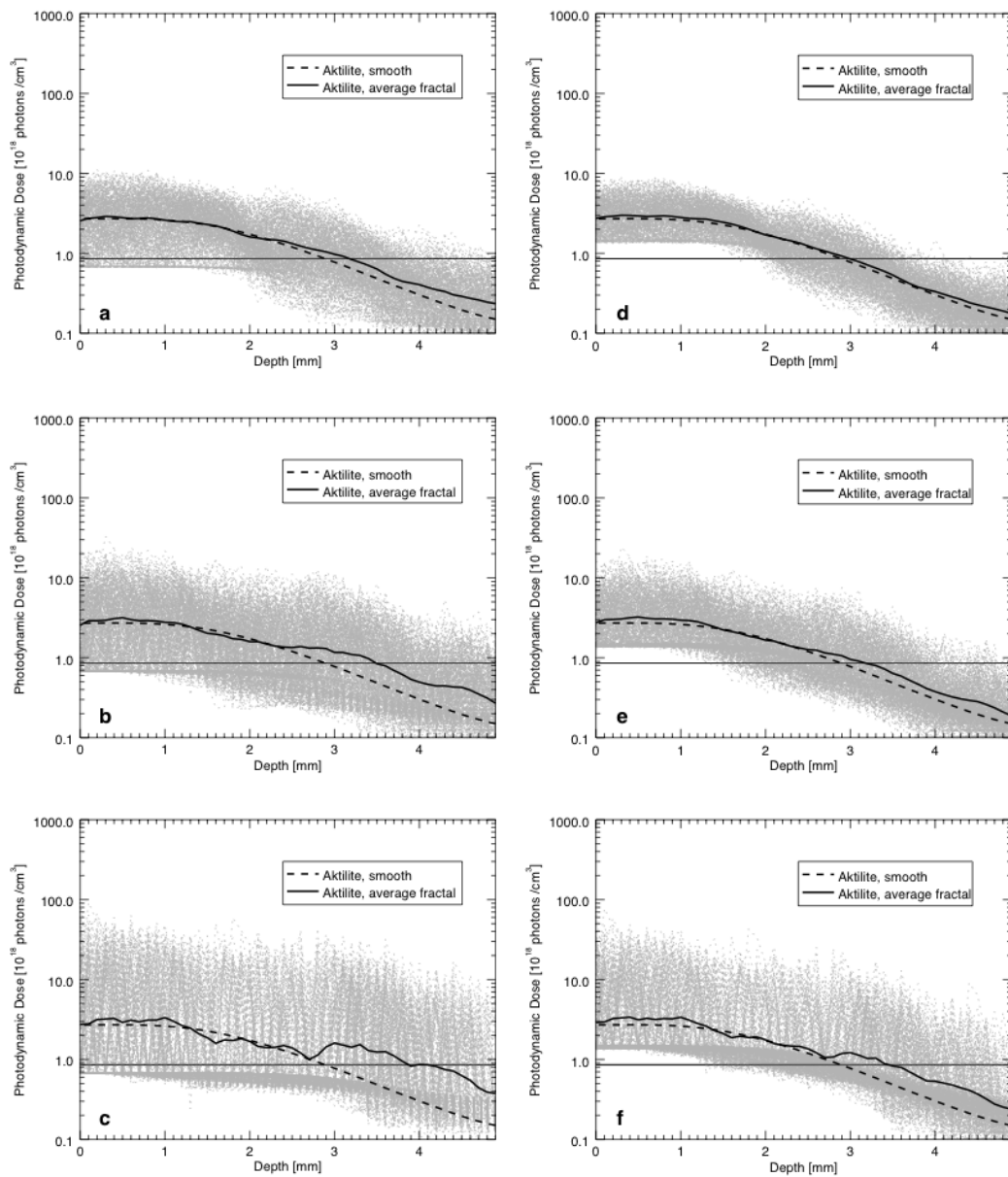


Figure 6.10: Photodynamic dose (PDD) for fractal structures a) 1 b) 2, c) 3, d) 4, e) 5 and f) 6 for the case when the Aktlite is used as the illuminating source. Both the average of the fractal models (solid) and the equivalent smooth model (dashed) are included. The grey lines corresponds to the different vertical sample sections and demonstrate the range of PDD across the tumour volume. The average PDD for the fractal model is comparatively noisy in figure c due to the larger change in density in the vertical direction associated with this density structure (figure 6.4 c). Only the total light dose of 75 J cm^{-2} is plotted in the figure, since this is believed to be a typical light dose delivered during light treatment. For fractal dimension equal to two (c and f) there is a kink in the data which is explained by redistribution of the tumour mass which is more prominent for a lower fractal dimension.

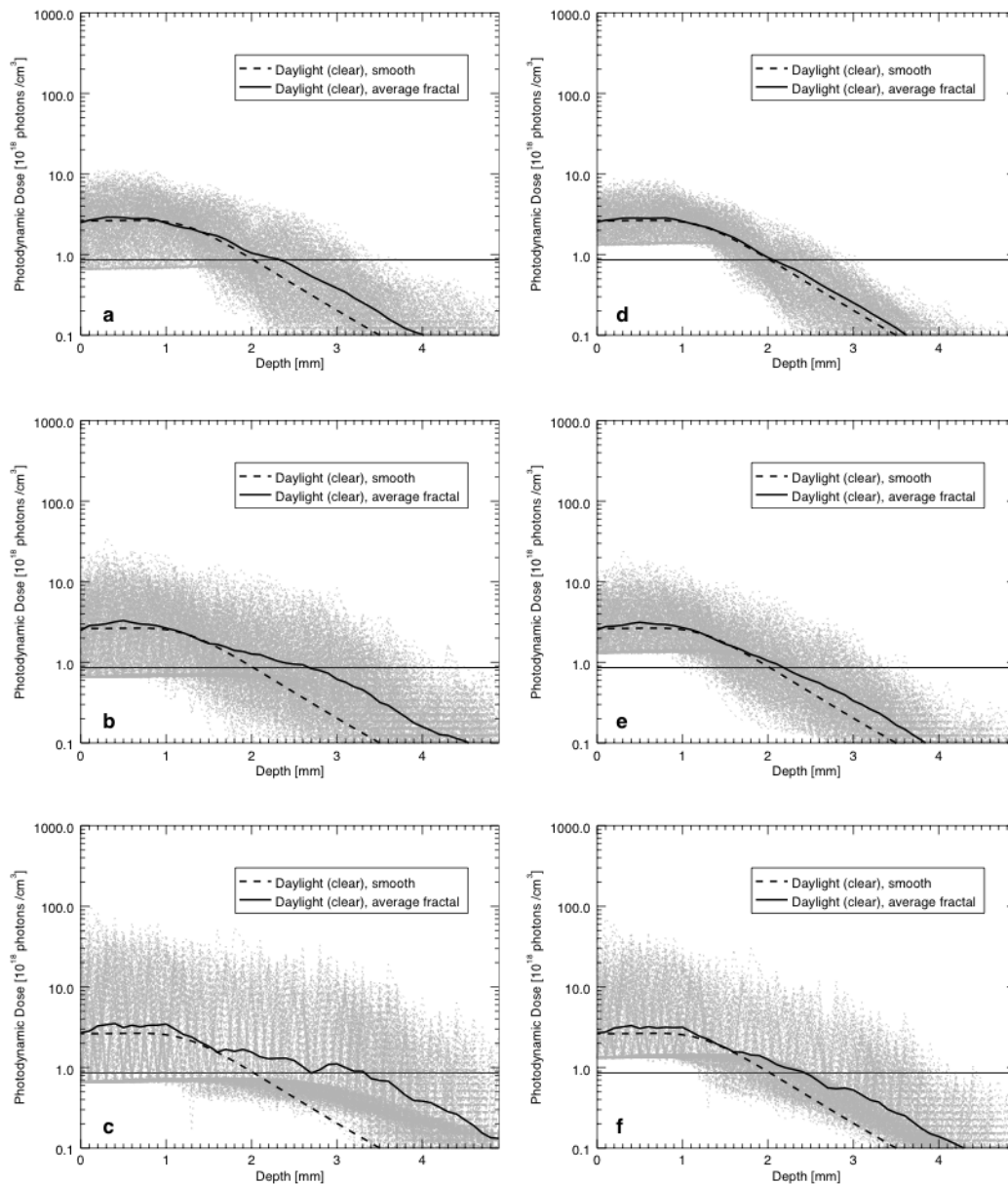


Figure 6.11: Photodynamic dose (PDD) for fractal structures a) 1 b) 2 , c) 3, d) 4, e) 5 and f) 6 for the case of daylight PDT during clear conditions. Both the average of the fractal models (solid) and the equivalent smooth model (dashed) are included. The grey lines corresponds to the different vertical sample sections and demonstrate the range of PDD across the tumour volume. Only the total light dose of 75 J cm^{-2} is plotted in the figure, since this is believed to be a typical light dose delivered during light treatment.

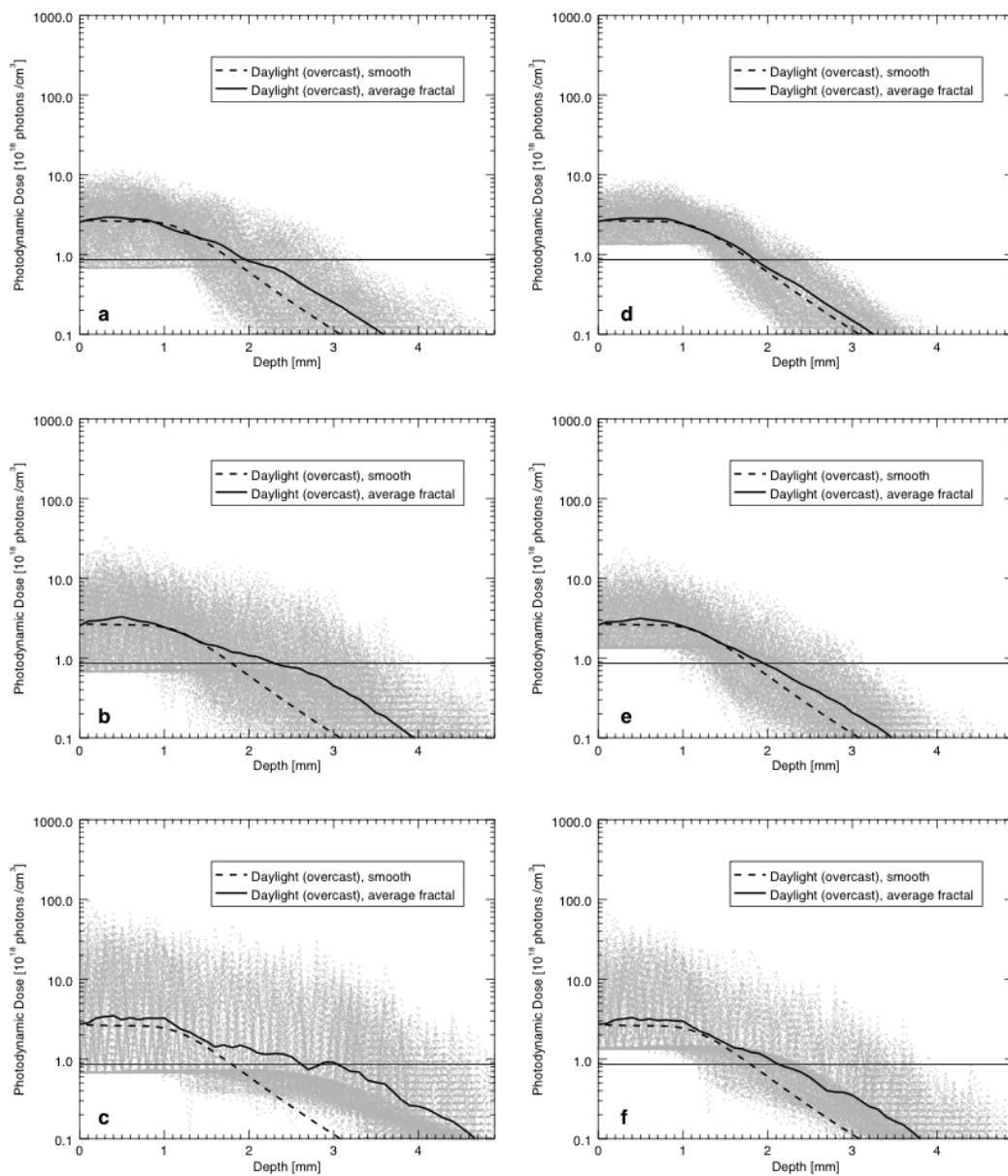


Figure 6.12: Photodynamic dose (PDD) for fractal structures a) 1 b) 2, c) 3, d) 4, e) 5 and f) 6 for the case of daylight PDT during overcast conditions. Both the average of the fractal models (solid) and the equivalent smooth model (dashed) are included. The grey lines corresponds to the different vertical sample sections and demonstrate the range of PDD across the tumour volume. Only the total light dose of 75 J cm^{-2} is plotted in the figure, since this is believed to be a typical light dose delivered during light treatment.

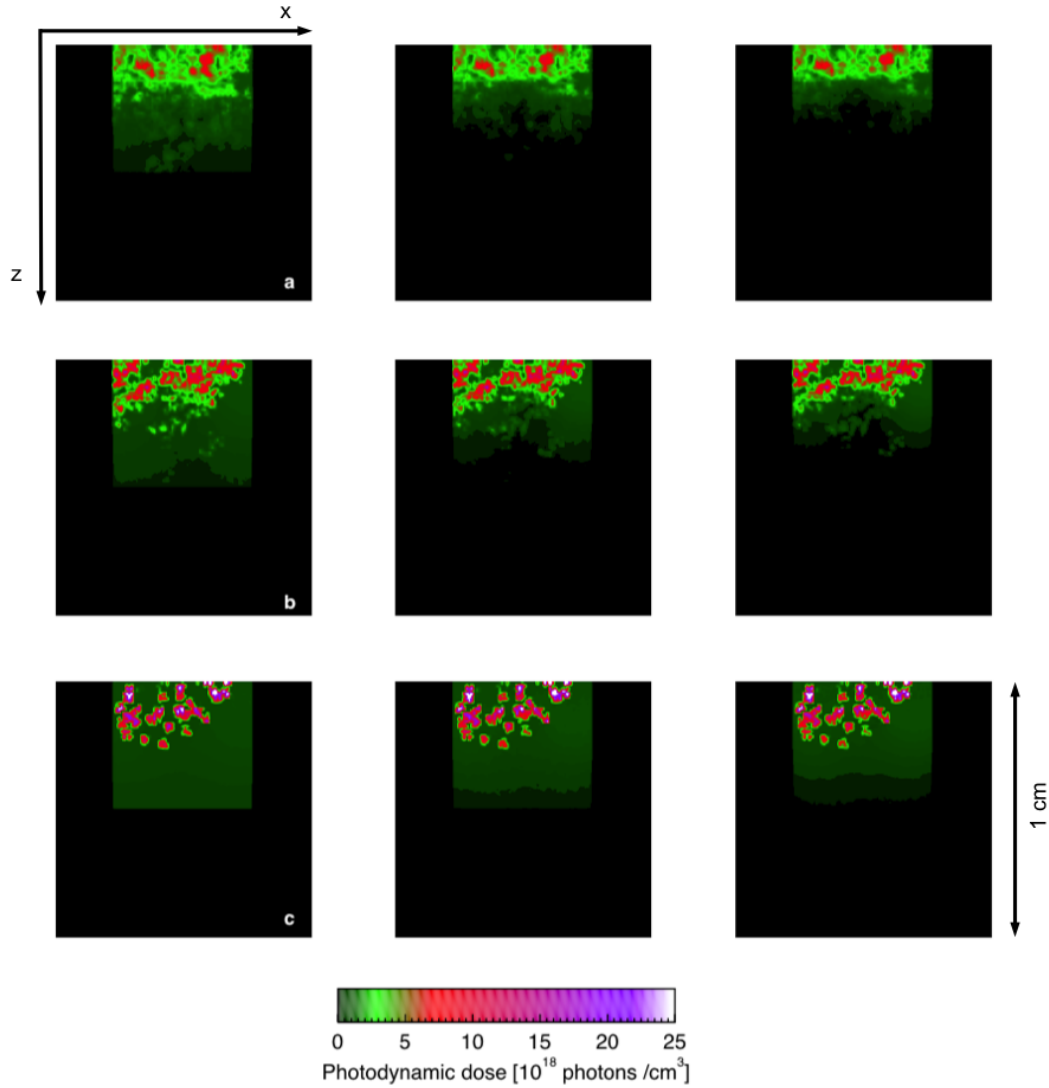


Figure 6.13: Demonstrating the photodynamic dose (PDD) through a pixel wide slice through the tumour tissue after a total delivered light dose of 75 J cm^{-2} . Three different light conditions were simulated. The left column corresponds to illumination by the Aktelite (conventional PDT), the middle column corresponds to illumination by daylight during clear conditions and the right column corresponds to illumination by daylight during overcast conditions. The different tumour structures that are compared (table 6.1) are a) 1 b) 2 and c) 3.

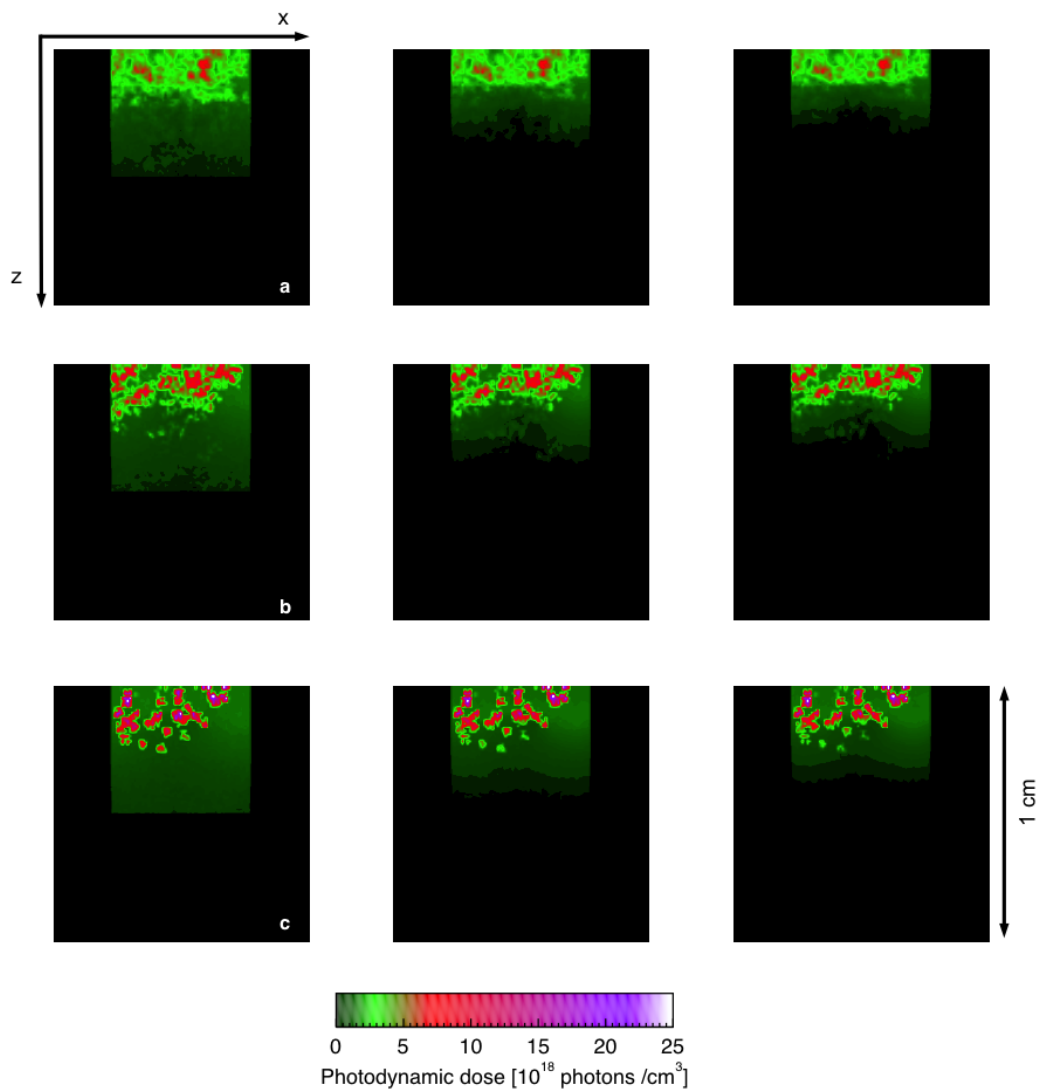


Figure 6.14: Demonstrating the photodynamic dose (PDD) through a pixel wide slice through the tumour tissue after a total delivered light dose of 75 Jcm^{-2} . Three different light conditions were simulated. The left column corresponds to illumination by the Aktelite (conventional PDT), the middle column corresponds to illumination by daylight during clear conditions and the right column corresponds to illumination by daylight during overcast conditions. The different tumour structures that are compared (table 6.1) are a) 4 b) 5 and c) 6.

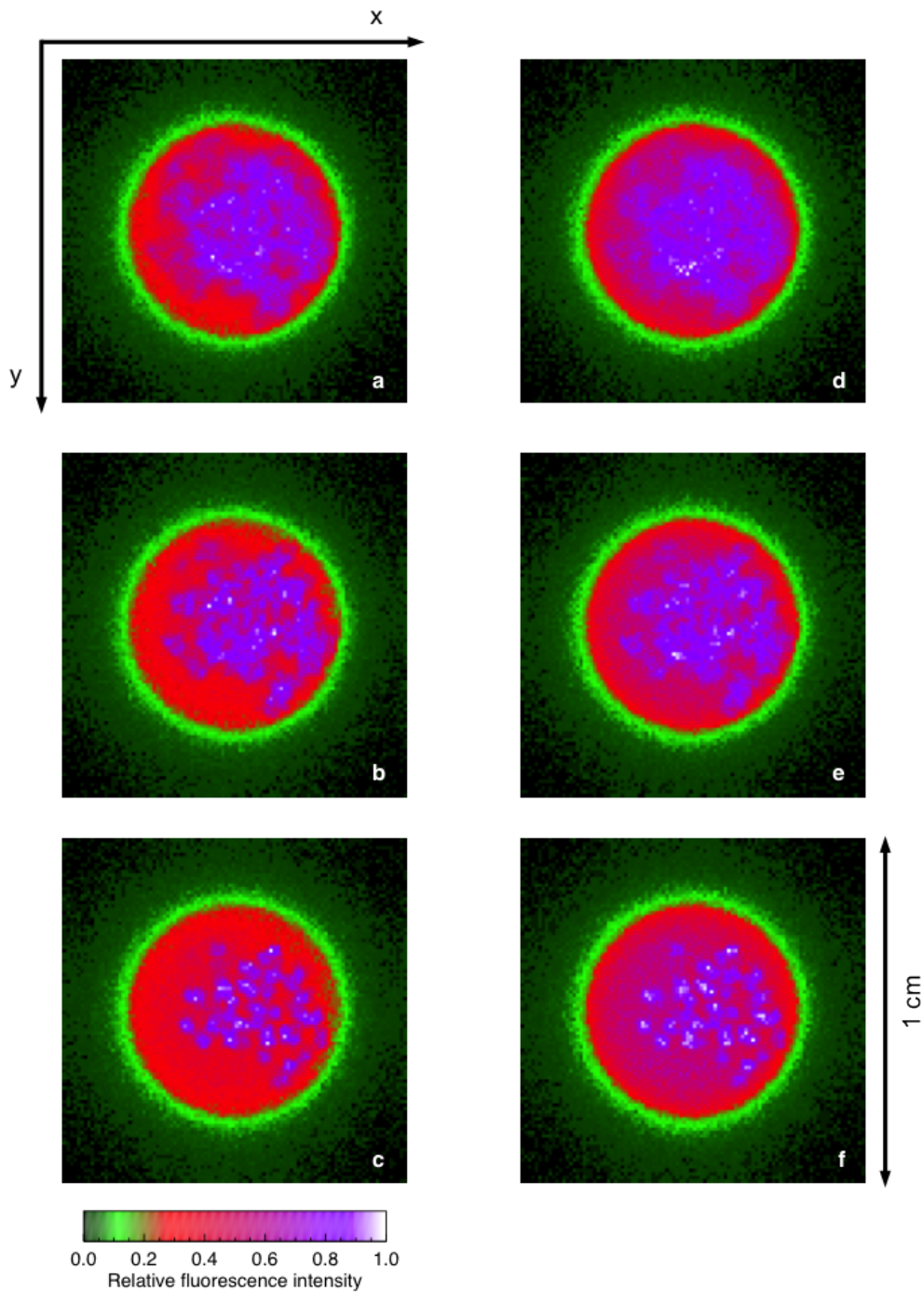


Figure 6.15: Figure demonstrating the simulated wide field fluorescence for fractal structures a) 1 ($f_{dim} = 3$ and $f_{smooth} = 0.25$), b) 2 ($f_{dim} = 2.5$ and $f_{smooth} = 0.25$), c) 3 ($f_{dim} = 2$ and $f_{smooth} = 0.25$), d) 4 ($f_{dim} = 3$ and $f_{smooth} = 0.5$), e) 5 ($f_{dim} = 2.5$ and $f_{smooth} = 0.5$) and f) 6 ($f_{dim} = 2$ and $f_{smooth} = 0.5$). The image shows both a more uniform fluorescence signal compared to the cross section of the density (figures 6.4 and 6.5) as well as a variation in fluorescence over small distances. The image dimensions are 1 cm on a side.

6.5 Discussion

The work presented here explores the importance of including 3D tumour structures within theoretical simulations of PDT. Most existing models only consider uniform densities of different tissue types, however it is shown that tissue with a non-uniform distribution significantly affects the light penetration in tissue. Different degrees of redistribution of the tumour mass were compared but the average density over the whole tumour region was the same for all models. The results presented in this work suggest that if there are non-uniformities within tissue, 3D effects should be considered in theoretical models. From the different models compared in this chapter it is evident that when simulating daylight PDT it is especially important to consider 3D effects. The results show that the significance of including 3D effects is considerably larger when shorter wavelengths are included. This is further demonstrated by the difference in fluence rate at different wavelengths (figure 6.7) as well as by the PDD for different treatment conditions.

The different vertical sample sections in figures 6.10 - 6.12 demonstrate the range of the penetration through different parts of the tumour. The spread increases as the smooth component, f_{smooth} becomes more dominant. For a structure where the mass redistribution forms tight clusters with high density, the majority of the volume is made up of the smooth component. Hence the majority of the propagating photons will experience a medium of lower opacity which results in larger average fluence rates deeper in the tissue. The resulting regions of lower density of PpIX results in an insufficient PDD in these regions, since there are not enough absorption events possible to reach the estimated threshold. There is more absorption in regions of higher density on the other hand and consequently a higher PDD. This explains the larger spread in PDD associated with the vertical sample sections from fractal structures 3 and 6 compared to fractal structures 1 and 4, where the density difference between regions is lower (figure 6.6). When studying the vertical sample sections a trend becomes obvious which demonstrates the PDD in tissue where the photons only experience the smooth component. The PDD at the surface will therefore not be lower than the PDD caused by tissue with density corresponding to the smooth component (f_{smooth}).

The work presented here assumed that the PpIX distribution mimics that of the tumour tissue. Therefore the initial distribution of PpIX was assumed to be the same for the different light conditions that were considered. The topical application of the pro-drug for different

occlusive treatment times were not considered. Extending this chapter would include the PpIX production method developed in chapter 4.

The presented models do not consider a density dependent toxic threshold. The threshold that is introduced is consistent with previous chapters in this thesis. When the density of tumour tissue is lower, fewer absorbed photons might be required to result in efficient tissue destruction. The threshold that is adopted here is what is believed to be an approximation of the average number of required absorption events. The cross sectional images figures 6.13 and 6.14 do not indicate voids where the tumour density is too high to allow photons to penetrate through. Enough light has to be able to reach regions of high density to efficiently destroy the tumour cells. Such a density dependent toxic threshold is not considered in the presented model and should be considered in future work. In addition, the difference in PpIX production in regions of varied density is not considered.

The wide field fluorescence images (figure 6.15) comprise fluorescence light emitted not only from the surface but also contributions from the tumour below the surface. The increasing inhomogeneity of the images varies as expected between the different fractal structures. Point measurements will vary over small distances due to the clusters of higher densities. This could be one of the reason why the clinical measurements presented in chapter 7 show a large spread. Measurements using a probe with a small collection region can be different at two positions close to each other.

The work presented here is to my knowledge the first to consider the effects of 3D tissue structure on light distributions during PDT. Even though the structures considered are constructed from mathematical algorithms they illustrate the effects of a non-uniform distribution on the light penetration. The method of using these algorithms also allows for easy comparison to the equivalent smooth model to assess the importance of 3D affects. Future work should include more realistic tumour models perhaps based on histological samples.

6.6 Conclusion

3D tumour structures were introduced with the purpose of theoretically studying topical PDT. The effects of non-uniformities within the tissue were explored by including fractal clustered tumour models. By changing the fractal dimensions of the density structures, different degrees of redistributions were investigated. It was found that light penetration is strongly affected by

the distribution of tissue and encourages continued usage of 3D MCRT models when studying light propagation through skin tissue.

7

A quantitative study of in vivo protoporphyrin IX fluorescence build-up during occlusive treatment phases

7.1 Summary

Protoporphyrin IX (PpIX) is a strongly fluorescing molecule. Fluorescence measurements can therefore be used as an indicator of the amount of PpIX present within the tissue. In this chapter a clinical study is presented where the fluorescence measurements were used to investigate the build-up of PpIX within the tumour tissue during the 3 hour long occlusive treatment prior to irradiation. The data was explored using statistical frameworks to appropriately consider the nature of the data. The predictive models suggest that there is a significant difference in PpIX production between lesion location. However no difference is demonstrated between different lesion types. The study presented includes 40 lesions from 40 individual patients where the majority of the lesions were actinic keratosis and basal cell carcinoma.

7.2 Introduction

During topical photodynamic therapy (PDT), the prodrug is applied to the skin in the form of a cream containing aminolevulinic acid (ALA) or methyl aminolevulinate (MAL). The lesion is then covered with an occlusive dressing which blocks out any ambient light. During this occlusive treatment (with a typical duration of three hours) the cream diffuses through the skin and is converted to the photosensitive molecule protoporphyrin IX (PpIX) in the tumour cells [58]. PpIX is a naturally occurring molecule which is produced in the mitochondria as part of the heme biosynthesis. When precursors to PpIX are added to the tumour cells, rate limiting steps are bypassed and an excess amount of PpIX is selectively accumulated in the tumour cells. For a more detailed description see chapter 1 (section 1.5).

Many skin properties change when removed from the body. Therefore, *in vivo* data is important for accurate representations of skin dynamics. Clinical studies are for this reason vital for development of the PDT treatment as well as determination of skin properties to allow accurate theoretical simulations. In PDT the *in vivo* data acquisition is mostly limited to surface measurements, due to the non-invasive nature of the treatment. Due to the strong fluorescence characteristics of the PpIX, the level of fluorescence indicates the amount of PpIX in tissue [211]. The decay in fluorescence can, for example, be used to determine PpIX photobleaching properties during illumination [100]. In the present study the fluorescence observations were used to measure the production of PpIX prior to the exposure to the light source. The study presented here compares different lesion characteristics where the fluorescence signal was measured every 20 minutes for a full 3 hours. The primary objective for the study was to determine how the PpIX fluorescence signal changed with time from the application of the prodrug and how this was affected by the patient and lesion characteristics. The secondary objective was to combine the clinical data with theoretical models to gain more knowledge about the characteristics of the PpIX production. The secondary objective has already been discussed in chapter 4 where the clinical study was replicated theoretically in an attempt to gain more knowledge about the PpIX production.

The measurements were performed at Hospital Amaral Carvalho, Jaú, Brazil. The data collected in Jaú was part of an initial collaboration with the University of São Paulo. The hospital is the centre for cancer and PDT, which covers an area approximately 500 km in diameter and closely collaborates with the University of São Paulo. The patients that are

treated in the hospital are typically from rural areas and have spent a majority of their working lives outside without using any sun protection. From observations, the sun damage in many patients was extensive and a wide spread problem throughout the country [212]. Figure 7.1 shows a patient with a large area of the arms covered with actinic keratosis (AK), a type of precancerous lesion. The high throughput of patients as well as the opportunity of sharing knowledge made Brazil a good study site.

All measurements were recorded by me, during my time in Brazil.



Figure 7.1: Patient with extensive Aktinic Keratosis (AK) on both arms.

7.3 Method

The majority of the lesions included in the study were basal cell carcinoma (BCC) (26) and actinic keratoses (AK) (11) however a few Bowen's disease (BD) and squamous cell carcinomas (SCCs) were determined from the biopsy. These lesions were still included within the study however when a comparison of the lesion type was investigated only AK and BCCs were included.

Many patients presented with more than one lesion, and a maximum of 4 lesions per patient was recorded. However, only one lesion per person was included in the analysis of the data presented here. Most patients returned for a second treatment, one week after

the initial treatment. When appropriate, both the first and second sessions were recorded. The measurements from the first treatment and the second treatment are not statistically independent data sets. For the purposes of the work presented here the two treatments were independently analysed and compared. All statistical modelling was done using R [213].

The study was conducted in compliance with the regulations and standards of good clinical practice (GCP). The study was conducted under the ethical approval accepted by the ethics committee at Hospital Amarel Carvalho (CEPFHAC-140/11). All supporting documents can be found in appendix D.

7.3.1 Study design

Appropriate lesions were examined and selected for the study by a qualified dermatologist. Before the cream was added to the lesion, the lesion was lightly scraped removing the surface crust using a sharp blade. This removed some of the potential interference associated with the prodrug diffusion. After this routine surface preparations (curettage), a cream containing 20% MAL (PDTPharma LTDA., Carvinhos-SP, Brazil) was applied to the lesion of interest. The biopsy that was removed during the curettage was sent away for analysis which allowed for a specification of the lesion type. After the cream application, the lesion was covered with a plastic film and a compress, which was secured with surgical tape. The occlusive dressing was applied for a total of three hours and ensured that the interaction with ambient light was minimised. During this occlusive treatment period the fluorescence signal was recorded at a regular time interval. At each measurement point the dressing was removed, any excess cream was removed and the fluorescence signal was recorded from the lesion. Five repeated measurements (from approximately the same area) were recorded before the cream and dressing was reapplied. This was repeated every 20 min for a total of 3 hours. When required, additional cream was added to the lesion to ensure that there was always an excess amount of cream present on the lesion. The fluorescence signal was additionally recorded prior to the surface preparation, after the surface preparations (before cream application) as well as directly after the completed illumination.

The fluorescence measurements were recorded using an optical biopsy system (OBS), which houses a blue, 405 nm laser diode. Section 2.5.1 (chapter 2) describes the OBS in more detail. The probe was placed perpendicular in contact with the skin lesion, and the measurements were performed in a darkened environment. Due to a significant amount of

ambient light in the treatment room, a black-out cap was designed. The cap was placed over the probe to reduce the disturbance from the ambient light (figure 7.2).

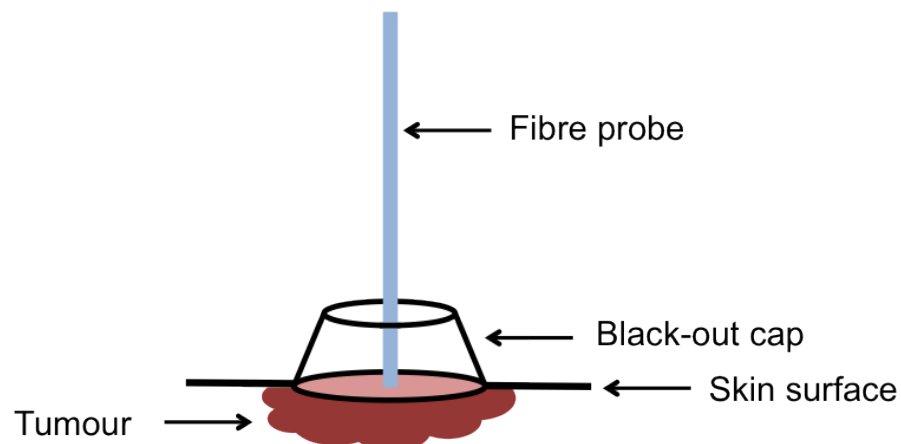


Figure 7.2: A black out cap was designed to remove artefacts from ambient light. The cap was placed on top of the probe before each measurement.

Following the occlusive treatment the lesion was treated using the therapeutic light source for 20 minutes. In the case presented here the LINCE was used, which is a red LED array based light source with an irradiance of 125 mW cm^{-2} [212]. Figure 7.3 shows a patient undergoing PDT where the LINCE was adopted.

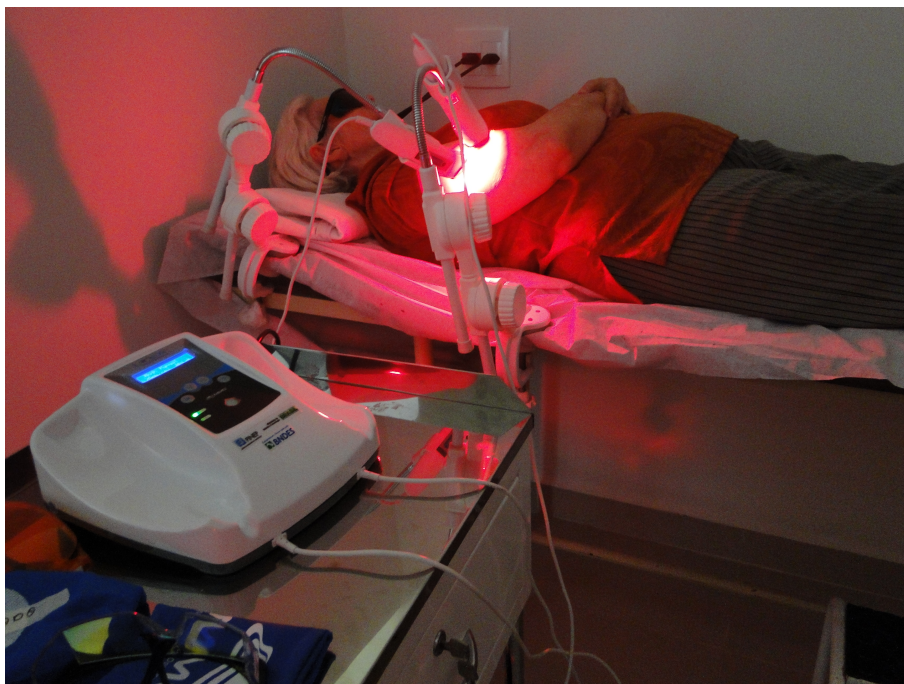


Figure 7.3: Patient undergoing PDT using the LINCE developed in Brazil. Here three different lesions are treated with three individual light sources.

7.3.2 Study population

40 lesions were included in the analysis presented here. Only one lesion per patient was included to ensure that the different lesions were independent. The lesion that was included within the study was randomly selected for each patient presenting multiple lesions. In addition, the lesions that were excluded were those demonstrating a negative fluorescence signal since this indicates inaccurate measurements.

7.3.3 Statistical model development

The observations were normalised by subtracting the background signal (measurement before cream application) from each observation, removing the effects of autofluorescence. By doing this some of the differences in the optical properties were corrected for and the relative increase of the fluorescence due to PpIX production could be determined [214]. This was carried out for each individual patient and session individually since the autofluorescence will be different for different subjects and potentially may also vary day to day. To analyse the data, the characteristic peak fluorescence signal at ~ 635 nm was recorded for each measurement to investigate how the peak changed with time from cream application.

The aim was to generate a statistical model that accurately predicts the fluorescence signal as it changes with time for different patient conditions such as different skin types and lesion types. The easiest and most straight forward approach to relating the fluorescence signal (response) to the time (explanatory variable) is by applying a simple linear regression. This framework can be further extended to include other features of the data set, such as correlation, which are important to gain more accurate information. Here the conditions for a simple linear regression will be described followed by a discussion of where this model breaks down for the data set in question. Expansions and developments of this model will thereafter be discussed and explored, and the benefits and limitations will be considered.

A simple linear regression assumes normality, homogeneity and independence [215]. If a simple linear regression is adopted, these assumptions should be verified. The data is normally distributed if the data points have a Gaussian distribution at all x values (here time). The homogeneity applies if the data displays equal variance for all values of x . Independence assumes that there is no dependence between different data points. Violation of the independence assumption can lead to over fitted models and can lead to misleading results.

For simple linear regression one assumes that the observations Y_i have a normal distribution (normal distribution of the unexpected differences between the observations and the model) with mean

$$E(Y_i) = \gamma + \alpha X_i \quad (7.1)$$

For $i=1, \dots, n$, where n is the total number of observations. Here X_i is the explanatory variable, Y_i is the response and α and γ are the parameters explaining the relationship between the response and the variable. γ represents the intercept in the model and α represents the slope. The goal is to determine the parameters to be able to explain the response as accurately as possible. This is commonly done through maximum likelihood estimations, based on finding the parameter values that are most probable, given the observations and the given model [216,217].

Model diagnostics are crucial when justifying a particular model and help to validate the accuracy of the applied model. The residuals are defined as the observed values minus the predicted values by the model and the shape of the residuals usually reveals a lot about the appropriateness of the applied model. If the residuals are plotted as a function of the fitted values the homogeneity can also be explored. If no trends or shapes are obvious through the residuals, the applied model is supported. Therefore it is not only important to observe the fit of the data, but also the residuals should be investigated.

If in the data set acquired the assumptions about independence, homogeneity and normality are violated, alternative frameworks have to be applied. A simple linear regression assumes a normal distribution of the observations. To generalise and allow for a non-normal error distribution, generalised linear models (GLM) are adopted. This introduces transformations of the linear model to allow for the different distributions of the error component. Below, the nature of the data will be discussed followed by a description and motivation for the frame work that is adopted.

Nature of the data

The data in question is clearly correlated. The amount of PpIX present in a tumour after 60 min depends on the amount of PpIX after 40 min. This results in a correlation of the fluorescence measurements. Typically a longitudinal data set such as the one discussed here,

is autocorrelated, where the dependence decreases exponentially with time. For this reason the data points cannot be assumed to be independent and a simple linear regression such as the one above, is possibly not appropriate [217]. Previous studies show an initial linear increase which eventually levels off. An initial analysis of the data showed that the data supports the linear trend previously published [218,219]. For this reason the adopted model was assumed to follow a positive linear trend. Negative fluorescence signals should not be possible, therefore the data is positive and the slope of the linear trend should also be positive. Since all data points were normalised by the measurements before the cream was applied at time zero, the intercept was forced to be zero. The skewness of the residuals in combination with the requirements of a positive model indicates a Gamma distribution of the observations, where the variance increases quadratically with expectations [217,220].

Generalized Linear Mixed Effects Model (GLMM)

A common and convenient way of modelling variation between individuals within a data set is by adopting random effects. The random effects represents the variation not explained by the covariates (fixed effects). The difference in for example genetic make-up associated with different individuals results in slightly different PpIX production rates. This effect is not considered within the fixed effects model. The additional noise that is not explained by the fixed effects, can be further explained by the addition of random effects. This is also an attempt to gain more understanding of the population as a whole. The collected data represents a small subsection of the wider population. Hence by including the random effects associated with the individual and explaining the associated noise, the information gained from the estimated model can be applied to the wider population and not only the small subset of patients included in the study [217].

GLMM requires probability distributions that are conditional on the random effects. GLMM models introduce effects that are not only fixed but also randomly allocated, which makes the likelihood function complicated. The resulting function can, for the majority of the cases, not be solved analytically and therefore different numerical approaches are required. For this reason statistical programs are useful for generating solutions and here R [213] was chosen to assist in the estimation of parameters and associated standard errors [216,217,220].

The model of interest should initially include all the different covariates of interest such as gender, location, skin type and lesion type. The model proposed is a multiplicative model to

ensure a positive slope with an intercept of zero. The observations are assumed to be gamma distributed, as a result of which the variation increases as a function of expected value. The conditional mean, i.e. the mean value of Y_{ijk} is conditional on the value α_i , can be expressed as,

$$E(Y_{ijk}|\alpha_i) = \alpha_i X_j \beta_{gi} \beta_{li} \beta_{sti} \beta_{ti} \quad (7.2)$$

Here Y_{ijk} is the observation k at time j for patient i . α_i is the slope associated with each patient from the simple linear regression. The simple linear regression has been extended to include β_{gi} which is the contribution from the gender, β_{li} that corresponds to the location of the lesion, β_{sti} the skin type of lesion and β_{ti} that corresponds to the type of lesion. To determine the different contributions from the fixed effects gender, location, skin type and lesion type and the significant relevance, the observation is divided by the time X_j and the log transform is applied to the remaining expression,

$$\log\left(E\left(\frac{Y_{ijk}}{X_j}|\alpha_i\right)\right) = \log\alpha_i + \log\beta_{gi} + \log\beta_{li} + \log\beta_{sti} + \log\beta_{ti} = a + b_g + b_l + b_{st} + b_t \quad (7.3)$$

This is a linear model similar to the simple linear regression described above (equation 7.1). However here the combination of the different contributions becomes the slope of the model describing the relationship between the observation and the time. The final slope will be expressed as $e^{a+b_g+b_l+b_{st}+b_t}$. Combining the log transform and the skewness of the data a gamma log link function GLMM was applied to the model, where the observations are assumed to have a gamma distribution. The GLMM allows for the repeated measurements to be included where the within-subject correlation is considered within the developed model. Only the explanatory variables that showed a significant difference, i.e. with a p-value below 0.05, were kept in the model. Other covariates were dropped from the model.

The different treatment sessions (1 and 2) were analysed independently. The two sessions were also compared to investigate significant effects in the fluorescence signal between the two sessions.

7.4 Results

Figure 7.4 shows a patient with multiple lesions with typical characteristics for the study. This figure corresponds to two superficial BCC lesions on the shoulder/back. The size of the lesions were approximately 2 cm (left) and 1.5 cm (right). Only one of the lesions (right) was included within the study and is in the figure magnified. The characteristic fluorescence signal generated from the PpIX within the lesion tissue is shown in figure 7.5. In the figure the characteristic peaks at 635 nm and 705 nm are shown. The work presented here focuses on the peak at 635 nm since this is the most prominent peak.

All the peak observations (~ 635 nm) during the first for all patients, subtracted by the autofluorescence, including all the repeated measurements are shown in figure 7.6. The x-axis shows the occlusive treatment time, where the measurements are repeated every 20 minutes. A jitter was added to the plot to spread out the data points at each time point (x-axis) to more clearly show the density. For an easier representation of the data, the averages of the repeated measurements for each patient are displayed in figure 7.7. In this figure a linear trend within the data can be noted, however a large variability is also displayed, the median standard deviation between patients was determined to be 108% over all time points. The individual representation of the patients included in the study can be found in appendix E. A random selection of five patients was generated and the repeated measurements were plotted in figure 7.8 (first session). The median standard deviation for the repeated measurements, i.e. the intra-variation, including all patients, was determined to be 59%. For the second session, the data are shown in figure 7.9 (repeated observations) and 7.10 (average observations). When applying a simple linear regression (equation 7.1), the resulting fitted model with associated 95% confidence intervals is displayed graphically in figure 7.11 (first session) and 7.13 (second session). For the simple regression models only the average of the repeated measurements are included. This was motivated by a need to reduce the level of correlation. However there are still correlations present within the data set which have to be further considered.



Figure 7.4: Image of typical lesions included within the study. Two superficial BCCs are displayed in the image. Only the lesion to the right (magnified) was included within the study.

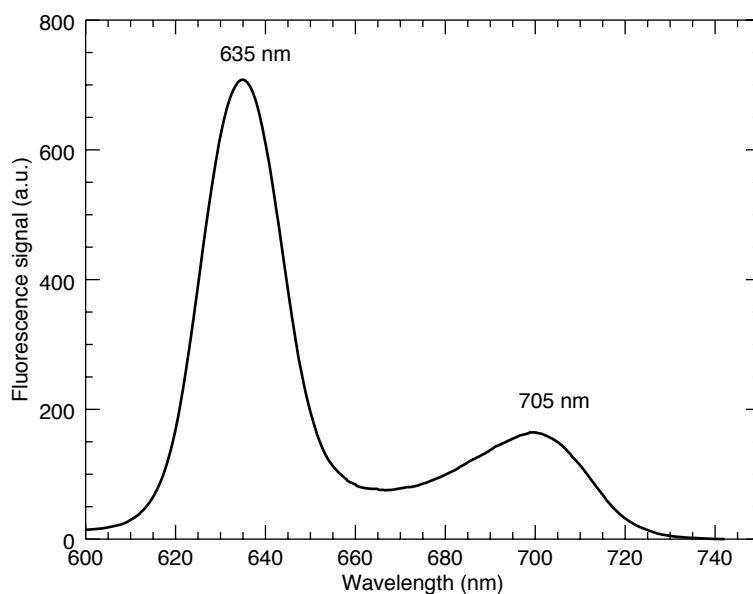


Figure 7.5: Figure showing a typical fluorescence signal (arbitrary units (a.u.)) observed from one of the patients included within the study. The fluorescence signal is generated when the PpIX is exposed to blue, 405 nm, light. The fluorescence spectrum displays two characteristic peaks at 635 nm and 705 nm. In the analysis presented here, the focus lies within the peak at 635 nm.

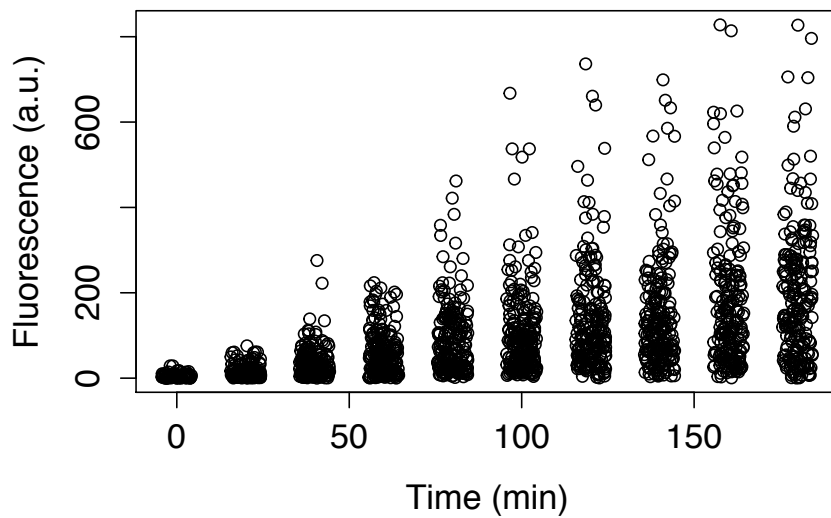


Figure 7.6: Figure showing the data for the repeated measurements for the first treatment session. All observations are normalised by the observation prior to cream application. This corrects for different optical properties and autofluorescence.

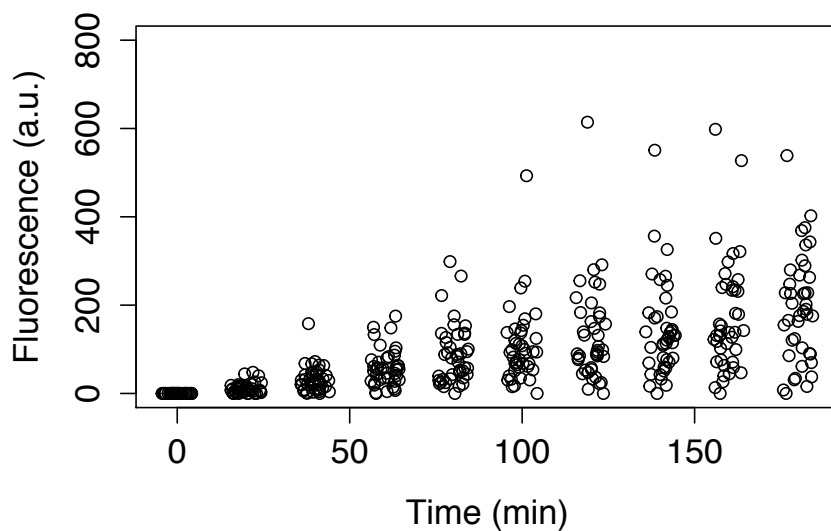


Figure 7.7: Figure showing the average of the repeated measurements for the first treatment session. The observation prior to cream application (time = 0 min) have been subtracted for each individual at each time point to normalise the observations. This introduces the restriction of a zero intercept model.

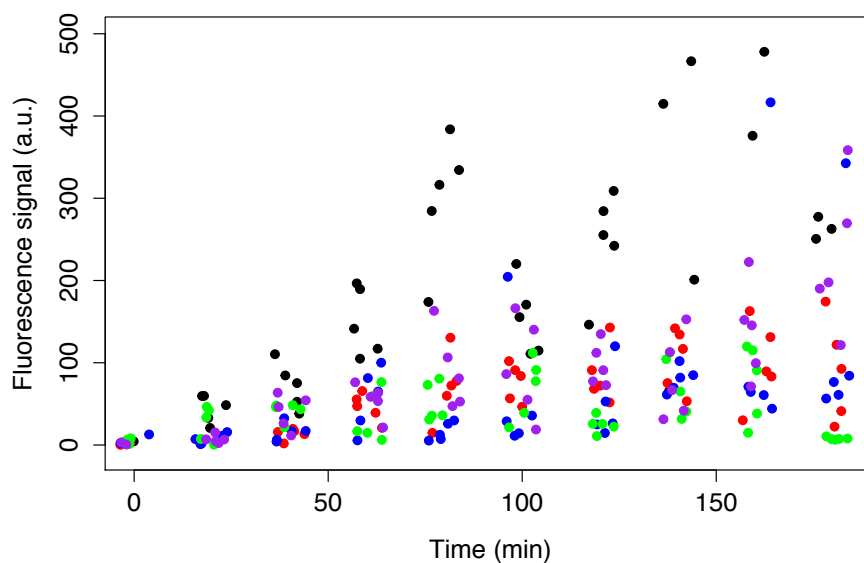


Figure 7.8: Figure showing the data associate with five randomly sampled patients from the total data set of patients. The repeated measurements of the fluorescence signal (arbitrary units, a.u.) are included within the plot and the different colours corresponds to the five different patients. To see all the measurements for the first session, see appendix E.

The resulting residuals from the simple linear regression for both session one and two are shown in figure 7.12 and 7.14. The residuals show that both the assumption of normality and the homogeneity are violated. Therefore a more complex framework is required for the correct analysis of the data where both increase of the variance with time as well as correlation and skewness is considered.

As previously discussed, a more appropriate statistical framework to apply is a GLMM. The GLMM suggested (equation 7.3) indicates a significant difference ($p < 0.05$) between lesion location during the first session. The model showed a difference between lesions located on the face compared to other lesion locations. Originally the locations were divided into three groups: face, arms or back/chest. As the effects were not significant, the arms and back/chest lesions were grouped together and were compared to the lesions located on the face. The observations from the face showed a steeper slope and therefore an overall higher fluorescence signal, indicating a faster production of PpIX. Other properties such as lesion type, skin type and gender did not show any significant difference and were therefore dropped from the model. Figure 7.15 shows the predicted model for the data corresponding to the first session with the different lesion locations. The 95% confidence intervals are included in the

figure to demonstrate the uncertainty in the estimates.

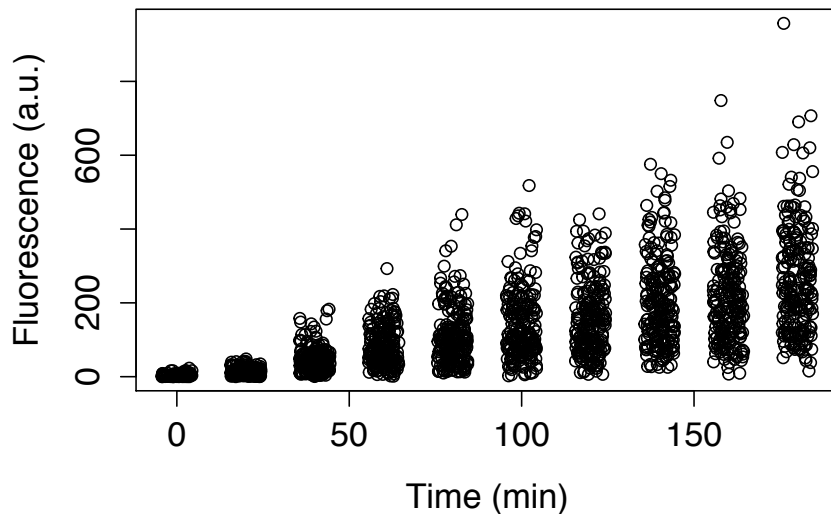


Figure 7.9: Figure showing the data for the repeated measurements for the second treatment session. All observations are normalised by the observation prior to cream application. This corrects for different optical properties and autofluorescence.

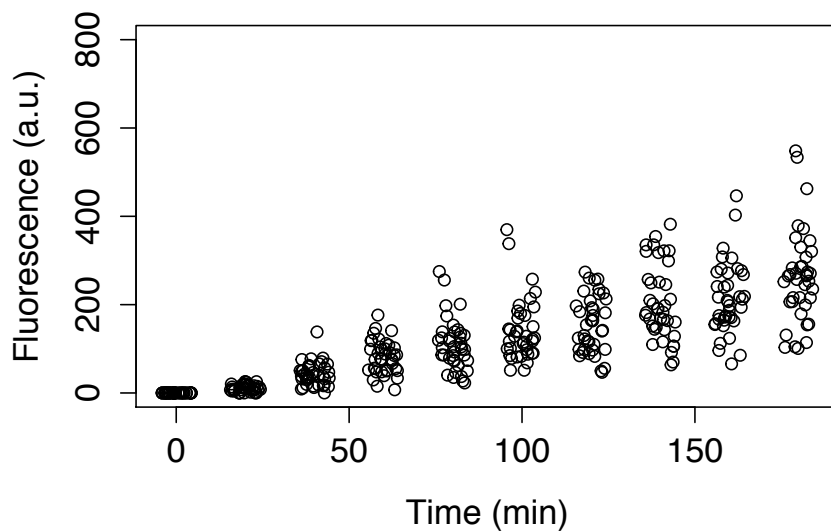


Figure 7.10: Figure showing the average of the repeated measurements for the second treatment session. The observation prior to cream application (time = 0 min) have been subtracted for each individual at each time point to normalise the observations.

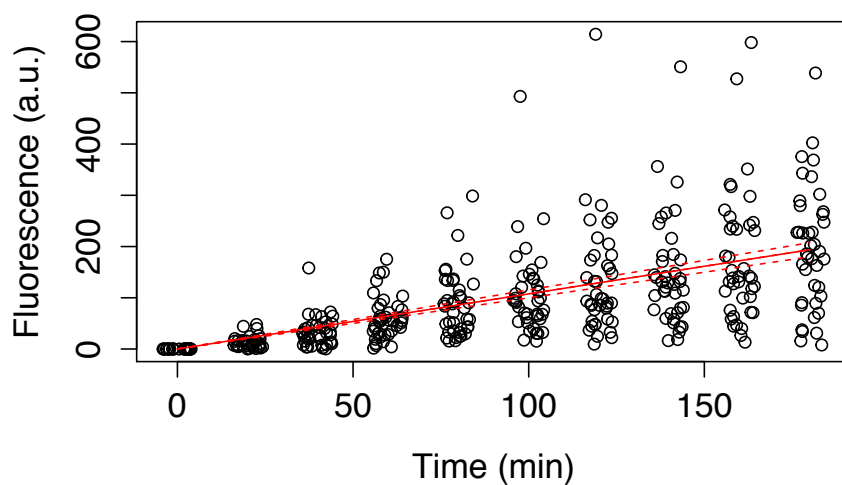


Figure 7.11: Figure showing a simple linear regression (first session) where the solid line corresponds to the predicted model with confidence intervals represented with dashed lines. The circles represents the average of the repeated measurements. The average of the repeated measurements were assumed in this model to be the absolute value to reduce correlation within the observations.

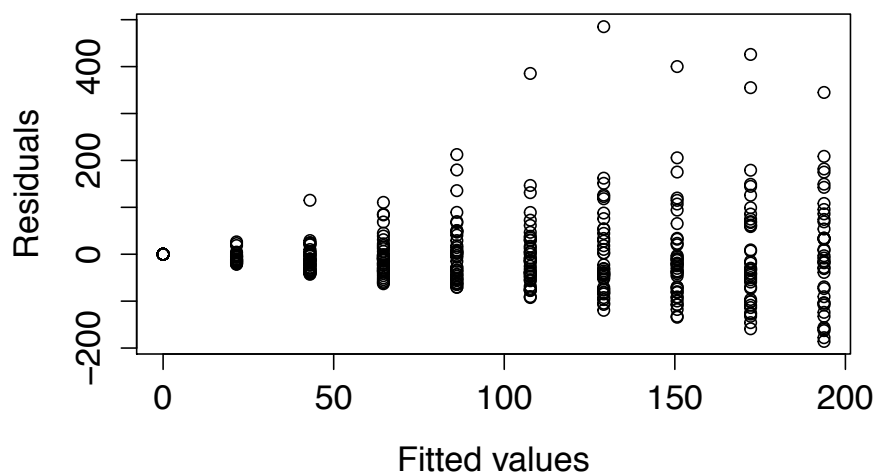


Figure 7.12: Residuals as a function of the fitted values (first session). The residuals give us an indication of the normality of the data set. The residuals for the simple linear regression shows a skewness that indicates that the data is neither normally distributed nor homogeneous. In addition, no trend is observed which supports the linear assumption.

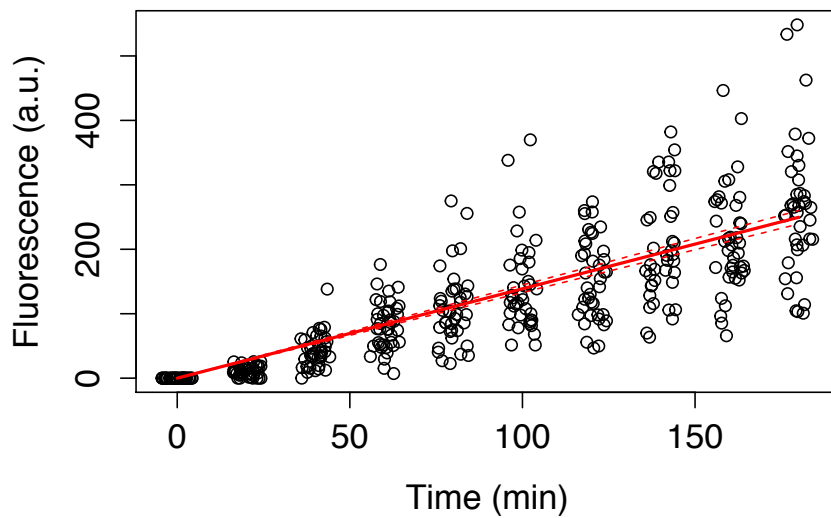


Figure 7.13: Figure showing a simple linear regression for the second session where the solid line corresponds to the predicted model with confidence intervals represented with dashed lines. The circles represents the average of the repeated measurements. The average of the repeated measurements were assumed in this model to be the absolute value to reduce correlation within the observations.

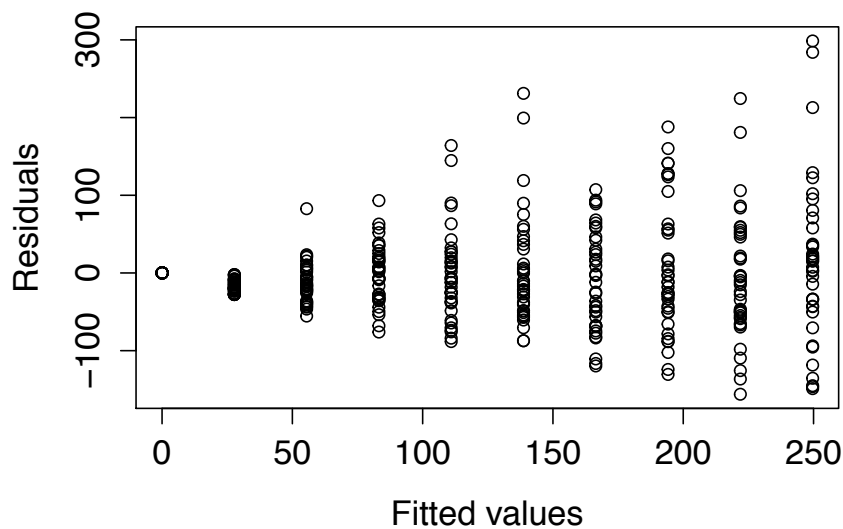


Figure 7.14: Residuals as a function of the fitted values. The residuals give us an indication of the normality of the data set. The residuals for the simple linear regression shows a skewness that indicates that the data is neither normally distributed nor heterogenous.

The appropriate residual representation is displayed in figure 7.16 since this considers the

non-normal distribution of the observations. This can be compared to figure 7.12, where the residuals associated with the GLMM indicates a better fit.

When the second session was investigated no significance was demonstrated for lesion location, lesion type, gender or skin type. However a significant difference ($p < 0.05$) between the different sessions was demonstrated when comparing the data for both sessions. The second session resulted in a steeper slope parameter compared to the observations for the first session. The predicted GLMM model for the different locations (ignoring all other explanatory variables) is shown in figure 7.17.

The results were generated using the 'glmmPQL' function in the 'MASS' package in R, however the 'glmer' function in the 'lme4' package gave approximately the same results. The different functions uses different approaches to solving the maximum likelihood, however the results are equivalent therefore only the results from the glmmPQL function are displayed. The different slope parameters estimated by the different models discussed are summarised and presented in table 7.1. The boundaries for the GLMM models reported in table 7.1 are not uniform due to the exponential nature of the model. Therefore the upper and lower limits are presented in the table to present the deviance of the slope.

Table 7.1: Table showing the different parameters estimated from the different models explored. Upper and lower boundaries are represented in terms of $\pm 1.96 \sigma$ where σ represented the standard error. Here α is the slope of the parameter where $Y = \alpha X$.

Model	Slope α	Lower boundary $\alpha - 1.96 \sigma$	Upper boundary $\alpha + 1.96 \sigma$
Simple linear regression			
session 1	1.050	0.976	1.124
session 2	1.387	1.334	1.440
GLMM location			
session 1			
Face	1.072	0.685	1.678
Other locations	0.628	0.467	0.846
GLMM session			
session 1	0.835	0.705	0.989
session 2	1.129	1.078	1.183

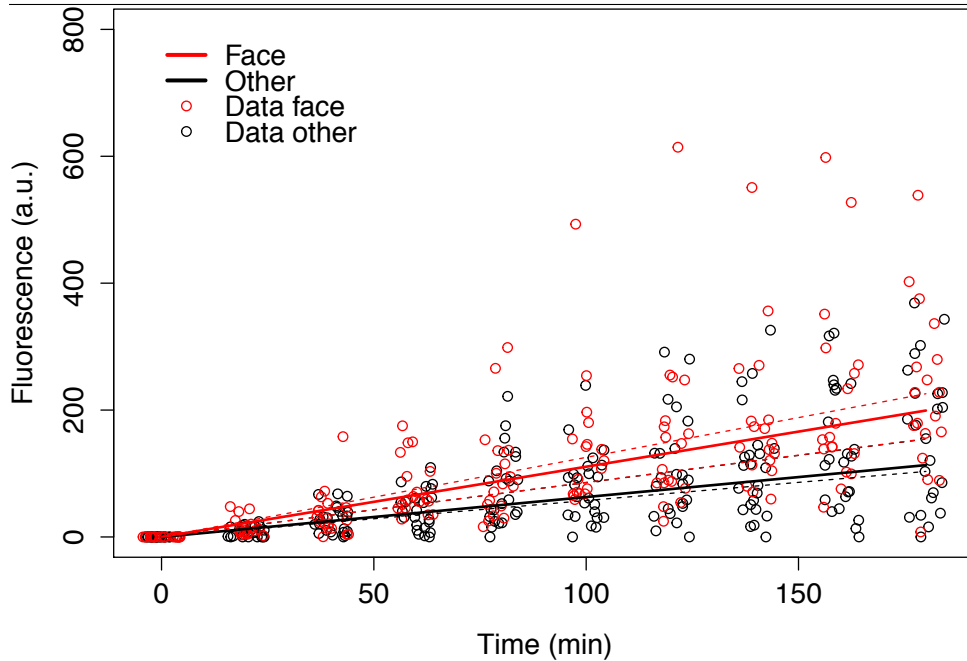


Figure 7.15: Figure showing the linear trend between the fluorescence signal (arbitrary units, a.u.) and time (minutes) for the first treatment. The predicted model was generated using a Generalized Linear Mixed Effects Model (GLMM) where the results demonstrate a significant difference ($p < 0.05$) between lesions located on the face compared to other body sites. The fluorescence was shown to be higher for lesions located on the face (red). The circles show observations, where the repeated measurements were averaged to reduce clutter on the graph. However all repeated (five) measurements were used to fit the model. The black circles represents lesions located on other body sites other than the face and the red circles corresponds to observations from lesions on the face. The confidence intervals (dashed) are included for the different situations. Note that the lower confidence interval for the face group (red) overlaps with the upper confidence interval for the other locations (black).

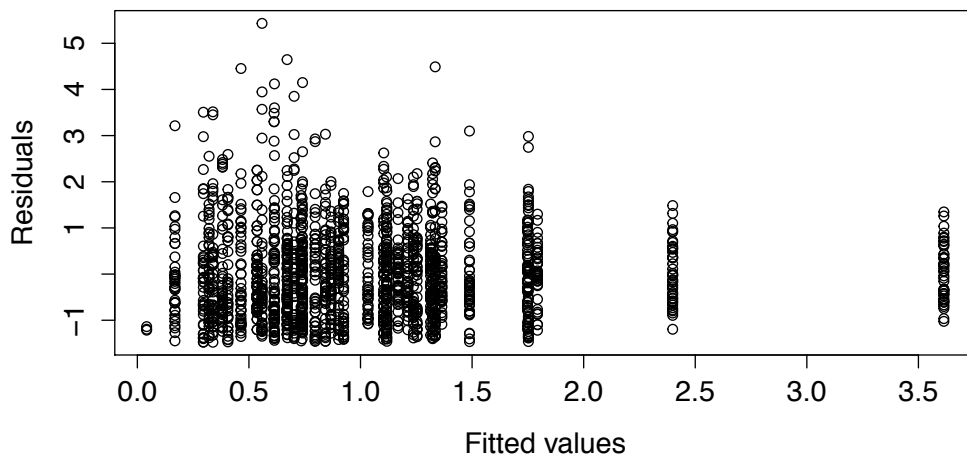


Figure 7.16: Figure showing the residuals for the GLMM model. The residuals indicates that the model is a considerably better fit compared to the simple linear regression

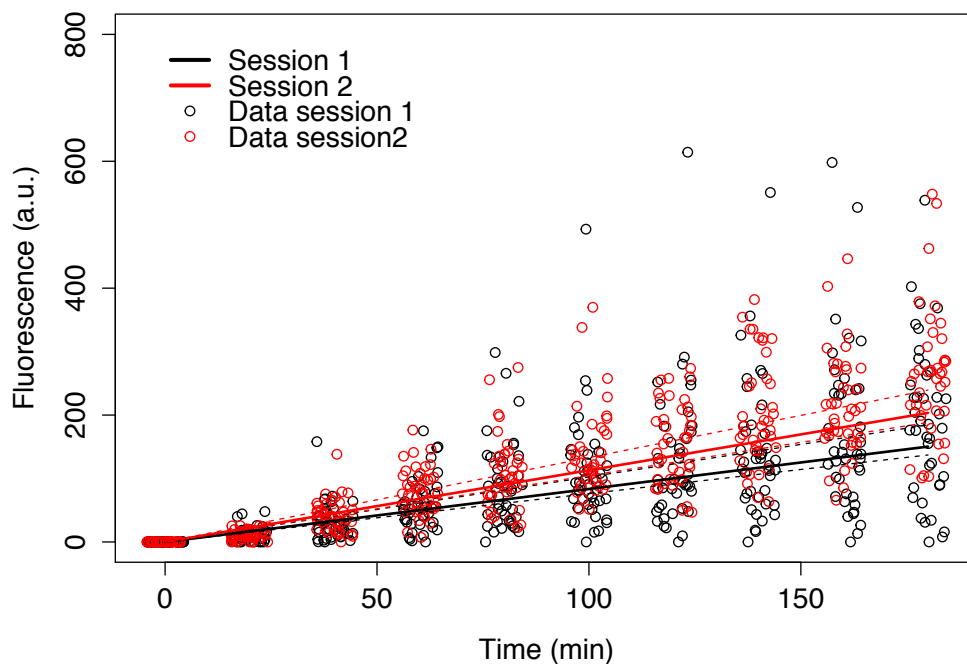


Figure 7.17: Figure showing the comparison between session 1 (black) and session 2 (red). The two treatments are typically spaced one week apart. The applied model only compared the effect of different treatment session where the results indicates a higher fluorescence signal for the second treatment ($p < 0.05$).

7.5 Discussion

The aim of the clinical study was to quantify the increase of PpIX during the occlusive treatment time with the intention of investigating the effect that different lesion characteristics have on the amount of PpIX present within the tissue. As an indication of the amount of PpIX, the fluorescence signal produced by the PpIX was measured every 20 min during the full three hour long occlusive period. The resulting study suggested that the strength of the fluorescence signal was affected by the location of the lesion which supports previous findings [221]. However this significance was only indicated for the first (of two) treatment sessions. Other characteristics such as lesion type, gender and skin type did not show any significant difference to either treatment sessions. The lack of effect of gender and skin type can be explained by the fact that these factors should not have any effect on the lesion itself. A more significant difference between lesion type (comparing AK and BCC) was expected both due to potential anatomical and physiological variation between lesion types as well as previous published results [218]. However this significant difference was not found within the data.

The linear trend that was deduced to be the most appropriate is supported by previous

studies [218, 219], however there is no way of determining the shape after the three hours that were measured. It can be argued that the linear trend would flatten out if the occlusive treatment was extended due to the saturation of the PpIX. To measure this, subjects would have to stay in the clinic for a longer period of time and would not be able to undergo PDT during the same day. This study would therefore be considerably less convenient for the patients and would introduce additional visits to the hospital which is not desirable. The study performed here is not believed to affect the underlying PDT treatment and therefore no information beyond the three hours can be deduced. Only the linear increase in fluorescence and thereby PpIX production during the initial three hours can be successfully determined.

There are several issues associated with the study presented. Due to the location of the study (Brazil), the surface preparations were not carried out according to the standard protocol established in the UK which was impossible to establish prior to the start of the study. The curettage performed is clearly depending on the institute and the training of the staff. At Hospital Amaral Carvalho in Jaú the curettage was very deep which resulted in a lot of blood production. Two issues arise from this. First of all is the possibility of the fluorescence measurements being affected by blood due to the strong absorption properties of blood. Even though attempts to reduce the blood effects, there are high probabilities that some measurements, especially the background readings, could be affected by blood. The second effect that arises from the deep curettage is the removal of lesion. A lot of the lesion is removed during this deep curettage which means that the PpIX is limited to superficial layers and therefore the linear trend could be explained by the theoretical model developed in chapter 4. If a majority of the lesion is removed, the PpIX will only be produced to shallow depths. This is then in agreement with the theoretical model developed in chapter 4. To investigate the effect that the curettage had on the measurements and the PpIX production a study on a different study site should be carried out. This would allow the level of curettage to be investigated as well as support the study performed in Brazil.

The stability of the measurements could have been affected by the instability in the energy supply as well as the heat and humidity associated with the conditions within the hospital. The black out cap was produced to block out as much ambient light as possible, however it was not possible to explore the effects that this addition had on the measurements. Since the background autofluorescence measurements were performed with the black out cap, it could however be argued that the effect from the cap was considered within the normal-

isation (subtraction of background from subsequent measurements). It was assumed that no ambient light interacted with the already produced PpIX during the measurements. The measurements were performed as fast as possible, and the resulting photobleaching should not be significant. However measurement techniques where the removal of the dressing and the cream are avoided would be preferable since this would remove any possibilities of additional unwanted photobleaching.

The intra-subject variability could be explained by an inhomogeneous distribution of the PpIX in the horizontal plane. Even though the same area was targeted, due to the potential inhomogeneous nature of tumours this could explain the large variability displayed within an individual. There is also a large variability between individuals, as is displayed in the raw data (figure 7.6). This could be explained by the difference between the genetic make-up between patients which is the motivation behind the mixed effects model. Chapter 6 explored the fluorescence signal from heterogeneous tumour tissue which suggested large variability in the resulting signal on the sub-mm size scale.

Future work should include a quantification of the OBS to relate the fluorescence signal to an amount of PpIX. This could be done in a phantom of known optical properties with a known amount of PpIX. Other improvements involve, as previously mentioned, an additional study where the curettage is under better monitoring to establish effects associated with the level of curettage and the outcome of the treatment and the PpIX production.

Even though the study presented here is associated with some instabilities, the observations suggests a linear trend where only lesion location had a significant effect on the fluorescence signal. The complex statistical framework that was developed is appropriate for this study as well as other similar clinical studies and should be considered as a potential framework for future studies. The data collected extends previous knowledge where the frequency of measurements have been extended as well as the comparison between more explanatory variables has not previously been performed.

7.6 Conclusion

The PpIX fluorescence signal from patients presented with superficial skin lesions was measured at a regular time interval during the three hour long occlusive treatment phase. Due to the strong fluorescence characteristics associated with the PpIX, the fluorescence measure-

Chapter 7. A quantitative study of in vivo protoporphyrin IX fluorescence build-up during occlusive treatment phases

ments are useful for indication of the amount of PpIX present within the region of interest during a particular time. It was found that the PpIX increased linearly during the first three hours of the occlusive phase where results indicate a larger overall amount of PpIX for lesions located on the face compared to other lesion locations. No significance was found when comparing gender, lesion type and skin type. Even though the results show a large variability both intra- and inter-subject, the linear trend supports previously published results. The data was analysed using a generalised linear mixed effects model which appropriately considers the nature of the data. The resulting trend has been utilised in chapter 4 in an attempt to gain more information about the in homogenous distribution in the vertical direction of the produced PpIX.

8

Concluding remarks and future prospects

8.1 Summary

The main aim of this project was to improve existing theoretical models of topical photodynamic therapy (PDT) to better understand different aspects of light propagation through skin tissue during treatment. In a theoretical model, the accuracy of the outcome is highly dependent on the accuracy of the input parameters. Therefore it is important to include empirical data derived from the clinical environment and from experimental set-ups. The work presented here highlights both the potential and limitations of adopting theoretical models.

This chapter provides a short summary of each analytic chapter and discusses the primary results of the project in the context of future work.

8.1.1 Theoretical modelling of photodynamic therapy

Chapter 2 described the theory and details of the Mont Carlo radiation transfer (MCRT) model developed for this project. In this chapter the code was both experimentally and theoretically

validated prior to further investigation of PDT. The theoretical validation included reproduction of results generated from another MCRT model published in the literature [97]. The model provides a flexible and robust technique where many different aspects of PDT can be accurately represented. The main limitation is the requirement of knowledge of input parameters such as optical properties and photobleaching dynamics.

The code was then used in chapter 3 to simulate daylight PDT. This is the first known theoretical investigation of daylight PDT [127]. The depth dependent photo-toxicity for different weather conditions was generated and compared to conventional PDT. The results support the usage of daylight PDT for treating superficial skin lesions to a depth of over 2 mm. This chapter also highlights the variability caused by different input parameters such as initial distribution of the photosensitive molecule protoporphyrin IX (PpIX) and illumination angle. This improves on knowledge of the treatment conditions during PDT and demonstrates the importance of including accurate parameters. The code allows for these parameters to be investigated in a way that is impossible in the clinical environment and demonstrates the potential range in treatment depth associated with different treatment conditions.

To consider the different treatment protocols associated with daylight PDT and conventional PDT, chapter 4 incorporated a model where the distribution of PpIX varies both spatially and temporally. This allowed for the topical application of the pro-drug for different occlusive treatment times to be considered, resulting in a more accurate representation of different treatment modalities. The main challenge within this chapter was the allocation of appropriate PpIX production parameters. This was addressed by combining the model developed in this chapter with the clinical data collected in chapter 7. The results in chapter 4 suggest that treatment depth is not only limited by light penetration but also by the distribution and accumulation of PpIX molecules. A more complex model would introduce further parameters and would require detailed exploration of the production and accumulation of PpIX within human tumour tissue to ensure an accurate representation.

As discussed above, the accuracy of the modelled outcome is dependent on appropriately representing the skin tissue. Only when relevant optical properties are adopted within the MCRT model, accurate and useful information about the light propagation and energy deposition within the skin tissue can be generated. There is no such thing as a generic patient and the literature shows a large variability in optical properties between individuals [112]. For

this reason it is important to consider different patient characteristics to further individualise treatment parameters. In chapter 5 a range of optical properties were discussed and explored. This is the first known theoretical investigation of light penetration and treatment outcome which compares different patient characteristics such as age and skin type. The results show that older patients with a light complexion are associated with a deeper effective treatment. Chapter 5 only considered two properties that cause variation in the optical properties. If the data were available further development of this would include characteristics such as lesion location, lesion type and patient gender. Most patients are treated twice, the second treatment typically one week after the initial treatment. The histology of the skin and tumour tissue will potentially change between these two treatment locations. By investigating this, further treatment categorisation would be achieved and the importance of multiple treatments would be explored.

In chapter 6, the three dimensional properties of the model were developed to include non-homogeneous tumour tissue. This is believed to be the first theoretical investigation that includes heterogeneous skin tissue when exploring PDT. By adopting artificial tumour structures, comparison with uniform tumour models was possible. Different degrees of heterogeneity were explored to investigate the effect that these three dimensional heterogeneities have on the treatment outcome. The results show that heterogeneous tissue should be considered within future models since this has an effect on the simulated treatment depth. The wide field fluorescence light as a result of these heterogeneous tumour tissues was additionally simulated. The results suggest that fluorescence light not only from the top layer of the tumour, but also tumour tissue from lower layers contribute to the fluorescence signal exiting the surface of the tumour. The fluorescence simulations also show large variations over sub-mm size scales which could explain measurement variations experienced in chapter 7. Future work would include real tumour structures and would compare different tumour types at different growth stages. However the reason why this has not been done at this stage, is due to the limitations in available data.

Chapters 2 - 6 describe code developments and implementations in different situations, which have increased our understanding of light interaction with skin tissue for different treatment conditions of PDT. However to further improve and develop the model to achieve even more realistic and complex skin models additional issues must be considered. These include blood vessels and real tumour structures as well as other tissue characteristics. When

including finer structures within the simulation region an improved resolution is required. This can be achieved by increasing the number of grid cells or introducing a mesh based grid system. A mesh based grid system introduces a finer grid system only in regions where increased resolution is required. This technique makes it easier to consider curved surfaces [131] and allows details like surface roughness and small capillaries to be included in the skin model. The drawback with this is the increase in simulation time although more advanced computation techniques including parallelisation should mitigate these problems.

Oxygen depletion during PDT continues to be poorly understood. The level of oxygen is reduced due to the production of singlet oxygen molecules; simultaneously new oxygen is introduced to the tumour through vascularity. During the simulations presented in this thesis the oxygen levels have not been considered and it has been assumed that the oxygen availability has been unlimited. With a reduced oxygen availability, fewer singlet oxygen molecules can be produced which consequently results in a reduced photodynamic effect [69, 102, 222] and this will be important to consider in future developments of theoretical simulations of PDT.

Oxygen levels and thermal effects change the optical properties as a result of light exposure [223] resulting in changes in penetration and treatment depth. By including this in the model, treatment conditions would be explored that could be utilised to further optimise treatment parameters.

During daylight PDT, sunscreen is applied to exposed areas (including the tumour region). This results in a spectral filter which blocks some harmful wavelengths [83]. The motivation for not including this in the presented work is the small amount of overlap between the optical filter provided by common sunscreen lotions and the daylight spectrum. However different sunscreen lotions might block different wavelengths and therefore this should be considered when developing future models for daylight PDT.

8.1.2 Clinical data collection

Through *in vivo* measurements increased knowledge about appropriate model parameters can be achieved. In chapter 7 the build-up of PpIX was investigated by measuring the increase of the fluorescence signal from the PpIX during the occlusive treatment phase within the clinical environment. Since PpIX is associated with a characteristic fluorescence signal it is

thought to be a good indication of the amount of PpIX present within the skin tissue. Both Actinic Keratosis (AK) and Basal Cell Carcinoma (BCC) lesions were studied and a total of 40 patients were included. The resulting data suggest that the fluorescence signal increases linearly during the initial three hours of occlusive treatment. Different lesion characteristics were compared and it was found that the fluorescence signal increased faster in lesions located on the face compared to other locations. The data were associated with large variability which can potentially be explained by the non-uniformity in the fluorescence signal over sub-mm size scales which is demonstrated in chapter 6. It is believed that the level of curettage could affect the resulting data and an additional study would be able to investigate this. By extending the study to a different institute where the level of curettage is different the resulting trend of the fluorescence signal could be compared and the affect caused by the level of curettage could be explored.

8.2 Future prospects

The work that is presented in this thesis provides new knowledge about light interaction with skin tissue. The developed code provides a flexible and robust technique of exploring light penetration through a medium. There are aspects of PDT and especially daylight PDT which can be further explored using the developed code. However there are also other areas where the developed model can be applied by appropriately adjusting the simulation parameters. Some of these future application will be discussed below.

8.2.1 Further investigation of PDT

As previously mentioned, the change in concentration of oxygen during treatment is something important to consider for further improvements. When this is considered it will be possible to study fractionated PDT where the levels of oxygen is allowed to recover between intervals of light treatment [69, 70]. By theoretically simulating fractionated PDT the aim would be to investigate the potential and limitations of this treatment method further. This would allow for comparison with other treatment modalities and exploration of optimal treatment parameters during the fractionation. This includes the length of both the individual light bursts as well as the length of the 'dark' periods in-between bursts.

One of the main limitations of daylight PDT is the weather dependency. The number of days when daylight PDT is possible, is both limited and hard to predict, especially in places

in temperate and boreal latitudes. This results in difficulties in treatment planning and last-minute cancellations of treatments. Patient choice in treatment is now recognised as important, and, in this respect, it should be noted that daylight PDT is generally the preferred choice compared to conventional PDT [78]. However, patients who have made arrangements for daylight PDT should not have to reschedule due to bad weather. For this reason it seems reasonable to develop indoor facilities where patients can be treated irrespective of outdoor conditions all year round. By creating an environment which mimics daylight illumination this could be achieved. This would require the exploration of the suitability of different light sources and the arrangement of light within the room. The required total irradiance from the light sources experienced by the lesion at different places within the room has to be considered. An environment where patients can move around freely and comfortably would be the ideal situation, but to achieve this the light illumination across the allocated room has to be considered. The MCRT model developed in this thesis can assist the comparison of different light sources to establish the most appropriate light source to implement.

Further investigations of daylight PDT that could be considered include the possibility of treating skin lesions through a glass window, for example in a conservatory. This would eliminate the minimum temperature restriction and might improve the comfort of patients. To achieve this, a glass layer and its associated parameters have to be included within the model.

Additionally, daylight PDT for different locations around the world should be considered. The irradiance of the daylight and the ratio between the direct and diffuse component will change for different locations and this could be explored using the model by adjusting the daylight spectra used to simulate daylight PDT.

The current photobleaching equation adopts a single exponential to estimate the photobleaching of PpIX during light illumination. However, recent work in our group suggests that the photobleaching equation could be better represented by a double exponential. This is motivated by a fast photobleaching during the initial illumination which subsequently slows down. Depending on the ratio between the two different photobleaching constants, deeper treatment than originally estimated could be achieved. The model has the potential to incorporate such changes in the photobleaching equation and also include investigations of alternative photobleaching equations. However the limitations lie within the available supporting

data required for efficient representation of the process.

8.2.2 Areas where MCRT can be adopted for light based treatments

Even though MCRT modelling has proven to be a useful tool for investigations of PDT, it is not the only area of research where it can be adopted. Other light based therapies such as port wine stains, acne treatment, hair removal and tattoo removal can adopt this simulation technique to further explore the interaction between skin tissue and light. Even though many of these research areas have already adopted MCRT modelling [123, 224, 225] further development can be made by incorporating techniques discussed in this thesis.

PDT and photodiagnosis is not only adopted for topical applications of skin tissue. It has also been proven to be a useful tool in other areas of medicine such as brain tumours [226] and disorders in the urinary tracts [227]. In brain tumours the selective accumulation of PpIX within brain tumours tissue can be used to assist the surgery. The fluorescence signal produced by the PpIX allows for tumour segments to be identified that would otherwise easily be missed. PDT can also be adopted to selectively treat small tumour segments which are otherwise difficult to remove using surgery [228, 229]. MCRT modelling would assist the development of these treatment regimes since it is important to understand the penetration of light through the tissue during both the photodiagnosis and PDT. Determining where the fluorescence light comes from and the possible treatment depth would allow further exploration of the potential role that light could take during surgery. To accurately simulate this, both optical properties and tissue structures have to be established.

8.2.3 Further experimental and clinical explorations

Accurate input parameters are based on experimentally and clinically determined data. One of the main limitations throughout this thesis has been to determine appropriate tissue parameters. Further determination of *in vivo* optical properties of different tissue types is required to extend and improve the existing models. For example, to be able to compare different tumour types, the optical properties of these have to be determined over the required wavelength range.

In a similar way to methods described in chapter 7 it is common to use fluorescence measurements to monitor treatment progress. PpIX fluorescence is most commonly measured as a result of excitation using blue light. Since the characteristic red fluorescence light is spectrally

very different from the illuminating blue light source it is easy to develop optical instruments for this situation. One limitation with using this approach is the shallow penetrated depth associated with blue light. This has the consequence of only fluorescence light from the most superficial layers being recorded. An alternative approach would be to adopt a red light source which would achieve deeper penetration. With appropriate filters to block out the excitation wavelengths, it would be possible to record fluorescence light from deeper situated tissue segments. It would also be of interest to explore the wide field fluorescence properties to investigate the distribution of fluorescence light across the tumour tissue [230].

8.3 Conclusion

Even though PDT is widely used for treating NMSC, there are still treatment parameters that are not yet optimised. This thesis has focused on theoretical simulations of PDT using MCRT modelling in an attempt to further explore different treatment parameters. By exploring different treatment conditions knowledge about light interaction with skin tissue during PDT has increased. This thesis has also explored daylight as an alternative light source for treating superficial skin lesions, the temporal and spatial dependence of PpIX production as well as different tissue structures. The main issue with theoretical simulation of skin tissue is that there is no such thing as a generic or average patient. Tumour and skin properties will vary between people which makes standardising treatment protocols difficult. For this reason the future focuses should lie in individualising treatments according to patient characteristics. By combining theoretical simulations with data from the clinical environment further improvement and developments can be made to achieve better treatment outcomes for individual patients.



Appendix: Monte Carlo radiation transfer modelling, code set-up and validation

A.1 Path length summation

To improve the signal to noise ratio, a path length summation approximation was adopted. This was first introduced by Lucy in 1999 [141]. The two quantities in section 2.4.1 that were considered, fluence rate and absorption rate are described in further detail here.

A.1.1 Absorption rate

The absorption rate is defined as the amount of energy absorbed per cubic centimetre per unit time. Instead of counting each individual absorption event, the energy from each photon multiplied by the probability of being absorbed within a grid cell is considered. This way, the contribution from photons that do not interact within a grid cell is still considered. This therefore results in an improved signal to noise. Hence for each grid cell the energy from a

single photon packet can be expressed by,

$$E_{prop} = E_i \mu_a l \quad (\text{A.1})$$

Where E_i is the energy of a single photon packet, μ_a is the absorption coefficient within the grid cell and l is the distance travelled within the grid cell. The absorption coefficient corresponds to the probability of a photon being absorbed, and $\mu_a l$ is therefore the probability of a photon being absorbed over the travelled distance l . Hence, E_{prop} is the proportion of energy from that energy packet which contribute to the total absorbed energy within that grid cell. By dividing by the voxel volume, ΔV and the total time of the illumination Δt and summing for all photon contributions within the grid cell, the energy absorption rate per cubic centimetre is determined,

$$Q = \frac{E_i}{\Delta V \Delta t} \sum_i \mu_a l = \frac{IA}{N \Delta V} \sum_i \mu_a l \quad (\text{A.2})$$

Here the sum, \sum_i corresponds to the summation of all contribution within the grid cell. A corresponds to the illumination region and I corresponds to the irradiance or the light source. The calculation is performed for all the grid cell in the simulated region.

A.1.2 Fluence rate

The fluence rate is defined as the energy flow per unit area per unit time regardless of the flow direction. The energy density u_e (J cm^{-3}) is defined as the optical energy per unit volume and is obtained by,

$$u_e = \frac{\psi}{c} \quad (\text{A.3})$$

Where c is the speed of light in the medium. To determine the energy volume density the following steps can be applied. The time each photon packet spends within each grid cell is defined as $\delta t = l/c$, where l is the propagating distance within the grid cell. From this the energy contribution from the energy to the grid cell is,

$$E_{\text{contr}} = E_i \frac{\delta t}{\Delta t} = \frac{E_i l}{\Delta t c} \quad (\text{A.4})$$

Where E_i is the energy of a photon packet. If the contributions from all the photo packets propagating through the grid cell, the energy volume density is obtained,

$$u_e = \frac{\sum_i E_{\text{contr}}}{\Delta V} = \frac{\sum_i E_i l}{\Delta t \Delta V c} = \frac{IA \Delta t}{N} \frac{1}{\Delta t \Delta V c} \sum_i l = \frac{IA}{\Delta V N c} \sum_i l \quad (\text{A.5})$$

Hence the fluence rate can be expressed using the following path length summation

$$\psi = \frac{IA}{\Delta V N} \sum_i l \quad (\text{A.6})$$

The absorption rate is defined as the absorbed energy from the propagating photons and can therefore be expressed as $Q = \mu_a \psi$, which is clear from equation A.2 and A.6.

B

Appendix: Theoretical determination of continuous protoporphyrin IX production

The toxicity, concentration profile and fluorescence signal for sets 1-8 in table 4.2 were generated using the MCRT model developed in chapter 4. Different weather conditions (clear and overcast) during daylight PDT as well as conventional PDT, where the Aktelite was simulated, were compared. The motivation for exploring all the sets of parameters suggested in table 4.2 was to determine the effect that the different parameters had on the concentration, toxicity as well as fluorescence signal during the incubation time. The graphical representation of the different sets for the toxicity/photodynamic dose (PDD) as well as the fluorescence is displayed in this appendix. From the results, a discussion of the effect the different parameters had on the treatment depths and fluorescence was carried out and summarised in table 4.3 in chapter 4.

As a comparison the PDD (figure B.1) as well as the fluorescence (figure B.2) for set 1 (table 4.2) are displayed in the appendix as well as in chapter 4.

Appendix B. Appendix: Theoretical determination of continuous protoporphyrin IX production

The second set of parameters (set 2, table 4.2) were taken from the literature [181]) although argued to not be reasonable due to the short clearance rate. However this set of parameters, shown in figure B.3, generated treatment depths similar to that of the first set of parameters. Even though the clearance rate is fast, the initial concentration was high and the conversion rate from MAL to PpIX was slow. From equation 4.8, this generated a PpIX distribution that is similar to the one suggested by the initial set of parameters. The results are displayed in figure 4.4. However it is important to also consider the relevance of the values of the parameters. Since the PpIX distribution was comparable the evolution of the fluorescence signal with time during the incubation period was also comparable and displayed in figure B.4, which also shows similar trend as set 1.

For the third set of parameters, the parameter A was reduced compared to the initial set. This is equivalent to a reduced initial concentration, a reduced yield or a slower conversion rate from MAL to PpIX. This resulted in a lower concentration of PpIX and due to the nature of equation 4.9 has the same shape as set 1, however with a lower absolute value. Understandably this also resulted in more shallow light penetration, as shown in figure B.5. Due to the lower distribution of PpIX the fluorescence signal gradually increased in a more linear fashion, displayed in figure B.6, compared to sets 1 and 2. When adopting set 4, parameter A was instead increased which resulted in a higher PpIX concentration where the PpIX reached into deeper levels. Consequently this resulted in deeper treatment depths, indicated in figure B.7. The fluorescence signal resulted in an instantaneous increase in strength, where this level was then maintained throughout the following 170 min. Hence even though the distribution of PpIX builds up within the tissue, only the fluorescence signal from superficial layers will be detected through the surface observations. When the relaxation time determining the rate at which PpIX was cleared from the tissue (τ_p) was increased and reduced by a factor of 100, there was not a significant change of the fluorescence signal indicated in figures B.10 and B.12, from the model however there was a larger difference in treatment depth as demonstrated in figure B.9 and B.11. The concentration profile for these two sets of parameters are illustrated in figure 4.4 and indicates a large difference in PpIX distribution, which is not carried through to the fluorescence signal. However when the relaxation time was reduced even further (set B2, table 4.4) the fluorescence signal displayed a more linear trend (figure 4.12).

When the diffusivity was reduced or alternatively increased the distribution of PpIX was

reduced and increased accordingly. A higher diffusion coefficient allows the prodrug to diffuse quicker into the skin. Following previous arguments this resulted in a fast increase of the fluorescence signal due to the high concentration of PpIX at superficial layers seen in figure B.14. The opposite effect occurred when the diffusivity was lower which resulted in a significantly different change in fluorescence signal with time, as demonstrated in figure B.16. Similarly set B1 hosts a low diffusion coefficient and therefore also resulted in a linear increase in the fluorescence signal (figure 4.11).

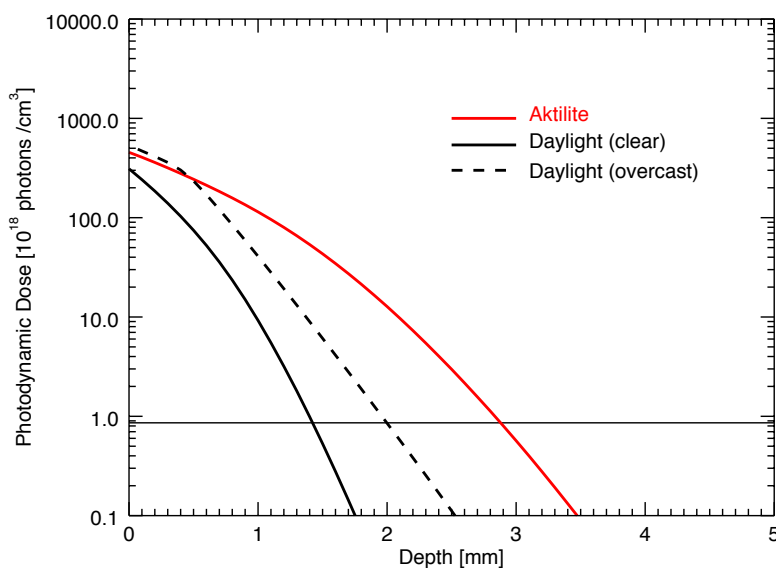


Figure B.1: Figure showing the PDD for set 1 of the parameters in table 4.2 where $A = 3.47 \times 10^{15} \text{ m}^{-3} \text{ s}^{-1}$, $\tau_p = 4680 \text{ s}$ and $D = 0.69 \times 10^{-10} \text{ m}^2 \text{ s}^{-1}$.

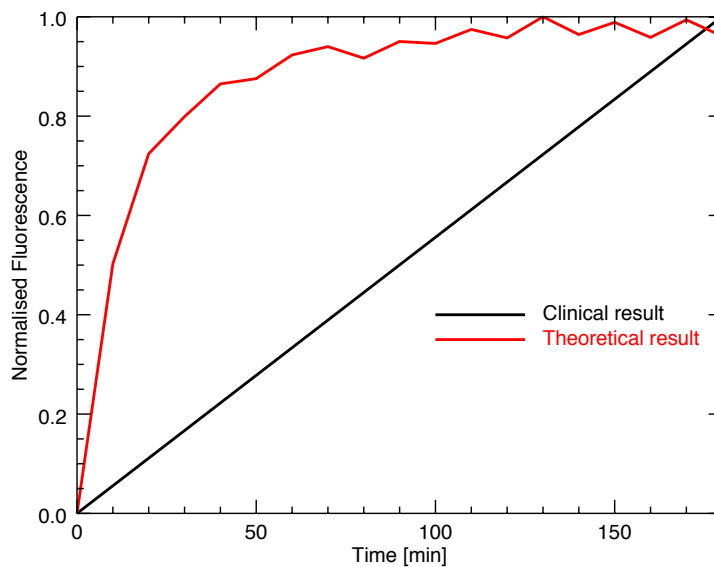


Figure B.2: Figure showing how the fluorescence signal changes with time during the occlusive treatment phase. This figure corresponds to set 2 of the parameters in table 4.2 where $A = 3.47 \times 10^{15} \text{ m}^{-3} \text{ s}^{-1}$, $\tau_p = 4680 \text{ s}$ and $D = 0.69 \times 10^{-10} \text{ m}^2 \text{ s}^{-1}$. The linear line (black) corresponds to the trend determined from the clinical data in chapter 6 and the fluorescence signal for set 3 (red) is compared to the fluorescence signal for set 1 (dashed).

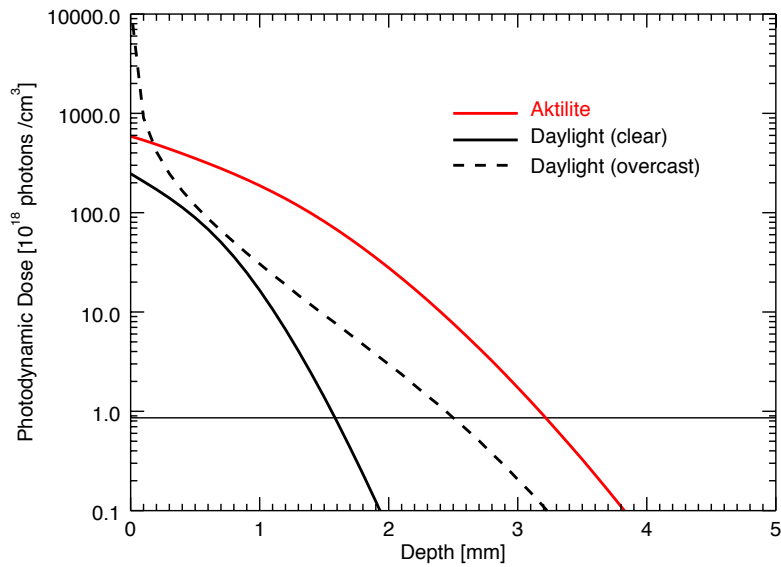


Figure B.3: Figure showing the PDD for set 2 of the parameters in table 4.2 where $A = 3.47 \times 10^{15} \text{ m}^{-3} \text{ s}^{-1}$, $\tau_p = 84 \text{ ms}$ and $D = 0.69 \times 10^{-10} \text{ m}^2 \text{ s}^{-1}$.

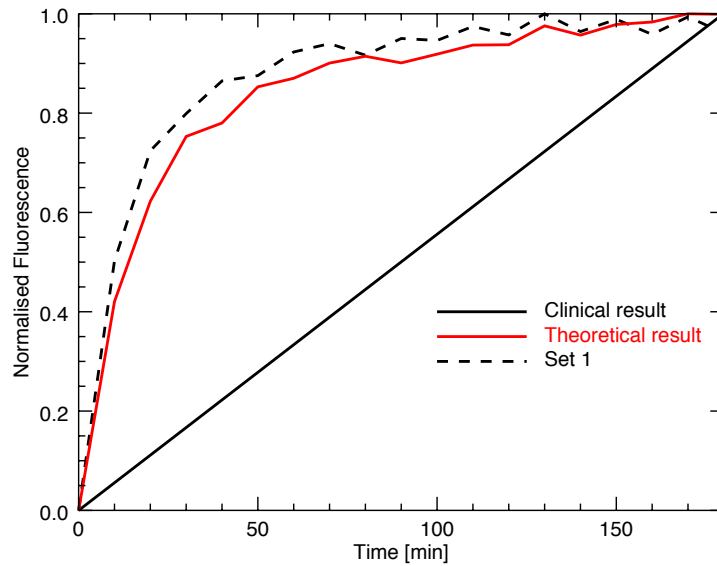


Figure B.4: Figure showing how the fluorescence signal changes with time during the occlusive treatment phase. This figure corresponds to set 2 of the parameters in table 4.2 where $A = 3.47 \times 10^{15} \text{ m}^{-3} \text{ s}^{-1}$, $\tau_p = 84 \text{ ms}$ and $D = 0.69 \times 10^{-10} \text{ m}^2 \text{ s}^{-1}$. The linear line (black) corresponds to the trend determined from the clinical data in chapter 6 and the fluorescence signal for set 3 (red) is compared to the fluorescence signal for set 1 (dashed).

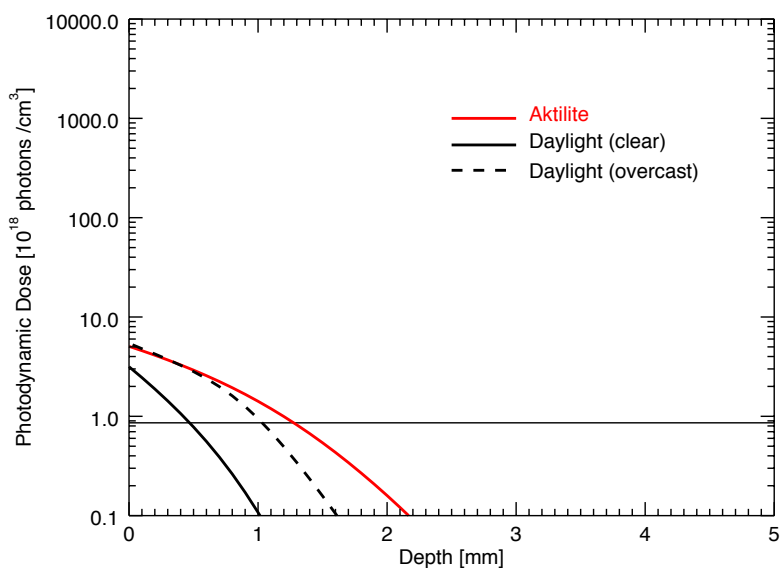


Figure B.5: Figure showing the PDD for set 3 of the parameters in table 4.2 where $A = 3.47 \times 10^{10} \text{ m}^{-3} \text{ s}^{-1}$, $\tau_p = 4680 \text{ s}$ and $D = 0.69 \times 10^{-10} \text{ m}^2 \text{ s}^{-1}$.

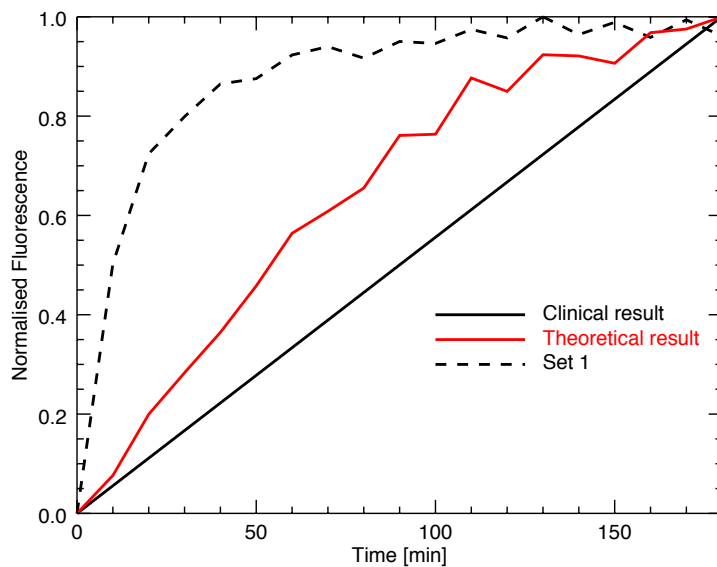


Figure B.6: Figure showing how the fluorescence signal changes with time during the occlusive treatment phase. This figure corresponds to set 3 of the parameters in table 4.2 where $A = 3.47 \times 10^{10} \text{ m}^{-3} \text{ s}^{-1}$, $\tau_p = 4680 \text{ s}$ and $D = 0.69 \times 10^{-10} \text{ m}^2 \text{ s}^{-1}$. The linear line (black) corresponds to the trend determined from the clinical data in chapter 6 and the fluorescence signal for set 3 (red) is compared to the fluorescence signal for set 1 (dashed).

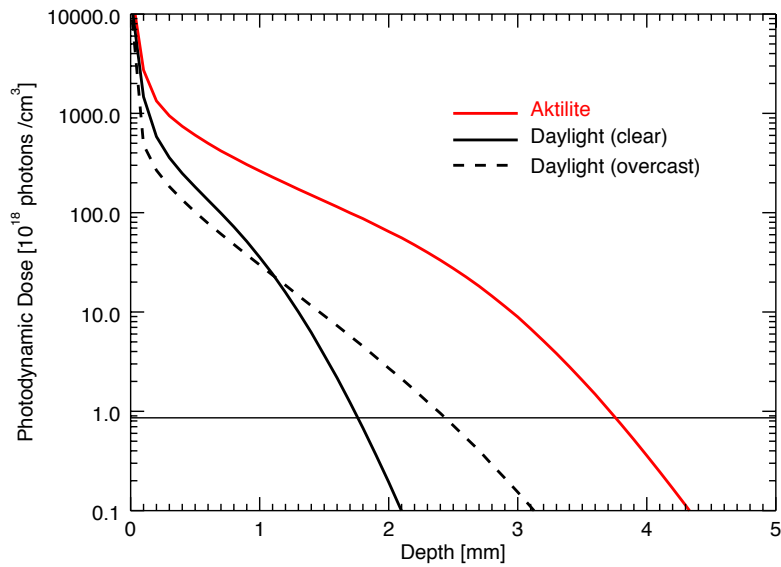


Figure B.7: Figure showing the PDD for set 4 of the parameters in table 4.2 where $A = 3.47 \times 10^{14} \text{ m}^{-3} \text{ s}^{-1}$, $\tau_p = 4680 \text{ s}$ and $D = 0.69 \times 10^{-10} \text{ m}^2 \text{ s}^{-1}$.

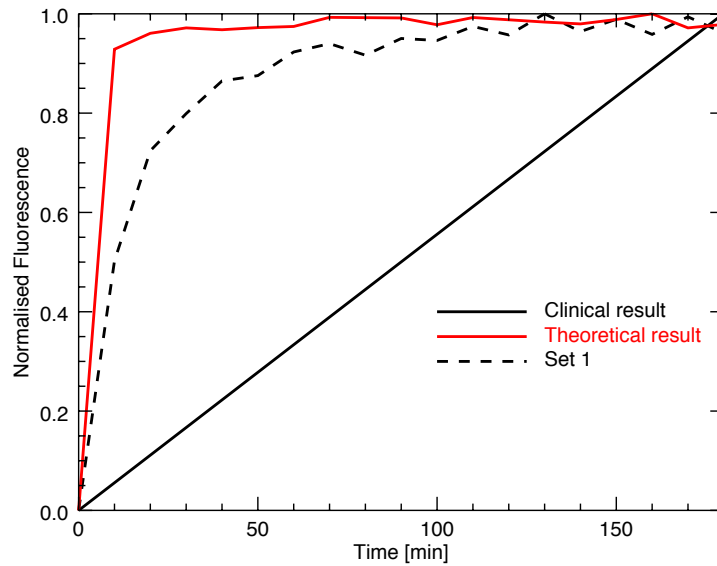


Figure B.8: Figure showing how the fluorescence signal changes with time during the occlusive treatment phase. This figure corresponds to set 4 of the parameters in table 4.2 where $A = 3.47 \times 10^{14} \text{ m}^{-3} \text{ s}^{-1}$, $\tau_p = 4680 \text{ s}$ and $D = 0.69 \times 10^{-10} \text{ m}^2 \text{ s}^{-1}$. The linear line (black) corresponds to the trend determined from the clinical data in chapter 6 and the fluorescence signal for set 4 (red) is compared to the fluorescence signal for set 1 (dashed).

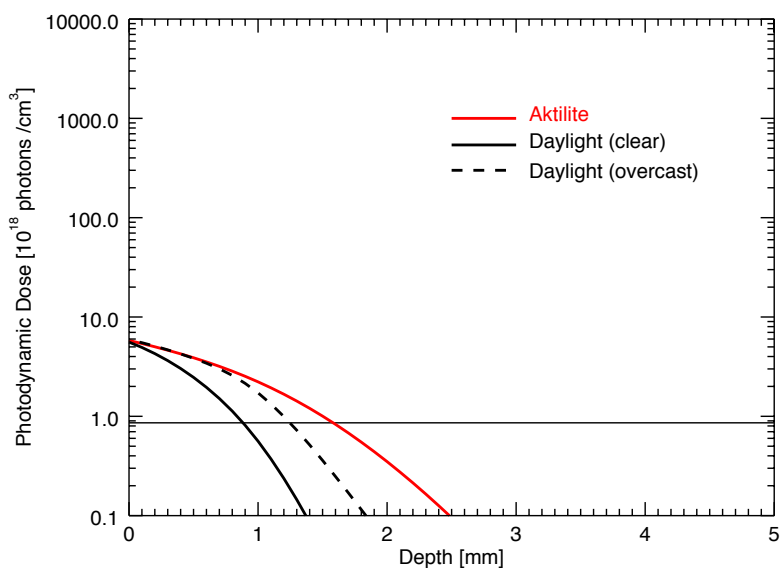


Figure B.9: Figure showing the PDD for set 5 of the parameters in table 4.2 where $A = 3.47 \times 10^{12} \text{ m}^{-3} \text{ s}^{-1}$, $\tau_p = 46.80 \text{ s}$ and $D = 0.69 \times 10^{-10} \text{ m}^2 \text{ s}^{-1}$.

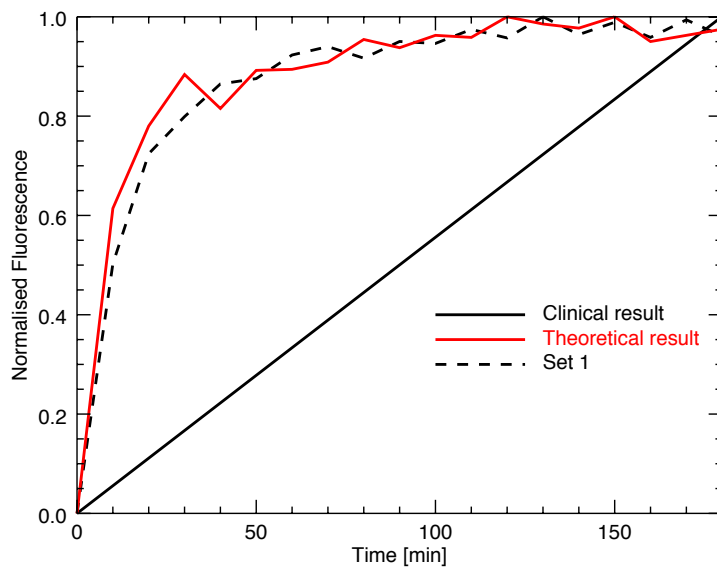


Figure B.10: Figure showing how the fluorescence signal changes with time during the occlusive treatment phase. This figure corresponds to set 5 of the parameters in table 4.2 where $A = 3.47 \times 10^{12} \text{ m}^{-3} \text{ s}^{-1}$, $\tau_p = 46.80 \text{ s}$ and $D = 0.69 \times 10^{-10} \text{ m}^2 \text{ s}^{-1}$. The linear line (black) corresponds to the trend determined from the clinical data in chapter 6 and the fluorescence signal for set 5 (red) is compared to the fluorescence signal for set 1 (dashed).

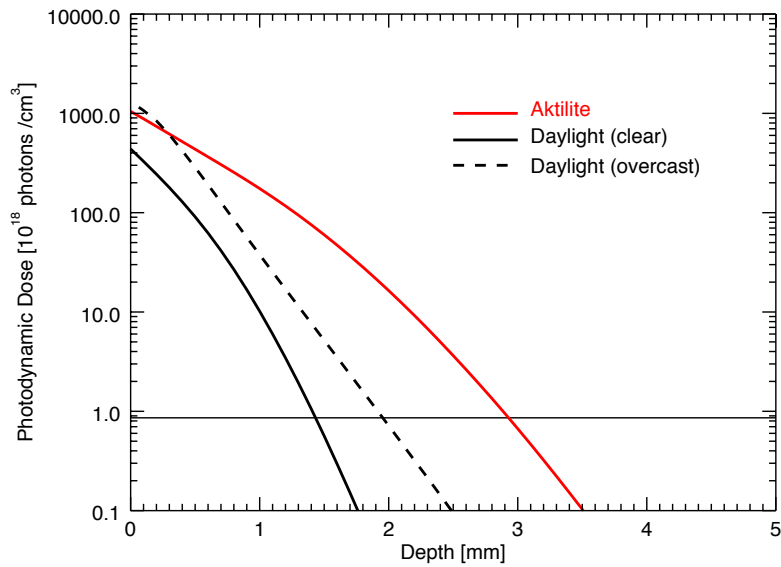


Figure B.11: Figure showing the PDD for set 6 of the parameters in table 4.2 where $A = 3.47 \times 10^{12} \text{ m}^{-3} \text{ s}^{-1}$, $\tau_p = 468000 \text{ s}$ and $D = 0.69 \times 10^{-10} \text{ m}^2 \text{ s}^{-1}$.

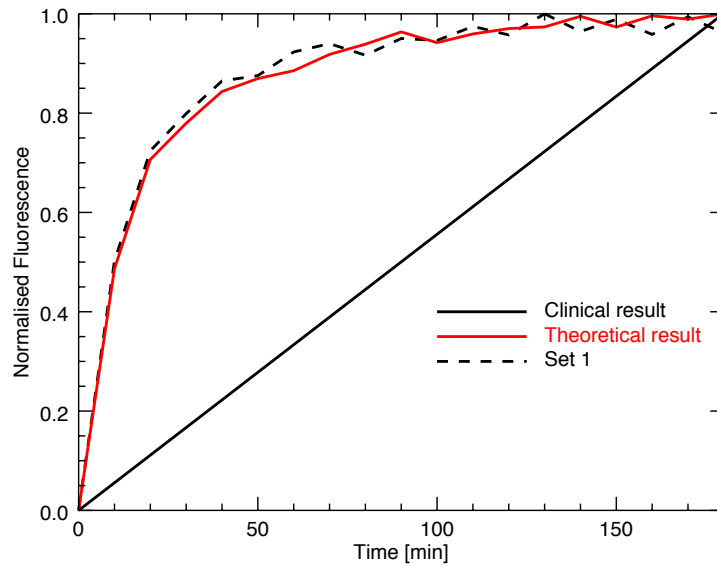


Figure B.12: Figure showing how the fluorescence signal changes with time during the occlusive treatment phase. This figure corresponds to set 6 of the parameters in table 4.2 where $A = 3.47 \times 10^{12} \text{ m}^{-3} \text{ s}^{-1}$, $\tau_p = 468000 \text{ s}$ and $D = 0.69 \times 10^{-10} \text{ m}^2 \text{ s}^{-1}$. The linear line (black) corresponds to the trend determined from the clinical data in chapter 6 and the fluorescence signal for set 6 (red) is compared to the fluorescence signal for set 1 (dashed).

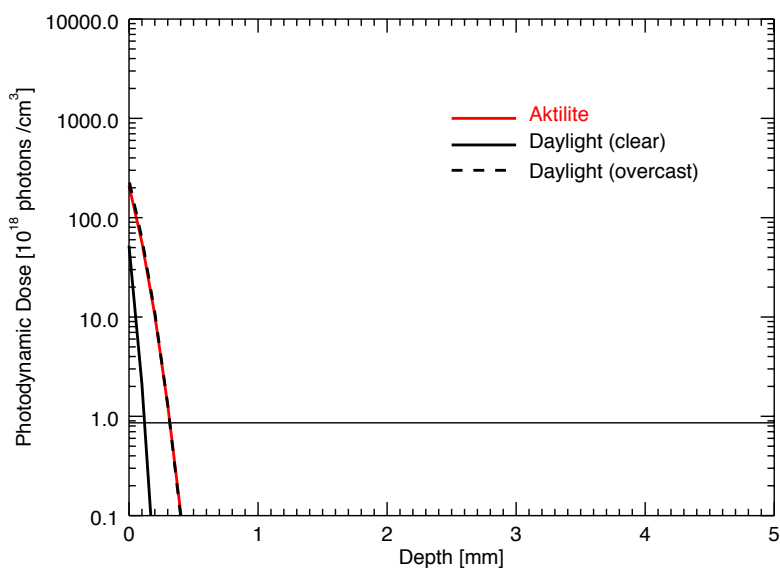


Figure B.13: Figure showing the PDD for set 7 of the parameters in table 4.2 where $A = 3.47 \times 10^{12} \text{ m}^{-3} \text{ s}^{-1}$, $\tau_p = 4680 \text{ s}$ and $D = 1 \times 10^{-12} \text{ m}^2 \text{ s}^{-1}$.

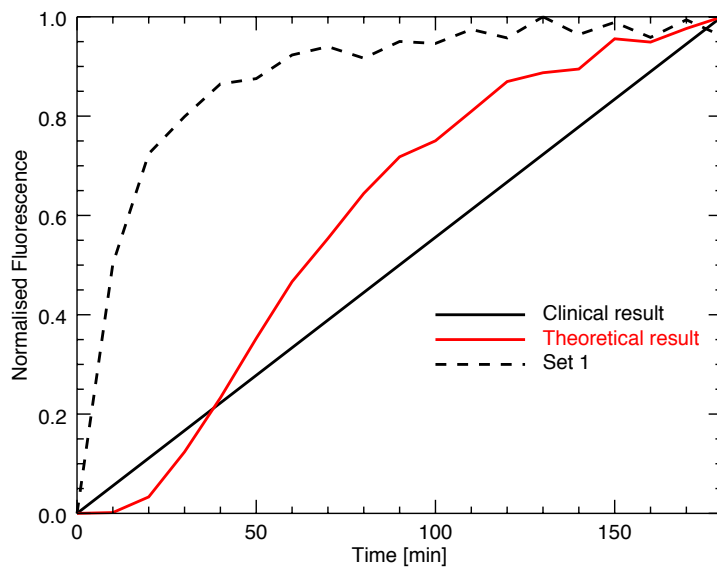


Figure B.14: Figure showing how the fluorescence signal changes with time during the occlusive treatment phase. This figure corresponds to set 7 of the parameters in table 4.2 where $A = 3.47 \times 10^{12} \text{ m}^{-3} \text{ s}^{-1}$, $\tau_p = 4680 \text{ s}$ and $D = 1 \times 10^{-12} \text{ m}^2 \text{ s}^{-1}$. The linear line (black) corresponds to the trend determined from the clinical data in chapter 6 and the fluorescence signal for set 7 (red) is compared to the fluorescence signal for set 1 (dashed).

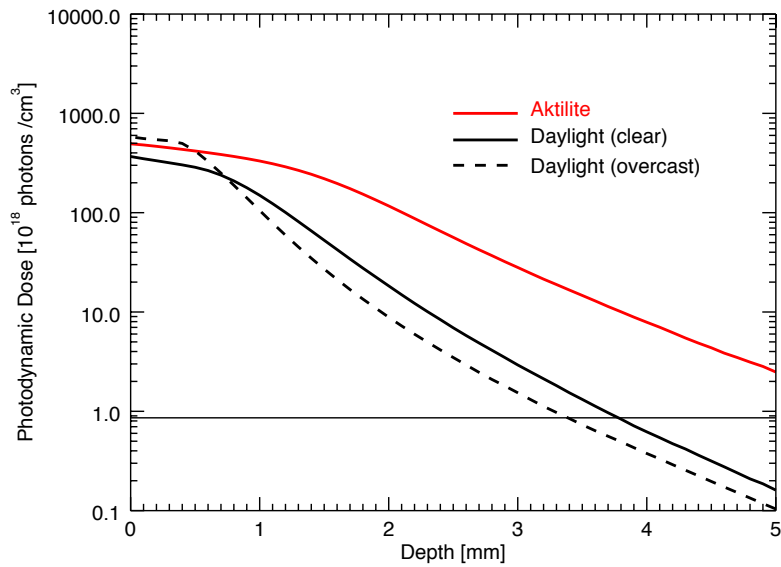


Figure B.15: Figure showing the PDD for set 8 of the parameters in table 4.2 where $A = 3.47 \times 10^{12} \text{ m}^{-3} \text{ s}^{-1}$, $\tau_p = 4680 \text{ s}$ and $D = 1 \times 10^{-8} \text{ m}^2 \text{ s}^{-1}$.

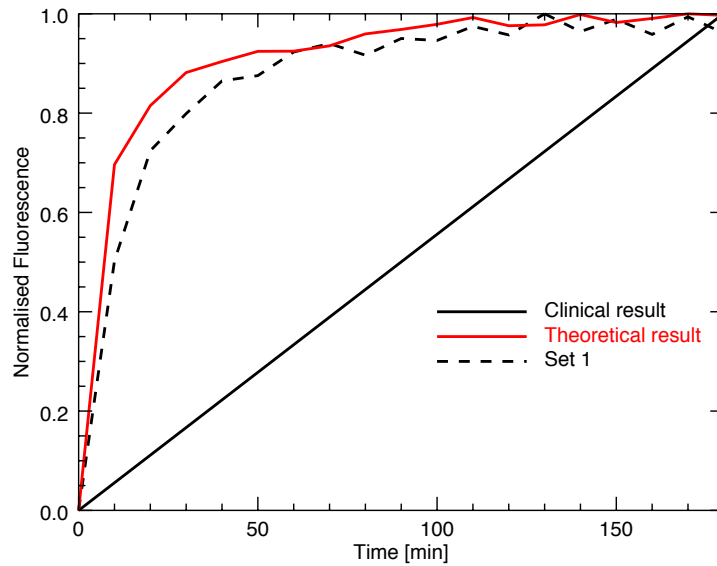
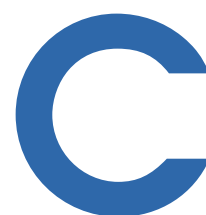


Figure B.16: Figure showing how the fluorescence signal changes with time during the occlusive treatment phase. This figure corresponds to set 8 of the parameters in table 4.2 where $A = 3.47 \times 10^{12} \text{ m}^{-3} \text{ s}^{-1}$, $\tau_p = 4680 \text{ s}$ and $D = 1 \times 10^{-8} \text{ m}^2 \text{ s}^{-1}$. The linear line (black) corresponds to the trend determined from the clinical data in chapter 6 and the fluorescence signal for set 8 (red) is compared to the fluorescence signal for set 1 (dashed).



Appendix: Light distribution modelling of skin ageing and different skin types

The absorption properties for the epidermal layers not shown in chapter 5 are shown in figure C.1. The absorption properties for skin type II, IV and V are graphically represented for ages 30, 55 and 80 years.

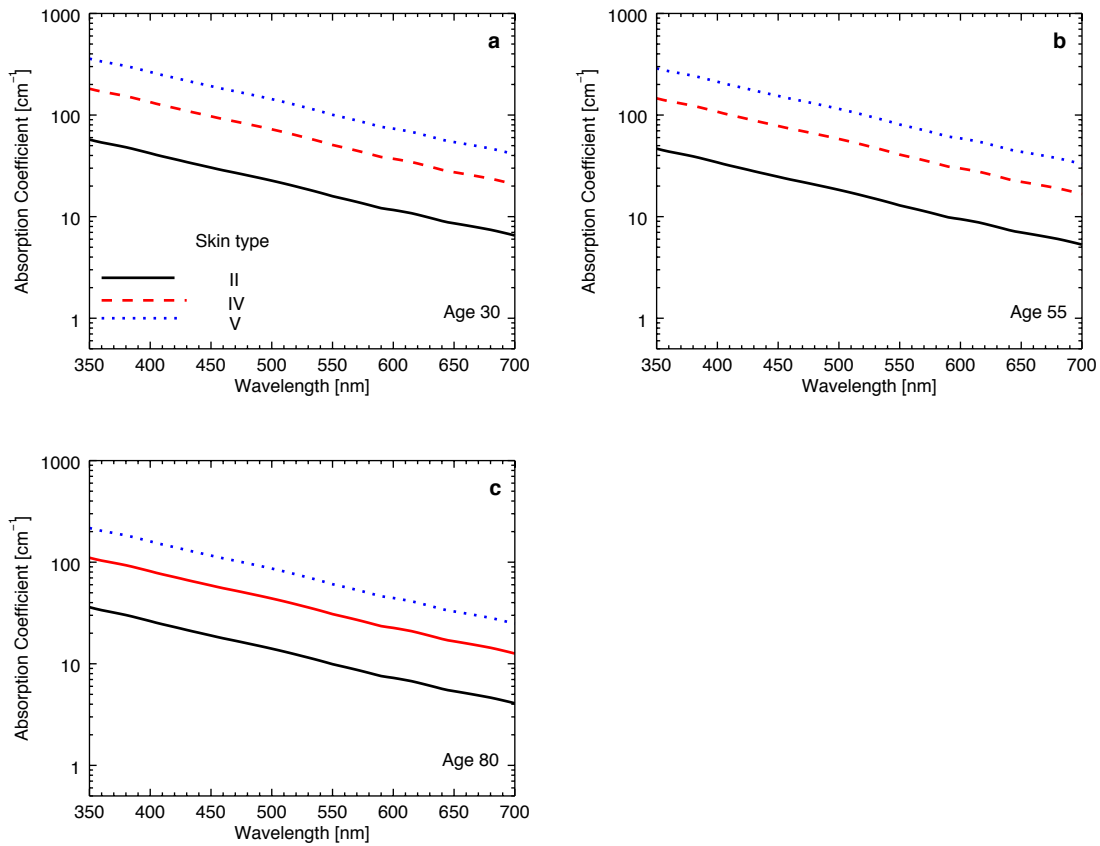


Figure C.1: Figure showing the optical properties adopted in the MCRT model to represent different ages and skin types. The absorption properties for the epidermal layers are shown in the figure for three different skin types: II(black), IV (red) and V(blue) for three different ages a) 30 years, b) 55 years and c) 80 years.

Figure C.2 shows the normalised fluence rate for two different ages for skin types II, IV and V. The normalised fluence rate is defined as the fluence rate divided by the irradiance of the incident light. Three different wavelengths were simulated using the Monte Carlo radiation transfer (MCRT) code developed and described in chapter 5. The wavelengths that were simulated were 405 nm, 540 nm and 630 nm.

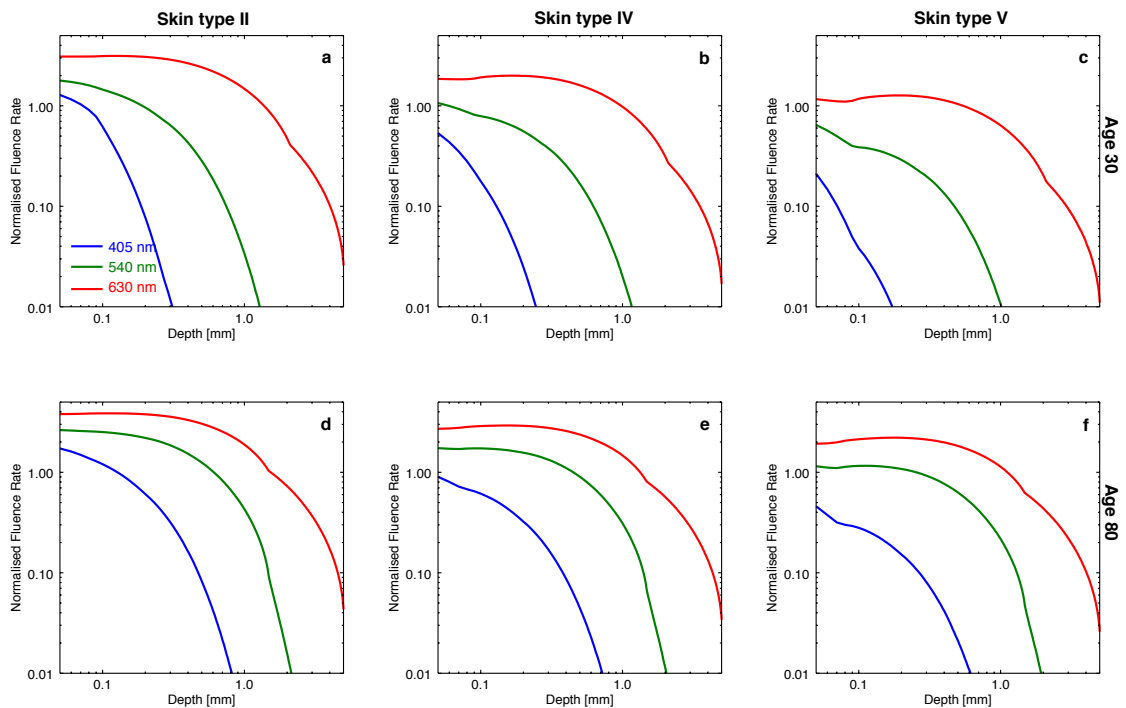


Figure C.2: Figure showing normalised fluence rate as a function of depth for different ages and skin types. Each figure demonstrates fluence rate for a certain age and skin type where three different wavelengths were investigated: 405 nm (blue), 540 nm (green) and 630 nm (red). The figures each correspond to the fluence rate for a) skin type II, age 30, b) skin type IV, age 30 c) skin type V age 30 d) skin type I, age 80, e) skin type IV, age 30 and d) skin type V age 80.

Figure C.3 shows the photodynamic dose (PDD) for three different light conditions, daylight (clear conditions), daylight (overcast conditions) as well as the Aktilite. Where the figure shows the results generated after a total delivered light dose of 75 J cm^{-2} . The total irradiance for the different light sources were assumed to be: daylight, clear: 41 mW/cm^2 , daylight, overcast: 8 mW cm^{-2} and the Aktilite: 82 mW cm^{-2} . Hence the same light dose corresponds to different treatment times. Figure C.3 shows the PDD for three different ages (30, 55 and 80 years) for three different skin types (II, IV and V). The results supports the results found in chapter 5, where the treatment depth increases with age but reduces with skin type classification number.

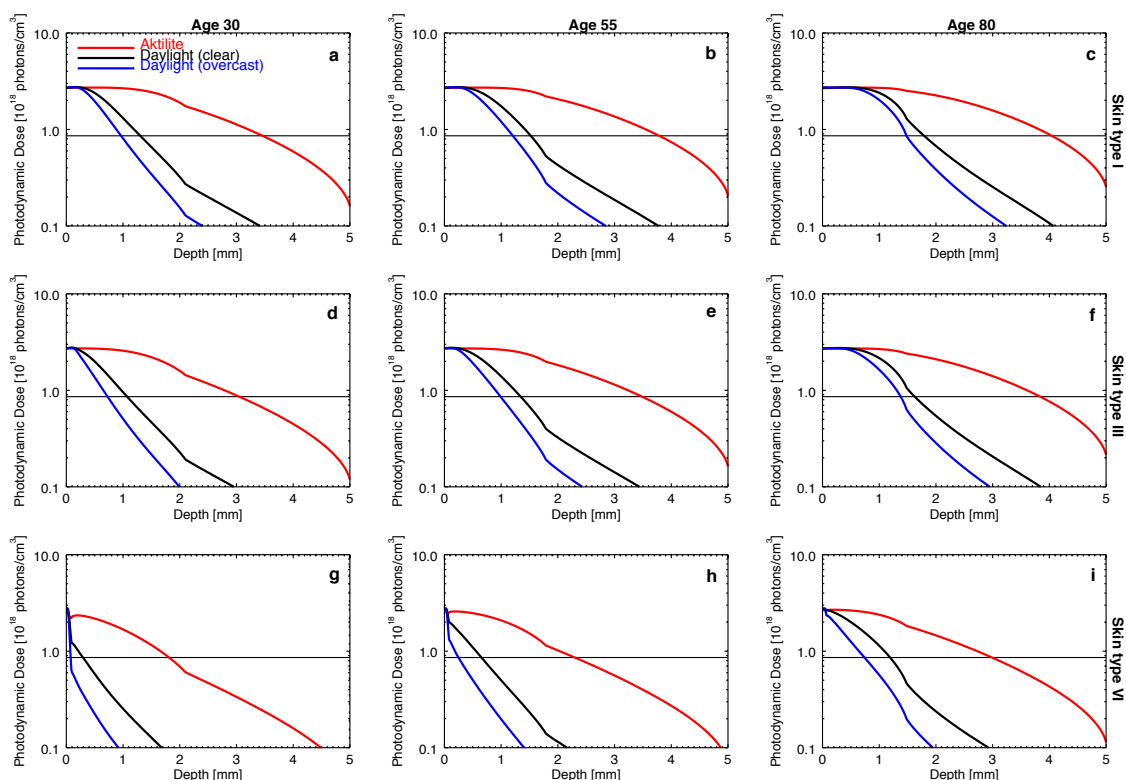


Figure C.3: Photodynamic dose corresponding to 75 Jcm^{-2} for the different light sources at age 30, 55 and 80 and for skin types II, IV and V. Three light sources were compared: daylight for clear conditions (black), daylight during overcast (blue) and the artificial light source, Aktlita (red). The results show the change in effective penetration depth with age and skin type. The horizontal line corresponds to the adopted toxic threshold, which is the same threshold adopted in previous chapters. The different figures correspond to: a) skin type II, age 30, b) skin type II, age 55, c) skin type II, age 80, d) skin type IV, age 30, e) skin type IV, age 55, f) skin type IV, age 80, g) skin type V, age 30, h) skin type V, age 55 and i) skin type V, age 80.

D

Appendix: A quantitative study of in vivo protoporphyrin IX fluorescence build up during occlusive treatment phases: ethical approval



15th January 2015
Catherine Louise Campbell
School of Physics and Astronomy

Ethics Reference No: <i>Please quote this ref on all correspondence</i>	PA11325
Project Title:	Quantitative Study of In vivo Protoporphyrin IX Fluorescence during build up
Researchers Name(s):	Catherine Louise Campbell
Supervisor(s):	K Wood & CTA Brown

Thank you for submitting your application which was considered at the School of Physics and Astronomy School Ethics Committee meeting on the 8th January 2015. The following documents were reviewed:

1. Ethical Application Form 15th January 2015

The University Teaching and Research Ethics Committee (UTREC) approves this study from an ethical point of view. Please note that where approval is given by a School Ethics Committee that committee is part of UTREC and is delegated to act for UTREC.

Approval is given for three years. Projects, which have not commenced within two years of original approval, must be re-submitted to your School Ethics Committee.

You must inform your School Ethics Committee when the research has been completed. If you are unable to complete your research within the 3 three year validation period, you will be required to write to your School Ethics Committee and to UTREC (where approval was given by UTREC) to request an extension or you will need to re-apply.

Any serious adverse events or significant change which occurs in connection with this study and/or which may alter its ethical consideration, must be reported immediately to the School Ethics Committee, and an Ethical Amendment Form submitted where appropriate.

Approval is given on the understanding that the 'Guidelines for Ethical Research Practice' <https://www.st-andrews.ac.uk/utrec/guidelines/> are adhered to.

Yours sincerely

Wendy Clark

UTREC Administrator for Physics and Astronomy
On behalf of
Convenor of the School Ethics Committee



F U N D A Ç Ã O
AMARAL CARVALHO

COMITÊ DE ÉTICA EM PESQUISA Fundação Hospital Amaral Carvalho

Rua Dr. Miranda Junior, 16, Jardim Alvorada – CEP 17.210-300 – Jaú / SP - ☎ (014) 3602-1194 – Ramal - 1552.

Parecer CEPFHAC – 140/11 - Recurso.

Projeto de Pesquisa:

“Diagnóstico e Tratamento do Câncer de Pele por Terapia Fotodinâmica”

Documentos Analisados:

- ✓ Declaração assinada pelo pesquisador Vanderlei Salvador Bagnato, datada de 28 de novembro de 2011;
- ✓ Novo Termo de Consentimento Livre e Esclarecido, versão 2.

Responsável pelo Estudo:

Autoria: Vanderlei Salvador Bagnato – livre-docente – USP

Dra. Ana Gabriela Sálvio – médica dermatologista do Hospital Amaral Carvalho

Trata-se de recurso ao Parecer CEPFHAC nº. 140/11, datado de 25 de novembro de 2011, onde os documentos analisados foram considerados aprovados com recomendação, sendo está o compromisso dos pesquisadores em custear os métodos contraceptivos.

O pesquisador apresentou uma declaração e um novo Termo de Consentimento Livre e Esclarecido contemplando a recomendação do parecer anterior, não restando qualquer óbice.

Diante do exposto, manifestamo-nos pela aprovação sem restrições dos documentos avaliados.

Informamos que os referidos documentos são rubricados pelo colaborador do CEPFHAC, Ricardo Augusto Sartori, e que nenhum dos pesquisadores envolvidos no estudo participou da votação.

Aproveito para recordar-lhe do compromisso de enviar relatórios semestrais referentes à evolução do estudo.

Jaú, 01 de dezembro de 2011.

Dr. Éderson Roberto de Mattos
Coordenador do Comitê de Ética em Pesquisa
Fundação Hospital Amaral Carvalho

PARECER CONSUBSTANCIADO DO CEP

DADOS DO PROJETO DE PESQUISA

Título da Pesquisa: "Acompanhamento da produção de PpIX em carcinoma basocelular de pacientes em tratamento por Terapia Fotodinâmica no Centro de Fototerapia e Fotodiagnóstico do Hospital Amaral Carvalho, em Jaú-São Paulo".

Pesquisador: ANA GABRIELA SALVIO

Área Temática:

Versão: 1

CAAE: 50984515.4.0000.5434

Instituição Proponente: FUNDACAO DOUTOR AMARAL CARVALHO

Patrocinador Principal: UNIVERSIDADE DE SAO PAULO
MM OPTICS LTDA

DADOS DO PARECER

Número do Parecer: 1.404.320

Apresentação do Projeto:

O presente projeto vai avaliar pacientes em tratamento de carcinoma basocelular com o uso de terapia fotodinâmica.

Objetivo da Pesquisa:

O objetivo do projeto é avaliar 12 pacientes do ambulatório de pele e partes moles do Hospital Amaral Carvalho que já se realizam tratamento com terapia fotodinâmica e um creme com aminolevulinato de metila para tratamento de carcinoma de pele, e será realizado a cada 30 minutos a medida do sinal de fluorescência para poder ver se o tempo de três horas de oclusão pode ser reduzido sem prejuízo da eficácia da terapia.

Avaliação dos Riscos e Benefícios:

A terapia já é a padrão para o tratamento desses pacientes, portanto o único risco é o fato do paciente a cada 30 minutos ter que realizar a medida do sinal de fluorescência, o que é um risco mínimo.

Comentários e Considerações sobre a Pesquisa:

O potencial benefício do estudo é poder diminuir o tempo do paciente dentro do hospital, o que

Endereço: Rua das Palmeiras, 89

Bairro: VILA ASSIS

CEP: 17.210-120

UF: SP

Município: JAU

Telefone: (14)3602-1194

Fax: (14)3602-1207

E-mail: cep.aurea@amaralcarvalho.org.br

Continuação do Parecer: 1.404.320

sempre é muito importante em termos de custo e em qualidade de vida do paciente.

Considerações sobre os Termos de apresentação obrigatória:

Foi apresentado o projeto de pesquisa detalhado, o TCLE de forma clara e de fácil entendimento, apresentação da folha de rosto.

Recomendações:

Apresentação dos resultados finais ao CEP.

Conclusões ou Pendências e Lista de Inadequações:

sem pendências

Considerações Finais a critério do CEP:

O colegiado acompanha o parecer do relator.

Informamos que nenhum dos pesquisadores envolvidos no estudo participou da votação.

Aproveito para recordar-lhe do compromisso de enviar relatórios semestrais referentes à evolução do estudo.

Este parecer foi elaborado baseado nos documentos abaixo relacionados:

Tipo Documento	Arquivo	Postagem	Autor	Situação
Informações Básicas do Projeto	PB_INFORMAÇÕES_BÁSICAS_DO_PROJETO_608581.pdf	10/11/2015 15:58:43		Aceito
Folha de Rosto	FolhaDeRosto.pdf	10/11/2015 14:49:32	Jeferson Rodrigo Ramos do Couto	Aceito
Outros	Autorizacaodds.pdf	10/11/2015 14:47:17	Jeferson Rodrigo Ramos do Couto	Aceito
Projeto Detalhado / Brochura Investigador	LattesVanderleiSalvadorBagnato.pdf	20/10/2015 17:26:50	ANA GABRIELA SALVIO	Aceito
Projeto Detalhado / Brochura Investigador	LattesNataliaMayumiInada.pdf	20/10/2015 17:26:33	ANA GABRIELA SALVIO	Aceito
Projeto Detalhado / Brochura Investigador	LattesAnaGabrielaSalvio.pdf	20/10/2015 17:26:21	ANA GABRIELA SALVIO	Aceito
Outros	Documentoscpc.pdf	20/10/2015	Jeferson Rodrigo	Aceito

Endereço: Rua das Palmeiras, 89

Bairro: VILA ASSIS

UF: SP

Telefone: (14)3602-1194

CEP: 17.210-120

Município: JAU

Fax: (14)3602-1207

E-mail: cep.aurea@amaralcarvalho.org.br

Continuação do Parecer: 1.404.320

Outros	Documentoscpc.pdf	11:47:13	Ramos do Couto	Aceito
Outros	onusfinanceiro.pdf	20/10/2015 11:46:24	Jeferson Rodrigo Ramos do Couto	Aceito
Outros	OficioCEPFHAC.pdf	14/10/2015 18:51:40	ANA GABRIELA SALVIO	Aceito
TCLE / Termos de Assentimento / Justificativa de Ausência	TCLEGabriela.pdf	14/10/2015 18:50:40	ANA GABRIELA SALVIO	Aceito
Projeto Detalhado / Brochura Investigador	PPGabrielaPplX.pdf	14/10/2015 18:49:42	ANA GABRIELA SALVIO	Aceito

Situação do Parecer:

Aprovado

Necessita Apreciação da CONEP:

Não

JAU, 05 de Fevereiro de 2016

Assinado por:
Oswaldo Contador Junior
(Coordenador)

Endereço: Rua das Palmeiras, 89

CEP: 17.210-120

Bairro: VILA ASSIS

UF: SP

Município: JAU

Telefone: (14)3602-1194

Fax: (14)3602-1207

E-mail: cep.aurea@amaralcarvalho.org.br

Scanned by CamScanner

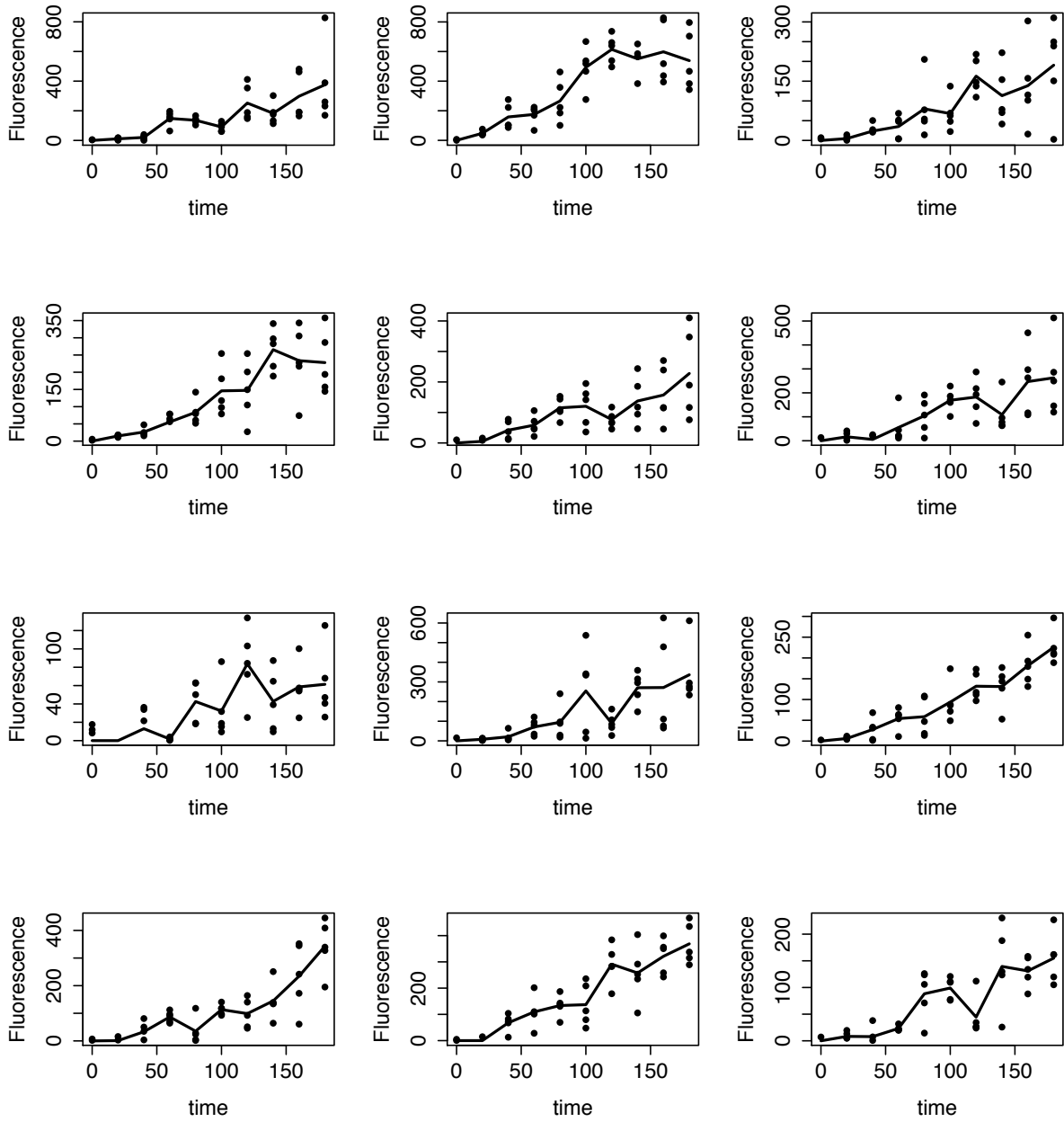
Appendix D. Appendix: A quantitative study of in vivo protoporphyrin IX fluorescence build up during occlusive treatment phases: ethical approval

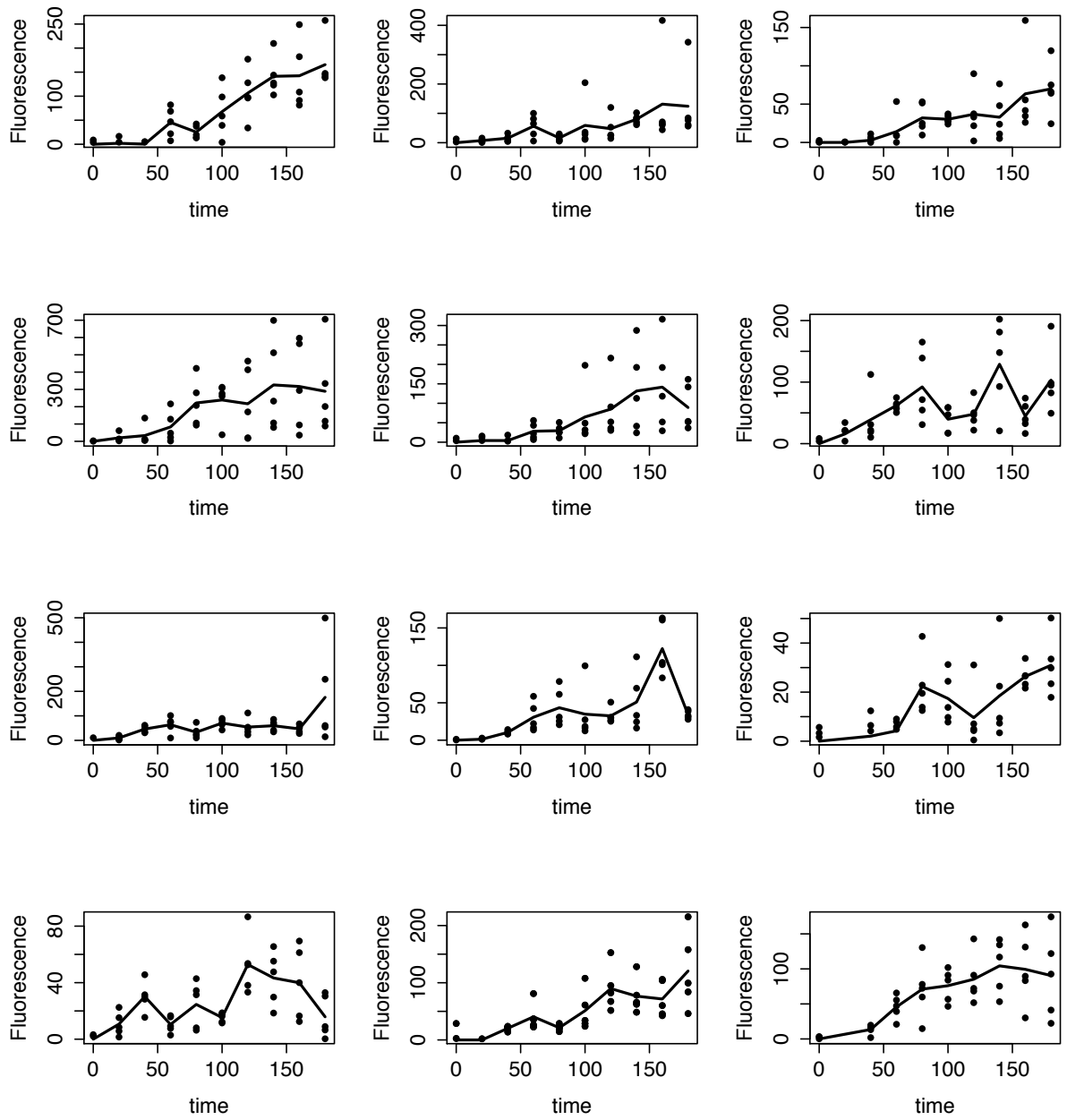
E

Appendix: A quantitative study of in vivo protoporphyrin IX fluorescence build up during occlusive treatment phases: individual patient measurements

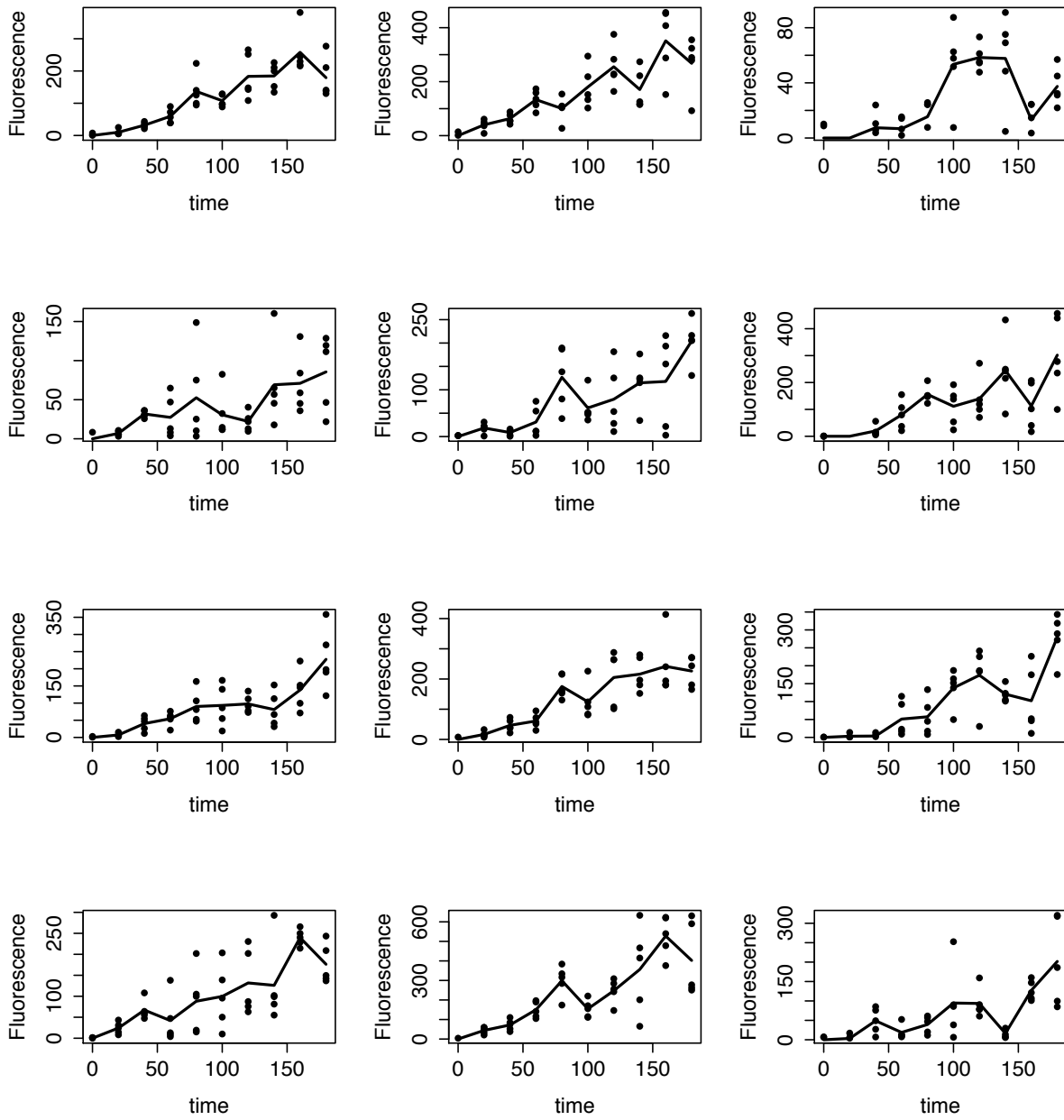
The data collected in the clinical study presented in chapter 7 for each individual patient is shown below (during the first session). The measurements have been corrected for by the autofluorescence from each individual patient and the line through the data corresponds to the mean of the repeated data points. Each individual plot corresponds to a single patient where the different data points corresponds to the repeated measurements for that patient. The plotted line corresponds a line that is drawn through the average fluorescence signal at each time point which is measured, for each patient. The overall analysis of the data is described and presented in chapter 7.

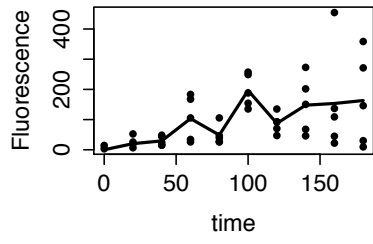
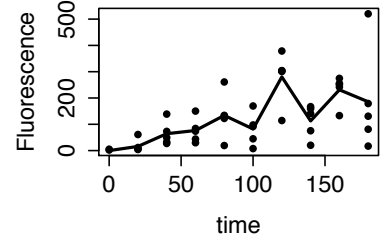
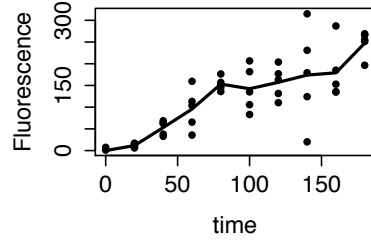
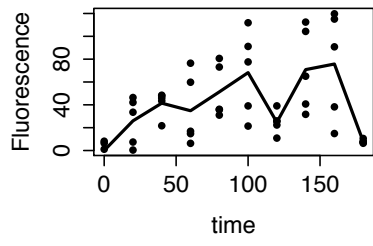
Appendix E. Appendix: A quantitative study of *in vivo* protoporphyrin IX fluorescence build up during occlusive treatment phases: individual patient measurements





Appendix E. Appendix: A quantitative study of in vivo protoporphyrin IX fluorescence build up during occlusive treatment phases: individual patient measurements







Appendix: A quantitative study of in vivo protoporphyrin IX fluorescence build-up during occlusive treatment phases: pain during treatment

During the light treatment the pain experienced by individual subjects was recorded. In this section the pain was compared to different patient characteristics such as gender, age and lesion location. The pain was also compared to the fluorescence signal measured during the study presented in chapter 6. It was found that male patients experiences a statistically significant higher level of pain and lesions located on the face also showed a higher level of experienced pain compared to other lesion locations.

F.1 Method

After the three hour long occlusive treatment discussed in chapter 6, the lesions included within the study were exposed to a light source for 20 min. During this light treatment, the pain score was recorded every 3 min. The patients were asked to state the level of experienced pain on a scale of 0 - 10, where 10 was the highest imaginable pain and 0 was no experienced pain. The question of pain experienced was repeated every 3 min during the full treatment.

In this analysis only the patients with pain scoring were adopted and only people treated with the standard 20 min irradiation was included. 26 recordings for treatment session 1 and 39 recordings for treatment session 2 were included in the study. The average pain scoring during the treatment was compared for size of the lesion, age of the patient, gender of the patient, location of the lesion, session as well as the fluorescence signal after 3 hours of occlusive treatment.

The statistical analysis that was adopted was independent Student's t-test as well as simple linear regression. The aim was to only compare different groups of patients to investigate the effect that different characteristics had on the level of experienced pain.

F.2 Results

The pain experienced during the first and the second session was compared where the recordings from the same individual was assumed to be independent. This analysis showed that there was no significant difference in the mean recorded pain during the irradiation. Figure F.1 shows a box plot of the average recorded pain score for session one and two demonstrating the insignificance between the different sessions.

The size of the lesion was recorded prior to the cream application. The average recorded pain score in relation to the size (diameter) of the lesion is shown in figure F.2.

The patients included in the study presented here were between 43 and 92 years old. The average age was 68 (± 11) years with a median age of 72 years. No relationship was found between the age of the patients and the level of pain experienced.

The relationship between pain and the fluorescence signal after 180 min of occlusive treatment was explored. Figure F.3 shows the fluorescence signal vs. recorded pain, and no signi-

ficant relationship was found between the two variables.

When the gender was investigated a significant difference in experienced pain was recorded where the females recorded a significantly lower pain score ($p < 0.05$). This is displayed in the box plot in figure F.4.

It was found from the analysis that lesions located on the face was experienced to be significantly ($p < 0.05$) more painful compared to the lesions located on other body sites. The plot displaying the distribution in the different categories are shown in in figure F.5.

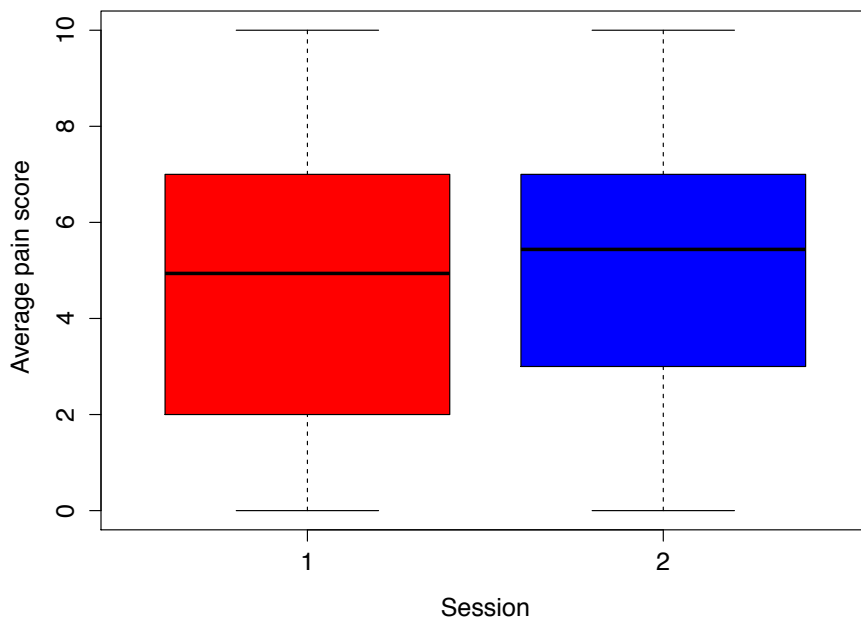


Figure F1: Figure showing box plot of the average recorded pain (0 - 10) during the first and the second treatment session. The different treatment sessions were most commonly spaced 7 days apart. The number of observations for session one was 26 and for session two, 38. No significant difference was found between the two groups of observations ($p > 0.05$)

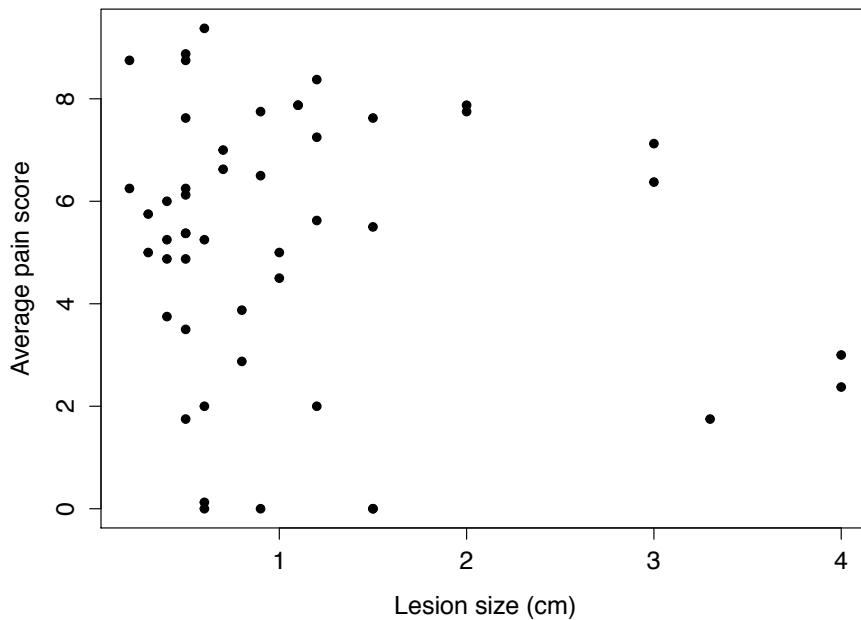


Figure F2: Figure showing box plot of the average recorded pain (0 - 10) for different sizes of the lesion. No relationship was found between the two parameters.

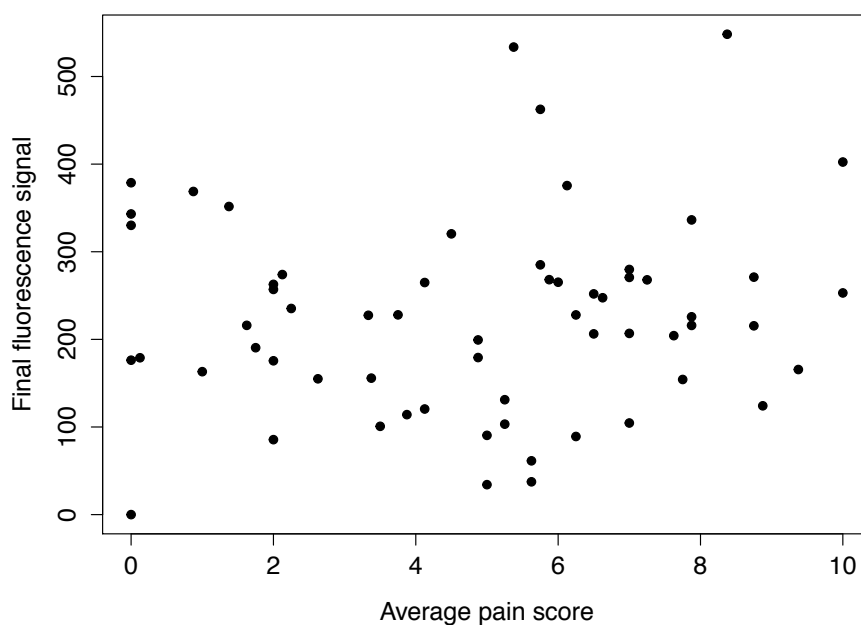


Figure E3: Figure shown the scatterplot of the fluorescence signal prior to the light irradiance and the corresponding average recorded pain score. No significant relationship was found between the signal and the experienced pain.

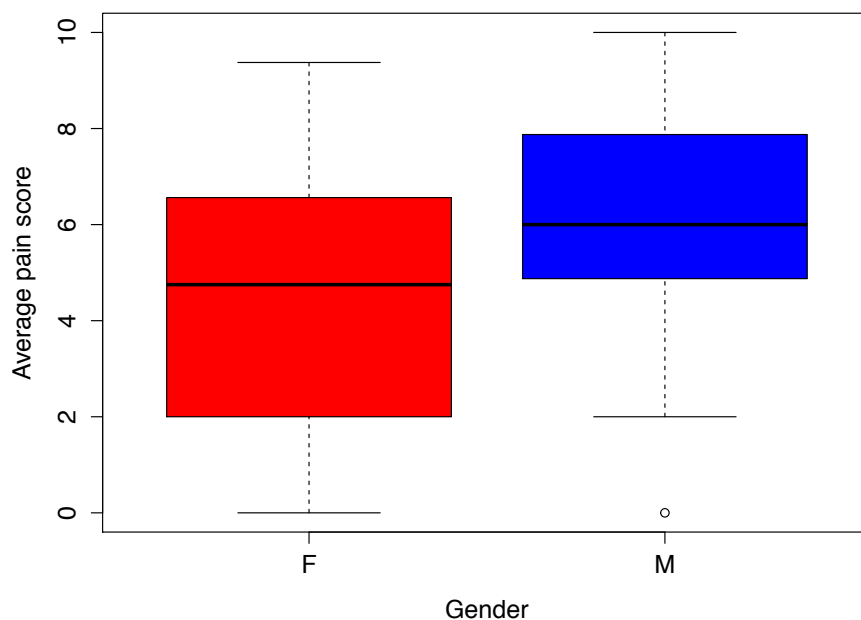


Figure E4: Boxplot of the experienced pain for males and females. It was found that males reports a significantly higher experienced pain score ($p < 0.05$) compared to the females where 18 male observations (both sessions) and 44 female observations (both sessions) were included within the analysis.

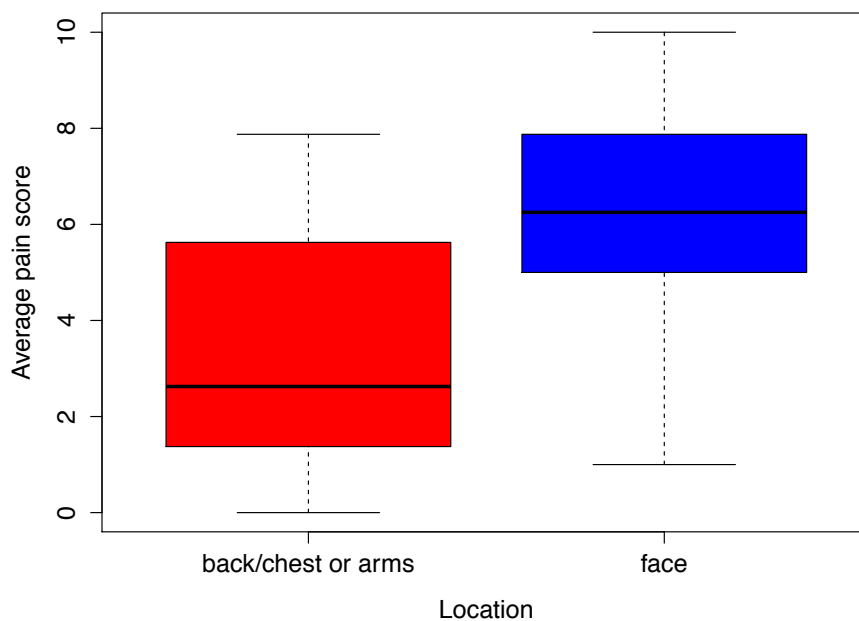


Figure F.5: Boxplot of the experienced pain for different lesion locations. The only significant body location was lesions located on the face, which was found to be associated with a higher experience pain compared to other lesion locations.

F.3 Discussion

Pain is a big disadvantage of (conventional) PDT where some patients find the treatment extremely painful [231]. This chapter discusses the level of pain experienced by the patients included within the study presented in chapter 7. The only significant difference was found between different genders and locations of the lesion. The model does not combine the different explored parameters, but looks at each aspect individually.

It has previously been found that pain is both size and gender dependent while no effect has been suggested for skin type (table 5.2) or dose. Different published results indicate different levels of significance between the pain and the fluorescence intensity [79, 152, 231]. In agreement with previous publication the lesions on the face region was found here to be associated with a higher level of pain. The gender dependency found in this work also agrees with previous findings. However no significance was found between the level of fluorescence intensity prior to the illumination (after 3 hours of occlusive treatment).

Pain is a difficult quantity to measure since the experienced pain will significantly vary

between individuals and can be subjective. This should always be considered when comparing the pain experienced between different patients. Even so, it is important to investigate pain, since an ideal treatment method would be associated with lower pain levels or no pain at all. Methods that have been associated with lower experienced pain is daylight PDT or ambulatory PDT [76, 77, 80].

F4 Conclusion

The work presented here compares the pain experienced during PDT treatment for the patients included in the clinical study presented in chapter 7. It was found that the highest level of pain was associated with lesions on the face, where male patients overall experienced higher levels of pain, supporting previously published results. Other parameters such as skin type, lesion size and fluorescence intensity did not indicate a correlation with the experienced level of pain.

Bibliography

- [1] B.C Wilson and M.S Patterson. The physics, biophysics and technology of photodynamic therapy. *Physics in Medicine and Biology*, 53(9):R61, 2008.
- [2] R. Darlenski and J.W. Fluhr. Photodynamic therapy in dermatology: past, present, and future. *Journal of Biomedical Optics*, 18(6):061208–061208, 2012.
- [3] A.P. Castano, T.N. Demidova, and M.R. Hamblin. Mechanisms in photodynamic therapy: part one - photosensitizers, photochemistry and cellular localization. *Photodiagnosis and Photodynamic Therapy*, 1(4):279 – 293, 2004.
- [4] Antony R Young. Chromophores in human skin. *Physics in Medicine and Biology*, 42(5):789, 1997.
- [5] M.H. Ross and W. Pawlina. *Histology*. Lippincott Williams & Wilkins, 2006.
- [6] Ko Nishino Takanori Igarashi and Shree K. Nayar. The appearance of human skin: A survey. *Foundations and Trends in Computer Graphics and Vision*, 3(1):1–95, 2007.
- [7] David S. Strayer, E. Rubin, and J.E. Saffitz. *Rubin's Pathology: Clinicopathologic Foundations of Medicine*. M - Medicine Series. Wolters Kluwer Health, 2014.
- [8] D.J. Gawkrödger. *Dermatology: An Illustrated Colour Text*. Illustrated colour text. Churchill Livingstone, 2002.
- [9] Fitzpatrick TB. The validity and practicality of sun-reactive skin types i through vi. *Archives of Dermatology*, 124(6):869–871, 1988.
- [10] J. Naish and D.S. Court. *Medical Sciences*. Elsevier Health Sciences UK, 2014.
- [11] R. Corona. Epidemiology of nonmelanoma skin cancer: a review. *Ann Ist Super Sanita*, 32(1):37–42, 1996.
- [12] Dallas R English, Bruce K Armstrong, Anne Kricker, and Claire Fleming. Sunlight and cancer. *Cancer causes & control*, 8(3):271–283, 1997.
- [13] A. Lomas, J. Leonardi-Bee, and F. Bath-Hextall. A systematic review of worldwide incidence of nonmelanoma skin cancer. *British Journal of Dermatology*, 166(5):1069–1080, 2012.
- [14] B.L. Diffey and J.A.A. Langtry. Skin cancer incidence and the ageing population. *British Journal of Dermatology*, 153(3):679–680, 2005.

- [15] Nora Eisemann, Annika Waldmann, Alan C Geller, Martin A Weinstock, Beate Volkmer, Ruediger Greinert, Eckhard W Breitbart, and Alexander Katalinic. Non-melanoma skin cancer incidence and impact of skin cancer screening on incidence. *Journal of Investigative Dermatology*, 134(1):43–50, 2014.
- [16] A Green. Changing patterns in incidence of non-melanoma skin cancer. *Epithelial cell biology*, 1(1):47–51, 1992.
- [17] Vishal Madan, John T Lear, and Rolf-Markus Szeimies. Non-melanoma skin cancer. *The Lancet*, 375(9715):673 – 685, 2010.
- [18] S.J. Salasche. Epidemiology of actinic keratoses and squamous cell carcinoma. *J Am Acad Dermatol*, 42(1 Pt 2):4–7, 2000.
- [19] CSM Wong, RC Strange, and JT Lear. Basal cell carcinoma. *BMJ: British Medical Journal*, 327(7418):794, 2003.
- [20] Cornelia S.L. Mueller and Jörg Reichrath. Histology of melanoma and nonmelanoma skin cancer. In Jörg Reichrath, editor, *Sunlight, Vitamin D and Skin Cancer*, volume 624 of *Advances in Experimental Medicine and Biology*, pages 215–226. Springer New York, 2008.
- [21] Lasse R. Braathen, Rolf-Markus Szeimies, Nicole Basset-Seguin, Robert Bissonnette, Peter Foley, David Pariser, Rik Roelandts, Ann-Marie Wennberg, and Colin A. Morton. Guidelines on the use of photodynamic therapy for nonmelanoma skin cancer: An international consensus. *Journal of the American Academy of Dermatology*, 56(1):125 – 143, 2007.
- [22] S Rosso, R Zanetti, C Martinez, MJ Tormo, S Schraub, H Sancho-Garnier, S Franceschi, L Gafa, E Perea, C Navarro, et al. The multicentre south european study ‘helios’. ii: Different sun exposure patterns in the aetiology of basal cell and squamous cell carcinomas of the skin. *British journal of cancer*, 73(11):1447, 1996.
- [23] J.T. Lear, A.G. Smith, R.C. Strange, and A.A. Fryer. Detoxifying enzyme genotypes and susceptibility to cutaneous malignancy. *British Journal of Dermatology*, 142(1):8–15, 2000.
- [24] N.P. Galletly, J. McGinty, C. Dunsby, F. Teixeira, J. Requejo-Isidro, I. Munro, D.S. Elson, M.A.A. Neil, A.C. Chu, P.M.W. French, and G.W. Stamp. Fluorescence lifetime imaging distinguishes basal cell carcinoma from surrounding uninvolved skin. *British Journal of Dermatology*, 159(1):152–161, 2008.
- [25] M. Ulrich, E. Stockfleth, J. Roewert-Huber, and S. Astner. Noninvasive diagnostic tools for nonmelanoma skin cancer. *British Journal of Dermatology*, 157:56–58, 2007.
- [26] Marco Manfredini, Federica Arginelli, Christopher Dunsby, Paul French, Clifford Talbot, Karsten König, Giovanni Pellacani, Giovanni Ponti, and Stefania Seidenari. High-resolution imaging of basal cell carcinoma: a comparison between multiphoton microscopy with fluorescence lifetime imaging and reflectance confocal microscopy. *Skin Research and Technology*, 19(1):e433–e443, 2013.

- [27] I. Man, I.K. Crombie, R.S. Dawe, S.H. Ibbotson, and J. Ferguson. The photocarcinogenic risk of narrowband uvb (tl-01) phototherapy: early follow-up data. *British Journal of Dermatology*, 152(4):755–757, 2005.
- [28] Robert S. Stern, Elissa J. Liebman, and Liisa Väkevä. Oral psoralen and ultraviolet-a light (puva) treatment of psoriasis and persistent risk of nonmelanoma skin cancer. *Journal of the National Cancer Institute*, 90(17):1278–1284, 1998.
- [29] Lichter MD, Karagas MR, Mott LA, and et al. Therapeutic ionizing radiation and the incidence of basal cell carcinoma and squamous cell carcinoma. *Archives of Dermatology*, 136(8):1007–1011, 2000.
- [30] Margaret R Karagas, Therese A Stukel, Virginia Umland, Maria M Tsoukas, Leila A Mott, Henrik T Sorensen, Annette O Jensen, Heather H Nelson, Steven K Spencer, Ann E Perry, et al. Reported use of photosensitizing medications and basal cell and squamous cell carcinoma of the skin: results of a population-based case-control study. *Journal of Investigative Dermatology*, 127(12):2901–2903, 2007.
- [31] Margaret R Karagas, Tim Waterboer, Zhongze Li, Heather H Nelson, Kristina M Michael, Jan Nico Bouwes Bavinck, Ann E Perry, Steven K Spencer, Janet Daling, Adele C Green, and Michael Pawlita. Genus Ĩš human papillomaviruses and incidence of basal cell and squamous cell carcinomas of skin: population based case-control study. *BMJ*, 341, 2010.
- [32] Karl Wilkins, Ryan Turner, Jacqueline C. Dolev, Philip E. LeBoit, Timothy G. Berger, and Toby A. Maurer. Cutaneous malignancy and human immunodeficiency virus disease. *Journal of the American Academy of Dermatology*, 54(2):189 – 206, 2006.
- [33] C. Kennedy, C.D. Bajdik, R. Willemze, and J.N. Bouwes Bavinck. Chemical exposures other than arsenic are probably not important risk factors for squamous cell carcinoma, basal cell carcinoma and malignant melanoma of the skin. *British Journal of Dermatology*, 152(1):194–197, 2005.
- [34] S.R. Wiegell, V. Skodt, and H.C. Wulf. Daylight-mediated photodynamic therapy of basal cell carcinomas - an explorative study. *Journal of the European Academy of Dermatology and Venereology*, 2013.
- [35] John D. Spikes. Photodynamic action: From paramecium to photochemotherapy. *Photochemistry and Photobiology*, 65:142S–147S, 1997.
- [36] Roger Ackroyd, Clive Kelty, Nicola Brown, and Malcolm Reed. The history of photodetection and photodynamic therapy. *Photochemistry and Photobiology*, 74(5):656–669, 2001.
- [37] Katrin Kalka, Hans Merk, and Hasan Mukhtar. Photodynamic therapy in dermatology. *Journal of the American Academy of Dermatology*, 42(3):389 – 413, 2000.
- [38] Michael R. Detty, Scott L. Gibson, and Stephen J. Wagner. Current clinical and preclinical photosensitizers for use in photodynamic therapy. *Journal of Medicinal Chemistry*, 47(16):3897–3915, 2004. PMID: 15267226.

- [39] Dennis E.J.G.J. Dolmans, Dai Fukumura, and Rakesh K. Jain. Photodynamic therapy for cancer. *Nature Reviews Cancer*, 3(5):380–387, 2003.
- [40] P. Calzavara-Pinton, R.M. Szeimies, and B. Ortel. *Photodynamic Therapy and Fluorescence Diagnosis in Dermatology*. Comprehensive Series in Photosciences. Elsevier Science, 2001.
- [41] A. Oakley, H. Waikato, and R. Suhonen. DermNet NZ.
- [42] Qian Peng, Ana Maria Soler, Trond Warloe, Jahn M Nesland, and Karl-Erik Giercksky. Selective distribution of porphyrins in skin thick basal cell carcinoma after topical application of methyl 5-aminolevulinate. *Journal of Photochemistry and Photobiology B: Biology*, 62(3):140 – 145, 2001.
- [43] Valentina Faina Carmen Cantisani, Giovanni Paolino. Overview on topical 5-ala photodynamic therapy use for non melanoma skin cancers. *Journal of Photoenergy*, 2014, 2014.
- [44] CA Morton, KE McKenna, and LE Rhodes. Guidelines for topical photodynamic therapy: update. *British Journal of Dermatology*, 159(6):1245–1266, 2008.
- [45] E Christensen, T Warloe, S Kroon, J Funk, P Helsing, AM Soler, HJ Stang, Ø Vatne, and C Mørk. Guidelines for practical use of mal-pdt in non-melanoma skin cancer. *Journal of the European Academy of Dermatology and Venereology*, 24(5):505–512, 2010.
- [46] Mikael Tarstedt, Inger Rosdahl, Berit Berne, Katarina Svanberg, and A Wennberg. A randomized multicenter study to compare two treatment regimens of topical methyl aminolevulinate (metvix)-pdt in actinic keratosis of the face and scalp. *ACTA DERMATOVENEREOLÓGICA-STOCKHOLM-*, 85(5):424, 2005.
- [47] C. Morton, S. Campbell, G. Gupta, S. Keohane, J. Lear, I. Zaki, S. Walton, N. Kerrouche, G. Thomas, P. Soto, and on behalf of the AKtion Investigators. Intraindividual, right-left comparison of topical methyl aminolaevulinate-photodynamic therapy and cryotherapy in subjects with actinic keratoses: a multicentre, randomized controlled study. *British Journal of Dermatology*, 155(5):1029–1036, 2006.
- [48] R-M Szeimies, E Stockfleth, G Popp, F Borrosch, H Brüning, R Dominicus, H Mensing, U Reinhold, K Reich, ACE Moor, et al. Long-term follow-up of photodynamic therapy with a self-adhesive 5-aminolaevulinic acid patch: 12 months data. *British Journal of Dermatology*, 162(2):410–414, 2010.
- [49] C.A. Morton, R.-M. Szeimies, A. Sidoroff, and L.R. Braathen. European guidelines for topical photodynamic therapy part 1: treatment delivery and current indications - actinic keratoses, bowen’s disease, basal cell carcinoma. *Journal of the European Academy of Dermatology and Venereology*, 27(5):536–544, 2013.
- [50] PG Calzavara-Pinton, M Venturini, R Sala, R Capezzer, G Parrinello, C Specchia, and C Zane. Methylaminolaevulinate-based photodynamic therapy of bowen’s disease and squamous cell carcinoma. *British Journal of Dermatology*, 159(1):137–144, 2008.

- [51] RM Szeimies, S Ibbotson, DF Murrell, D Rubel, Y Frambach, D De Berker, R Dummer, N Kerrouche, and H Villemagne. A clinical study comparing methyl aminolevulinic acid photodynamic therapy and surgery in small superficial basal cell carcinoma (8–20 mm), with a 12-month follow-up. *Journal of the European Academy of Dermatology and Venereology*, 22(11):1302–1311, 2008.
- [52] C.A. Morton, S.B. Brown, S. Collins, S. Ibbotson, H. Jenkinson, H. Kurwa, K. Langmack, K. Mckenna, H. Moseley, A.D. Pearse, M. Stringer, D.K. Taylor, G. Wong, and L.E. Rhodes. Guidelines for topical photodynamic therapy: report of a workshop of the british photodermatology group. *British Journal of Dermatology*, 146(4):552–567, 2002.
- [53] Ryan F. Donnelly, Paul A. McCarron, and A. David Woolfson. Derivatives of 5-aminolevulinic acid for photodynamic therapy. *Perspectives in Medicinal Chemistry*, 1:49–63, 2007.
- [54] H Tappenier and A Jesionek. Therapeutische versuche mit fluoreszierenden stoffe. *Muench. Med. Wochenschr*, 1:2042, 1903.
- [55] R. Valentine. Biological aspects of photodynamic therapy. *Ph.D. Thesis, University of St Andrews*, 2011.
- [56] R. M. Valentine, S.H. Ibbotson, K. Wood, C.T.A. Brown, and H. Moseley. Modelling fluorescence in clinical photodynamic therapy. *Photochem. Photobiol. Sci.*, 12:203–213, 2013.
- [57] Carin Sandberg, CB Halldin, MB Ericson, O Larkö, A-L Krogstad, and A-M Wennberg. Bioavailability of aminolaevulinic acid and methylaminolaevulinic acid in basal cell carcinomas: a perfusion study using microdialysis in vivo. *British Journal of Dermatology*, 159(5):1170–1176, 2008.
- [58] M. Wachowska, A. Muchowicz, M. Firczuk, M. Gabrysiak, M. Winiarska, M. Wanczyk, K. Bojarczuk, and J. Golab. Aminolevulinic acid (ala) as a prodrug in photodynamic therapy of cancer. *Molecules*, 16(5):4140–4164, 2011.
- [59] Hubert Van Den Bergh and JP Ballini. Principles of photodynamic therapy. *Chap*, 2:11–42, 2004.
- [60] Yvette Niamien Konan, Robert Gurny, and Eric All'mann. State of the art in the delivery of photosensitizers for photodynamic therapy. *Journal of Photochemistry and Photobiology B: Biology*, 66(2):89 – 106, 2002.
- [61] B.W. Henderson and T.J. Dougherty. How does photodynamic therapy work? *Photochemistry and Photobiology*, 55(1):145–157, 1992.
- [62] M. Ochsner. Photophysical and photobiological processes in the photodynamic therapy of tumours. *Journal of Photochemistry and Photobiology B: Biology*, 39(1):1 – 18, 1997.

- [63] John W. Snyder, Esben Skovsen, John D. C. Lambert, Lars Poulsen, and Peter R. Ogilby. Optical detection of singlet oxygen from single cells. *Phys. Chem. Chem. Phys.*, 8:4280–4293, 2006.
- [64] Thomas J. Dougherty, Charles J. Gomer, Barbara W. Henderson, Giulio Jori, David Kessel, Mladen Korbelik, Johan Moan, and Qian Peng. Photodynamic therapy. *Journal of the National Cancer Institute*, 90(12):889–905, 1998.
- [65] Ryan F. Donnelly, Paul A. McCarron, and A. David Woolfson. Drug delivery of aminolevulinic acid from topical formulations intended for photodynamic therapy. *Photochemistry and Photobiology*, 81(4):750–767, 2005.
- [66] BC Wilson, MS Patterson, and L Lilge. Implicit and explicit dosimetry in photodynamic therapy: a new paradigm. *Lasers in medical science*, 12(3):182–199, 1997.
- [67] Ron R Allison and Claudio H Sibata. Oncologic photodynamic therapy photosensitizers: a clinical review. *Photodiagnosis and photodynamic therapy*, 7(2):61–75, 2010.
- [68] Kristian P Nielsen, Asta Juzeniene, Petras Juzenas, Knut Stamnes, Jakob J Stamnes, and Johan Moan. Choice of optimal wavelength for pdt: the significance of oxygen depletion. *Photochemistry and photobiology*, 81(5):1190–1194, 2005.
- [69] Nadia Naghavi, MohammadHossein Miranbaygi, and Ameneh Sazgarnia. Simulation of fractionated and continuous irradiation in photodynamic therapy: study the differences between photobleaching and singlet oxygen dose deposition. *Australasian Physical Engineering Sciences in Medicine*, 34(2):203–211, 2011.
- [70] Hannah C De Vijlder, Tom A Middelburg, Henriette S De Bruijn, Dominic J Robinson, HA Martino Neumann, and Ellen RM De Haas. Fractionated pdt with 5-aminolevulinic acid: effective, cost effective, and patient friendly. In *12th World Congress of the International Photodynamic Association*, pages 73806A–73806A. International Society for Optics and Photonics, 2009.
- [71] Henriëtte S de Bruijn, Adriana G Casas, Gabriela Di Venosa, Lautato Gandara, Henricus JCM Sterenberg, Alcira Batlle, and Dominic J Robinson. Light fractionated ala-pdt enhances therapeutic efficacy in vitro; the influence of ppix concentration and illumination parameters. *Photochemical & Photobiological Sciences*, 12(2):241–245, 2013.
- [72] H. Moseley. Light distribution and calibration of commercial pdt led arrays. *Photochem. Photobiol. Sci.*, 4:911–914, 2005.
- [73] Rebecca Richards-Kortum and Eva Sevick-Muraca. Quantitative optical spectroscopy for tissue diagnosis. *Annual review of physical chemistry*, 47(1):555–606, 1996.
- [74] Lasers Brancaleon and H Moseley. Laser and non-laser light sources for photodynamic therapy. *Lasers in medical science*, 17(3):173–186, 2002.
- [75] R M Valentine, K Wood, C T A Brown, S H Ibbotson, and H Moseley. Monte carlo simulations for optimal light delivery in photodynamic therapy of non-melanoma skin cancer. *Physics in Medicine and Biology*, 57(20):6327, 2012.

- [76] H. Moseley, J.W. Allen, S. Ibbotson, A. Lesar, A. McNeill, M.A. Camacho-Lopez, I.D.W. Samuel, W. Sibbett, and J. Ferguson. Ambulatory photodynamic therapy: a new concept in delivering photodynamic therapy. *British Journal of Dermatology*, 154(4):747–750, 2006.
- [77] S.K. Attili, A. Lesar, A. McNeill, M. Camacho-Lopez, H. Moseley, S. Ibbotson, I.D.W. Samuel, and J. Ferguson. An open pilot study of ambulatory photodynamic therapy using a wearable low-irradiance organic light-emitting diode light source in the treatment of nonmelanoma skin cancer. *British Journal of Dermatology*, 161(1):170–173, 2009.
- [78] CA Morton, HC Wulf, RM Szeimies, Y Gilaberte, N Basset-Seguin, E Sotiriou, S Piaserico, RE Hunger, S Baharlou, A Sidoroff, et al. Practical approach to the use of daylight photodynamic therapy with topical methyl aminolevulinate for actinic keratosis: a european consensus. *Journal of the European Academy of Dermatology and Venereology*, 2015.
- [79] SR Wiegell, J Skiveren, PA Philipsen, and Hans Chr Wulf. Pain during photodynamic therapy is associated with protoporphyrin ix fluorescence and fluence rate. *British Journal of Dermatology*, 158(4):727–733, 2008.
- [80] S.R. Wiegell, M. Hadersdal, PA. Philipsen, P Eriksen, C.D. Enk, and H.C. Wulf. Continuous activation of ppix by daylight is as effective as and less painful than conventional photodynamic therapy for actinic keratoses; a randomized, controlled, single-blinded study. *British Journal of Dermatology*, 158(4):740–746, 2008.
- [81] S.R. Wiegell, J. Heydenreich, S. Fabricius, and H.C. Wulf. Continuous ultra-low-intensity artificial daylight is not as effective as red led light in photodynamic therapy of multiple actinic keratoses. *Photodermatology, Photoimmunology Photomedicine*, 27(6):280–285, 2011.
- [82] S.R. Wiegell, S. Fabricius, I.M. Stender, B. Berne, S. Kroon, B.L. Andersen, C. Mork, C. Sandberg, G.B.E. Jemec, M. Mogensen, K.M. Brocks, PA. Philipsen, J. Heydenreich, M. Hadersdal, and H.C. Wulf. A randomized, multicentre study of directed daylight exposure times of 1 1/2 vs. 2 1/2 h in daylight-mediated photodynamic therapy with methyl aminolaevulinate in patients with multiple thin actinic keratoses of the face and scalp. *British Journal of Dermatology*, 164(5):1083–1090, 2011.
- [83] S.R. Wiegell, M. Hadersdal, P Eriksen, and H.C. Wulf. Photodynamic therapy of actinic keratoses with 8% and 16% methyl aminolaevulinate and home-based daylight exposure: a double-blinded randomized clinical trial. *British Journal of Dermatology*, 160(6):1308–1314, 2009.
- [84] M.C. Fargnoli, A. Piccioni, L. Neri, S. Tambone, C. Pellegrini, and K. Peris. Conventional vs. daylight methyl aminolevulinate photodynamic therapy for actinic keratosis of the face and scalp: an intra-patient, prospective, comparison study in italy. *Journal of the European Academy of Dermatology and Venereology*, 29(10):1926–1932, 2015.

- [85] J-P Lacour, C. Ulrich, Y. Gilaberte, V. Von Felbert, N. Basset-Seguin, B. Dreno, C. Girard, P. Redondo, C. Serra-Guillen, I. Synnerstad, M. Tarstedt, A. Tsianakas, A.W. Venema, N. Kelleners-Smeets, H. Adamski, B. Perez-Garcia, M.J. Gerritsen, S. Leclerc, N. Kerrouche, and R-M. Szeimies. Daylight photodynamic therapy with methyl aminolevulinate cream is effective and nearly painless in treating actinic keratoses: a randomised, investigator-blinded, controlled, phase iii study throughout europe. *Journal of the European Academy of Dermatology and Venereology*, 2015.
- [86] O’Gorman SM, Clowry J, Manley M, and et al. Artificial white light vs daylight photodynamic therapy for actinic keratoses: A randomized clinical trial. *JAMA Dermatology*, 2016.
- [87] Noora Neittaanmäki-Perttu, Mari Grönroos, Taneli Tani, and Erna Snellman. Long-term outcome of daylight photodynamic therapy with 5-aminolaevulinate nanoemulsion and methyl-5-aminolaevulinate for actinic keratoses. *Acta dermato-venereologica*, 2016.
- [88] Giovanni Genovese, Dario Fai, Carlotta Fai, Luciano Mavilia, and Santo R. Mercuri. Daylight methyl-aminolevulinate photodynamic therapy versus ingenol mebutate for the treatment of actinic keratoses: an intraindividual comparative analysis. *Dermatologic Therapy*, 2016.
- [89] D.M. Rubel, L. Spelman, D.F. Murrell, J.-A. See, D. Hewitt, P. Foley, C. Bosc, D. Kerob, N. Kerrouche, H.C. Wulf, and S. Shumack. Daylight photodynamic therapy with methyl aminolevulinate cream as a convenient, similarly effective, nearly painless alternative to conventional photodynamic therapy in actinic keratosis treatment: a randomized controlled trial. *British Journal of Dermatology*, 171(5):1164–1171, 2014.
- [90] Kathryn LS Lane, Whitney Hovenic, Kaity Ball, and Christopher B Zachary. Daylight photodynamic therapy: The southern california experience. *Lasers in surgery and medicine*, 47(2):168–172, 2015.
- [91] Beni Grinblat, Gaston Galimberti, Edgardo Chouela, Gloria Sanclemente, Miguel Lopez, Daniel Alcalá, Luíís Torezan, and Gonzalo Pantoja. Daylight-mediated photodynamic therapy for actinic damage in latin america: consensus recommendations. *Photodermatology, Photoimmunology Photomedicine*, 2015.
- [92] S.R. Wiegell, S. Fabricius, J. Heydenreich, C.D. Enk, S. Rosso, W. Baumler, B.T. Balduresson, and H.C. Wulf. Weather conditions and daylight-mediated photodynamic therapy: protoporphyrin ix-weighted daylight doses measured in six geographical locations. *British Journal of Dermatology*, 168(1):186–191, 2013.
- [93] S.R. Wiegell, H.C. Wulf, R.-M. Szeimies, N. Basset-Seguin, R. Bissonnette, M.-J.P. Gerritsen, Y. Gilaberte, P. Calzavara-Pinton, C.A. Morton, A. Sidoroff, and L.R. Braathen. Daylight photodynamic therapy for actinic keratosis: an international consensus. *Journal of the European Academy of Dermatology and Venereology*, 26(6):673–679, 2012.

- [94] Wulf H. Photodynamic therapy in daylight for actinic keratoses. *JAMA Dermatology*, 2016.
- [95] Elise A. Olsen, M. Lisa Abernethy, Carol Kulp-Shorten, Jeffrey P Callen, Scott D. Glazer, Arthur Huntley, Michael McCray, Alicia B. Monroe, Eduardo Tschen, and John E. Wolf Jr. A double-blind, vehicle-controlled study evaluating masoprocol cream in the treatment of actinic keratoses on the head and neck. *Journal of the American Academy of Dermatology*, 24(5, Part 1):738 – 743, 1991.
- [96] Rhodes LE, de Rie M, Enström Y, and et al. Photodynamic therapy using topical methyl aminolevulinate vs surgery for nodular basal cell carcinoma: Results of a multicenter randomized prospective trial. *Archives of Dermatology*, 140(1):17–23, 2004.
- [97] S.L. Jacques, R. Joseph, and G. Gofstein. How photobleaching affects dosimetry and fluorescence monitoring of pdt in turbid media. *Proc. SPIE*, 1881:168–179, 1993.
- [98] Stephen T Flock, Michael S Patterson, Brian C Wilson, and Douglas R Wyman. Monte carlo modeling of light propagation in highly scattering tissues. i. model predictions and comparison with diffusion theory. *Biomedical Engineering, IEEE Transactions on*, 36(12):1162–1168, 1989.
- [99] BC Wilson and G Adam. A monte carlo model for the absorption and flux distributions of light in tissue. *Medical physics*, 10(6):824–830, 1983.
- [100] R.M. Valentine, C.T.A. Brown, H. Moseley, S. Ibbotson, and K. Wood. Monte carlo modeling of in vivo protoporphyrin ix fluorescence and singlet oxygen production during photodynamic therapy for patients presenting with superficial basal cell carcinomas. *Journal of Biomedical Optics*, 16(4):048002–048002–11, 2011.
- [101] ML De Jode. Monte carlo simulations of light distributions in an embedded tumour model: studies of selectivity in photodynamic therapy. *Lasers in medical science*, 15(1):49–56, 2000.
- [102] Baochang Liu, Thomas J Farrell, and Michael S Patterson. A dynamic model for ala-pdt of skin: simulation of temporal and spatial distributions of ground-state oxygen, photosensitizer and singlet oxygen. *Physics in Medicine and Biology*, 55(19):5913, 2010.
- [103] T.J. Pfefer, K.T. Schomacker, M.N. Ediger, and N.S. Nishioka. Light propagation in tissue during fluorescence spectroscopy with single-fiber probes. *Selected Topics in Quantum Electronics, IEEE Journal of*, 7(6):1004–1012, 2001.
- [104] I. V. Meglinski. Monte carlo simulation of reflection spectra of random multilayer media strongly scattering and absorbing light. *Quantum Electronics*, 31(12):1101–1107, 2001.
- [105] I.V. Meglinski and S.J. Matcher. Computer simulation of the skin reflectance spectra. *Computer Methods and Programs in Biomedicine*, 70(2):179 – 186, 2003.

- [106] G. Yoon, A.J. Welch, M. Motamedi, and M.v. Gemert. Development and application of three-dimensional light distribution model for laser irradiated tissue. *Quantum Electronics, IEEE Journal of*, 23(10):1721–1733, 1987.
- [107] C. Zhu and Q. Liu. Review of monte carlo modeling of light transport in tissues. *Journal of Biomedical Optics*, 18(5):050902–050902, 2013.
- [108] J. Swartling, A. Pifferi, A.M.K. Enejder, and S. Andersson-Engels. Accelerated monte carlo models to simulate fluorescence spectra from layered tissues. *J. Opt. Soc. Am. A*, 20(4):714–727, 2003.
- [109] T. Binzoni, T.S. Leung, R. Giust, D. Rufenacht, and A.H. Gandjbakhche. Light transport in tissue by 3d monte carlo: Influence of boundary voxelization. *Computer Methods and Programs in Biomedicine*, 89(1):14 – 23, 2008.
- [110] Fatmir Asllanaj, Sylvain Contassot-Vivier, Andre Liemert, and Alwin Kienle. Radiative transfer equation for predicting light propagation in biological media: comparison of a modified finite volume method, the monte carlo technique, and an exact analytical solution. *Journal of Biomedical Optics*, 19(1):015002, 2014.
- [111] T. Lister, P.A. Wright, and P.H. Chappell. Optical properties of human skin. *Journal of Biomedical Optics*, 17(9):090901–1–090901–15, 2012.
- [112] S.L. Jacques. Optical properties of biological tissues: a review. *Physics in Medicine and Biology*, 58(11):R37, 2013.
- [113] L.V. Wang and H. Wu. *Biomedical Optics: Principles and Imaging*. Wiley, 2007.
- [114] S. Chandrasekhar. *Radiative Transfer*. Dover Books on Intermediate and Advanced Mathematics. Dover Publications, 1960.
- [115] G. Yoon, S. A. Prahl, and A. J. Welch. Accuracies of the diffusion approximation and its similarity relations for laser irradiated biological media. *Appl. Opt.*, 28:2250–2255, 1989.
- [116] Lihong V Wang and Steven L Jacques. Source of error in calculation of optical diffuse reflectance from turbid media using diffusion theory. *Computer methods and programs in biomedicine*, 61(3):163–170, 2000.
- [117] S.A. Prahl, M. Keijzer, S.L. Jacques, and A.J. Welch. A monte carlo model of light propagation in tissue. In *SPIE Proceedings of Dosimetry of Laser Radiation in Medicine and Biology*, pages 102–111. Press, 1989.
- [118] Nicholas Metropolis and Stanislaw Ulam. The monte carlo method. *Journal of the American statistical association*, 44(247):335–341, 1949.
- [119] Marleen Keijzer, Steven L. Jacques, Scott A. Prahl, and Ashley J. Welch. Light distributions in artery tissue: Monte carlo simulations for finite-diameter laser beams. *Lasers in Surgery and Medicine*, 9(2):148–154, 1989.

- [120] A.J. Welch and M.J.C. van Gemert. *Optical- Response of Laser-Irradiated Tissue*. Lasers, Photonics, and Electro-Optics. Springer US, 1995.
- [121] Sachin V Patwardhan, Atam P Dhawan, Patricia Relue, et al. Monte carlo simulation of light-tissue interaction: three-dimensional simulation for trans-illumination-based imaging of skin lesions. *Biomedical Engineering, IEEE Transactions on*, 52(7):1227–1236, 2005.
- [122] Peter Lutzke, Stefan Heist, Peter Kühmstedt, Richard Kowarschik, and Gunther Notni. Monte carlo simulation of three-dimensional measurements of translucent objects. *Optical Engineering*, 54(8):084111–084111, 2015.
- [123] T Lister, PA Wright, and PH Chappell. A new monte carlo program for simulating light transport through port wine stain skin. *Lasers in medical science*, 29(3):1017–1028, 2014.
- [124] AJ Welch, Craig Gardner, Rebecca Richards-Kortum, Eric Chan, Glen Criswell, Josh Pfeffer, and Steve Warren. Propagation of fluorescent light. *Lasers in surgery and medicine*, 21(2):166–178, 1997.
- [125] Caigang Zhu and Quan Liu. Hybrid method for fast monte carlo simulation of diffuse reflectance from a multilayered tissue model with tumor-like heterogeneities. *Journal of biomedical optics*, 17(1):0105011–0105013, 2012.
- [126] Lihong V Wang, Robert E Nordquist, and Wei R Chen. Optimal beam size for light delivery to absorption-enhanced tumors buried in biological tissues and effect of multiple-beam delivery: a monte carlo study. *Applied optics*, 36(31):8286–8291, 1997.
- [127] CL Campbell, K Wood, RM Valentine, CTA Brown, and H Moseley. Monte carlo modelling of daylight activated photodynamic therapy. *Physics in medicine and biology*, 60(10):4059, 2015.
- [128] David Boas, J Culver, J Stott, and A Dunn. Three dimensional monte carlo code for photon migration through complex heterogeneous media including the adult human head. *Optics express*, 10(3):159–170, 2002.
- [129] Andreas H Hielscher, Hanli Liu, Britton Chance, Frank K Tittel, and Steven L Jacques. Time-resolved photon emission from layered turbid media. *Applied optics*, 35(4):719–728, 1996.
- [130] Eiji Okada and David T Delpy. Near-infrared light propagation in an adult head model. i. modeling of low-level scattering in the cerebrospinal fluid layer. *Applied optics*, 42(16):2906–2914, 2003.
- [131] Qianqian Fang. Mesh-based monte carlo method using fast ray-tracing in plücker coordinates. *Biomedical optics express*, 1(1):165–175, 2010.
- [132] Anton V Gorshkov and Mikhail Yu Kirillin. Monte carlo simulation of brain sensing by optical diffuse spectroscopy. *Journal of Computational Science*, 3(6):498–503, 2012.

- [133] Steven L Jacques. Optical assessment of cutaneous blood volume depends on the vessel size distribution: a computer simulation study. *Journal of biophotonics*, 3(1):75, 2010.
- [134] Gerald W Lucassen, Wim Verkruyse, Marleen Keijzer, and Martin JC van Gemert. Light distributions in a port wine stain model containing multiple cylindrical and curved blood vessels. *Lasers in surgery and medicine*, 18(4):345–357, 1996.
- [135] Lihong V Wang. Rapid modeling of diffuse reflectance of light in turbid slabs. *JOSA A*, 15(4):936–944, 1998.
- [136] Keneth Wood. <http://www-star.st-and.ac.uk/~kw25/>. *Monte Carlo Radiation Transfer*, 2013.
- [137] K. Wood and R.J. R. J. Reynolds. A model for the scattered light contribution and polarization of the diffuse h β galactic background. *The Astrophysical Journal*, 525(2):799, 1999.
- [138] V. Tuchin. *Tissue Optics: Light Scattering Methods and Instruments for Medical Diagnosis*. Spie Press Series. SPIE Optical Engineering Press, 2000.
- [139] Julia L. Sandell and Timothy C. Zhu. A review of in-vivo optical properties of human tissues and its impact on pdt. *Journal of Biophotonics*, 4(11-12):773–787, 2011.
- [140] E. Hecht. *Optics*. Addison-Wesley, 2002.
- [141] L. B. Lucy. Computing radiative equilibria with Monte Carlo techniques. *Astron. Astrophys.*, 344:282–288, 1999.
- [142] Rene Michels, Florian Foschum, and Alwin Kienle. Optical properties of fat emulsions. *Opt. Express*, 16(8):5907–5925, 2008.
- [143] Valerie Nadeau, Martin O’Dwyer, Khaled Hamdan, Iain Tait, and Miles Padgett. In vivo measurement of 5-aminolaevulinic acid-induced protoporphyrin ix photobleaching: a comparison of red and blue light of various intensities. *Photodermatology, Photoimmunology Photomedicine*, 20(4):170–174, 2004.
- [144] R. Valentine. Biological aspects of photodynamic therapy. *Ph.D. Thesis, University of St Andrews*, 2011.
- [145] Stephen T. Flock, Brian C. Wilson, and Michael S. Patterson. Total attenuation coefficients and scattering phase functions of tissues and phantom materials at 633 nm. *Medical Physics*, 14(5):835–841, 1987.
- [146] I Driver, J W Feather, P R King, and J B Dawson. The optical properties of aqueous suspensions of intralipid, a fat emulsion. *Physics in Medicine and Biology*, 34(12):1927, 1989.
- [147] A.J.L Jongen and H.J.C.M Sterenberg. Mathematical description of photobleaching in vivo describing the influence of tissue optics on measured fluorescence signals. *Physics in Medicine and Biology*, 42(9):1701, 1997.

- [148] M. S. Patterson, B.C. Wilson, and R. Graff. In vivo tests of the concept of photodynamic threshold dose in normal rat liver photosensitized by aluminum chlorosulphonated phthalocyanine. *Photochemistry and Photobiology*, 51(3):343–349, 1990.
- [149] Thomas J. Farrell, Brian C. Wilson, Michael S. Patterson, and Malini C. Olivo. Comparison of the in vivo photodynamic threshold dose for photofrin, mono- and tetrasulfonated aluminum phthalocyanine using a rat liver model. *Photochemistry and Photobiology*, 68(3):394–399, 1998.
- [150] Thomas J. Farrell, Michael S. Patterson, and Brian Wilson. A diffusion theory model of spatially resolved, steady state diffuse reflectance for the noninvasive determination of tissue optical properties in vivo. *Medical Physics*, 19(4):879–888, 1992.
- [151] A.E. Karsten, A. Singh, P.A. Karsten, and M.W.H. Braun. Diffuse reflectance spectroscopy as a tool to measure the absorption coefficient in skin: system calibration. *Lasers in Medical Science*, 28(2):437–444, 2013.
- [152] William J. Cottrell, Anne D. Paquette, Kenneth R. Keymel, Thomas H. Foster, and Allan R. Oseroff. Irradiance-dependent photobleaching and pain in delta-aminolevulinic acid-photodynamic therapy of superficial basal cell carcinomas. *Clinical Cancer Research*, 14(14):4475–4483, 2008.
- [153] J. Premru, M. Milanic, and B. Majaron. Monte carlo simulation of radiation transfer in human skin with geometrically correct treatment of boundaries between different tissues. *Proc. SPIE*, 8579:85790Z–85790Z–13, 2013.
- [154] D. Yudovsky and L. Pilon. Rapid and accurate estimation of blood saturation, melanin content, and epidermis thickness from spectral diffuse reflectance. *Appl. Opt.*, 49(10):1707–1719, 2010.
- [155] D. Yudovsky and L. Pilon. Retrieving skin properties from in vivo spectral reflectance measurements. *Journal of Biophotonics*, 4(5):305–314, 2011.
- [156] E. Salomatina, B. Jiang, J. Novak, and A. N. Yaroslavsky. Optical properties of normal and cancerous human skin in the visible and near-infrared spectral range. *Journal of Biomedical Optics*, 11(6):064026–064026–9, 2006.
- [157] D.J. Robinson, H.S. de Bruijn, N. van der Veen, M.R. Stringer, S.B. Brown, and W.M. Star. Fluorescence photobleaching of ala-induced protoporphyrin ix during photodynamic therapy of normal hairless mouse skin: the effect of light dose and irradiance and the resulting biological effect. *Photochem Photobiol*, 67(1):140–9, 1998.
- [158] M.B. Ericson, C. Sandberg, B. Stenquist, F. Gudmundson, M. Karlsson, A-M. Ros, A. Rosèn, O. Larkö, A-M. Wennberg, and I. Rosdahl. Photodynamic therapy of actinic keratosis at varying fluence rates: assessment of photobleaching, pain and primary clinical outcome. *British Journal of Dermatology*, 151(6):1204–1212, 2004.
- [159] T.J. Farrell, R.P. Hawkes, M.S. Patterson, and B.C. Wilson. Modeling of photosensitizer fluorescence emission and photobleaching for photodynamic therapy dosimetry. *Appl. Opt.*, 37(31):7168–7183, 1998.

- [160] A. Usami and N. Kawasaki. Modeling of solar spectral irradiance data from cloudless to overcast skies. *Japanese Journal of Applied Physics*, 51:10NF06, 2012.
- [161] R.E. Bird and C. Riordan. Simple Solar Spectral Model for Direct and Diffuse Irradiance on Horizontal and Tilted Planes at the Earth's Surface for Cloudless Atmospheres. *Journal of Applied Meteorology*, 25:87–97, 1986.
- [162] T.K. Van Heuklon. Estimating atmospheric ozone for solar radiation models. *Solar Energy*, 22(1):63 – 68, 1979.
- [163] B. Diffey. A behavioral model for estimating population exposure to solar ultraviolet radiation. *Photochemistry and Photobiology*, 84(2):371–375, 2008.
- [164] G. Schauburger. Model for the global irradiance of the solar biologically-effective ultraviolet-radiation on inclined surfaces. *Photochemistry and Photobiology*, 52(5):1029–1032, 1990.
- [165] J.C. Finlay and T.H. Foster. Effect of pigment packaging on diffuse reflectance spectroscopy of samples containing red blood cells. *Opt. Lett.*, 29(9):965–967, 2004.
- [166] N. Rajaram, A. Gopal, X. Zhang, and J.W. Tunnell. Experimental validation of the effects of microvasculature pigment packaging on in vivo diffuse reflectance spectroscopy. *Lasers in Surgery and Medicine*, 42(7):680–688, 2010.
- [167] Lars O. Svaasand, Pius Wyss, Marie-Therese Wyss, Yona Tadir, Bruce J. Tromberg, and Michael W. Berns. Dosimetry model for photodynamic therapy with topically administered photosensitizers. *Lasers in Surgery and Medicine*, 18(2):139–149, 1996.
- [168] Willem M. Star, Maurice C. G. Aalders, Arnoldo Sac, and Henricus J. C. M. Sterenberg. Quantitative model calculation of the time-dependent protoporphyrin ix concentration in normal human epidermis after delivery of ala by passive topical application or iontophoresis. *Photochemistry and Photobiology*, 75(4):424–432, 2002.
- [169] J. Tyrrell, C. Thorn, A. Shore, S. Campbell, and A. Curnow. Oxygen saturation and perfusion changes during dermatological methylaminolaevulinate photodynamic therapy. *British Journal of Dermatology*, 165(6):1323–1331, 2011.
- [170] Baochang Liu, Thomas J Farrell, and Michael S Patterson. A dynamic model for ala-pdt of skin: simulation of temporal and spatial distributions of ground-state oxygen, photosensitizer and singlet oxygen. *Physics in Medicine and Biology*, 55(19):5913, 2010.
- [171] B.W. Henderson, T.M. Busch, L.A. Vaughan, N.P. Frawley, D. Babich, T.A. Sosa, J.D. Zollo, A.S. Dee, M.T. Cooper, D.A. Bellnier, W.R. Greco, and A.R. Oseroff. Photofrin photodynamic therapy can significantly deplete or preserve oxygenation in human basal cell carcinomas during treatment, depending on fluence rate. *Cancer Research*, 60(3):525–529, 2000.
- [172] Johanna T. H. M. van den Akker, Vladimir Iani, Willem M. Star, Henricus J. C. M. Sterenberg, and Johan Moan. Topical application of 5-aminolevulinic acid hexyl ester and

- 5-aminolevulinic acid to normal nude mouse skin: Differences in protoporphyrin ix fluorescence kinetics and the role of the stratum corneum. *Photochemistry and Photobiology*, 72(5):681–689, 2000.
- [173] Maurice C. G. Aalders, Nine Van Der Vange, Willem M. Star, and Henricus J. C. M. Sterenberg. A mathematical evaluation of dose-dependent ppix fluorescence kinetics in vivo. *Photochemistry and Photobiology*, 74(2):311–317, 2001.
- [174] A. Casas, H. Fukuda, G. Di Venosa, and A.M. Del C. batlle. The influence of the vehicle on the synthesis of porphyrins after topical application of 5-aminolaevulinic acid. implications in cutaneous photodynamic sensitization. *British Journal of Dermatology*, 143(3):564–572, 2000.
- [175] Z. Malik, G. Kostenich, L. Roitman, B. Ehrenberg, and A. Orenstein. Topical application of 5-aminolevulinic acid, dmsa and edta: protoporphyrin ix accumulation in skin and tumours of mice. *Journal of Photochemistry and Photobiology B: Biology*, 28(3):213 – 218, 1995.
- [176] Petras Juzenas, Asta Juzeniene, Vladimir Iani, and Johan Moan. Depth profile of protoporphyrin ix fluorescence in an amelanotic mouse melanoma model. *Photochemistry and Photobiology*, 85(3):760–764, 2009.
- [177] Danielle I Kuijpers, Monique R Thissen, Carleine A Thissen, and Martino H Neumann. Similar effectiveness of methyl aminolevulinate and 5-aminolevulinate in topical photodynamic therapy for nodular basal cell carcinoma. *Journal of drugs in dermatology : JDD*, 5(7):642–645, 2006.
- [178] Peter Schleier, Alexander Berndt, Susann Kolossa, Witold Zenk, Peter Hyckel, and Stefan Schultze-Mosgau. Comparison of aminolevulinic acid (ala)-thermogel-pdt with methyl-ala-thermogel-pdt in basal cell carcinoma. *Photodiagnosis and Photodynamic Therapy*, 4(3):197 – 201, 2007.
- [179] Jean-Michel Gaullier, Kristian Berg, Qian Peng, Helle Anholt, Pål Kristian Selbo, Li-Wei Ma, and Johan Moan. Use of 5-aminolevulinic acid esters to improve photodynamic therapy on cells in culture. *Cancer Research*, 57(8):1481–1486, 1997.
- [180] Ronan M. Valentine, Sally H. Ibbotson, C. Tom A. Brown, Kenny Wood, and Harry Moseley. A quantitative comparison of 5-aminolaevulinic acid- and methyl aminolevulinate-induced fluorescence, photobleaching and pain during photodynamic therapy. *Photochemistry and Photobiology*, 87(1):242–249, 2011.
- [181] Irene Salas-García, Félix Fanjul-Vélez, and José Luis Arce-Diego. Photosensitizer absorption coefficient modeling and necrosis prediction during photodynamic therapy. *Journal of Photochemistry and Photobiology B: Biology*, 114(0):79 – 86, 2012.
- [182] Irene Salas-García, Félix Fanjul-Vélez, and José Luis Arce-Diego. Superficial radially resolved fluorescence and 3d photochemical time-dependent model for photodynamic therapy. *Opt. Lett.*, 39(7):1845–1848, 2014.

- [183] D. Braichotte, J.-F. Savary, T. Glanzmann, P. Monnier, G. Wagnières, and H. Van Den Bergh. Optimizing light dosimetry in photodynamic therapy of the bronchi by fluorescence spectroscopy. *Lasers in Medical Science*, 11(4):247–254, 1996.
- [184] Thomas J. Farrell, Robert P. Hawkes, Michael S. Patterson, and Brian C. Wilson. Modeling of photosensitizer fluorescence emission and photobleaching for photodynamic therapy dosimetry. *Appl. Opt.*, 37(31):7168–7183, 1998.
- [185] Jessica Tyrrell, Sandra M. Campbell, and Alison Curnow. Monitoring the accumulation and dissipation of the photosensitizer protoporphyrin ix during standard dermatological methyl-aminolevulinic acid photodynamic therapy utilizing non-invasive fluorescence imaging and quantification. *Photodiagnosis and Photodynamic Therapy*, 8(1):30–38, 2011.
- [186] J. Crank. *The mathematics of diffusion* / by J. Crank. Clarendon Press Oxford [England], 2nd ed. edition, 1975.
- [187] J. L. Jiménez Pérez, A. Cruz-Orea, E. Ramón-Gallegos, R. Gutierrez Fuentes, and J. F. Sanchez Ramirez. Photoacoustic spectroscopy to determine in vitro the non radiative relaxation time of protoporphyrin ix solution containing gold metallic nanoparticles. *The European Physical Journal Special Topics*, 153(1):353–356, 2008.
- [188] Asta Juzeniene, Vladimir Iani, and Johan Moan. Clearance mechanism of protoporphyrin {IX} from mouse skin after application of 5-aminolevulinic acid. *Photodiagnosis and Photodynamic Therapy*, 10(4):538–545, 2013.
- [189] C. Louise Campbell, Craig Christison, C. Tom A. Brown, Kenneth Wood, Ronan M. Valentine, and Harry Moseley. 3d monte carlo radiation transfer modelling of photodynamic therapy, 2015.
- [190] A N Bashkatov, E A Genina, V I Kochubey, and V V Tuchin. Optical properties of human skin, subcutaneous and mucous tissues in the wavelength range from 400 to 2000 nm. *Journal of Physics D: Applied Physics*, 38(15):2543, 2005.
- [191] Jose A. Iglesias-Guitian, Carlos Aliaga, Adrian Jarabo, and Diego Gutierrez. A biophysically-based model of the optical properties of skin aging. *Computer Graphics Forum (EUROGRAPHICS 2015)*, 2015.
- [192] George Zonios and Aikaterini Dimou. Light scattering spectroscopy of human skin in vivo. *Opt. Express*, 17(3):1256–1267, 2009.
- [193] M.J.C Van Gemert, S.L. Jacques, H.J.C.M. Sterenborg, and W. M. Star. Skin optics. *Biomedical Engineering, IEEE Transactions on*, 36(12):1146–1154, 1989.
- [194] Aletta E. Karsten and Jacoba E. Smit. Modeling and verification of melanin concentration on human skin type. *Photochemistry and Photobiology*, 88(2):469–474, 2012.
- [195] Tadeusz Sarna and Harold A. Swartz. *The Physical Properties of Melanins*, pages 311–341. Blackwell Publishing Ltd, 2007.

- [196] Miranda A. Farage, Kenneth W. Miller, and Howard I. Maibach. Degenerative changes in aging skin. In Miranda A. Farage, Kenneth W. Miller, and Howard I. Maibach, editors, *Textbook of Aging Skin*, pages 25–35. Springer Berlin Heidelberg, 2010.
- [197] Christina Raschke and Peter Elsner. Skin aging: A brief summary of characteristic changes. In Miranda A. Farage, Kenneth W. Miller, and Howard I. Maibach, editors, *Textbook of Aging Skin*, pages 37–43. Springer Berlin Heidelberg, 2010.
- [198] Jeanette M. Waller and Howard I. Maibach. Age and skin structure and function, a quantitative approach (i): blood flow, pH, thickness, and ultrasound echogenicity. *Skin Research and Technology*, 11(4):221–235, 2005.
- [199] B.A. Gilchrist and G. Szabo. Effects of ageing and chronic sun exposure on melanocytes in human skin. *Journal of Investigative Dermatology*, 73(2):141–143, 1979.
- [200] Chung J, Yano K, Lee M, and et al. Differential effects of photoaging vs intrinsic aging on the vascularization of human skin. *Archives of Dermatology*, 138(11):1437–1442, 2002.
- [201] Y. Lee and K. Hwang. Skin thickness of Korean adults. *Surgical and Radiologic Anatomy*, 24(3-4):183–189, 2002.
- [202] C.V. Nissen, P.A. Philipsen, and H.C. Wulf. Protoporphyrin IX formation after topical application of methyl aminolaevulinate and 6-aminolaevulinic acid declines with age. *British Journal of Dermatology*, 173(3):760–766, 2015.
- [203] CL Campbell, K Wood, CTA Brown, and H Moseley. Monte Carlo modelling of photodynamic therapy treatments comparing clustered three dimensional tumour structures with homogeneous tissue structures. *Physics in medicine and biology (in press)*, 2016.
- [204] Valery V Tuchin, Sergei R Utz, and Ilya V Yaroslavsky. Tissue optics, light distribution, and spectroscopy. *Optical Engineering*, 33(10):3178–3188, 1994.
- [205] Lihong Wang, Steven L Jacques, and Liqiong Zheng. MCML - Monte Carlo modeling of light transport in multi-layered tissues. *Computer methods and programs in biomedicine*, 47(2):131–146, 1995.
- [206] Mitchell A Davis, SM Shams Kazmi, Adrien Ponticorvo, and Andrew K Dunn. Depth dependence of vascular fluorescence imaging. *Biomedical optics express*, 2(12):3349–3362, 2011.
- [207] Patrick Scheibe, Ulf-Dietrich Braumann, Jens-Peer Kuska, Markus Löffler, Jan C Simon, Uwe Paasch, and Tino Wetzig. Image-processing chain for a three-dimensional reconstruction of basal cell carcinomas. *Experimental dermatology*, 19(7):689–691, 2010.
- [208] A Neil Crowson. Basal cell carcinoma: biology, morphology and clinical implications. *Modern pathology*, 19:S127–S147, 2006.
- [209] Bruce G. Elmegreen. Intercloud structure in a turbulent fractal interstellar medium. *The Astrophysical Journal*, 477(1):196, 1997.

- [210] Kenneth Wood, LM Haffner, RJ Reynolds, John S Mathis, and Greg Madsen. Estimating the porosity of the interstellar medium from three-dimensional photoionization modeling of h ii regions. *The Astrophysical Journal*, 633(1):295, 2005.
- [211] Jacqueline Hewett, Tracy McKechnie, Wilson Sibbett, James Ferguson, Colin Clark, and Miles Padgett. Fluorescence detection of superficial skin cancers. *Journal of Modern Optics*, 47(11):2021–2027, 2000.
- [212] Dora P Ramirez, Cristina Kurachi, Natalia M. Inada, Lilian T. Moriyama, Ana G. Salvio, José D. Vollet Filho, Layla Pires, Hilde H. Buzzá, Cintia Teles de Andrade, Clovis Greco, and Vanderlei S. Bagnato. Experience and {BCC} subtypes as determinants of malpdt response: Preliminary results of a national brazilian project. *Photodiagnosis and Photodynamic Therapy*, 11(1):22 – 26, 2014.
- [213] R Core Team. *R: A Language and Environment for Statistical Computing*. R Foundation for Statistical Computing, Vienna, Austria, 2013.
- [214] Ulas Sunar, Daniel J. Rohrbach, Janet Morgan, Natalie Zeitouni, and Barbara W. Henderson. Quantification of ppix concentration in basal cell carcinoma and squamous cell carcinoma models using spatial frequency domain imaging. *Biomed. Opt. Express*, 4(4):531–537, 2013.
- [215] Julian J. Faraway. *Linear Models with R*. Chapman Hall/CRC, 2004.
- [216] Julian J. Faraway. *Extending Linear Models with R: Generalized Linear, Mixed Effects and Nonparametric Regression Models*. Chapman Hall/CRC, 2006.
- [217] Alain Zuur, Elena N. Ieno, Neil Walker, Anatoly A. Saveiliev, and Graham M. Smith. *Mixed Effects Models and Extensions in Ecology with R*. Springer, 2009.
- [218] Even Angell-Petersen, Roar Sørensen, Trond Warloe, Ana Maria Soler, Johan Moan, Qian Peng, and Karl-Erik Giercksky. Porphyrin formation in actinic keratosis and basal cell carcinoma after topical application of methyl 5-aminolevulinate. *Journal of investigative dermatology*, 126(2):265–271, 2006.
- [219] Christine B. Warren, Sara Lohser, Lauren C. Wene, Brian W. Pogue, Philip L. Bailin, and Edward V. Maytin. Noninvasive fluorescence monitoring of protoporphyrin ix production and clinical outcomes in actinic keratoses following short-contact application of 5-aminolevulinate. *Journal of Biomedical Optics*, 15(5):051607–051607–8, 2010.
- [220] A.J. Dobson. *An Introduction to Generalized Linear Models, Second Edition*. Chapman & Hall/CRC Texts in Statistical Science. Taylor & Francis, 2010.
- [221] Olena Kulyk, Sally H. Ibbotson, Harry Moseley, Ronan M. Valentine, and Ifor D.W. Samuel. Development of a handheld fluorescence imaging device to investigate the characteristics of protoporphyrin {IX} fluorescence in healthy and diseased skin. *Photodiagnosis and Photodynamic Therapy*, 12(4):630 – 639, 2015.

- [222] Timothy C Zhu, Michele M Kim, Xing Liang, Jarod C Finlay, and Theresa M Busch. In-vivo singlet oxygen threshold doses for pdt. *Photonics & lasers in medicine*, 4(1):59–71, 2015.
- [223] Jennifer K Barton. Dynamic changes in optical properties. In *Optical-Thermal Response of Laser-Irradiated Tissue*, pages 321–349. Springer, 2011.
- [224] Caihua Liu, Rui Shi, Min Chen, and Dan Zhu. Quantitative evaluation of enhanced laser tattoo removal by skin optical clearing. *Journal of Innovative Optical Health Sciences*, page 1541007, 2014.
- [225] Caerwyn Ash, Kelvin Donne, Gwenaelle Daniel, Godfrey Town, Marc Clement, and Ronan Valentine. Mathematical modeling of the optimum pulse structure for safe and effective photo epilation using broadband pulsed light. *Journal of Applied Clinical Medical Physics*, 13(5), 2012.
- [226] M. Sam Eljamel, Carol Goodman, and Harry Moseley. Ala and photofrin fluorescence-guided resection and repetitive pdt in glioblastoma multiforme: a single centre phase iii randomised controlled trial. *Lasers in Medical Science*, 23(4):361–367, 2007.
- [227] Slawomir G. Kata, Omar M. Aboumarzouk, Abdullah Zreik, Bhaskar Somani, Sarfraz Ahmad, Ghulam Nabi, Ronald Buist, Carol Goodman, Piotr Chlosta, Tomasz Golabek, and Harry Moseley. Photodynamic diagnostic ureterorenoscopy: A valuable tool in the detection of upper urinary tract tumour. *Photodiagnosis and Photodynamic Therapy*, 2015.
- [228] Denise Bechet, Serge R. Mordon, François Guillemin, and Muriel A. Barberi-Heyob. Photodynamic therapy of malignant brain tumours: A complementary approach to conventional therapies. *Cancer Treatment Reviews*, 40(2):229 – 241, 2014.
- [229] M Sam Eljamel. Brain pdd and pdt unlocking the mystery of malignant gliomas. *Photodiagnosis and Photodynamic therapy*, 1(4):303–310, 2004.
- [230] C.T. Andrade, J.D. Vollet-Filho, A.G. Salvio, V.S. Bagnato, and C. Kurachi. Identification of skin lesions through aminolaevulinic acid-mediated photodynamic detection. *Photodiagnosis and Photodynamic Therapy*, 11(3):409 – 415, 2014.
- [231] S. Grapengiesser, F. Gudmundsson, O. Larkö, M. Ericson, A. Rosén, and A.-M. Wenberg. Pain caused by photodynamic therapy of skin cancer. *Clinical and Experimental Dermatology*, 27(6):493–497, 2002.